MODELING OF PERIODIC DIELECTRIC STRUCTURES (ELECTROMAGNETIC CRYSTALS)

by

John David Shumpert

A dissertation submitted in partial fulfillment
of the requirements for the degree of
Doctor of Philosophy
(Electrical Engineering)
in The University of Michigan
2001

Doctoral Committee:

Professor Linda P. B. Katehi, Chair
Associate Professor Kamal Sarabandi
Emeritus Professor Thomas B. A. Senior
Professor Wayne E. Stark

"Almighty God, Who hast created man in Thine own Image, and made him a living soul that he might seek after Thee, and have dominion over Thy creatures, teach us to study the works of Thy hands, that we may subdue the earth to our use, and strengthen our reason for Thy service; and so to receive Thy blessed word, that we may believe on Him whom Thou hast sent, to give us the knowledge of salvation and the remission of our sins. All which we ask in the name of the same Jesus Christ, our Lord."

— James Clerk Maxwell (1831–1879)

Sola Deo Gloria

ACKNOWLEDGMENTS

I am grateful to Professor Linda P. B. Katehi for serving as my dissertation chair and for her continued support of my work. I also appreciate Professors Kamal Sarabandi, Thomas B. A. Senior, and Wayne E. Stark for their welcomed comments and suggestions and for graciously giving of their time to serve on my dissertation committee.

I am grateful to the National Science Foundation without whose financial support, in the form of the National Science Foundation Graduate Research Fellowship, some of my graduate work would not have been possible. I also gratefully acknowledge the support of the Department of Defense Research and Engineering (DDR&E) Multidisciplinary University Research Initiative (MURI) on "Low Energy Electronics Design for Mobile Platforms" managed by the Army Research Office (ARO) under Grant DAAH04–96–1–0377.

The completion of an extended period of directed research that is required to obtain an advanced degree is the product of hard work, perseverance, and the continued support of family, friends, and my fellow comrades-in-arms. The Radiation Laboratory at the University of Michigan is not simply the group of offices, laboratories, and classrooms that comprise the major portion of the third floor of the EECS Building; it is the collection of faculty, staff, and students who live and work together every day. In particular, staff members Mike Angelini, Michelle Shepherd, Carol Truskowski, and Patti Wolfe were vaults of hidden knowledge for myself and the other graduate students in the Lab. Carol, your indefatigable spirit is an invaluable asset to the graduate students in the Lab. I would like to thank my comrades-in-arms, current and former University of Michigan Radiation Lab graduate students Lars Andersen, Scott Barker, Andy Brown, Mark Casciato, Bill Chappell, Rashaunda Henderson, Katherine Herrick, Stephané Legault, Sergio Pacheco, Ron Reano, and Kyoung Yang, for the hours of enjoyable conversation and fun. I am thankful to Bill Chappell, Saqib Jalil, and Tom Ellis, for their help with the fabrication and design aspects of the slot antenna work.

I would like to especially thank Mark Casciato, Katherine Herrick, Stephané Legault, and Sergio Pacheco, without whom my short time at the University of Michigan would have seemed an eternity. I will dearly miss our many "not-so-technical" discussions. Your friendship has been and remains an invaluable asset to me and to my family.

I am very blessed to have the love and support of my family. Dad, I am now your colleague; you have always been my biggest fan. Mom, I thank you for your ever encouraging and joyful spirit. Simple words seem inadequate to express my love for you both and my appreciation for your continual prayers throughout this journey. Jim and Stephanie, your confidence in my ability to persevere was a welcomed voice at the other end of the telephone.

Caleb, I thank you for your unconditional love for Daddy.

> *Breanna, to you I express my deepest appreciation. Your prayers, unconditional love, constant encouragement, and unwavering devotion sustained me during the many long days of deriving pages of equations or sitting alone in front of a computer screen desperately debugging long Fortran codes. May our Lord, Jehovah, the God of the Bible, bless you with the desires of your heart for providing me with the strength and perseverance to complete this work.*

PREFACE

Electromagnetic band-gap (EBG) materials, often termed electromagnetic crystals or photonic band-gap (PBG) materials, are found to have unique properties that are advantageous for applications involving semiconductor integrated circuits (ICs). Preliminary results suggest that at microwave and millimeter-wave frequencies the propagation characteristics of these materials can be manipulated by carefully designing and fabricating periodic structures composed of regions of differing dielectric constants. Researchers from the diverse fields of classical electromagnetics, solid-state physics, optics, material science, condensed matter physics, and semiconductor physics, are actively contributing to this rediscovered field of physics. Active areas of electromagnetic and photonic crystal research include but are not limited to microwave and millimeter-wave antenna structures, quasi-optical microwave arrays, photonic crystal integrated circuits, high- and low-Q electromagnetic resonators, quantum optical electromagnetic cavity effects, and optical nano-cavities. In addition, sonic band-gap materials or artificial acoustic crystal substrates, are being developed and could impact sonar.

Recent attention in the field of EBGs has focused on the elimination of surface-wave formation in planar microwave and millimeter-wave antenna applications. A number of numerical techniques, including finite difference methods, finite element methods, spectral domain analysis, and integral equation (IE)/moment methods (MoM), have been implemented to help understand the properties of surface and leaky waves on a layered, periodic structure. The IE/MoM approach is a useful approach because information about the physical system (propagation constants, mode structure, etc.) can be obtained easily and directly from the formulation. A full-wave IE/MoM code has been developed to determine the band structure (propagating modes) of periodic one- and two-dimensional inhomogeneous dielectric regions for specific use in planar antenna applications. This work derives the integral equation approach along with several examples showing the unique spectral characteristics of EBGs.

TABLE OF CONTENTS

LIST OF TABLES

Table

LIST OF FIGURES

Figure

LIST OF APPENDICES

CHAPTER 1

Introduction

For many years, electromagnetic theorists were provided with two primary means of predicting electromagnetic phenomena: measurements and analytical solutions. Measurements of electromagnetic systems provide the scientist/engineer with reams of data and a physical intuition for the mechanisms involved in producing the response. However, the feasibility of fabricating new devices for each design change can be time-consuming and, depending on the architecture or application, expensive. These two limitations are often addressed by using analytical techniques to predict electromagnetic behavior. Solution techniques including asymptotic analysis, variational analysis, integral transforms, contour integration, and perturbation theory are the staple of analytical electromagnetic prediction and design. Improvements in computer speed and memory helped to provide the framework for the rapid development of computational electromagnetics (CEM) methods including, but not limited to, the finite element (FE) method, the finite difference methods in both time (FDTD) and frequency domains (FDFD), the transmission line matrix (TLM) method, and method of moments (MoM) solutions. CEM techniques have added significantly to the toolboxes of scientists and engineers alike. In fact, the hybridization of many of the aforementioned techniques to solve large and complex problems may provide revolutionary new solution capabilities for the near future.

With the recent advent of general purpose electromagnetics (EM) codes[1], a third solution method has been introduced to the technical community, *simulation*. One might conclude that the availability of high performance commercial EM software has mitigated the need to solve specific electromagnetic problems by writing original computer codes. For example, the late availability of commercial codes that incorporate periodic boundary

[1] An extensive repository of commercial general purpose computational electromagnetic codes and locally free software is found at the Electromagnetics Library (EMLIB), `http://emlib.jpl.nasa.gov`.

conditions is a prime example of a recent simulation tool that has renewed the interest in developing new circuit and antenna devices. Certainly, one of the advantages of the general EM solver is its ability to solve a wide variety of problems. The disadvantage of the general EM solver is its inability to address specific theoretical or numerical issues that can significantly affect the accuracy of a solution. This is not to say that general EM solvers are not extremely useful for design and have not revolutionized the way that electromagnetics research is being performed. However, every CEM code writer will attest to the many nuances and small singular changes that must be included in an original numerical code to achieve maximum performance. Complex, real-world problems are not always amenable to general purpose solutions and often require customized solutions and programs to solve them. Computational electromagnetics which includes electromagnetic theory, sophisticated analytical techniques, and numerical methods is used to characterize and analyze the merits and demerits of a new design.

The rapidly growing field of wireless communications is providing new opportunities to develop novel structures that will enhance or even replace existing circuits and antennas. Devices that incorporate periodicity as a key feature of the design are promising unrivaled performance in microwave circuits and antennas. Periodic electromagnetic structures are commonplace in many of the items we rely on every day – from the magnetron in a microwave oven to the ultraviolet radiation protection provided by polarized sunglasses. Commenting on the recent inundation of applications for periodic structures, Maddox [57] remarks, "If only it were possible to make materials [photonic band-gap materials] in which electromagnetic waves cannot propagate at certain frequencies, all kinds of almost-magical things would happen." It is important, nevertheless, to dispel some of the myths about what photonic band-gap (PBG) materials are and are not. PBGs are periodic dielectric and/or metallic structures that when designed and implemented correctly can improve the performance of specific devices. PBGs are not magical structures that defy basic laws of physics and have only of late appeared in the literature.

Photonic band-gap materials, sometimes referred to as *electromagnetic band-gap (EBG)* materials, *electromagnetic crystals (EC)* or *photonic crystals*, are inhomogeneous structures composed of periodic regions of material with a specific permittivity immersed in a homogeneous background of different permittivity. These artificial, composite structures have been found to have unique properties that are advantageous in applications involving semiconductor integrated circuits. Researchers from the diverse fields of classical electromagnetics, solid-state physics, optics, material science, condensed matter physics, and semiconductor physics, are actively contributing to the base of electromagnetic crystal knowledge. Active areas of electromagnetic and photonic crystal research include but are not limited to microwave and millimeter-wave antenna structures, quasi-optical microwave arrays, photonic crystal integrated circuits, high- and low-Q electromagnetic resonators, quantum optical electromagnetic cavity effects, and optical nano-cavities. In addition, sonic band-gap materials or artificial acoustic crystal substrates, are being developed and could impact sonar.

From solid-state theory, we know that semiconductors allow electron conduction without scattering only for electrons that have energies within a specific range of energy, often termed *band-gaps*. Electromagnetic wave propagation in periodic dielectric media is analogous to electron-wave propagation in semiconductor crystals. Although fundamentally different propagation mechanisms are involved, preliminary results suggest that at microwave and millimeter-wave frequencies the propagation characteristics of these crystals can be manipulated by carefully designing and fabricating structures composed of regions of differing dielectric constants. Early work by Yablonovitch [125] successfully demonstrated that light propagation could be inhibited in certain frequency gaps in special photonic band-gap crystals (PBGs). Scalar-wave-based theories were developed to determine a suitable candidate for the first three-dimensional (3-D) photonic crystal. However, it became apparent that scalar-wave-based solutions were inadequate for the task. Vector-wave-based solutions implemented using the plane wave expansion (PWE) method for Maxwell's equations, being developed concurrently by Leung *et al.* [52], Zhang *et al.* [138], and Ho *et al.* [36], offered the potential of finding a true photonic band-gap structure.[2] Indeed, soon thereafter, a structure that possesses a full photonic band-gap was identified. Theoretical work by Ho *et al.* [36] confirmed the existence and structure of the first (3-D) photonic crystal, the diamond dielectric structure. Concurrently, band structures for two-dimensionally periodic structures were being calculated in a similar manner by Plihal *et al.* [73]. However, it was McCall *et al.* [60] who were the first to calculate *and* measure microwave propagation and reflection in a two-dimensional (2-D) array of low-loss high-dielectric-constant cylinders. With the confirmation of realizable 2-D and 3-D photonic crystal structures, attention shifted to applying these materials in new designs and architectures.

Reviews of early photonic band-gap research can be found in special issues of the *Journal of the Optical Society of America B* [1] and the *Journal of Modern Optics* [2]. Recently, a book outlining photonic band theory and covering a wide range of photonic crystal applications was published by Joannopoulos [38]. Although previous research had focused almost

[2] Earlier experimental work had only verified a pseudo-band-gap, not a true photonic band-gap. See [126].

exclusively on optical and quasi-optical applications for the PBG materials, it quickly became apparent that numerous applications for similar periodic structures in the microwave and infrared frequency range were being developed. Consequently, a joint special issue of the *IEEE Transactions on Microwave Theory and Techniques* [3] and the *Journal of Lightwave Technology* [4] was published to catalog the design, synthesis, and application of electromagnetic crystal structures begin developed in the microwave and millimeter-wave community. Concurrently, a special issue that focused on the particular theoretical and numerical aspects of photonic band-gap structure research was released by the journal *Electromagnetics* [5].

It is the purpose of this work to analyze periodic structures to determine effective and realizable uses for microwave circuits and antennas. In Chapter 2, full-wave integral equation (IE)/method of moments (MoM) solutions are developed and implemented to determine the band structure (propagating modes) of a periodic, one-dimensional inhomogeneous dielectric region. A single electric field integral equation (EFIE) or coupled EFIEs incorporating both the periodic free-space Green's function (1-D) and equivalent electric polarization currents are formulated to determined the quantities of interest. Subsequently, the geometry and integral equation(s) are discretized, and the method of moments is used to numerically solve the resulting matrix equation. A nontrivial solution for the fields requires the matrix determinant to be zero, which results in a characteristic equation. The eigenvalues (propagation constants) are obtained from the roots of this equation. For a lossless structure, the propagation constants of a guided wave are real numbers. However, in the stopbands, the propagation constants are complex-valued. To validate the solution obtained through the use of the IE/MoM approach, the solution of the exact eigenvalue equation for the one-dimensional periodic problem is also obtained using the plane wave expansion (PWE) method.

In Chapter 3, similar approaches as implemented in Chapter 2 are used to extend the solution to two-dimensionally periodic media. Additional integral equation (IE)/method of moments (MoM) codes are developed and implemented, but this time to determine the band structure (propagating modes) of a periodic, two-dimensional inhomogeneous dielectric region. A single EFIE or coupled EFIEs are formulated using a periodic Green's function (2-D) along with equivalent electric polarization currents, and the method of moments is again used to numerically solve the resulting matrix equation. The exact eigenvalue equation for the two-dimensional periodic problem is solved as before using the PWE method to verify the IE/MoM solution. To simplify the computation of the band structure for two-dimensionally periodic media, *effective medium theory* is applied in Section 3.4 to reduce the two-dimensional periodic structure to a one-dimensional equivalent structure. This useful technique can be applied when the period of the structure is much smaller than the wavelength.

Recently, Ansoft, a leading developer of computational electromagnetic software, extended the capabilities of their 3-D commercial finite element software package to include linked boundary conditions, their particular implementation of periodic boundary conditions. The new capability enables Ansoft to perform new calculations on infinite arrays similar to the waveguide simulator concept developed in the 1960s to determine array performance without building an entire array assembly. A number of modeling methodologies including direct-transmission methods, dispersion diagram methods, and reflection phase analysis methods were examined to test the new linked boundary conditions [77]. To validate the accuracy of the direct-transmission method, Ansoft chose to repeat the solution developed in Chapter 3 and published by this author *et al.* in [91] to determine the band structure (propagating modes) of a periodic, two-dimensional inhomogeneous dielectric region. The confidence in the accuracy of the full-wave integral equation (IE)/method of moments (MoM) solution developed in this work provides a standard with which the new linked boundary condition solution could be compared.

A number of researchers have designed electromagnetic crystal structures for use in planar antenna and circuit applications, particularly for use as reflectors in planar dipole antenna structures [18, 21, 17, 41, 95, 97]. Planar antennas are ideal for use in many wireless networks including personal communications systems (PCS) and mobile satellite communications. Microstrip antennas are of interest to many wireless users because of their low aerodynamic profile (survivability/durability issue), light weight (volume/size), and low cost. Microstrip antennas also have the advantage of being both conformal and easily integrated into thin-film circuits. Unfortunately, microstrip antennas have relatively low gain and narrow bandwidths due to substrate surface wave formation. By designing special artificial substrates, surface wave formation may be reduced or even eliminated in some planar antennas. This would dramatically increase both the available bandwidth and gain to levels usually reserved for non-planar antennas. To this end, periodic structures may serve as the material that can change the physical properties of substrates used in fabricating planar circuits and antennas.

Only recently, have researchers developed periodic structures for application in slotted antennas. Leung *et al.* [53] measured the radiation patterns of a slot antenna placed on a layer-by-layer photonic band gap crystal. For planar antennas operating at a frequency in the band-gap of the three-dimensional PBG crystal, energy which would have been radiated into the substrate is reflected. However, at the interface between the PBG and the air, the period of the PBG is broken and a parasitic mode (surface state) can exist. These surface states decrease the efficiency by stripping power away from the radiating element. However, by fabricating a resonant slot over a reflecting back plate and filling the resulting parallel-plate with an appropriately designed artificial electromagnetic band-gap structure, noticeable enhancements in both radiation pattern and bandwidth can be achieved using a significantly lower profile than traditional designs. This design is detailed extensively in Appendix D of this work.

As the need for very wideband, omni-directional antennas for use in mobile communication networks grows at an increasing rate, so does the need to develop custom solutions (and the resulting codes) for novel antenna architectures and designs. The salient properties of the antenna, such as its radiation pattern and efficiency, its input impedance, bandwidth and gain, are all determined by the antenna's electrical size, physical configuration, and the environment in which it is located. In order to optimize the performance of the antenna, a number of design parameters must be considered. Element shape, resonant frequency, gain, and bandwidth of the individual element must be properly chosen. For planar circuits and antennas, substrate characteristics must be designed that take into account the effect of dispersion on the effective dielectric constant and the effect of substrate surface wave formation. Other concerns, including the environmental effects of temperature, humidity, and aging; the mechanical concerns of vibration effects and durability; and the ease of conformability/machinability must also be addressed. Additionally, feed structures must be designed to minimize insertion loss, to maximize space utilization, and to minimize discontinuities.

Until recently [77], general EM solvers were unable to solve even simple periodic structures such as artificial dielectrics or large antenna arrays. Consequently, custom codes are being developed to characterize important parameters such as the reflection coefficient, radiation pattern, and radiation efficiency for planar antennas mounted on layered periodic substrates. Significant attention has been directed to developing an entire class of structures termed *frequency selective surfaces* [66]. A frequency selective surface is usually designed to transmit or reflect electromagnetic radiation within a band of frequencies (or within specific angular bands) from propagating through the surface. This is often accomplished by placing metallic patch elements or aperture elements, such as annular rings, crossed slots, crossed dipoles, or jerusalem crosses, in a periodic fashion on the surface of a dielectric layer. Radiation near the resonant frequency of the element will be transmitted or reflected through the surface as the design permits. Applications for such structures include broadband microwave antenna radome design, narrow-band frequency selective surfaces, and polarizers. These structure are often evaluated using a generalized scattering matrix technique [135] that cascades the propagation through the different layers. Less attention has been focused on three-dimensional frequency selective layers (volumes). The solutions developed in Chapters 4 and 5 of this work are amenable to FSS design and have applications both for substrate and superstrate design.

Recent numerical work in determining the microwave scattering from periodic material implants in a layered medium has been done by Sarabandi [85], Sarabandi *et al.* [87], Tsay *et al.* [114], Yang [130, 134], and Yang *et al.* [135, 136]. In Chapter 4, the solution by Sarabandi [84] for the two-dimensional scattering from an inhomogeneous periodic layer above a half-space layered medium is extended to general three-dimensional scattering from an inhomogeneous doubly periodic layer above a half-space layered medium. The solution of this problem is derived and implemented using a full-wave integral equation/method of moments approach similar to the formulation for the one- and two-dimensional periodic structures of Chapters 2 and 3.

Of particular concern in the solution of periodic structures is the convergence of the resulting Floquet series. Even though the contribution of the off-plane periodic elements converges very quickly, the convergence of the on-plane periodic elements is notoriously slow. In order to compute the impedance matrix elements in a reasonable amount of time, various series acceleration techniques and transformations have been suggested [42]. Summation acceleration techniques convert a slowly converging series to a rapidly converging one by allowing the series to be transformed into a second series that converges to the same limit but does so in a rapid fashion. For the problems of interest in Chapter 4, the combination of a Poisson transformation [70] and a Shanks' transformation [90] are successfully implemented to improve both the speed and the accuracy of the impedance matrix element computations. This is the first known successful implementation of a Shanks' transformation applied to each of the series in the double sum found in the planar two-dimensional, periodic free-space Green's function. Additionally, Kummer's method [51] is applied to specific series to compare the convergence rate of these different series acceleration techniques. A complete treatment of these and other series acceleration techniques is found in Section 4.5.

Of interest to the applied microwave community is the implementation of a microstrip patch antenna on a doubly periodic dielectric layered medium. The solution procedure developed in Chapter 4 to determine the scattering from doubly periodic dielectric layered medium is used to validate an equivalent model that replaces the periodic layer with an equivalent uniaxial layered medium. The ability of the model to emulate the periodic layer is validated using plane wave reflection coefficients for various combinations of filling fractions, angles, and permittivities and the limitations of the model are addressed. Subsequently, the solution for a rectangular microstrip patch element radiating over the equivalent uniaxial layered medium is carried out accurately and efficiently using a commercial finite element package packages that incorporates anisotropic substrates. Conclusions about the effect of the anisotropy on various antenna parameters such as resonant length, pattern shape, and array coupling are drawn and numerical examples that illustrate the salient features of the single patch antenna integrated on a uniaxial substrate are presented in Chapter 5.

Traditionally, microstrip patch antennas have been integrated on relatively low permittivity substrates in order to improve antenna performance. Integrating the antenna on higher permittivity substrates is preferred to minimize circuit size and spurious radiation [75, 89] but at the cost of confining the potential radiating energy even more tightly. This trade-off between good antenna performance and good circuit performance is a key design feature found in many microstrip antenna designs. Although a good deal of attention has focused on integrating microstrip patches on homogeneous substrates, many of the practical substrates with higher permittivities in use today such as sapphire have a significant amount of (uniaxial) anisotropy. The primary effect of anisotropy on rectangular patch antenna design is the change in its resonant length (frequency). This is significant because of the narrow bandwidth of the patch itself. The relatively large shift in resonant frequency produced in many of the modern substrates may actually force a rectangular patch designed to operate at a specific frequency to radiate outside of the antenna bandwidth [74]. Additionally, anisotropic effects are found that shape the radiation pattern of the patch and thus in an array configuration, the coupling to other elements. Because uniaxial substrates are often expensive to manufacture and have limited flexibility for design, uniaxial substrates can be emulated (and easily fabricated) by incorporating periodic inclusions in an otherwise homogeneous substrate. The doubly periodic structure can be constructed using simple milling or etching techniques from simple inexpensive, homogeneous substrates. This is significant because some common uniaxial materials such as sapphire that are expensive to grow [6] can be "artificially" replicated easily and inexpensively. Additionally, the artificial nature of the periodic uniaxial substrate permits the creative design of new substrates with the expanded freedom of anisotropic ratio, background permittivity, and/or fabrication technique.

A number of potential applications for the solution techniques developed in this work are outlined in Chapter 6. The specification of an arbitrarily shaped dielectric is one interesting design feature that can be optimized in the solution of the one- and two-dimensional periodic media. Additionally, lattices of dielectric elements with differing dielectric constants can be included to provide additional freedom for the design. Two potential applications for effective medium theory that promise to be of value are the extension of EMT to off-axis propagation in two-dimensional lattices and to out-of-plane propagation in two-dimensional lattices. A number of new applications can be developed using the solution technique implemented in Chapters 4 and 5 including new frequency selective surfaces (volumes), incorporating separate periodicities (non-commensurate periodicities) for each layer, incorporating material implants within each layer of differing relative permittivity (dielectric and/or metallic loading), and the extension of the solution to large planar antenna elements. Perhaps the most significant development would be incorporation of many of the above suggestions to eliminate surface wave formation in planar antenna applications.

CHAPTER 2

One-Dimensional Periodic Dielectric Structures

2.1 Introduction

One-dimensional periodic electromagnetic structures are commonplace in many of the items we rely on every day – from the magnetron in a microwave oven to the ultraviolet (UV) radiation protection provided by polarized sunglasses. In particular, the field of optics is replete with one-dimensional periodic structures. How periodicity is incorporated into each device is what distinguishes one design from another. For example, the direction of period in some structures is in the direction of stratification, whereas in others, the period is in a transverse plane to the direction of stratification. Bragg mirrors (reflectors) are an excellent example of periodicity in the direction of stratification. The highly reflective coatings used in Bragg reflectors are produced by "sandwiching" layers of differing dielectric material with highly reflective properties. A recent example of active research in this area has been reported in [22] where *total* omni-directional reflections from one-dimensional dielectric lattices have been reported. Other application in this class include specialized thin-film waveguiding, quarter-wave stacks, and folded Sôlc filters [137]. Alternating layers of metal and dielectric are being developed constantly that provide almost unbelievable new applications. Transparent metallic structures have been developed that permit the transmission of light over a tunable range of frequencies, effectively blocking both UV and infrared and lower frequencies from propagating through [88]. Optical and quasi-optical researchers have produced new sensor and eye protection devices, heat reflecting windows, better ultraviolet blocking films, transparent electrodes for light emitting diodes, and light crystal displays. The second class of periodicity, corrugation along the surface of a dielectric medium, is used in devices such as diffraction gratings and high-reflectance distributed-

Bragg-reflector (DBR) lasers. Diffraction gratings are the most commonly known application of corrugations and are used to provide certain spectral or angular characteristics for reflection and transmission of electromagnetic radiation. Other interesting applications include distributed-feedback (DFB) lasers where an active layer provides gain, TM-to-TE mode conversion, and forward-backward mode conversion.

For microwave and RF engineers, the gridded traveling wave tube (GTWT) amplifier is a prime example of harnessing the potential power of a periodic device. The GTWT uses a helical waveguide to convert the high-energy of an electron beam to microwave energy and is implemented on almost every airborne radar in the world. At lower frequencies, the remote sensing community is actively studying naturally occurring one-dimensional periodic structures such as traveling ocean waves and periodic geological structures and man-made periodic structures such as periodic vegetation [112].

A fundamental understanding of how electromagnetic fields behave in a periodic medium is required not only to apply these unique properties correctly but also to critique designs or theories where they are applied incorrectly. The foundation for electromagnetic wave propagation in periodic media is provided in Section 2.2. The phase constants for electromagnetic waves propagating in a one-dimensional lattice of dielectric slabs in an air background is found explicitly using two different techniques. The first solution, detailed in Section 2.3, incorporates the use of a Fourier series representation for the periodic field and is determined by solving the one-dimensional wave (differential) equation for periodic media. The second solution is found by deriving an integral equation for the periodic field and numerically solving the resulting linear system and is presented in Section 2.4. A number of representative structures are used in the chapter to show the behavior of electromagnetic fields in one-dimensional periodic media and observations about the salient features of each are discussed. Although theoretical band structures are useful, actual realizable devices that incorporate a design and that can be fabricated also provide valuable insight for understanding the propagation mechanisms at work. An example solution for the microstrip excitation of a one-dimensional periodic dielectric structure is presented in Section 2.5. Since the fields produced by the quasi-TEM mode of the microstrip (for high dielectric constant) are confined relatively close to the microstrip itself, the dielectric substrate is modelled as a hi-Z, low-Z filter. The filter design is shown to match closely to that of periodic plane wave propagation in a lattice of dielectric slabs and to the measured response of the microstrip line itself.

2.2 Fundamental Concepts

2.2.1 Maxwell's Equations

The fundamental equations that form the foundation for electromagnetic theory are Maxwell's equations. Written in differential form, these equations are

$$\nabla \times \mathbf{E} = -\frac{\partial \mathbf{B}}{\partial t} \tag{2.1a}$$

$$\nabla \times \mathbf{H} = \mathbf{J} + \frac{\partial \mathbf{D}}{\partial t} \tag{2.1b}$$

$$\nabla \cdot \mathbf{D} = \rho \tag{2.1c}$$

$$\nabla \cdot \mathbf{B} = 0 \tag{2.1d}$$

where $\mathbf{E}$ is the electric field intensity, $\mathbf{B}$ is the magnetic flux density, $\mathbf{H}$ is the magnetic field intensity, and $\mathbf{D}$ is the electric flux density. The electric current density $\mathbf{J}$ and electric charge density ρ are the sources of the electromagnetic fields.

For linear and isotropic media, $\mathbf{E}$ and $\mathbf{D}$ and $\mathbf{B}$ and $\mathbf{H}$ are related by the constitutive relations

$$\mathbf{D} = \varepsilon_r \varepsilon_0 \mathbf{E} \tag{2.2a}$$

$$\mathbf{B} = \mu_r \mu_0 \mathbf{H}, \tag{2.2b}$$

where ε_0, μ_0, ε_r, and μ_r are the free-space permittivity, free-space permeability, relative permittivity, and relative permeability, respectively.

The equation of continuity provides the relation between the electric charge density and electric current density through

$$\nabla \cdot \mathbf{J} = -\frac{\partial \rho}{\partial t} \tag{2.3}$$

which is statement of the conservation of charge.

The remaining fundamental equation, Lorentz's force equation, determines the total electromagnetic force on a charge q to be

$$\mathbf{F} = q\left(\mathbf{E} + \mathbf{u} \times \mathbf{B}\right) \tag{2.4}$$

where $\mathbf{u}$ is the velocity of the moving charge.

The eight equations, comprised of the four Maxwell's equations (2.1), together with the constitutive relations (2.2), the equation of continuity (2.3), and Lorentz's force equation (2.4), provide the necessary framework to predict all macroscopic electromagnetic interactions. Although the four equations (2.1a)–(2.1d) are not independent, equations (2.1c) and (2.1d) can be derived from (2.1b) and (2.1a) using (2.3).

2.2.2 Propagation of Waves in a Periodic Medium

One of the many interesting problems in mathematical physics is the solution of the wave equation in periodic media. The solution of this type of equation is usually derived using a form of *Floquet's theorem*. Floquet's theorem, as it was originally presented [120], determined a particular periodic solution of Mathieu's equation, the equation of wave motion. Subsequently, this solution was extended for Hill's equation, a generalization of Mathieu's equation, for any periodic function, providing the basis for one of the great successes in applied physics: quantum band theory. Band theory, which describes the properties of electrons in a periodic potential due to the atomic arrangement of atoms in a crystal, is the foundation for the understanding of electronic transport in metals, semiconductors, and insulators. The solution of the periodic potential problem can be expressed in mathematical form as Bloch's theorem. Bloch's theorem states that the eigenfunctions of the Schrödinger equation for a periodic potential are the product of a plane wave and a function which has the same period as the periodic potential [98]. A number of similarities can be seen in the solution of electron wave propagation in semiconductors and electromagnetic wave propagation in periodic dielectric media, and Bloch's theorem can be extended to electromagnetic wave propagation in periodic media.

For propagating modes in a periodic dielectric structure, the field in an adjacent cell is related by a complex constant. That is,

$$E(x,y,z+a) = E(x,y,z)\ e^{-j\beta_0 a} \tag{2.5}$$

where $E(x,y,z)$ is a periodic function of z with period a and β_0 is the phase constant in the z direction. If the propagating mode in the structure has the form

$$E(x,y,z) = E_p(x,y,z)\ e^{-j\beta_0 z} \tag{2.6}$$

where $E_p(x,y,z)$ is a periodic function of z with period a, then

$$E(x,y,z+a) = E_p(x,y,z+a)\ e^{-j\beta_0(z+a)}. \tag{2.7}$$

Since $E_p(x,y,z)$ is periodic with period a,

$$E_p(x,y,z+a) = E_p(x,y,z). \tag{2.8}$$

Substituting (2.8) into (2.7) yields

$$E(x,y,z+a) = E_p(x,y,z)\ e^{-j\beta_0(z+a)}. \tag{2.9}$$

But, using (2.6),

$$E(x, y, z + a) = E(x, y, z)\; e^{-j\beta_0 a}, \tag{2.10}$$

which is exactly (2.5), a statement of Floquet's (or Bloch's) theorem.

From the theory of Fourier series, the periodic electric field with period a can be expanded as a periodic function in x and prescribed phase constant β_0 and is given by

$$E(x, y, z) = \sum_n E_n(x, y)\; e^{-j\frac{2\pi n}{a}z}\; e^{-j\beta_0 z} = \sum_n E_n(x, y)\; e^{-j\beta_n z} \tag{2.11}$$

where

$$E_n(x, y) = \frac{1}{a}\int_0^a E_n(x, y, z)\; e^{j\frac{2\pi n}{a}z}\; dz$$

are the coefficients that serve to represent the dependence on x and y, and

$$\beta_n = \beta_0 + \frac{2\pi n}{a}$$

is the phase constant of the n^{th} harmonic.

Thus, the field in a periodic structure can be expanded in an infinite set of harmonics through Floquet's theorem, each with frequency f and propagation constant β_n. The phase velocity ν_n of the n^{th} harmonic is

$$\nu_n = \frac{\omega}{\beta_n} = \frac{\omega}{\beta_0 + \frac{2\pi n}{a}}. \tag{2.12}$$

For slow-wave structures, the phase velocity of the n^{th} harmonic can be less than the free-space velocity, or $\nu_n < c$. However, the group velocity, ν_g, found from

$$\nu_g = \frac{1}{\partial\beta_n/\partial\omega} = \frac{1}{\partial\left(\beta_0 + \frac{2\pi n}{a}\right)/\partial\omega} = \frac{\partial\omega}{\partial\beta_0} \tag{2.13}$$

is independent of n.

2.3 Plane Wave Expansion Method

2.3.1 Analytical Techniques

A straight forward solution to the exact eigenvalue equation for the one-dimensional periodic problem is obtained through the use of the Fourier series. A representative one-dimensional periodic array of dielectric slabs with period a and dielectric insert width b is

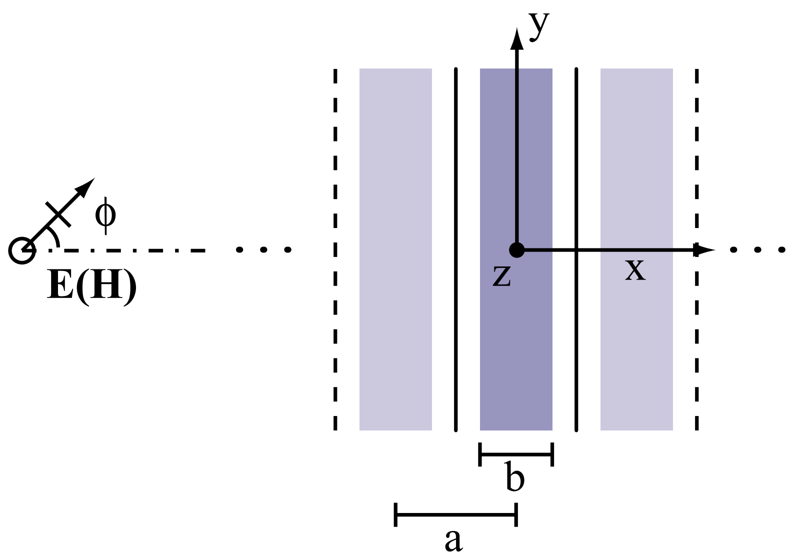

Figure 2.1: One dimensional lattice of dielectric slabs of width b in a periodic lattice with period a

illustrated in cross section in Figure 2.1. If the electric field does not have a component in the x-direction (the direction of period or stratification), the mode is denoted TE_x or *horizontal*. If the magnetic field does not have a component in the x-direction, the mode is denoted TM_x or *vertical*. For normal incidence, the modes are degenerate (TE_x is equivalent to TM_x).

Transverse Electric (TE_x) Case

The electric field can be expanded as a periodic function of plane waves in x with period a and prescribed propagation constant of k_{x_0} and is given by

$$\mathbf{E}(x,y) = \hat{\mathbf{z}}E_z(x,y) = \hat{\mathbf{z}}E_p(x)\ e^{-jk_{x_0}x}\ e^{-jk_y y} \tag{2.14}$$

where $E_p(x)$ is the periodic electric field that propagates only in the xy-plane, *i.e.* $k_z = 0$, without loss of generality. Since the electric field must satisfy the wave equation, we now apply the operator $\left(\nabla_{xy}^2 + k^2\right)$ to $E_z(x,y)$ of (2.14) noting that the dielectric constant is a function of x

$$\nabla_{xy}^2 E_z(x,y) + k_0^2 \varepsilon_r(x) E_z(x,y) = 0. \tag{2.15}$$

Assuming the parallel slabs are infinite in the y and z directions, (2.15) can be simplified to

$$-\frac{d^2}{dx^2}E_z(x,y) + k_y^2 E_z(x,y) = k_0^2 \varepsilon_r(x) E_z(x,y). \tag{2.16}$$

The periodic electric field is expanded in a Fourier series in x with unknown coefficients a_n which serve to represent the dependence on y

$$E_p(x) = \sum_n a_n \; e^{-j\frac{2\pi n}{a}x}. \tag{2.17}$$

Since the dielectric function is also periodic, it is appropriate to expand it in another Fourier series with coefficients b_m

$$\varepsilon_r(x) = \sum_m b_m \; e^{-j\frac{2\pi m}{a}x}. \tag{2.18}$$

Substituting the Fourier expansions for the field and the dielectric into (2.16) and carrying out the algebraic operations, we obtain

$$\sum_n \left[\left(\frac{2\pi n}{a} + k_{x0}\right)^2 + k_y^2\right] a_n \; e^{-j\frac{2\pi n}{a}x} = k_0^2 \sum_n \sum_m a_n b_m \; e^{-j\frac{2\pi m}{a}x} \; e^{-j\frac{2\pi n}{a}x}. \tag{2.19}$$

In order to determine the unknown coefficients a_n and b_m, (2.19) is multiplied by an orthogonal function and integrated over one unit cell which produces a Kronecker delta function for a specific index

$$\sum_n \left[\left(\frac{2\pi n}{a} + k_{x0}\right)^2 + k_y^2\right] a_n \delta\left(\frac{2\pi p}{a} - \frac{2\pi n}{a}\right) = k_0^2 \sum_n \sum_m a_n b_m \delta\left(\frac{2\pi p}{a} - \frac{2\pi m}{a} - \frac{2\pi n}{a}\right). \tag{2.20}$$

The convolution in equation (2.20) is easily cast into the following general matrix form

$$\left[\left(\frac{2\pi n}{a} + k_{x0}\right)^2 + k_y^2\right] a_n = k_0^2 \sum_m b_{n-m} a_m \tag{2.21}$$

where

$$\begin{aligned} b_{n-m} = \frac{1}{a}\int_{-b/2}^{b/2} (\varepsilon_r - 1) \; e^{-j\frac{2\pi(n-m)}{a}x} \; dx + \frac{1}{a}\int_{-a/2}^{a/2} (1) \; e^{-j\frac{2\pi(n-m)}{a}x} \; dx \\ = \frac{b}{a}(\varepsilon_r - 1)\,\mathrm{sinc}\,\frac{\pi(n-m)b}{a} + \delta_{n-m}. \end{aligned} \tag{2.22}$$

A generalized linear eigensystem problem is represented by $Ax = \lambda Bx$ where A and B are $n \times n$ matrices. The value λ is an *eigenvalue* and $x \neq 0$ is the corresponding *eigenvector*. The propagating modes in the TE_x case are solutions of the generalized linear eigensystem in (2.21).

Transverse Magnetic (TM_x) Case

The solution for the TM_x case is similar to the TE_x case with the significant difference that the electric field in (2.14) is replaced by the magnetic field in the wave equation

$$\nabla \times \left\{ \frac{1}{\varepsilon_r(x)} \nabla \times \hat{\mathbf{z}} H_z(x,y) \right\} + k_0^2 \hat{\mathbf{z}} H_z(x,y) = 0. \tag{2.23}$$

In the derivation of (2.15), the curl operator is applied to both sides of (2.1a). The expression for the magnetic field found from (2.1b) is then substituted into the resulting equation which when simplified, yields (2.16). However, when the curl operator is applied to (2.1b) first, as it is in the TM_x case, the operator acts on both the field and the periodic dielectric function. Careful attention must be directed to correctly evaluating the specified operators. The resulting equation that must be solved is

$$\frac{1}{\varepsilon_r(x)} \hat{\mathbf{z}} \cdot \nabla \times \nabla \times \hat{\mathbf{z}} H_z(x,y) + \hat{\mathbf{z}} \cdot \nabla \left\{ \frac{1}{\varepsilon_r(x)} \right\} \times \nabla \times \hat{\mathbf{z}} H_z(x,y) = -k_0^2 H_z(x,y). \tag{2.24}$$

The Fourier series representation of the periodic magnetic field with unknown coefficients a_n is

$$H_p(x) = \sum_n a_n \, e^{-j\frac{2\pi n}{a}x} \tag{2.25}$$

and for the inverse of the dielectric function, it is

$$\frac{1}{\varepsilon_r(x)} = \sum_m b_m \, e^{-j\frac{2\pi m}{a}x} \tag{2.26}$$

with coefficients b_m different from coefficients b_m in (2.18) for the TE_x case. By substituting the expressions for the field and dielectric function into (2.24), carrying out the curl and gradient operations, and simplifying the resulting expression yields

$$\begin{aligned} \sum_m b_m e^{-j\frac{2\pi m}{a}x} \left\{ -\frac{d^2}{dx^2} \sum_n a_n \, e^{-j\frac{2\pi n}{a}x} \, e^{-jk_{x0}x} + k_y^2 \sum_n a_n \, e^{-j\frac{2\pi n}{a}x} \, e^{-jk_{x0}x} \right\} \\ - \frac{d}{dx} \sum_m b_m e^{-j\frac{2\pi m}{a}x} \frac{d}{dx} \sum_n a_n \, e^{-j\frac{2\pi n}{a}x} \, e^{-jk_{x0}x} = -k_0^2 \sum_n a_n \, e^{-j\frac{2\pi n}{a}x} \, e^{-jk_{x0}x}. \end{aligned} \tag{2.27}$$

If the derivatives in (2.27) are evaluated and integrated over one unit cell, then the resulting expression can be cast into a different matrix equation to solve for the unknown eigenvalues

$$\sum_m b_{n-m} a_m \left[\left(\frac{2\pi n}{a} + k_{x0} \right)^2 + k_y^2 - \frac{2\pi(n-m)}{a} \left(\frac{2\pi n}{a} + k_{x0} \right) \right] = -k_0^2 a_n \tag{2.28}$$

where

$$b_{n-m} = \frac{1}{a} \int_{-b/2}^{b/2} \left(\frac{1}{\varepsilon_r} - 1 \right) e^{-j\frac{2\pi(n-m)}{a}x} \, dx + \frac{1}{a} \int_{-a/2}^{a/2} (1) \, e^{-j\frac{2\pi(n-m)}{a}x} \, dx$$

$$= \frac{b}{a} \left(\frac{1}{\varepsilon_r} - 1 \right) \operatorname{sinc} \frac{\pi(n-m)b}{a} + \delta_{n-m}. \quad (2.29)$$

An ordinary linear eigensystem problem is represented by the equation $Ax = \lambda x$ where A denotes an $n \times n$ matrix. The propagating modes in the TM_x case are solutions of the ordinary eigensystem problem in (2.28).

2.3.2 Matrix Solution of the Eigensystem

The solution of (2.21) or (2.28) is amenable to fast computation using the commercial software package MATLAB. The resulting eigenvalues of the matrix are the squares of the frequencies of the propagating modes in the structure. The solution of the frequencies of the propagating modes in the structure are found for specific values of phase shift $k_{x_0}a \in [0, 2\pi]$. Of course, if an infinite number of Floquet modes are used in the solution, then an infinite number of frequencies (space harmonics) will satisfy (2.21) or (2.28). However, the limitation of a finite computer memory requires that only a finite number of frequencies can be found for a given phase shift. If the resulting eigenvalues are sorted from largest to smallest, the last eigenvalue yields the lowest space harmonic that will propagate for a given phase shift. Additional propagating modes are found from the ascending eigenvalues.

In Figure 2.2 is plotted a finite portion of the Brillouin zone (BZ) diagram[1] for a normally incident TE_x mode (k_y=0) in a periodic array of dielectric slabs with filling fraction b/a=0.1 and relative dielectric constant ε_r=8.9. The filling fraction is defined as the volumetric ratio of dielectric material to the total volume. The band structure is shown for normalized propagation values $k_{x_0}a \in [-3\pi, 3\pi]$. The dark regions are the stop bands. Seeing that the diagram repeats itself every 2π, only normalized propagation values between 0 and π need to be calculated to determine all of the propagating modes in the structure. This region is often termed the *irreducible Brillouin zone* [38, 44]. For one-dimensional periodic structures, this a trivial determination. For the two-dimensional structures encountered in Chapter 3, the irreducible Brillouin zone becomes more complicated. A complete treatment of the Brillouin zone for two-dimensional lattices is given in Appendix B.

[1] For band structures in the literature, the normalized propagation constant is plotted on the abscissa and the normalized frequency is usually plotted on the ordinate.

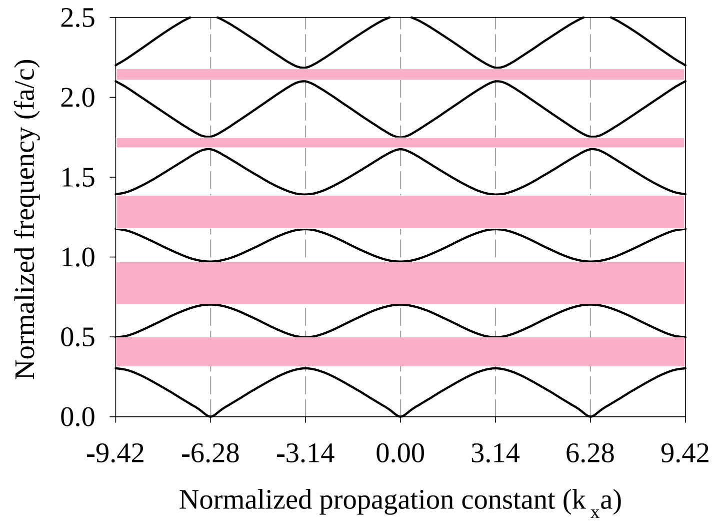

Figure 2.2: Full band structure for a normally incident mode in a periodic array of dielectric slabs with b/a=0.1 and ε_r=8.9

The width of the stopbands and passbands is a function of the relative dielectric constant ε_r and the filling fraction b/a of the one-dimensional lattice. To illustrate this fact, representative band structures for a one dimensional lattice of dielectric slabs with filling fraction b/a=0.5 for various combinations of dielectric contrast are shown in Figure 2.3 for $k_{x_0}a \in [-\pi, \pi]$. When the permittivity difference between the two regions is negligible (Figure 2.3(a)), the wave propagates uninhibited for all frequencies, *i.e.*, no stopgaps. If a small dielectric contrast is introduced between the two materials (Figure 2.3(b)), small gaps can form. However, the required interference effect between the periods is simply too small to produce a gap of any consequence. Large contrasts in dielectric constant can produce significant gaps as seen in Figure 2.3(c).

A number of simple checks can be performed to determine whether the solution for the periodic slabs is correct in addition to checking the calculated values against published data. For convenience, the slab is placed in the center of the unit cell and the propagation constant is determined for a specific combination of electrical and geometrical parameters. However, the particular location of the slab within the unit cell should have no effect on the propagating structure. In particular, this is found to be true for two small strips of dielectric material each half the original dielectric insert width located at the edges of the unit cell. Other observations are drawn from the calculations by reducing the geometrical and electrical parameters to special cases, including the following: (*i.*) as the filling frac-

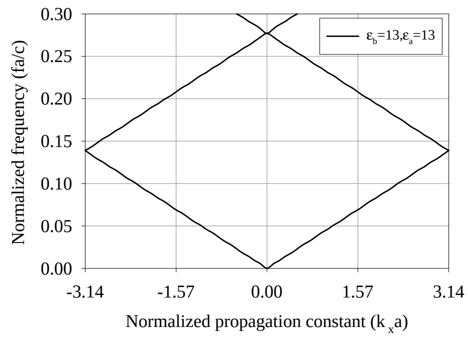

(a)

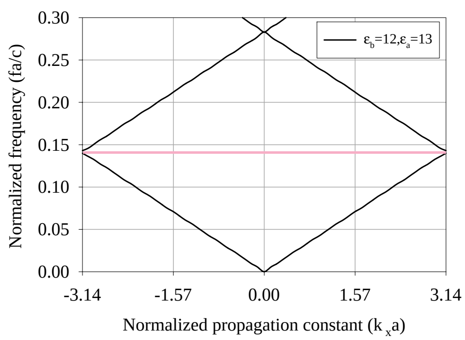

(b)

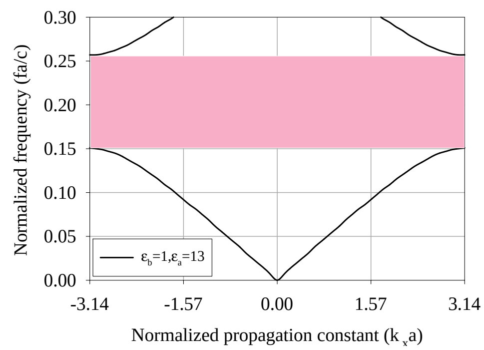

(c)

Figure 2.3: Band structure for one dimensional lattice of dielectric slabs of with filling fraction b/a=0.5 for (a) ε_b=ε_a=13, (b) ε_b=12, ε_a=13, and (c) ε_b=1, ε_a=13

tion decreases to zero, the calculated propagation constant k_{x_0} approaches the minimum value, the free-space propagation constant k_0 (Figure 2.4); (*ii.*) as the filling fraction increases to 1, the calculated propagation constant approaches the maximum value, $k_0\sqrt{\varepsilon_r}$ (Figure 2.4); and (*iii.*) as the relative dielectric constant ε_r is reduced to 1, the calculated propagation constant approaches the minimum value, the free-space propagation constant k_0 (Figure 2.5).

In Figure 2.6, the band structure (TM$_x$) for the lowest order mode of a periodic array of dielectric slabs with filling fraction b/a=0.3545 and ε_r=8.9 is shown for different values of off-axis propagation. The values for the filling fraction and the relative dielectric constant are obtained from a two-dimensional structure in [64, 129]. In order to determine the correctness of the results obtained for the two-dimensional periodic structure, the filling fraction in one lattice direction is allowed to increase until an equivalent one-dimensional

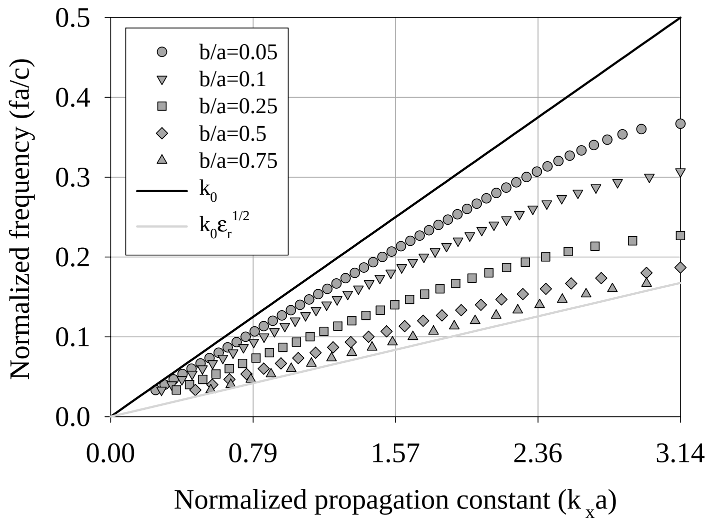

Figure 2.4: Band structure (TM_x) for lowest order mode of a periodic array of dielectric slabs as a function of filling fraction b/a for normal incidence and ε_r=8.9

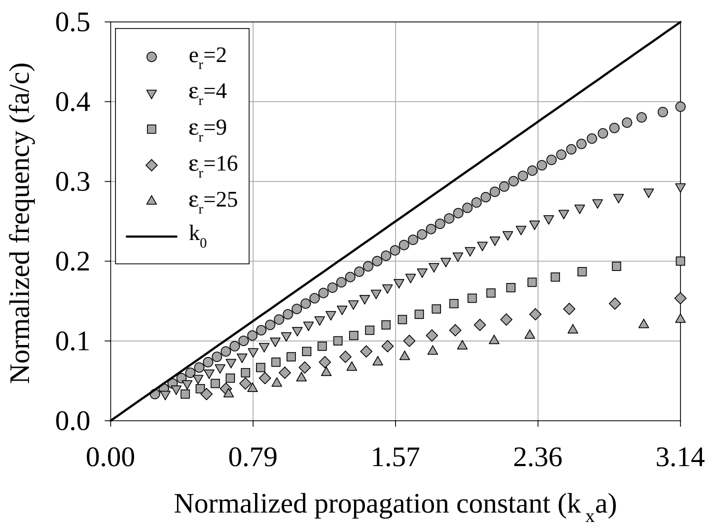

Figure 2.5: Band structure (TM_x) for lowest order mode of a periodic array of dielectric slabs as a function of dielectric constant ε_r for normal incidence and filling fraction b/a=0.3545

periodic structure is obtained. Thus, the solution of the one-dimensional equivalent structure is needed. Similar results for the band structure of the lowest order TE_x mode are not shown. Note that for normal incidence ($k_{y0} = 0$), the first (and lowest) band does not open up until the normalized frequency $f_0 \geq 0.2$. However, when the mode is allowed to propagate with an off-axis component, *i.e.* $\phi_0 \neq 0°$), the lowest band opens up for small normalized frequencies. As the off-axis propagation constant increases, the bandwidth of the lowest stopband increases and the bandwidth of the lowest passband decreases. In the limit as the off-axis propagation increase, the passband becomes effectively flat over a small range of frequencies that correspond to discrete propagating modes in a inhomogeneously-filled parallel plate waveguide [55] and is also found to hold for two-dimensional structures (waveguides) as well [96].

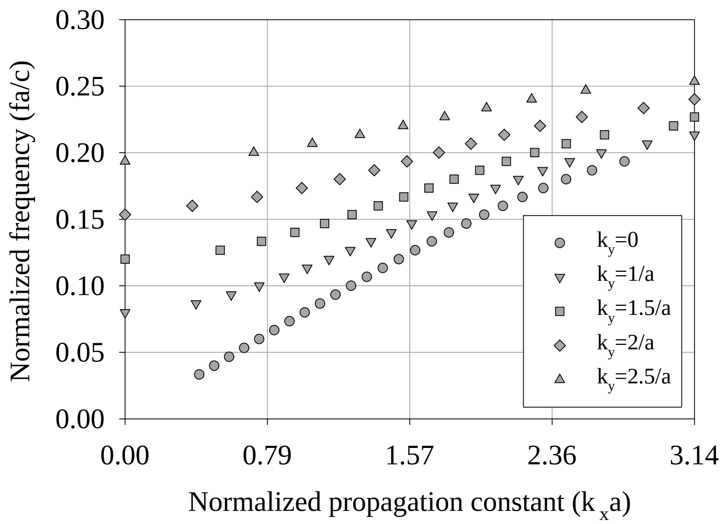

Figure 2.6: Band structure (TM_x) for lowest order mode of a periodic array of dielectric slabs as a function of off-axis propagation constant k_{y_0} for filling fraction b/a=0.3545 and ε_r=8.9

Another check to determine if the code is calculating the correct propagation constant is found by setting the filling fraction equal to some value x between zero (0) and one (1) and obtaining a solution for the propagation constant. Subsequently, the filling fraction is set equal to $(1-x)$, the quantity $(\varepsilon_r - 1)$ is replaced by $(1-\varepsilon_r)$ in (2.21) and (2.25), and a new solution is calculated. The solutions should be and are found to be exactly the same.

Asymptotic solutions are another effective way to check the solution. For small filling fractions, the propagation constant k_{x_0} approaches $k_0\sqrt{\varepsilon_{\text{eff}}}$ where ε_{eff} is the effective dielectric constant given by the volumetric average of the constitutive phases [24]

$$\varepsilon_{\text{eff}} = \left(1 + (\varepsilon_r - 1)\frac{b}{a}\right).$$

For a dielectric slab (ε_r=11) with a filling fraction of 0.1, the effective dielectric constant ε_{eff} is estimated to be 2, corresponding to a propagation constant $k_{x_0} \simeq 1.4k_0$. This approximation is only accurate to within 1% for relatively low normalized frequencies f_0=$fa/c < 0.1$.

2.4 Formulation of Integral Equations

In this section, volume integral equations (IE) are derived from Maxwell's equations (2.1a)–(2.1d) and the boundary conditions, that when solved, yield propagation constants from which the propagating mode structure can be determined. For the inhomogeneous problems found throughout this work, integral equations are derived that incorporate equivalent volume polarization currents.[2] The integral equations are discretized and cast into a matrix equation form through the use of the method of moments (MoM) numerical solution technique. The unknown is obtained from the solution of the resulting linear system. For the problems solved in Chapters 2 and 3, the solution of the linear system returns the eigenvalues (propagation constants) of the structure.

2.4.1 Derivation of Electric Field Integral Equation

In many scattering problems, the total electric field can be viewed as the sum of an incident field $\mathbf{E}^i(\mathbf{r})$ due to radiation from a known source with the dielectric absent and a scattered field $\mathcal{E}[\mathbf{J};\mathbf{r};V]$ which is due to radiation by equivalent volume equivalent currents $\mathbf{J}$ in a volume V

$$\mathbf{E}(\mathbf{r}) = \mathcal{E}[\mathbf{J};\mathbf{r};V] + \mathbf{E}^i(\mathbf{r}), \tag{2.30}$$

in which the operator $\mathcal{E}[\mathbf{J};\mathbf{r};V]$ can be expressed in terms of a Hertz potential [108] as

$$\mathcal{E}[\mathbf{J};\mathbf{r};V] = k_0^2\mathbf{\Pi(r)} + \nabla\nabla\cdot\mathbf{\Pi(r)} \tag{2.31a}$$

with

$$\mathbf{\Pi}(\mathbf{r}) = \frac{Z_0}{jk_0}\iiint\limits_V \mathbf{J}(\mathbf{r}')\frac{e^{-jk_0|\mathbf{r}-\mathbf{r}'|}}{4\pi|\mathbf{r}-\mathbf{r}'|}\, d\mathbf{r}' \tag{2.31b}$$

where $k_0 = \omega\sqrt{\mu_0\varepsilon_0}$ is the free-space wavenumber of the background, ω is the frequency of operation, $Z_0 = \sqrt{\mu_0/\varepsilon_0}$ is the intrinsic impedance of free-space, and V represents the volume in which the sources reside. The field must satisfy

$$\mathcal{E}[\mathbf{J};\mathbf{r};V] + \mathbf{E}^i(\mathbf{r}) = \mathbf{E}(\mathbf{r}), \quad \mathbf{r}\in V. \tag{2.32}$$

[2] In some homogeneous problems, integral equations are derived using equivalent surface currents reducing the complexity and computational cost of determining the solution.

2.4.2 Equivalent Polarization Currents

The dielectric flux density $\mathbf{D}$ inside a dielectric immersed in a background medium of free-space permittivity ε_0 is equal to

$$\mathbf{D} = \varepsilon_0 \mathbf{E} + \mathbf{P} \tag{2.33}$$

where the polarization $\mathbf{P}$ is the electric dipole moment per unit volume. The polarization current $\mathbf{J}$ is the time rate of change of the electric dipole moment per unit volume

$$\mathbf{J} = \frac{\partial}{\partial t}\mathbf{P}. \tag{2.34}$$

Relating the polarization current to the difference between the induced electric flux density and the electric flux density inside the dielectric through

$$\mathbf{J} = \frac{\partial}{\partial t}\left(\mathbf{D} - \varepsilon_0 \mathbf{E}\right) \tag{2.35}$$

yields the following expression for linear media

$$\mathbf{J} = \frac{\partial}{\partial t}\left(\varepsilon \mathbf{E} - \varepsilon_0 \mathbf{E}\right). \tag{2.36}$$

For time harmonic fields ($e^{j\omega t}$), the equivalent polarization currents are related to the total electric field by

$$\begin{aligned}\mathbf{J} &= j\omega\left(\varepsilon - \varepsilon_0\right)\mathbf{E} \\ &= jk_0 Y_0 \left(\varepsilon_r - 1\right)\mathbf{E}\end{aligned} \tag{2.37}$$

where $Y_0 = 1/Z_0$ is the intrinsic admittance of free-space.

TE$_x$ Case

Consider the representative dielectric slab (period not shown) in Figure 2.7 with period a and dielectric insert width b. The slabs are excited by an incident time harmonic ($e^{j\omega t}$) plane wave with its electric field perpendicular to the plane of incidence (x-y plane) which induces an electric current $\mathbf{J}$ with a z component only. Note that, since all quantities are z invariant and because the induced electric current is z directed, $\nabla' \cdot \mathbf{J}(\mathbf{r}')$ of (2.31a) is zero. The total electric field everywhere is computed as the sum of the scattered field produced by the equivalent induced electric current and the incident electric field given by $\mathbf{E}^i = \hat{\mathbf{z}} E_0 e^{-jk_0(x\cos\phi_0 + y\sin\phi_0)}$, which impinges on the slab in the $\hat{\mathbf{k}} = (\hat{\mathbf{x}}\cos\phi_0 + \hat{\mathbf{y}}\sin\phi_0)$ direction defined by an angle ϕ^i with respect to the x axis (ϕ_0=0°). This mode is denoted

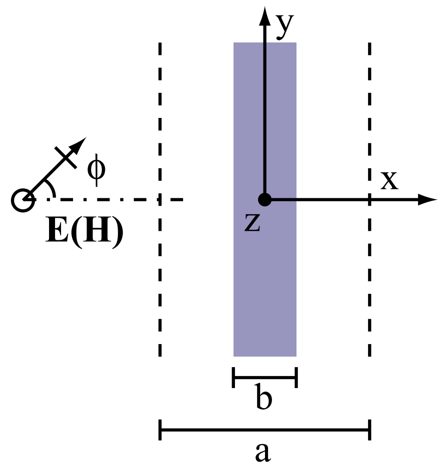

Figure 2.7: Representative dielectric slab of width b with period a

as transverse electric to x, TE$_x$, since for all angles of incidence the electric field does not have a component in the x direction, the direction of stratification.

The dielectric material is replaced with equivalent volume currents using (2.37). For the TE$_x$ case (assuming k_z=0 without loss of generality),

$$J_z(x) = jk_0 Y_0 \left(\varepsilon_r(x) - 1\right) E_z(x) \tag{2.38}$$

where $\varepsilon_r(x)$ is the permittivity function of the slabs within a unit cell given by

$$\varepsilon(x) = \begin{cases} \varepsilon_r, & -b/2 < x < b/2; \\ 1, & \text{otherwise.} \end{cases} \tag{2.39}$$

Since the dielectric material is periodic in x with period a, the resulting equivalent currents must satisfy

$$J_z(x + pa) = J_z(x)e^{-jk_{x0}pa} \tag{2.40}$$

for a prescribed phase shift $k_{x0}a$ in the x direction. The scattered field is determined from (2.31) by incorporating the periodic equivalent currents (2.40)

$$E_z^s(x) = -jk_0 Z_0 \int_{-\frac{b}{2}}^{\frac{b}{2}} J_z(x') \sum_p e^{-jk_{x0}pa} \frac{e^{-j\sqrt{k_0^2 - k_y^2}|x-x'-pa|}}{2j\sqrt{k_0^2 - k_y^2}} \, dx' \tag{2.41}$$

where p is the Floquet mode index. Using $E_z(x) = E_z^s(x) + E_z^i(x)$, one can formulate the following electric field integral equation (EFIE) to determine the equivalent currents

$$jk_0 Z_0 \int_{-\frac{b}{2}}^{\frac{b}{2}} J_z(x') \sum_p e^{-jk_{x_0}pa} \frac{e^{-j\sqrt{k_0^2-k_y^2}|x-x'-pa|}}{2j\sqrt{k_0^2-k_y^2}} \, dx' + \frac{J_z(x)}{jk_0 Y_0(\varepsilon_r(x)-1)} = E_z^i(x). \quad (2.42)$$

One-dimensional periodic free-space Green's function The spatial form of the one-dimensional periodic free-space Green's function can be easily written in a more convenient form through the use of the Poisson sum formula [70]. From Table I of [51],

$$\begin{aligned}\sum_p f(p) &= \sum_p \frac{1}{2jk} e^{-jk|x-pa|} \\ &= \sum_p \frac{1}{a} \left[\left(\frac{2\pi p}{a} \right)^2 - k^2 \right]^{-1} e^{-j\frac{2\pi p}{a}x} \\ &= -\frac{1}{a} \sum_p \frac{1}{\left[k^2 - \left(\frac{2\pi p}{a} \right)^2 \right]} e^{-j\frac{2\pi p}{a}x}\end{aligned} \quad (2.43)$$

where a is the unit cell width, k is the wavenumber of the medium, and p is the Floquet index. Equation (2.43) becomes, upon substitution of a phase shift k_{x_0},

$$\sum_p e^{-jk_{x_0}pa} \frac{1}{2jk} e^{-jk|x-pa|} = -\frac{1}{a} \sum_p \frac{e^{-jk_{x_p}x}}{k^2 - k_{x_p}^2} \quad (2.44)$$

where

$$k_{x_p} = \frac{2\pi p}{a} + k_{x_0}.$$

Thus, (2.42) becomes upon substitution

$$-\frac{jk_0 Z_0}{a} \int_{-\frac{b}{2}}^{\frac{b}{2}} J_z(x') \sum_p \frac{e^{-jk_{x_p}(x-x')}}{k_0^2 - k_y^2 - k_{x_p}^2} \, dx' + \frac{J_z(x)}{jk_0 Y_0(\varepsilon_r(x)-1)} = E_z^i(x). \quad (2.45)$$

TM$_x$ Case

Similarly for the the TM$_x$ case, the dielectric material is replaced with equivalent volume currents. However, since the slabs are excited by an incident plane wave with its electric field parallel to the plane of incidence, the induced electric current $\mathbf{J}$ can have both x and y components. The total electric field everywhere is computed as the sum of the scattered field produced by the equivalent induced electric current and the incident electric field given by $\mathbf{E}^i = (\hat{\mathbf{z}} \times \hat{\mathbf{k}}) E_0 e^{-jk_0(x\cos\phi^i + y\sin\phi^i)}$ which impinges on the slab in the $\hat{\mathbf{k}}$ direction with ϕ^i

defined eariler. This mode is denoted as transverse magnetic to x, TM_x, since for all angles of incidence (assuming k_z=0 without loss of generality), the magnetic field does not have a component in the x direction.

For the TM_x case, the dielectric material is replaced with equivalent volume currents for both the x and y components

$$J_x(x) = jk_0 Y_0(\varepsilon_r - 1)E_x(x) \tag{2.46a}$$

$$J_y(x) = jk_0 Y_0(\varepsilon_r - 1)E_y(x). \tag{2.46b}$$

Using the periodic form of (2.46) in (2.31), the scattered field is found by integrating over the induced current

$$\begin{aligned} E_x^s(x) = -jk_0 Z_0 \left(1 + \frac{1}{k_0^2}\frac{\partial^2}{\partial x^2}\right) \int_{-\frac{b}{2}}^{\frac{b}{2}} J_x(x') \sum_p e^{-jk_{x0}pa} \frac{e^{-j\sqrt{k_0^2-k_y^2}|x-x'-pa|}}{2j\sqrt{k_0^2-k_y^2}}\, dx' \\ - \frac{k_y Z_0}{k_0}\frac{\partial}{\partial x} \int_{-\frac{b}{2}}^{\frac{b}{2}} J_y(x') \sum_p e^{-jk_{x0}pa} \frac{e^{-j\sqrt{k_0^2-k_y^2}|x-x'-pa|}}{2j\sqrt{k_0^2-k_y^2}}\, dx' \end{aligned} \tag{2.47a}$$

$$\begin{aligned} E_y^s(x) = -\frac{k_y Z_0}{k_0}\frac{\partial}{\partial x} \int_{-\frac{b}{2}}^{\frac{b}{2}} J_x(x') \sum_p e^{-jk_{x0}pa} \frac{e^{-j\sqrt{k_0^2-k_y^2}|x-x'-pa|}}{2j\sqrt{k_0^2-k_y^2}}\, dx' \\ - jk_0 Z_0 \left(1 - \frac{k_y^2}{k_0^2}\right) \int_{-\frac{b}{2}}^{\frac{b}{2}} J_y(x') \sum_p e^{-jk_{x0}pa} \frac{e^{-j\sqrt{k_0^2-k_y^2}|x-x'-pa|}}{2j\sqrt{k_0^2-k_y^2}}\, dx'. \end{aligned} \tag{2.47b}$$

Using $\mathbf{E}(x) = \mathbf{E}^s(x) + \mathbf{E}^i(x)$, one can formulate the following coupled EFIEs to determine the equivalent currents

$$\begin{aligned} jk_0 Z_0 \left(1 + \frac{1}{k_0^2}\frac{\partial^2}{\partial x^2}\right) \int_{-\frac{b}{2}}^{\frac{b}{2}} J_x(x') \sum_p e^{-jk_{x0}pa} \frac{e^{-j\sqrt{k_0^2-k_y^2}|x-x'-pa|}}{2j\sqrt{k_0^2-k_y^2}}\, dx' \\ + \frac{k_y Z_0}{k_0}\frac{\partial}{\partial x} \int_{-\frac{b}{2}}^{\frac{b}{2}} J_y(x') \sum_p e^{-jk_{x0}pa} \frac{e^{-j\sqrt{k_0^2-k_y^2}|x-x'-pa|}}{2j\sqrt{k_0^2-k_y^2}}\, dx' + \frac{J_x(x)}{jk_0 Y_0(\varepsilon_r(x) - 1)} = E_x^i(x) \end{aligned} \tag{2.48a}$$

$$jk_0 Z_0 \left(1 - \frac{k_y^2}{k_0^2}\right) \int_{-\frac{b}{2}}^{\frac{b}{2}} J_y(x') \sum_p e^{-jk_{x_0}pa} \frac{e^{-j\sqrt{k_0^2-k_y^2}|x-x'-pa|}}{2j\sqrt{k_0^2-k_y^2}} \, dx'$$

$$+ \frac{k_y Z_0}{k_0} \frac{\partial}{\partial x} \int_{-\frac{b}{2}}^{\frac{b}{2}} J_x(x') \sum_p e^{-jk_{x_0}pa} \frac{e^{-j\sqrt{k_0^2-k_y^2}|x-x'-pa|}}{2j\sqrt{k_0^2-k_y^2}} \, dx' + \frac{J_y(x)}{jk_0 Y_0(\varepsilon_r(x)-1)} = E_y^i(x). \tag{2.48b}$$

Using the Poisson sum formula (2.44) shown on page 26, and carrying out the derivatives in (2.48) yields the coupled equations necessary to solve for the unknown equivalent currents J_x and J_y,

$$-\frac{jk_0 Z_0}{a} \left(1 - \frac{k_{x_p}^2}{k_0^2}\right) \int_{-\frac{b}{2}}^{\frac{b}{2}} J_x(x') \sum_p \frac{e^{-jk_{x_p}(x-x')}}{k_0^2 - k_y^2 - k_{x_p}^2} \, dx'$$

$$- \frac{k_y k_{x_p} Z_0}{jk_0 a} \int_{-\frac{b}{2}}^{\frac{b}{2}} J_y(x') \sum_p \frac{e^{-jk_{x_p}(x-x')}}{k_0^2 - k_y^2 - k_{x_p}^2} \, dx' + \frac{J_x(x)}{jk_0 Y_0(\varepsilon_r(x)-1)} = E_x^i(x) \tag{2.49a}$$

$$-\frac{jk_0 Z_0}{a} \left(1 - \frac{k_y^2}{k_0^2}\right) \int_{-\frac{b}{2}}^{\frac{b}{2}} J_y(x') \sum_p \frac{e^{-jk_{x_p}(x-x')}}{k_0^2 - k_y^2 - k_{x_p}^2} \, dx'$$

$$- \frac{k_y k_{x_p} Z_0}{jk_0 a} \int_{-\frac{b}{2}}^{\frac{b}{2}} J_x(x') \sum_p \frac{e^{-jk_{x_p}(x-x')}}{k_0^2 - k_y^2 - k_{x_p}^2} \, dx' + \frac{J_y(x)}{jk_0 Y_0(\varepsilon_r(x)-1)} = E_y^i(x). \tag{2.49b}$$

For a normally incident plane wave excitation, *i.e.* ϕ_i=0°, the modes are degenerate (TE_x is equivalent to TM_x).

2.4.3 Method of Moments Formulation

The first step in the method of moments (MoM) numerical method [34, 119] is to discretize the geometry and approximate the unknown electric current in the dielectric region with either subsectional or entire domain basis functions. The equivalent polarization currents are expanded in a linear combination of these basis functions, and the equations are tested in order to obtain an adequate number of equations to solve for the unknown coefficients of the basis functions. In order to provide verification of the IE/MoM procedure, computer codes have been written in Fortran to determine the propagating modes of a periodic array of dielectric slabs.

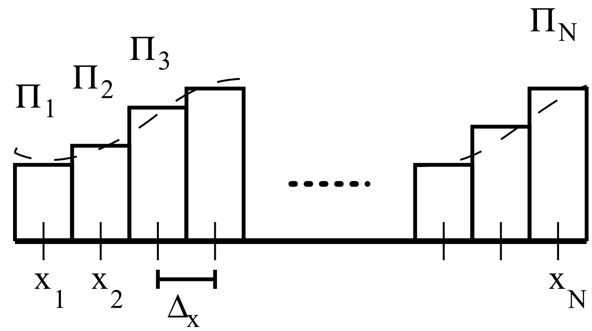

(a) Piecewise constant basis functions

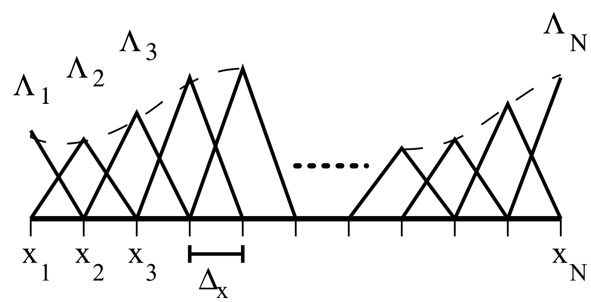

(b) Piecewise linear basis functions

Figure 2.8: Piecewise constant and piecewise linear basis functions used in this work

TE$_x$ Case

Piecewise constant expansion / Piecewise constant testing The dielectric region is discretized into N piecewise constant subsections, commonly referred to as *pulse* basis functions, of width $\Delta_x = b/N$ shown in Figure 2.8(a). The polarization current J_z is approximated by a linear combination of N piecewise constant basis functions with unknown current coefficients $\{J_{z_n}\}$ located at the centers of the piecewise constant segments $x_n = -\frac{b}{2} + \Delta_x(n - \frac{1}{2})$,

$$J_z = \sum_{n=1}^{N} J_{z_n} \Pi_n(x) \tag{2.50}$$

where

$$\Pi_n(x) = \begin{cases} 1, & x_n - \frac{\Delta_x}{2} < x < x_n + \frac{\Delta_x}{2}; \\ 0, & \text{otherwise.} \end{cases} \tag{2.51}$$

Inserting (2.50) into (2.42), yields

$$\sum_{n=1}^{N} J_{z_n} \left\{ \frac{jk_0 Z_0}{a} \int_{x_n-\frac{\Delta x}{2}}^{x_n+\frac{\Delta x}{2}} \sum_p \frac{e^{-jk_{x_p}(x-x')}}{k_0^2 - k_y^2 - k_{x_p}^2}\, dx' - \frac{\Pi_n(x)}{jk_0 Y_0 \left(\varepsilon_r - 1\right)} \right\} = E_z^i(x). \tag{2.52}$$

Testing (2.52) with piecewise constant functions[3] located at x_m, and setting the excitation to zero, yields the following equation

$$\sum_{n=1}^{N} J_{z_n} \left\{ \frac{jk_0 Z_0}{a} \int_{x_m-\frac{\Delta x}{2}}^{x_m+\frac{\Delta x}{2}} \int_{x_n-\frac{\Delta x}{2}}^{x_n+\frac{\Delta x}{2}} \sum_p \frac{e^{-jk_{x_p}(x-x')}}{k_0^2 - k_y^2 - k_{x_p}^2}\, dx'\, dx - \int_{x_m-\frac{\Delta x}{2}}^{x_m+\frac{\Delta x}{2}} \frac{\Pi_m(x)\Pi_n(x)}{jk_0 Y_0 \left(\varepsilon_r - 1\right)}\, dx \right\}$$
$$= 0, \quad m = 1, 2, \ldots, N \tag{2.53}$$

which can be written in matrix form as

$$\left[Z_{mn} + \delta Z\right]\left[J_{z_n}\right] = \left[0\right], \tag{2.54}$$

where $[J_{z_n}]$ is a column vector containing the unknown coefficients and $[Z_{mn} + \delta Z]$ is a matrix whose elements are found by carrying out the integrations in (2.53). Specifically,

$$Z_{mn} = \frac{jk_0 Z_0 \Delta_x^2}{a} \sum_p \operatorname{sinc}^2\left(\frac{k_{x_p}\Delta_x}{2}\right) \frac{e^{-jk_{x_p}(x_m-x_n)}}{k_0^2 - k_y^2 - k_{x_p}^2} \tag{2.55a}$$

$$\delta Z = -\frac{\delta_{mn}\Delta_x}{jk_0 Y_0 \left(\varepsilon_r - 1\right)}. \tag{2.55b}$$

The transforms of the piecewise constant testing and expansion functions, denoted $\tilde{\Pi}_m(k_x)$ and $\tilde{\Pi}_n(k_x)$, are

$$\tilde{\Pi}_m(k_x) = \Delta \operatorname{sinc}\left(\frac{k_x \Delta}{2}\right) e^{-jk_x x_m} \tag{2.56a}$$

$$\tilde{\Pi}_n(k_x) = \Delta \operatorname{sinc}\left(\frac{k_x \Delta}{2}\right) e^{jk_x x_n}. \tag{2.56b}$$

Piecewise linear expansion / Piecewise linear testing Using piecewise linear functions, commonly referred to as *triangle* basis functions, the dielectric region is discretized into N subdomains of width $\Delta = b/(N-1)$ that approximate the dielectric as shown in Figure 2.8(b). The polarization current J_z is approximated with a linear combination of these N basis functions with unknown current coefficients $\{J_{z_n}\}$ centered at $x_n = -\frac{b}{2} + \Delta_x(n-1)$,

$$J_z = \sum_{n=1}^{N} J_{z_n} \Lambda_n(x) \tag{2.57}$$

[3] When the expansion and testing functions are the same, the testing procedure is referred to as the Galerkin method [34, 83].

where

$$\Lambda_n(x) = \begin{cases} 1 - \frac{|x-x_n|}{\Delta_x}, & x_n - \Delta_x < x < x_n + \Delta_x; \\ 0, & \text{otherwise.} \end{cases} \tag{2.58}$$

Inserting the piecewise linear approximation for the current into (2.45) and testing the resulting equation with piecewise linear basis functions, the elements of the impedance matrix $[Z_{mn} + \delta Z]$ in (2.54) are found to be

$$Z_{m1} = \frac{jk_0 Z_0 \Delta_x^2}{a} \sum_p \frac{\left(1 + jk_{x_p}\Delta_x - e^{jk_{x_p}\Delta_x}\right)}{\left(k_{x_p}\Delta_x\right)^2} \operatorname{sinc}^2\left(\frac{k_{x_p}\Delta_x}{2}\right) \frac{e^{-jk_{x_p}(x_m - x_1)}}{k_0^2 - k_y^2 - k_{x_p}^2} \tag{2.59a}$$

$$Z_{mn} = \frac{jk_0 Z_0 \Delta_x^2}{a} \sum_p \operatorname{sinc}^4\left(\frac{k_{x_p}\Delta_x}{2}\right) \frac{e^{-jk_{x_p}(x_m - x_n)}}{k_0^2 - k_y^2 - k_{x_p}^2} \tag{2.59b}$$

$$Z_{mN} = \frac{jk_0 Z_0 \Delta_x^2}{a} \sum_p \frac{\left(1 - jk_{x_p}\Delta_x - e^{-jk_{x_p}\Delta_x}\right)}{\left(k_{x_p}\Delta_x\right)^2} \operatorname{sinc}^2\left(\frac{k_{x_p}\Delta_x}{2}\right) \frac{e^{-jk_{x_p}(x_m - x_N)}}{k_0^2 - k_y^2 - k_{x_p}^2} \tag{2.59c}$$

$$\delta Z = -\frac{\delta_{mn}\Delta_x}{jk_0 Y_0 \left(\varepsilon_r - 1\right)}. \tag{2.59d}$$

The transforms of the piecewise linear testing and expansion basis functions, denoted $\tilde{\Lambda}_m(k_x)$ and $\tilde{\Lambda}_n(k_x)$, are

$$\tilde{\Lambda}_m(k_x) = \Delta \operatorname{sinc}^2\left(\frac{k_x\Delta}{2}\right) e^{-jk_x x_m} \tag{2.60a}$$

$$\tilde{\Lambda}_n(k_x) = \Delta \operatorname{sinc}^2\left(\frac{k_x\Delta}{2}\right) e^{jk_x x_n}. \tag{2.60b}$$

The boundary condition at the edge of the dielectric insert requires continuity of the tangential electric field. When using linear elements, this requires incorporating the two "half-basis" functions, denoted $\Lambda_1(x)$ and $\Lambda_N(x)$, in Figure 2.8(b). The transforms of the two "half-basis" functions in (2.59), $\tilde{\Lambda}_1$ and $\tilde{\Lambda}_N$, are

$$\tilde{\Lambda}_1(k_x) = \Delta \frac{e^{jk_x x_1}}{(k_x\Delta)^2} \left(1 + jk_x\Delta - e^{jk_x\Delta}\right) \tag{2.61a}$$

$$\tilde{\Lambda}_N(k_x) = \Delta \frac{e^{jk_x x_N}}{(k_x\Delta)^2} \left(1 - jk_x\Delta - e^{-jk_x\Delta}\right). \tag{2.61b}$$

TM$_x$ Case

Piecewise linear expansion / Piecewise linear testing Care must be taken to correctly evaluate (2.49) because of the noticeable derivatives. The dielectric region is discretized into N subsections of width $\Delta = b/(N-1)$. The equivalent current $\mathbf{J} = \hat{\mathbf{x}}J_x + \hat{\mathbf{y}}J_y$

is expanded with a linear combination of N piecewise linear functions basis functions with unknown current coefficients $\{J_{x_n}, J_{y_n}\}$ centered at $x_n = -\frac{b}{2} + \Delta_x(n-1)$,

$$J_x = \sum_{n=1}^{N} J_{x_n}\Lambda_n(x) \tag{2.62a}$$

$$J_y = \sum_{n=1}^{N} J_{y_n}\Lambda_n(x) \tag{2.62b}$$

with $\Lambda_n(x)$ given in (2.58). Inserting (2.62) into (2.49) and testing the resulting equation with piecewise linear functions yields

$$\begin{aligned}
\sum_{n=1}^{N} J_{x_n}\Bigg\{&-\frac{jk_0Z_0}{a}\left(1-\frac{k_{x_p}^2}{k_0^2}\right)\int\limits_{x_m-\Delta}^{x_m+\Delta}\Lambda_m(x)\int\limits_{x_n-\Delta}^{x_n+\Delta}\Lambda_n(x')\ \sum_p \frac{e^{-jk_{x_p}(x-x')}}{k_0^2-k_y^2-k_{x_p}^2}\ dx'\ dx \\
&+\int\limits_{x_m-\Delta}^{x_m+\Delta}\frac{\Lambda_m(x)\Lambda_n(x)}{jk_0Y_0(\varepsilon_r(x)-1)}\ dx\Bigg\} \\
&- J_{y_n}\left\{\frac{k_yk_{x_p}Z_0}{jk_0a}\int\limits_{x_m-\Delta}^{x_m+\Delta}\Lambda_m(x)\int\limits_{x_n-\Delta}^{x_n+\Delta}\Lambda_n(x')\ \sum_p \frac{e^{-jk_{x_p}(x-x')}}{k_0^2-k_y^2-k_{x_p}^2}\ dx'\ dx\right\} \\
&= 0, \quad m = 1, 2, \ldots, N.
\end{aligned} \tag{2.63a}$$

$$\begin{aligned}
\sum_{n=1}^{N} J_{x_n}&\left\{-\frac{k_yk_{x_p}Z_0}{jk_0a}\int\limits_{x_m-\Delta}^{x_m+\Delta}\Lambda_m(x)\int\limits_{x_n-\Delta}^{x_n+\Delta}\Lambda_n(x')\ \sum_p \frac{e^{-jk_{x_p}(x-x')}}{k_0^2-k_y^2-k_{x_p}^2}\ dx'\ dx\right\} \\
&- J_{y_n}\Bigg\{\frac{jk_0Z_0}{a}\left(1-\frac{k_y^2}{k_0^2}\right)\int\limits_{x_m-\Delta}^{x_m+\Delta}\Lambda_m(x)\int\limits_{x_n-\Delta}^{x_n+\Delta}\Lambda_n(x')\ \sum_p \frac{e^{-jk_{x_p}(x-x')}}{k_0^2-k_y^2-k_{x_p}^2}\ dx'\ dx \\
&+\int\limits_{x_m-\Delta}^{x_m+\Delta}\frac{\Lambda_m(x)\Lambda_n(x)}{jk_0Y_0(\varepsilon_r(x)-1)}\ dx\Bigg\} \\
&= 0, \quad m = 1, 2, \ldots, N.
\end{aligned} \tag{2.63b}$$

Equation (2.63) can be written in matrix form as

$$\left[\begin{bmatrix} Z_{mn}^{xx} & Z_{mn}^{xy} \\ Z_{mn}^{yx} & Z_{mn}^{yy}\end{bmatrix} + \begin{bmatrix} \delta Z_{mm}^{xx} & 0 \\ 0 & \delta Z_{mm}^{yy}\end{bmatrix}\right]\begin{bmatrix} J_{x_n} \\ J_{y_n}\end{bmatrix} = \begin{bmatrix}0\end{bmatrix}, \tag{2.64}$$

where $[J_{x_n}\ J_{y_n}]$ is a column vector containing the unknown coefficients and $[Z_{mn}+\delta Z]$ is a matrix whose elements are found by carrying out the integrations in (2.63) yielding

$$Z_{xx}^{m1} = \frac{jk_0 Z_0 \Delta_x^2}{a}\left(1-\frac{k_{x_p}^2}{k_0^2}\right)\sum_p \frac{\left(1+jk_{x_p}\Delta_x - e^{jk_{x_p}\Delta_x}\right)}{\left(k_{x_p}\Delta_x\right)^2}\operatorname{sinc}^2\left(\frac{k_{x_p}\Delta_x}{2}\right)\frac{e^{-jk_{x_p}(x_m-x_1)}}{k_0^2-k_{x_p}^2} \tag{2.65a}$$

$$Z_{xx}^{mn} = \frac{jk_0 Z_0 \Delta_x^2}{a}\left(1-\frac{k_{x_p}^2}{k_0^2}\right)\sum_p \operatorname{sinc}^4\left(\frac{k_{x_p}\Delta_x}{2}\right)\frac{e^{-jk_{x_p}(x_m-x_n)}}{k_0^2-k_{x_p}^2} \tag{2.65b}$$

$$Z_{xx}^{mN} = \frac{jk_0 Z_0 \Delta_x^2}{a}\left(1-\frac{k_{x_p}^2}{k_0^2}\right)\sum_p \frac{\left(1-jk_{x_p}\Delta_x - e^{-jk_{x_p}\Delta_x}\right)}{\left(k_{x_p}\Delta_x\right)^2}\operatorname{sinc}^2\left(\frac{k_{x_p}\Delta_x}{2}\right)\frac{e^{-jk_{x_p}(x_m-x_N)}}{k_0^2-k_{x_p}^2} \tag{2.65c}$$

$$Z_{xy}^{m1} = \frac{k_y k_{x_p} Z_0 \Delta_x^2}{jk_0 a}\sum_p \frac{\left(1+jk_{x_p}\Delta_x - e^{jk_{x_p}\Delta_x}\right)}{\left(k_{x_p}\Delta_x\right)^2}\operatorname{sinc}^2\left(\frac{k_{x_p}\Delta_x}{2}\right)\frac{e^{-jk_{x_p}(x_m-x_1)}}{k_0^2-k_{x_p}^2} \tag{2.65d}$$

$$Z_{xy}^{mn} = \frac{k_y k_{x_p} Z_0 \Delta_x^2}{jk_0 a}\sum_p \operatorname{sinc}^4\left(\frac{k_{x_p}\Delta_x}{2}\right)\frac{e^{-jk_{x_p}(x_m-x_n)}}{k_0^2-k_{x_p}^2} \tag{2.65e}$$

$$Z_{xy}^{mN} = \frac{k_y k_{x_p} Z_0 \Delta_x^2}{jk_0 a}\sum_p \frac{\left(1-jk_{x_p}\Delta_x - e^{-jk_{x_p}\Delta_x}\right)}{\left(k_{x_p}\Delta_x\right)^2}\operatorname{sinc}^2\left(\frac{k_{x_p}\Delta_x}{2}\right)\frac{e^{-jk_{x_p}(x_m-x_N)}}{k_0^2-k_{x_p}^2} \tag{2.65f}$$

$$Z_{yx} = Z_{xy} \tag{2.65g}$$

$$Z_{yy}^{m1} = \frac{jk_0 Z_0 \Delta_x^2}{a}\left(1-\frac{k_y^2}{k_0^2}\right)\sum_p \frac{\left(1+jk_{x_p}\Delta_x - e^{jk_{x_p}\Delta_x}\right)}{\left(k_{x_p}\Delta_x\right)^2}\operatorname{sinc}^2\left(\frac{k_{x_p}\Delta_x}{2}\right)\frac{e^{-jk_{x_p}(x_m-x_1)}}{k_0^2-k_{x_p}^2} \tag{2.65h}$$

$$Z_{yy}^{mn} = \frac{jk_0 Z_0 \Delta_x^2}{a}\left(1-\frac{k_y^2}{k_0^2}\right)\sum_p \operatorname{sinc}^4\left(\frac{k_{x_p}\Delta_x}{2}\right)\frac{e^{-jk_{x_p}(x_m-x_n)}}{k_0^2-k_{x_p}^2} \tag{2.65i}$$

$$Z_{yy}^{mN} = \frac{jk_0 Z_0 \Delta_x^2}{a}\left(1-\frac{k_y^2}{k_0^2}\right)\sum_p \frac{\left(1-jk_{x_p}\Delta_x - e^{-jk_{x_p}\Delta_x}\right)}{\left(k_{x_p}\Delta_x\right)^2}\operatorname{sinc}^2\left(\frac{k_{x_p}\Delta_x}{2}\right)\frac{e^{-jk_{x_p}(x_m-x_N)}}{k_0^2-k_{x_p}^2} \tag{2.65j}$$

$$\delta Z_{xx}^{mm} = -\frac{\delta_{mn}\Delta_x}{jk_0 Y_0\left(\varepsilon_r-1\right)} \tag{2.65k}$$

$$\delta Z_{yy}^{mm} = -\frac{\delta_{mn}\Delta_y}{jk_0 Y_0\left(\varepsilon_r-1\right)} \tag{2.65l}$$

Piecewise constant expansion / Piecewise constant testing The solution can also be carried out for the TM_x case using piecewise constant expansion and testing functions. The dielectric region is discretized into N subsections of width $\Delta = b/N$. The current $\mathbf{J} = \hat{\mathbf{x}}J_x + \hat{\mathbf{y}}J_y$ is expanded in a linear combination of N piecewise constant basis functions with unknown current coefficients $\{J_{x_n}, J_{y_n}\}$ centered at $x_n = -\frac{b}{2} + \Delta_x(n - \frac{1}{2})$,

$$J_x = \sum_{n=1}^{N} J_{x_n} \Pi_n(x) \tag{2.66a}$$

$$J_y = \sum_{n=1}^{N} J_{y_n} \Pi_n(x) \tag{2.66b}$$

with $\Pi_n(x)$ given in (2.51). Inserting (2.66) into (2.49) and testing the resulting equation with piecewise constant functions, the elements of the impedance matrix $[Z_{mn} + \delta Z]$ in (2.64) are found to be

$$Z_{xx}^{mn} = \frac{jk_0 Z_0 \Delta_x^2}{a} \left(1 - \frac{k_{x_p}^2}{k_0^2}\right) \sum_p \mathrm{sinc}^2 \left(\frac{k_{x_p} \Delta_x}{2}\right) \frac{e^{-jk_{x_p}(x_m - x_n)}}{k_0^2 - k_{x_p}^2} \tag{2.67a}$$

$$Z_{xy}^{mn} = \frac{k_y k_{x_p} Z_0 \Delta_x^2}{jk_0 a} \sum_p \mathrm{sinc}^2 \left(\frac{k_{x_p} \Delta_x}{2}\right) \frac{e^{-jk_{x_p}(x_m - x_n)}}{k_0^2 - k_{x_p}^2} \tag{2.67b}$$

$$Z_{yx}^{mn} = Z_{xy} \tag{2.67c}$$

$$Z_{yy}^{mn} = \frac{jk_0 Z_0 \Delta_x^2}{a} \left(1 - \frac{k_y^2}{k_0^2}\right) \sum_p \mathrm{sinc}^2 \left(\frac{k_{x_p} \Delta_x}{2}\right) \frac{e^{-jk_{x_p}(x_m - x_n)}}{k_0^2 - k_{x_p}^2} \tag{2.67d}$$

$$\delta Z_{xx}^{mm} = -\frac{\delta_{mn} \Delta_x}{jk_0 Y_0 (\varepsilon_r - 1)} \tag{2.67e}$$

$$\delta Z_{yy}^{mm} = -\frac{\delta_{mn} \Delta_y}{jk_0 Y_0 (\varepsilon_r - 1)} \tag{2.67f}$$

2.4.4 Matrix Solution

In order to accurately determine the eigenvalues of the impedance matrices given in (2.55), (2.59), (2.65), and (2.67), a sufficient number of Floquet modes N_p and subsectional unknowns N_x must be included. A simple convergence criterion can be established to determine when the computation of the individual impedance matrix elements has converged adequately to its final value. A nontrivial solution for the fields requires the determinant of the impedance matrix to be zero, which results in a characteristic equation. The eigenvalues (propagation constants) are obtained from the roots of this equation. For a lossless structure, the propagation constants of a guided wave is a real number. However, in the stopbands, the propagation constant is complex-valued.

The eigenvalues are calculated by minimizing a function of N variables subject to bounds on the variables using a direct search algorithm. The algorithm uses the complex method to find a local minimum point of a function of N variables and is based on function comparison [139]. No derivative information is used in this technique. The minimization procedure is carried out by fixing the frequency of operation and allowing the optimization code to vary the propagation constant k_{x_0} until a minimum is found. If more than one minimum (eigenvalue) is found, implying that multiple modes are propagating in the structure, the corresponding eigenvectors are analyzed to determine which eigenvalue corresponds to which propagating mode. In the following tables, the propagation constant of the lowest order mode that propagates is listed.

Table 2.1: Normalized TE$_x$ propagation constant $k_{x_0}a$ for increasing number of Floquet modes for f_0=fa/c=1, ε_r=8.9, b=0.3545a, and N_x=40

	$k_{x_0}a$ (pulse)		$k_{x_0}a$ (triangle)	
N_p	ϕ_0=0°	ϕ_0=9.15°	ϕ_0=0°	ϕ_0=9.15°
7	2.471	2.547	2.474	2.550
11	1.723	1.789	1.733	1.799
21	1.691	1.758	1.702	1.768
31	1.688	1.754	1.699	1.766
41	1.687	1.754	1.698	1.765
51	**1.687**	**1.753**	**1.698**	**1.765**
$k_{x_0}a^*$	1.676	1.743	1.676	1.743

In Table 2.1, the normalized propagation constant $k_{x_0}a$ for a normally incident plane wave (ϕ_0=0°) and off-axis incident plane wave (ϕ_0=9.15°) for the TE$_x$ case is shown as function of the number of Floquet modes (N_p) and unknown basis set (pulse or triangle) for the combination of normalized frequency f_0=fa/c=1, 40 subsectional unknowns (N_x), relative permittivity ε_r=8.9, and filling fraction b/a=0.3545. The value of ϕ_0=9.15° corresponds to an off-axis propagation constant of k_{y_0}=$1/a$ which is equal to the inverse of the unit cell size. The off-axis propagation constant is set to this value because many authors use this specific parameter value as a reference data set [38, 129]. The bold values (error less than 1%) for N_p=51 and N_x=40 listed in Tables 2.1–2.4 correspond to the same solution and serve to represent a fixed parameter set to compare the relative convergence as a function of number of unknowns and Floquet mode contributions. The correct value, denoted $k_{x_0}a^*$ and listed at the bottom of Tables 2.1–2.4, is determined from a solution of the exact eigenvalue equation derived earlier in the chapter.

Note in Table 2.1 that the necessary convergence occurs for both the pulse and triangle basis cases for normal incidence and off-axis propagation as the number of Floquet modes increase. The accuracy of the eigenvalue solution is limited by both N_x and N_p. The advantage of expanding the current in piecewise linear functions and testing with a similar basis as opposed to piecewise constant expansion and testing functions would seem to be the increase in convergence of the resulting series using the higher order bases. For the piecewise constant expansion and testing functions, the Floquet series converges as $\mathcal{O}(p^{-4})$. However, using piecewise linear expansion and testing functions, the convergence rate increases to $\mathcal{O}(p^{-6})$. For even modest numbers of Floquet modes (N_p=31), the solution has converged to within 1% of the exact solution. Note the effect of the more complicated formulation on the accuracy using the triangle bases is not immediately noticeable as a function of increased Floquet contributions.

Table 2.2: Normalized TE$_x$ propagation constant $k_{x0}a$ for increasing number of unknowns for f_0=fa/c=1, ε_r=8.9, b=0.3545a, and N_p=51

	$k_{x0}a$ (pulse)		$k_{x0}a$ (triangle)	
N_x	ϕ_0=0°	ϕ_0=9.15°	ϕ_0=0°	ϕ_0=9.15°
10	1.825	1.810	2.030	2.097
15	1.744	1.781	1.833	1.897
20	1.715	1.781	1.763	1.830
40	**1.687**	**1.753**	**1.698**	**1.765**
60	1.681	1.748	1.685	1.754
80	1.679	1.746	1.685	1.754
$k_{x0}a^*$	1.676	1.743	1.676	1.743

In Table 2.2, the normalized propagation constant for a normally incident plane wave (ϕ_0=0°) and off-axis incident plane wave (ϕ_0=9.15°) for the TE$_x$ case is shown as function of the number of unknowns (N_x) and unknown basis set (pulse or triangle) for the combination of normalized frequency f_0=fa/c=1, 51 Floquet modes (N_p), relative permittivity ε_r=8.9, and filling fraction b/a=0.3545. Again, the results presented in Table 2.2 confirm that the necessary convergence occurs for both the pulse and triangle bases cases for normal incidence and off-axis propagation as the number of unknowns increase. For normalized frequency equal to unity (λ_0=a), the electrical length of the dielectric insert is $0.3545\lambda_0/\sqrt{\varepsilon_r}$=$0.1188/\lambda_0$. Thus, only a few unknowns should be required to accurately model the physical problem. For example, the solution obtained using only N_x=20 unknowns is within 5% of the exact solution. However, it is clear from the data that even though the Floquet series may converge more quickly using higher order bases, the error introduced to the final solution is dominated by the number of subsectional bases. Thus, using the minimum number of bases if the most efficient solution to the problem.

The computational cost of computing each individual element in the impedance matrix is proportional to N_p. Although the implementation of pulse basis functions provides a more slowly converging Floquet series than does the implementation using triangular bases, it achieves a more accurate solution using fewer subsectional bases. The piecewise linear functions are not only more expensive to compute than the simple pulse functions but are also more prone to coding error. Since the total cost of computing the full impedance matrix is proportional to $N_x^2 N_p$, incorporating fewer basis functions necessarily decreases this cost. Tables 2.1 and 2.2 clearly show that the accuracy of computing the propagation constant is more sensitive to the number of subsectional bases used in the approximation of the current than the number of Floquet modes used to compute the Floquet series.

Table 2.3: Normalized TM_x propagation constant $k_{x_0}a$ for increasing number of Floquet modes for $f_0 = fa/c = 1$, $\varepsilon_r = 8.9$, $b = 0.3545a$, and $N_x = 40$

	$k_{x_0}a$ (pulse)		$k_{x_0}a$ (triangle)	
N_p	$\phi_0=0°$	$\phi_0=9.15°$	$\phi_0=0°$	$\phi_0=9.15°$
7	2.471	2.538	2.460	2.544
11	1.723	1.793	1.712	1.800
21	1.691	1.763	1.681	1.775
31	1.688	1.761	1.678	1.767
41	1.687	1.760	1.696	1.767
51	**1.687**	**1.760**	**1.696**	**1.767**
$k_{x_0}a^*$	1.676	1.751	1.676	1.751

In Table 2.3, the normalized propagation constant for a normally incident plane wave ($\phi_0=0°$) and off-axis incident plane wave ($\phi_0 = 9.15°$) for the TM_x case is shown as function of the number of unknowns (N_x) and unknown basis set (pulse or triangle) for the combination of normalized frequency $f_0=fa/c=1$, 51 Floquet modes (N_p), relative permittivity $\varepsilon_r=8.9$, and filling fraction $b/a=0.3545$. As in the TE_x case, the value $\phi_0=9.15°$ corresponds to $k_{y0}=1/a$, the inverse of the unit cell size. In Table 2.4, the normalized propagation constant for a normally incident plane wave ($\phi_0=0°$) and off-axis incident plane wave ($\phi_0=9.15°$) for the TE_x case is shown as function of the number of Floquet modes

(N_p) and unknown basis set (pulse or linear) for the combination of normalized frequency f_0=fa/c=1, 40 subsectional unknowns (N_x), relative permittivity ε_r=8.9, and filling fraction b/a=0.3545.

Table 2.4: Normalized TM$_x$ propagation constant $k_{x0}a$ for increasing number of unknowns for f_0=fa/c=1, ε_r=8.9, b=0.3545a, and N_p=51

	$k_{x0}a$ (pulse)		$k_{x0}a$ (triangle)	
N_x	ϕ_0=0°	ϕ_0=9.15°	ϕ_0=0°	ϕ_0=9.15°
10	1.824	1.898	2.029	2.093
15	1.744	1.817	1.834	1.901
20	1.715	1.788	1.765	1.833
40	**1.687**	**1.760**	**1.696**	**1.767**
60	1.681	1.755	1.685	1.760
80	1.679	1.753	1.685	1.751
$k_{x0}a^*$	1.676	1.751	1.676	1.751

Similar conclusions are drawn in Tables 2.3 and 2.4 for the TM$_x$ case that are observed for the TE$_x$ case. The accuracy increases both by increasing the number of Floquet mode contributions and by modeling the equivalent current more carefully by increasing the number of unknowns. A simple pulse basis expansion serves to solve the problem quickly and accurately. This observation will hold true as well for the two-dimensional structures examined in Chapter 3.

In order to verify that the higher frequency solution of the propagation constants computed using the method of moments technique and the plane wave expansion method are correct, the band structure of a periodic array of dielectric slabs is calculated for a filling fraction b/a=0.3545, relative dielectric constant ε_r=8.9, and off-axis[4] propagation constant k_{y0}=$1/a$. Figure 2.9 shows the calculated band structure for both the TE$_x$ and TM$_x$ cases. The moment method solution includes 40 subsectional bases and 51 Floquet modes. The plane wave expansion method uses 63 Floquet modes. It is clear that the solutions obtained by the two methods are in excellent agreement. For an off-axis propagation constant of $k_{y0} = 1/a$ and for relatively lower normalized frequency ($f_0 \leq 0.4$), the two modal solutions (TE$_x$, TM$_x$) have different band gaps. At higher frequencies, the TE$_x$ and TM$_x$

[4]By virtue of the fact that the TE$_x$ and TM$_x$ modes for are degenerate for normal incidence, an off-axis propagation case must be computed to be sure that the derivatives for the TM$_x$ case are formulated and implemented correctly.

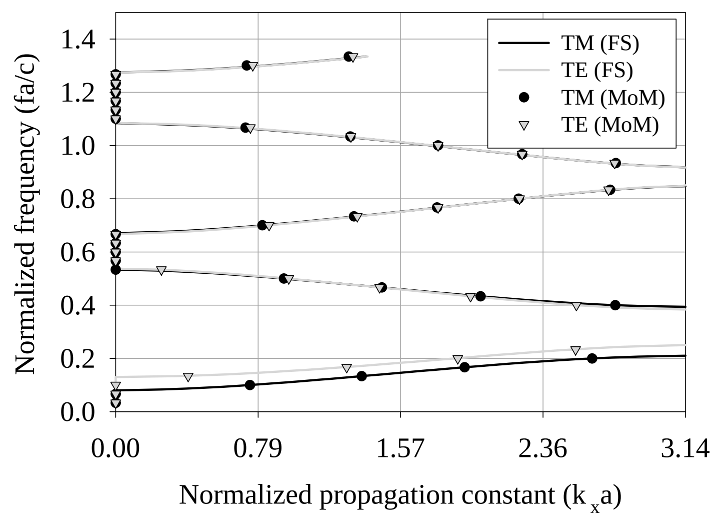

Figure 2.9: Band structure (TE_x, TM_x) of a periodic array of dielectric slabs for b/a= 0.3545, ε_r=8.9, and off-axis propagation constant k_{y0}=$1/a$ computed using method of moments technique (MoM) with N_p=51 and plane wave expansion (PWE) solution with N_p=63

bands are indistinguishable for the prescribed parameter set.

2.5 Experimental Verification

Experimental measurements with micromachined dielectrics were performed to verify that a similar band structure predicted theoretically using the method of moment solution or plane wave expansion (eigenvalue) solution for plane wave excitation of periodic media exists for microstrip excitation of a finite height periodic dielectric grating. Experimental and computational evidence indicates that the high dielectric constant material used to support the microstrip circuit effectively confines the field to near the region of the microstrip itself. Consequently, the quasi-TEM microstrip excitation simply "sees" a periodically changing dielectric constant – much like the periodic array of dielectric slabs excited using plane wave excitation. To corroborate the frequency response obtained through measurements of fabricated circuits, finite element simulations using the Ansoft High-Frequency Structure Simulator (HFSS) were carried out to model the exact structure of interest. Additionally, an equivalent model for a microstrip mounted over a periodic dielectric substrate (hi-Z, low-Z filter) was simulated using the Agilent EEsof EDA Series IV microstrip Libra component.

A one-dimensional periodic dielectric substrate, or grating, shown in Figure 2.10 was

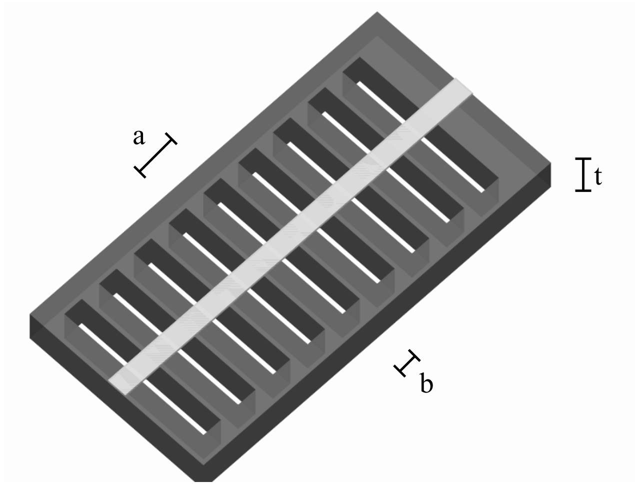

Figure 2.10: Microstrip mounted on 1-D periodic dielectric substrate with period a, filling fraction b/a=0.5, and height t

fabricated with period a=6.35 mm (250 mil) and filling fraction equal to 0.5 using Rogers Corporation RT/duroid having a dielectric constant of 10.2 and a thickness t of 0.635 mm (25 mil). The measured response of the milled one-dimensional grating microstrip circuit is shown in Figure 2.11. It is observed that the first stopband, defined by the 10 dB bandwidth in the figure, is centered around 12 GHz with a second gap located between 21 and 26 GHz. A third gap may or may not be visible around 36 GHz.

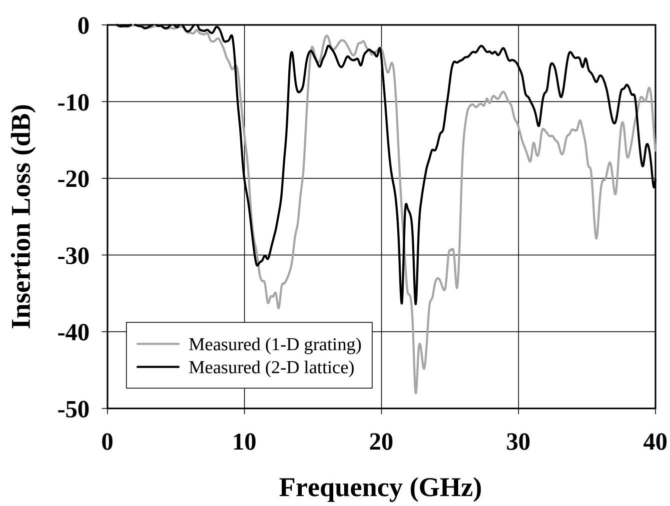

Figure 2.11: Measured frequency response of a microstrip mounted on a 1-D grating and 2-D lattice substrate

Concurrent to the circuit fabrication, the band structure for a one-dimensional periodic array of dielectric slabs with the same geometrical and electrical parameters (a=6.35 mm,

b=3.175 mm, and ε_r=10.2) was determined. Three stopgaps were found to exist within the measurement range of the HP8510 Network Analyzer, the first between 8.0 and 13.2 GHz, a second between 18.7 and 26.2 GHz, and another between 31.2 and 37.3 GHz. These results are in agreement with the measured response shown in Figure 2.11. The simulated response of an HFSS simulation of the structure and the response of a Libra simulation of an equivalent model are plotted in Figure 2.12. Due to the computational cost of implementing the HFSS simulation of the realizable structure, only frequencies between 5 and 15 GHz

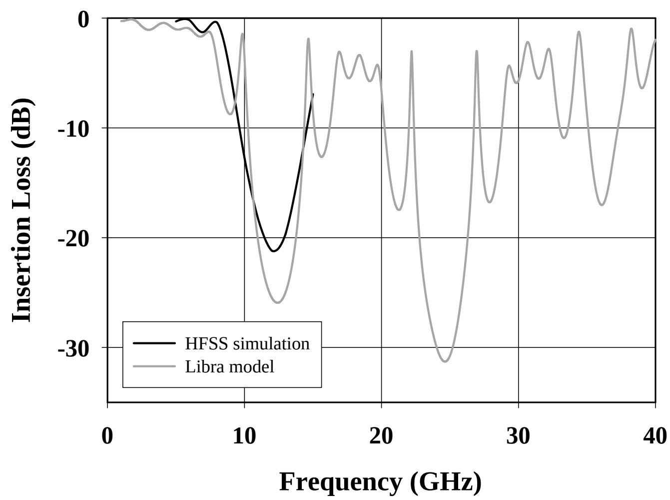

Figure 2.12: Simulated frequency response of HFSS and Libra simulations of a microstrip mounted on a 1-D grating

were analyzed. Note that both simulations reveal the first gap around 12 GHz and the Libra model predicts the second and third gaps at 24 GHz and 36 GHz, respectively. The gaps determined from the measurements and simulations of the finite structure reveal one noteworthy difference between the gaps (stopbands) produced by a finite lattice (filter) and the true gap (stopband) produced by an infinite lattice (filter), namely, that using a small number of lattice periods (five) necessarily changes the shape and center frequency of the response of the "filter."

The encouraging results led to the question of how much material could be removed while maintaining the response of the system, ultimately shedding light on the question of how well the quasi-TEM microstrip mode in these periodic circuits can be modeled by simple arrays of planar dielectric slabs. To this end, three substrates were designed that successively added material to the one-dimensional grating to produce a finite one-dimensional grating, a two-dimensional lattice of square air rods (holes), and finally, a two-dimensional lattice of circular holes. Incorporating circular rods in the design instead of square ones has the advantage of increased ease and speed of machining the substrates using simple milling procedures. Each of the new substrates shown in Figure 2.13 was designed to have a period equal to that of the one-dimensional periodic substrate shown in Figure 2.10. Consequently,

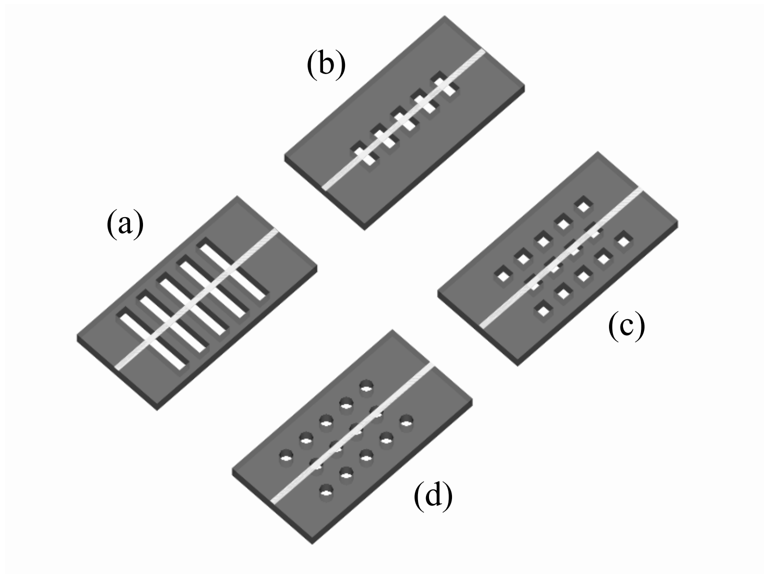

Figure 2.13: Microstrip mounted on (a) 1-D grating, (b) finite 1-D grating, (c) 2-D lattice of square holes, and (d) 2-D lattice of circular holes

the microstrip line would traverse effectively similar sections of dielectric material.

HFSS simulations were carried out for each of the three models for frequencies between 5 and 15 GHz to see the effect of the added material on the bandwidth and location of the first stopgap. The results of the finite element simulations of the three "equivalent" circuits are shown in Figure 2.14. Also shown is the response of a through line mounted on a homogeneous substrate of same thickness. Note that, for all intents and purposes, the responses of all of the periodic gratings are the same.

Finally, a two-dimensional periodic dielectric substrate, shown in Figure 2.15, was fabricated with period a=6.35 mm (250 mil), cell-to-cell distance $c=a/\sqrt{2}$=4.49 mm (177 mil), and circular hole diameter b=3.17 mm (125 mil) using RT/duroid having a dielectric constant of 10.2 and a thickness t of 0.635 mm (25 mil). The physical dimensions of the two-dimensional lattice were designed to produce the exact period a used in the one-dimensional periodic substrate. The band structure was originally adapted from band plots presented in [63] but has since been verified by solutions derived in Chapter 3. The frequency response of the two-dimensional periodic substrate is also included in Figure 2.11.

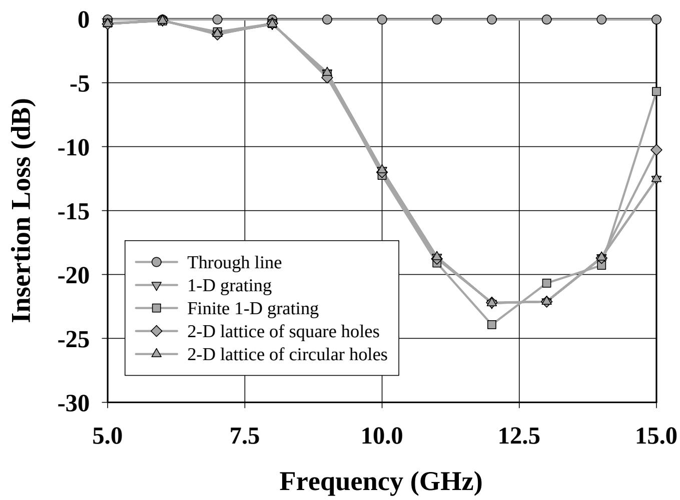

Figure 2.14: Simulated frequency response of a microstrip mounted on a 1-D grating, finite 1-D grating, 2-D lattice of square holes, and 2-D lattice of circular holes

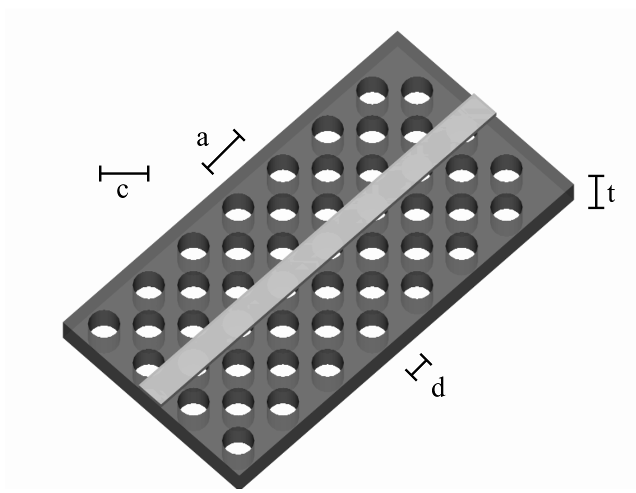

Figure 2.15: Microstrip mounted on two-dimensional periodic dielectric substrate with period a, cell-to-cell distance $c{=}a/\sqrt{2}$, hole diameter d, and height t

Noticeable differences in the frequency response of the one-dimensional grating and two-dimensional lattice are observed in Figure 2.11. Not only are the bandwidths of the first two stopbands of the two-dimensional substrate lattice narrower than the ones produced by the one-dimensional grating, the center frequencies are shifted slightly. The HFSS simulations shown in Figure 2.14 would seem to indicate that for microstrip excitation, the responses of the one- and two-dimensional lattices shown in Figures 2.10 and 2.15 are indistinguishable. This observation raises the question of how well HFSS can model the finite periodic dielectric substrate.

2.6 Conclusions

The solution for the propagation of electromagnetic energy through a one-dimensional periodic dielectric structure has been determined using two distinct solution techniques. A Fourier series solution has been implemented by solving the one-dimensional (differential) wave equation for periodic functions. Concurrently, a separate solution is obtained by deriving the integral equation solution for a one-dimensionally periodic media. The advantage of using the plane wave expansion method over the IE/MoM solution is the computational speed. The optimization procedure used in the IE/MoM solution requires the impedance matrix to be filled for each iteration of the computation of the propagation constant. Even using a highly efficient optimizer to quickly find the eigenvalue of interest, the process can be somewhat time-consuming. For one-dimensional structures, this does not present a serious problem. However, it will be clearly shown that for the two dimensional lattices of Chapter 3, this restriction has grave consequences. The accuracy of the plane wave expansion method increases with increased Floquet mode contributions whereas the accuracy of the IE/MoM solution increases both by increasing the number of Floquet mode contributions and by modeling the equivalent current more carefully by increasing the number of unknowns. It is observed that, for the IE/MoM solution, a simple pulse basis expansion serves to solve the problem quickly and accurately. This observation will hold true as well for the two-dimensional structures examined in Chapter 3.

Experimental verification of the one-dimensional band gaps is accomplished by determining the filtering effect of mounting a microstrip over a one-dimensional periodic substrate. The quasi-TEM fields of the microstrip excitation for the periodic substrate are modeled as plane waves incident on a one-dimensionally periodic medium. The band structure of the resulting microwave circuit is also modeled effectively using a simple hi-Z, low-Z filter and is similar to the band structure determined from the plane wave solution.

CHAPTER 3

Two-Dimensional Periodic Dielectric Structures

3.1 Introduction

As opposed to one-dimensional structures, where many applications are found at the higher quasi-optical and optical frequencies [1, 2], research into applications involving two-dimensional periodic structures is fruitful at microwave and lower frequencies. In fact, an entire class of artificial surfaces and/or materials termed *frequency selective surfaces* (FSS) incorporates the use of period to provide unique spectral characteristics in applications ranging from radar cross section reduction to antenna array beam-forming. Two-dimensional dielectric lattices are actively being incorporated into microwave circuit and antenna designs, high-Q filters and resonators, waveguides, and novel materials/surfaces. Although serious attention has been focused by the electromagnetics community on traditional frequency selective surfaces, new applications have recently emerged for more general two-dimensional periodic structures and are challenging traditional concepts and views about electromagnetic propagation in periodic media [3, 4, 5].

This chapter extends the solutions and techniques developed for one-dimensional period in Chapter 2 to structures that have periodicities in two directions. The phase constants for electromagnetic waves propagating in a two-dimensional lattice for both dielectric rods in an air background and air columns immersed in a dielectric media are found explicitly using two similar but decidedly different techniques. The first solution, detailed in Section 3.2, incorporates the use of a Fourier series representation for the periodic field and is determined by solving the differential equation (two-dimensional wave equation) for periodic media. The second solution is found by deriving an integral equation for the periodic field and numerically solving the resulting linear system and is presented in Section 3.3.

In light of the complicated nature of two-dimensional periodic media, effective medium theory (EMT) is applied to the lattice which reduces the problem to that of solving for the propagation in an equivalent one-dimensional array with an effective permittivity. In Section 3.4, the theory of EMT is outlined briefly and its advantages and limitations are discussed. One of the significant disadvantages of EMT is its limitation to electrically small lattice elements. A number of representative structures are used in the chapter to show the behavior of electromagnetic fields in two-dimensional periodic media and observations about the salient features of each are discussed. The particular application of a two-dimensional periodic dielectric structure in parallel-plate mode reduction in conductor-backed slots is presented extensively in Appendix D. For the structures shown in this chapter, only *in-plane* propagation is considered. This is significant because complete band gaps[1] only exist for in-plane propagation.

[1] A complete band gap (for a given polarization) is defined as one where over a range of frequencies (band), electromagnetic energy may not propagate in *any* direction. Some authors define a complete band gap as one where for *any* electromagnetic wave polarization, energy may not propagate in *any* direction.

3.2 Plane Wave Expansion Method

3.2.1 Analytical Techniques

For two-dimensional periodic problems, the solution of the exact eigenvalue equation can be obtained through the use of a double Fourier series. A representative two-dimensional

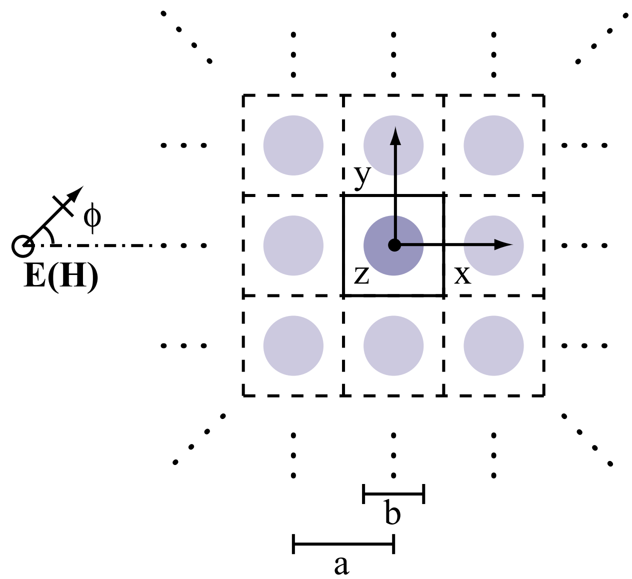

Figure 3.1: Cross-sectional view of two-dimensional array of dielectric rods of diameter b in a periodic square lattice with period a

periodic array of dielectric rods of diameter b in a periodic square lattice[2] with period a is illustrated in cross section in Figure 3.1. If the electric field has only an axial (or z-directed) component, the mode is transverse magnetic to z and is denoted TM$_z$. If the electric field has only components in the transverse x-y plane, the mode is transverse electric to z and is denoted TE$_z$.

TM$_z$ Case

The electric field is expanded as a periodic function with period a in the x-direction and prescribed propagation constant k_{x_0} and with period c in the y-direction and prescribed propagation constant k_{y_0} and is given by

$$\mathbf{E}(x, y) = \hat{\mathbf{z}} E_z(x, y) = \hat{\mathbf{z}} E_p(x, y)\ e^{-jk_{x_0}x}\ e^{-jk_{y_0}y} \tag{3.1}$$

[2]Square lattices are used in this chapter to simplify the notation and understanding. Extensions of the solutions to other two-dimensional lattices depicted in Figure B.3 of Appendix B is straightforward.

where $E_p(x, y)$ is the periodic electric field that propagates only in the xy-plane. Again, applying the operator $(\nabla_{xy}^2 + k^2)$ to the electric field in (3.1) yields an equation similar to (2.15) with $\varepsilon_r(x)$ replaced with $\varepsilon_r(x, y)$. If the rods are assumed to be infinite in the z direction $\left(\frac{\partial}{\partial z} = 0\right)$, then the wave equation simplifies to

$$-\frac{\partial^2}{\partial x^2}E_z(x, y) - \frac{\partial^2}{\partial y^2}E_z(x, y) = k_0^2 \varepsilon_r(x, y) E_z(x, y) \tag{3.2}$$

If the periodic field, expanded as in a double Fourier series in x and y with unknown coefficients a_{nq} which serve to represent the dependence on z,

$$E_p(x, y) = \sum_n \sum_q a_{nq}\; e^{-j\frac{2\pi n}{a}x}\; e^{-j\frac{2\pi q}{c}y}, \tag{3.3}$$

and the periodic dielectric rods, expanded in another double Fourier series with coefficients b_{mp},

$$\varepsilon_r(x, y) = \sum_m \sum_p b_{mp}\; e^{-j\frac{2\pi m}{a}x}\; e^{-j\frac{2\pi p}{a}y}, \tag{3.4}$$

are substituted into (3.2) and the algebraic operations are carried out, then

$$\begin{aligned}\sum_n \sum_q \left[\left(\frac{2\pi n}{a} + k_{x0}\right)^2 + \left(\frac{2\pi q}{c} + k_{y0}\right)^2\right] a_{nq}\; e^{-j\frac{2\pi n}{a}x}\; e^{-j\frac{2\pi q}{c}y} = \\ k_0^2 \sum_m \sum_p b_{mp}\; e^{-j\frac{2\pi m}{a}x}\; e^{-j\frac{2\pi p}{a}y} \sum_n \sum_q a_{nq}\; e^{-j\frac{2\pi n}{a}x}\; e^{-j\frac{2\pi q}{c}y}.\end{aligned} \tag{3.5}$$

In order to determine the coefficients a_{nq} and b_{mp}, (3.5) is multiplied by orthogonal functions in x and y and integrated over the unit cell. This integration produces a Kronecker delta function for specific indices in the x and y directions and

$$\begin{aligned}\sum_n \sum_q \left[\left(\frac{2\pi n}{a} + k_{x0}\right)^2 + \left(\frac{2\pi q}{c} + k_{y0}\right)^2\right] a_{nq}\delta\left(\frac{2\pi l}{c} - \frac{2\pi q}{c}\right)\delta\left(\frac{2\pi k}{a} - \frac{2\pi n}{a}\right) = \\ k_0^2 \sum_m \sum_p \sum_n \sum_q a_{nq} b_{mp}\delta\left(\frac{2\pi l}{c} - \frac{2\pi p}{c} - \frac{2\pi q}{c}\right)\delta\left(\frac{2\pi k}{a} - \frac{2\pi m}{a} - \frac{2\pi p}{a}\right).\end{aligned} \tag{3.6}$$

The convolution in (3.6) can be cast, albeit not as easily as (2.20), into the following general matrix form

$$a_{nq}\left[\left(\frac{2\pi n}{a} + k_{x0}\right)^2 + \left(\frac{2\pi q}{c} + k_{y0}\right)^2\right] = k_0^2 \sum_m \sum_p a_{nq} b_{n-m,q-p} \tag{3.7}$$

where for the square dielectric rod illustrated in Figure 3.2(a),

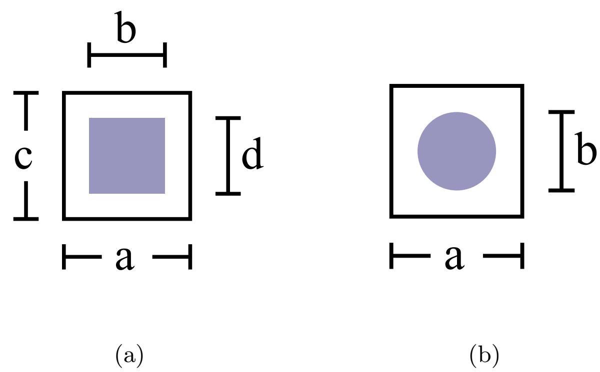

Figure 3.2: Unit cell dimensions for (a) rectangular dielectric rods and (b) circular dielectric rods where for the rectangular rod, a and c are the unit cell sizes, b and d are the element edge lengths, and for the circular rod, a is the unit cell size and b is the diameter

$$\begin{aligned} b_{n-m,q-p} =& \frac{1}{ac} \int_{-b/2}^{b/2} \int_{-d/2}^{d/2} (\varepsilon_r - 1)\; e^{-j\frac{2\pi(n-m)}{a}x}\; e^{-j\frac{2\pi(q-p)}{a}y}\; dx\; dy \\ &+ \frac{1}{ac} \int_{-a/2}^{a/2} \int_{-c/2}^{c/2} (1)\; e^{-j\frac{2\pi(n-m)}{a}x}\; e^{-j\frac{2\pi(q-p)}{a}y}\; dx\; dy \\ =& \frac{bd}{ac}(\varepsilon_r - 1)\, \mathrm{sinc}\, \frac{\pi(n-m)b}{a}\, \mathrm{sinc}\, \frac{\pi(q-p)d}{c} + \delta_{n-m,q-p} \end{aligned} \tag{3.8}$$

and for the circular dielectric rod illustrated in Figure 3.2(b),

$$\begin{aligned} b_{n-m,q-p} =& \frac{2\pi}{a^2} \int_{0}^{b/2} (\varepsilon_r - 1) J_0 \left(\sqrt{\left(\frac{2\pi(n-m)r}{a}\right)^2 + \left(\frac{2\pi(q-p)r}{a}\right)^2} \right) r\; dr \\ &+ \frac{2\pi}{a^2} \int_{0}^{a} (1) J_0 \left(\sqrt{\left(\frac{2\pi(n-m)r}{a}\right)^2 + \left(\frac{2\pi(q-p)r}{a}\right)^2} \right) r\; dr \\ =& \frac{\pi b^2}{a^2}(\varepsilon_r - 1) \frac{2J_1\left(\sqrt{\left(\frac{2\pi(n-m)b}{a}\right)^2 + \left(\frac{2\pi(q-p)b}{a}\right)^2} \right)}{\sqrt{\left(\frac{2\pi(n-m)b}{a}\right)^2 + \left(\frac{2\pi(q-p)b}{a}\right)^2}} + \delta_{n-m,q-p}. \end{aligned} \tag{3.9}$$

In Figure 3.2(a), a and c are the unit cell sizes, b and d are the square element edge lengths. In Figure 3.2(b), a is the unit cell size and b is the diameter of the circular element. With a little algebraic work, the coefficients $b_{n-m,q-p}$ in (3.8) and (3.9) can be manipulated to agree with similar expressions in [107] and [73].

If the dielectric rods are replaced by air columns, the coefficients $b_{n-m,q-p}$ become

$$\begin{aligned}
b_{n-m,q-p} =& \frac{1}{ac} \int\limits_{-a/2}^{a/2} \int\limits_{-c/2}^{c/2} (\varepsilon_r)\; e^{-j\frac{2\pi(n-m)}{a}x}\; e^{-j\frac{2\pi(q-p)}{a}y}\; dx\; dy \\
& - \frac{1}{ac} \int\limits_{-b/2}^{b/2} \int\limits_{-d/2}^{d/2} (\varepsilon_r - 1)\; e^{-j\frac{2\pi(n-m)}{a}x}\; e^{-j\frac{2\pi(q-p)}{a}y}\; dx\; dy \\
=& \varepsilon_r \delta_{n-m,q-p} - (\varepsilon_r - 1)\frac{bd}{ac} \operatorname{sinc} \frac{\pi(n-m)b}{a} \operatorname{sinc} \frac{\pi(q-p)d}{c}
\end{aligned} \tag{3.10}$$

for the rectangular air column shown in Figure 3.3(a), and

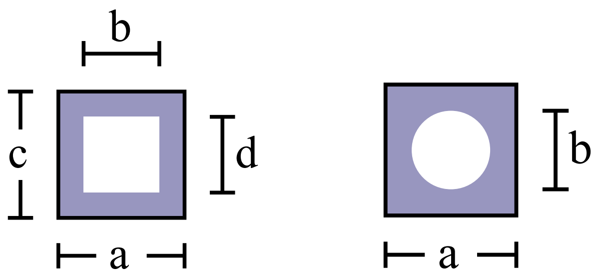

(a) (b)

Figure 3.3: Unit cell dimensions for (a) rectangular dielectric air columns and (b) circular air columns where for the rectangular column, a and c are the unit cell sizes, b and d are the element edge lengths, and for the circular column, a is the unit cell size and b is the diameter

$$\begin{aligned}
b_{n-m,q-p} =& \frac{2\pi}{a^2} \int\limits_{0}^{a} (\varepsilon_r) J_0 \left(\sqrt{\left(\frac{2\pi(n-m)r}{a}\right)^2 + \left(\frac{2\pi(q-p)r}{a}\right)^2} \right) r\; dr \\
& - \frac{2\pi}{a^2} \int\limits_{0}^{b/2} (\varepsilon_r - 1) J_0 \left(\sqrt{\left(\frac{2\pi(n-m)r}{a}\right)^2 + \left(\frac{2\pi(q-p)r}{a}\right)^2} \right) r\; dr \\
=& \varepsilon_r \delta_{n-m,q-p} - (\varepsilon_r - 1)\frac{\pi b^2}{a^2} \frac{2J_1 \left(\sqrt{\left(\frac{2\pi(n-m)b}{a}\right)^2 + \left(\frac{2\pi(q-p)b}{a}\right)^2} \right)}{\sqrt{\left(\frac{2\pi(n-m)b}{a}\right)^2 + \left(\frac{2\pi(q-p)b}{a}\right)^2}}
\end{aligned} \tag{3.11}$$

for the circular air column shown in Figure 3.3(b).

A generalized linear eigensystem problem is represented by $Ax = \lambda Bx$ where A and B are $n \times n$ matrices. The value λ is an *eigenvalue* and $x \neq 0$ is the corresponding *eigenvector*.

The propagating modes in the TM_z case are solutions of the generalized linear eigensystem in (3.7).

$\mathbf{TE}_z$ Case

For the TE_z case, the electric field is replaced by the magnetic field in the wave equation

$$\nabla \times \left\{ \frac{1}{\varepsilon_r(x,y)} \nabla \times \hat{\mathbf{z}} H_z(x,y) \right\} + k_0^2 \hat{\mathbf{z}} H_z(x,y) = 0 \tag{3.12}$$

where $\varepsilon_r(x)$ in (2.23) has been replaced with $\varepsilon_r(x,y)$. The same care must be taken to apply the wave equation operator to the magnetic field in the two dimensional case that was taken to apply it to the magnetic field in the one dimensional case. The resulting equation resembles (2.24)

$$\frac{1}{\varepsilon_r(x,y)} \hat{\mathbf{z}} \cdot \nabla \times \nabla \times \mathbf{H}(x,y) + \hat{\mathbf{z}} \cdot \nabla \left\{ \frac{1}{\varepsilon_r(x,y)} \right\} \times \nabla \times \mathbf{H}(x,y) = -k_0^2 H_z(x,y). \tag{3.13}$$

Expanding the periodic magnetic field in a double Fourier series,

$$H_p(x) = \sum_n \sum_q a_{nq} \; e^{-j\frac{2\pi n}{a}x} \; e^{-j\frac{2\pi q}{c}y}, \tag{3.14}$$

and the inverse of the dielectric function in another double Fourier series as

$$\frac{1}{\varepsilon_r(x,y)} = \sum_m \sum_p b_{mp} \; e^{-j\frac{2\pi m}{a}x} \; e^{-j\frac{2\pi p}{a}y}, \tag{3.15}$$

substituting the expansions into (3.13), and carrying out the curl and gradient operations yields

$$\begin{aligned}
&\sum_m \sum_p b_{mp} \; e^{-j\frac{2\pi m}{a}x} \; e^{-j\frac{2\pi p}{a}y} \Bigg\{ -\frac{\partial^2}{\partial x^2} \sum_n \sum_q a_{nq} \; e^{-j\frac{2\pi n}{a}x} \; e^{-j\frac{2\pi q}{c}y} \; e^{-jk_{x0}x} e^{-jk_{y0}y} \\
&\qquad - \frac{\partial^2}{\partial y^2} \sum_n \sum_q a_{nq} \; e^{-j\frac{2\pi n}{a}x} \; e^{-j\frac{2\pi q}{c}y} \; e^{-jk_{x0}x} \; e^{-jk_{y0}y} \Bigg\} \\
&- \frac{\partial}{\partial x} \sum_m \sum_p b_{mp} \; e^{-j\frac{2\pi m}{a}x} \; e^{-j\frac{2\pi p}{a}y} \frac{\partial}{\partial x} \sum_n \sum_q a_{nq} \; e^{-j\frac{2\pi n}{a}x} \; e^{-j\frac{2\pi q}{c}y} \; e^{-jk_{x0}x} \; e^{-jk_{y0}y} \\
&- \frac{\partial}{\partial y} \sum_m \sum_p b_{mp} \; e^{-j\frac{2\pi m}{a}x} \; e^{-j\frac{2\pi p}{a}y} \frac{\partial}{\partial y} \sum_n \sum_q a_{nq} \; e^{-j\frac{2\pi n}{a}x} \; e^{-j\frac{2\pi q}{c}y} \; e^{-jk_{x0}x} \; e^{-jk_{y0}y} \\
&\qquad = -k_0^2 \sum_n \sum_q a_{nq} \; e^{-j\frac{2\pi n}{a}x} \; e^{-j\frac{2\pi q}{c}y} \; e^{-jk_{x0}x} \; e^{-jk_{y0}y}.
\end{aligned} \tag{3.16}$$

Simplifying (3.16) by carrying out the derivatives and combining like series, integrating the result over one period, and simplifying the resulting expression yields an equation similar to (2.28)

$$\sum_m \sum_p a_{nq} b_{n-m,q-p} \Bigg[\left(\frac{2\pi n}{a} + k_{x_0} \right)^2 + \left(\frac{2\pi q}{c} + k_{y_0} \right)^2 - \frac{2\pi(n-m)}{a} \left(\frac{2\pi n}{a} + k_{x_0} \right) - \frac{2\pi(q-p)}{c} \left(\frac{2\pi q}{c} + k_{y_0} \right) \Bigg] = -k_0^2 a_{nq} \tag{3.17}$$

where for rectangular rods,

$$\begin{aligned} b_{n-m,q-p} =& \frac{1}{ac} \int_{-b/2}^{b/2} \int_{-d/2}^{d/2} \left(\frac{1}{\varepsilon_r} - 1 \right) \; e^{-j\frac{2\pi(n-m)}{a}x} \; e^{-j\frac{2\pi(q-p)}{a}y} \; dx \; dy \\ & + \frac{1}{ac} \int_{-a/2}^{a/2} \int_{-c/2}^{c/2} (1) e^{-j\frac{2\pi(n-m)}{a}x} \; e^{-j\frac{2\pi(q-p)}{a}y} \; dx \; dy \\ =& \frac{bd}{ac} \left(\frac{1}{\varepsilon_r} - 1 \right) \operatorname{sinc} \frac{\pi(n-m)b}{a} \operatorname{sinc} \frac{\pi(q-p)d}{c} + \delta_{n-m,q-p} \end{aligned} \tag{3.18}$$

and for circular rods,

$$\begin{aligned} b_{n-m,q-p} =& \frac{2\pi}{a^2} \int_0^b \left(\frac{1}{\varepsilon_r} - 1 \right) J_0 \left(\sqrt{ \left(\frac{2\pi(n-m)r}{a} \right)^2 + \left(\frac{2\pi(q-p)r}{a} \right)^2 } \right) r \; dr \\ & + \frac{2\pi}{a^2} \int_0^a (1) J_0 \left(\sqrt{ \left(\frac{2\pi(n-m)r}{a} \right)^2 + \left(\frac{2\pi(q-p)r}{a} \right)^2 } \right) r \; dr \\ =& \frac{\pi b^2}{a^2} \left(\frac{1}{\varepsilon_r} - 1 \right) \frac{ 2J_1 \left(\sqrt{ \left(\frac{2\pi(n-m)b}{a} \right)^2 + \left(\frac{2\pi(q-p)b}{a} \right)^2 } \right) }{ \sqrt{ \left(\frac{2\pi(n-m)b}{a} \right)^2 + \left(\frac{2\pi(q-p)b}{a} \right)^2 } } + \delta_{n-m,q-p} \end{aligned} \tag{3.19}$$

Again if the dielectric rods are replaced by air columns as before, the coefficients $b_{n-m,q-p}$ become

$$\begin{aligned} b_{n-m,q-p} =& \frac{1}{ac} \int_{-a/2}^{a/2} \int_{-c/2}^{c/2} \left(\frac{1}{\varepsilon_r} \right) \; e^{-j\frac{2\pi(n-m)}{a}x} \; e^{-j\frac{2\pi(q-p)}{a}y} \; dx \; dy \\ & - \frac{1}{ac} \int_{-b/2}^{b/2} \int_{-d/2}^{d/2} \left(\frac{1}{\varepsilon_r} - 1 \right) \; e^{-j\frac{2\pi(n-m)}{a}x} \; e^{-j\frac{2\pi(q-p)}{a}y} \; dx \; dy \\ =& \frac{1}{\varepsilon_r} \delta_{n-m,q-p} - \left(\frac{1}{\varepsilon_r} - 1 \right) \frac{bd}{ac} \operatorname{sinc} \frac{\pi(n-m)b}{a} \operatorname{sinc} \frac{\pi(q-p)d}{c}, \end{aligned} \tag{3.20}$$

for the rectangular air column shown in Figure 3.3(a), and

$$\begin{aligned} b_{n-m,q-p} =& \frac{2\pi}{a^2}\int_0^a \left(\frac{1}{\varepsilon_r}\right) J_0\left(\sqrt{\left(\frac{2\pi(n-m)r}{a}\right)^2+\left(\frac{2\pi(q-p)r}{a}\right)^2}\right) r\ dr \\ &-\frac{2\pi}{a^2}\int_0^{b/2} \left(\frac{1}{\varepsilon_r}-1\right) J_0\left(\sqrt{\left(\frac{2\pi(n-m)r}{a}\right)^2+\left(\frac{2\pi(q-p)r}{a}\right)^2}\right) r\ dr \\ =& \frac{1}{\varepsilon_r}\delta_{n-m,q-p} - \left(\frac{1}{\varepsilon_r}-1\right)\frac{\pi b^2}{a^2}\frac{2J_1\left(\sqrt{\left(\frac{2\pi(n-m)b}{a}\right)^2+\left(\frac{2\pi(q-p)b}{a}\right)^2}\right)}{\sqrt{\left(\frac{2\pi(n-m)b}{a}\right)^2+\left(\frac{2\pi(q-p)b}{a}\right)^2}}, \end{aligned} \tag{3.21}$$

for the circular air column in Figure 3.3(b). The explicit expressions for the coefficients $b_{n-m,q-p}$ in (3.10), (3.11), (3.18), (3.19), (3.20), and (3.21) have not been found in the literature.

An ordinary linear eigensystem problem is represented by the equation $Ax = \lambda x$ where A denotes an $n \times n$ matrix. The propagating modes in the TE$_x$ case are solutions of the ordinary eigensystem problem in (3.17).

3.2.2 Matrix Solution of the Eigensystem

The resulting eigenvalues of the matrices in (3.7) and (3.17) are the squares of the frequencies of the propagating modes in the structure. The solutions of the frequencies of the propagating modes in the structure are found for specific values of $\{k_{x_0}a, k_{y_0}a\} \in [0, 2\pi]$. The full band structure[3] (TM$_x$) for a normally incident mode in a periodic array of dielectric rods with b/a=0.3545 and ε_r=8.9 is shown in Figure 3.4. The values for the filling fraction and the relative dielectric constant are obtained from a two-dimensional structure in [64, 129]. The Brillouin zone for a square lattice is also included in the figure where the Γ, X, and M points are defined in Appendix B. A complete TM band gap exists over a significant range of frequencies. Certainly, larger incomplete bands exist (particularly in the Γ–M and Γ–X directions) where propagation is allowed for specific directions and these gaps are effectively used in designs that do not need total omni-directional stopbands. Notice that there exists no complete TE band gap. In fact, only a small TE gap exists in any direction (note the small gap at the X point in Figure 3.4) for this geometrical and electrical configuration.

[3] A full band structure is one where the propagation constant is determined along the edges of the Brillouin zone. Theoretically, one must determine the propagation constant for all of the unique combinations of k_{x_0} and k_{y_0}. Fortunately, physics dictates that the band gaps are found at the edges of the Brillouin zone (BZ). Thus, by sampling the edge of the BZ, one can quickly determine the requisite full band structure.

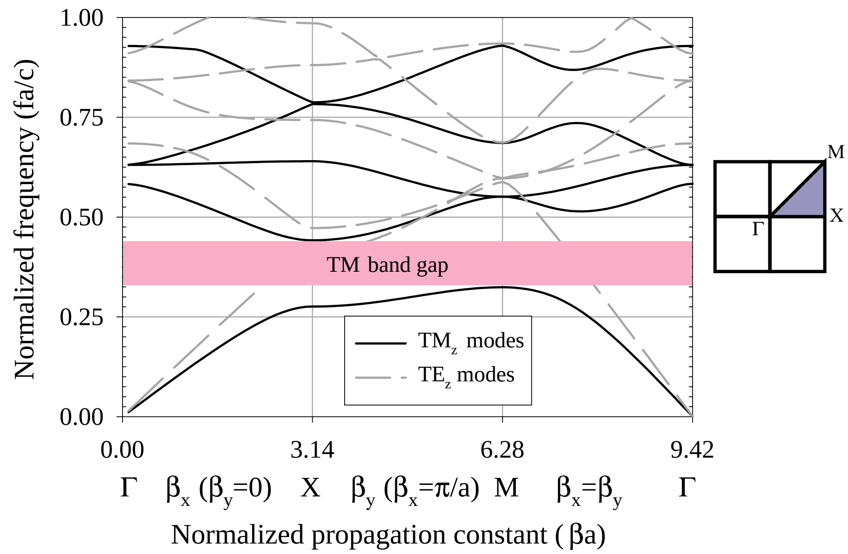

Figure 3.4: Band structure (TM$_z$) for a normally incident mode in a periodic array of dielectric rods with b/a=0.3545 and ε_r=8.9

Extensive research has concluded that large complete TM band gaps are most likely to be found using isolated regions of high dielectric constant material imbedded in a background of lower dielectric constant, whereas for TE band gaps, significant bands are found for isolated regions of lower dielectric constant immersed in a higher dielectric background [38, 129]. The latter conclusion can be seen in Figure 3.5 where the full band structure (TE$_x$) for a normally incident mode is shown for the periodic array of air columns with b=0.6455a and background dielectric constant ε_r=8.9. For this structure, which is complementary to the structure in Figure 3.4, no complete TM gap can be found. Small TM gaps been seen at the X and M points in the lattice but are too small to be of much value.

If the structures are viewed from a connectivity point of view, new insights can be gleaned from the preceding figures. The air cross of Figure 3.6(a) is equivalent to the dielectric square of Figure 3.2(a). Thus, regions of air that are "connected" to other cells by thin veins of air are useful for TM band gaps. The complementary dielectric cross of Figure 3.6(b) is equivalent to the air square of Figure 3.3(a). For useful TE band gaps, regions of dielectric should be connected to other cells by thin veins of dielectric. Either interpretation reveals that the electric field maintains a preference to distribute itself in certain ways depending on the polarization.

A simple check of the correctness of the results obtained from the two-dimensional periodic structure is to allow the filling fraction in one lattice direction to increase until an

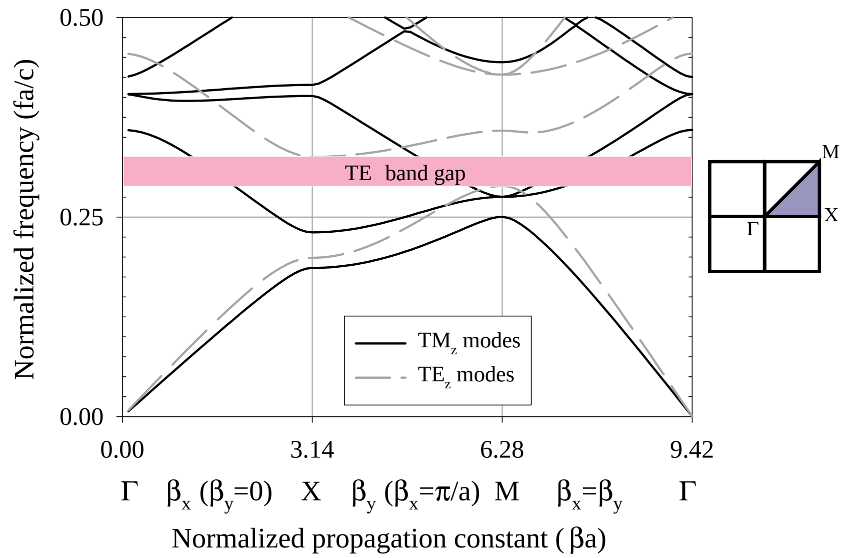

Figure 3.5: Band structure (TE$_z$) for a normally incident mode in a periodic array of air columns with b/a=0.6455 and ε_r=8.9

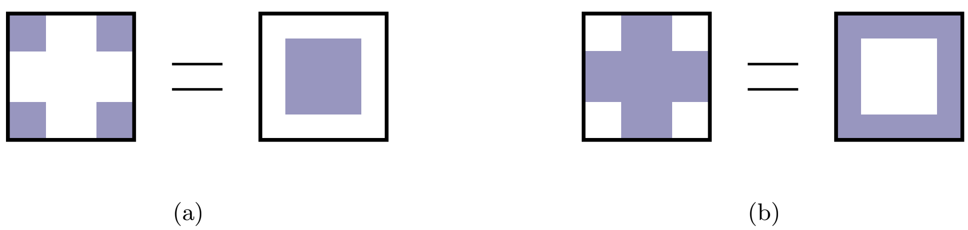

Figure 3.6: Equivalent structures for Figure 3.2(a) and Figure 3.3(a)

equivalent one-dimensionally periodic structure is obtained. As the unit cell geometry approaches the one-dimensional periodic structure of equal filling fraction, the propagation constant should approach the value of the one-dimensional propagation constant (k_y=0). In Figure 3.7 the normalized TM$_z$ propagation constant $k_{x0}a$ is shown as a function of d/c for normalized frequency f_0=fa/c=0.5, relative dielectric constant ε_r=10.2, normal incidence, and filling fraction b/a=0.2. Comparing the results with the normalized propagation constant obtained from the equivalent one-dimensional structure, $k_{x0}^{1\mathrm{D}}a$, one can conclude that indeed the solutions are the same. Similar results can be obtained for the normalized TE$_z$ propagation constant $k_{x0}a$ as a function of d/c.

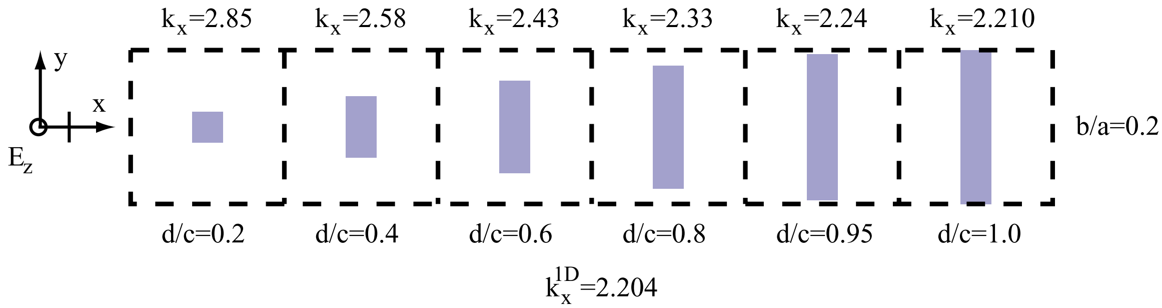

Figure 3.7: Normalized TM_z propagation constant $k_{x0}a$ as a function of d/c for f_0= fa/c=0.5, ε_r=10.2, k_y=0, and b/a=0.2

3.3 Formulation of Integral Equations

Great physical insight is often obtained through the necessary theoretical formulation of a problem from basic principles. This is particularly true when deriving two- and three-dimensional integral equations (IE) that when solved, yield the unknowns of interest. Applying the method of moments (MoM) numerical solution technique, where the physics of the problem is often intimately related to the formulation itself, also provides intuition about the quantities being studied.

3.3.1 Derivation of Electric Field Integral Equation

Similarly to the derivation of the one-dimensional case, the dielectric rods are replaced by equivalent (polarization) volume currents and the total field is determined as the sum of the incident field produced by a known source with the dielectric absent and a scattered field contributed by the equivalent currents induced in the periodic scatterers.

TM_z Case

Consider the representative dielectric rod (period not shown) of diameter b in a periodic square lattice with period a in Figure 3.8. The rods are excited by an incident time harmonic ($e^{j\omega t}$) plane wave propagating in a direction normal to the z axis (in-plane propagation) with its electric field parallel to the axis (TM_z) which induces an electric current $\mathbf{J} = J_z\,\hat{\mathbf{z}}$ with a z component only. Note that, for uniformity in the z direction, $\nabla \cdot \mathbf{J}$ of (2.31) is zero. The total electric field everywhere is computed as the sum of the scattered field produced by the equivalent induced electric current and the incident electric field given by $\mathbf{E}^i(x, y) = \hat{\mathbf{z}}E_0 e^{-jk_0(x\cos\phi_0 + y\sin\phi_0)}$, which impinges upon the rod along a ray in the

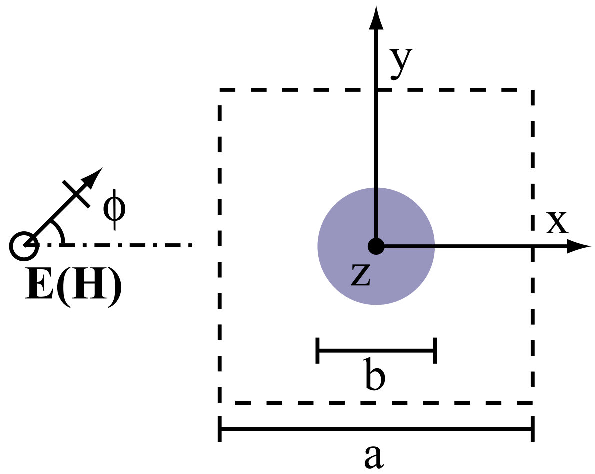

Figure 3.8: Representative dielectric rod of diameter b in a periodic square lattice with period a

$\hat{\mathbf{k}} = (\hat{\mathbf{x}} \cos\phi_0 + \hat{\mathbf{y}} \sin\phi_0)$ direction defined by an angle ϕ_0 with respect to the x axis ($\phi_0 = 0°$).

The first step is to replace the dielectric material with equivalent volume currents using (2.37). If we assume for simplicity that the two-dimensional periodic array in Figure 3.1 is composed of dielectric rectangular rods of cross section $b \times d$ in a periodic square lattice with cross section $a \times c$, then for the TM_z case,

$$J_z(x, y) = jk_0 Y_0 \left(\varepsilon_r(x, y) - 1\right) E_z(x, y) \tag{3.22}$$

where $\varepsilon_r(x, y)$ is the permittivity function of the rods defined by

$$\varepsilon_r(x, y) = \begin{cases} \varepsilon_r, & -b/2 < x < b/2, -d/2 < y < d/2; \\ 1, & \text{otherwise.} \end{cases} \tag{3.23}$$

Since the dielectric material is periodic in x with period a and in y with period c, the resulting equivalent currents must satisfy

$$J_z(x + pa, y + qc) = J_z(x, y) e^{-jk_{x_0} pa} e^{-jk_{y_0} qc} \tag{3.24}$$

for phase shifts $k_{x_0} a$ in the x direction and $k_{y_0} c$ in the y direction. Using (2.31), the scattered field is determined from the periodic equivalent currents (3.24) to be

$$E_z^s(x, y) = -jk_0 Z_0 \int_{-\frac{b}{2}}^{\frac{b}{2}} \int_{-\frac{d}{2}}^{\frac{d}{2}} J_z(x', y') G_p(x, y; x', y')\, dx'\, dy' \tag{3.25}$$

where $G_p(x,y;x',y')$ is the two-dimensional periodic free-space Green's function (PFSGF) given by

$$G_p(x,y;x',y') = \sum_{p,q} e^{-jk_{x0}pa}\ e^{-jk_{y0}qc}\frac{1}{4j}H_0^{(2)}\left(k_0\sqrt{(x-x'-pa)^2+(y-y'-qc)^2}\right) \tag{3.26}$$

and $\{p,q\}$ are the Floquet mode indices for propagation in the x and y directions, respectively. Using $E_z(x,y) = E_z^s(x,y) + E_z^i(x,y)$, one can formulate the following EFIE to determine the equivalent currents

$$jk_0Z_0\int_{-\frac{b}{2}}^{\frac{b}{2}}\int_{-\frac{d}{2}}^{\frac{d}{2}} J_z(x',y')G_p(x,y;x',y')\ dx'\ dy' + \frac{J_z(x,y)}{jk_0Y_0\left(\varepsilon_r(x,y)-1\right)} = E_z^i(x,y). \tag{3.27}$$

Two-dimensional periodic free-space Green's function The extension of the one-dimensional periodic free-space Green's function to a periodic two-dimensional periodic free-space Green's function is straight forward. The spatial form of the two-dimensional free-space periodic Green's function can also be easily transformed into its spectral form through the use of the Poisson sum formula [70]. From Table I of [51],

$$\begin{aligned}\sum_{p,q} f(p,q) &= \sum_{p,q}\frac{1}{4j}H_0^{(2)}\left(k\sqrt{(x-pa)^2+(y-qc)^2}\right)\\ &= \frac{1}{a}\sum_{p,q}\frac{1}{2j\sqrt{k^2-\left(\frac{2\pi p}{a}\right)^2}}e^{-j\sqrt{k^2-\left(\frac{2\pi p}{a}\right)^2}|y-qc|}e^{-j\frac{2\pi p}{a}x}.\end{aligned} \tag{3.28}$$

Again, using Table I of [51],

$$\begin{aligned}&\frac{1}{a}\sum_{p,q}\frac{1}{2j\sqrt{k^2-\left(\frac{2\pi p}{a}\right)^2}}e^{-j\sqrt{k^2-\left(\frac{2\pi p}{a}\right)^2}|y-qc|}e^{-j\frac{2\pi p}{a}x}\\ &\qquad = -\frac{1}{ac}\sum_{p}\frac{1}{\left[k^2-\left(\frac{2\pi p}{a}\right)^2-\left(\frac{2\pi q}{c}\right)^2\right]}e^{-j\frac{2\pi p}{a}x}e^{-j\frac{2\pi q}{c}y}\end{aligned} \tag{3.29}$$

where a is the unit cell width in the x-direction, b is the width of the dielectric region in the x-direction, c is the unit cell depth in the y-direction, d is the depth of the dielectric region in the y-direction, k is the wavenumber of the medium, and $\{p,q\}$ are the Floquet indices. Equation (3.29) becomes upon substitution of a phase shift $\hat{\mathbf{k}} = k_{x_0}\hat{\mathbf{x}} + k_{y_0}\hat{\mathbf{y}}$

$$\sum_{p,q}\frac{1}{4j}H_0^{(2)}\left(k\sqrt{(x-pa)^2+(y-qc)^2}\right)e^{-jk_{x_0}pa}e^{-jk_{y_0}qc} = -\frac{1}{ac}\sum_{p,q}\frac{e^{-jk_{x_p}x}e^{-jk_{y_q}y}}{k^2-k_{x_p}^2-k_{y_q}^2} \tag{3.30}$$

where

$$k_{x_p} = \frac{2\pi p}{a} + k_{x0}$$
$$k_{y_q} = \frac{2\pi q}{c} + k_{y0}.$$

Thus, (3.27) becomes upon substitution

$$-\frac{jk_0 Z_0}{ac} \int_{-\frac{b}{2}}^{\frac{b}{2}} \int_{-\frac{d}{2}}^{\frac{d}{2}} J_z(x', y') \sum_{p,q} \frac{e^{-jk_{x_p}(x-x')}\ e^{-jk_{y_q}(y-y')}}{k_0^2 - k_{x_p}^2 - k_{y_q}^2} dx'\ dy' + \frac{J_z(x, y)}{jk_0 Y_0 \left(\varepsilon_r(x, y) - 1\right)}$$
$$= E_z^i(x, y). \quad (3.31)$$

TE$_z$ Case

Similarly for the the TE$_z$ case, we replace the dielectric material with equivalent volume currents. However, note that since the rods are excited by an incident plane wave propagating in a direction normal to the z axis (in-plane propagation) with its magnetic field parallel to the axis (TE$_z$), the induced electric current $\mathbf{J}$ has only components in the transverse (x,y) plane.

In this case, the dielectric material is replaced with equivalent volume currents for both the x and y components

$$J_x(x, y) = jk_0 Y_0 \left(\varepsilon_r(x, y) - 1\right) E_x(x, y) \quad (3.32)$$

$$J_y(x, y) = jk_0 Y_0 \left(\varepsilon_r(x, y) - 1\right) E_y(x, y). \quad (3.33)$$

Substituting the periodic polarization currents into (2.31), the scattered field can be determined to be

$$E_x^s(x, y) = -jk_0 Z_0 \left(1 + \frac{1}{k_0^2} \frac{\partial^2}{\partial x^2}\right) \int_{-\frac{b}{2}}^{\frac{b}{2}} \int_{-\frac{d}{2}}^{\frac{d}{2}} J_x(x', y')\ G_p(x, y; x', y')\ dx'\ dy'$$
$$- \frac{Z_0}{jk_0} \frac{\partial^2}{\partial x \partial y} \int_{-\frac{b}{2}}^{\frac{b}{2}} \int_{-\frac{d}{2}}^{\frac{d}{2}} J_y(x', y')\ G_p(x, y; x', y')\ dx'\ dy' \quad (3.34a)$$

$$E_y^s(x,y) = -\frac{Z_0}{jk_0}\frac{\partial^2}{\partial x \partial y}\int_{-\frac{b}{2}}^{\frac{b}{2}}\int_{-\frac{d}{2}}^{\frac{d}{2}} J_x(x',y') \;\; G_p(x,y;x',y') \; dx' \; dy'$$

$$- jk_0 Z_0 \left(1 + \frac{1}{k_0^2}\frac{\partial^2}{\partial y^2}\right)\int_{-\frac{b}{2}}^{\frac{b}{2}}\int_{-\frac{d}{2}}^{\frac{d}{2}} J_y(x',y') \; G_p(x,y;x',y') \; dx' \; dy'. \quad (3.34b)$$

Using (2.32), one can formulate the following coupled EFIEs to determine the equivalent currents

$$jk_0 Z_0 \left(1 + \frac{1}{k_0^2}\frac{\partial^2}{\partial x^2}\right)\int_{-\frac{b}{2}}^{\frac{b}{2}}\int_{-\frac{d}{2}}^{\frac{d}{2}} J_x(x',y') \; G_p(x,y;x',y') \; dx' \; dy'$$

$$+ \frac{Z_0}{jk_0}\frac{\partial^2}{\partial x \partial y}\int_{-\frac{b}{2}}^{\frac{b}{2}}\int_{-\frac{d}{2}}^{\frac{d}{2}} J_y(x',y') \; G_p(x,y;x',y') \; dx' \; dy' + \frac{J_x(x,y)}{jk_0 Y_0 \left(\varepsilon_r(x,y) - 1\right)} = E_x^i(x,y)$$

$$(3.35a)$$

$$\frac{Z_0}{jk_0}\frac{\partial^2}{\partial x \partial y}\int_{-\frac{b}{2}}^{\frac{b}{2}}\int_{-\frac{d}{2}}^{\frac{d}{2}} J_x(x',y') \;\; G_p(x,y;x',y') \; dx' \; dy' + \frac{J_y(x,y)}{jk_0 Y_0 \left(\varepsilon_r(x,y) - 1\right)}$$

$$+ jk_0 Z_0 \left(1 + \frac{1}{k_0^2}\frac{\partial^2}{\partial y^2}\right)\int_{-\frac{b}{2}}^{\frac{b}{2}}\int_{-\frac{d}{2}}^{\frac{d}{2}} J_y(x',y') \; G_p(x,y;x',y') \; dx' \; dy' = E_y^i(x,y). \quad (3.35b)$$

Using the Poisson sum formula (3.30) shown on page 58, (3.35) becomes

$$jk_0 Z_0 \left(1 + \frac{1}{k_0^2}\frac{\partial^2}{\partial x^2}\right)\int_{-\frac{b}{2}}^{\frac{b}{2}}\int_{-\frac{d}{2}}^{\frac{d}{2}} J_x(x',y') \sum_{p,q} \frac{e^{-jk_{x_p}(x-x')} \; e^{-jk_{y_q}(y-y')}}{k_0^2 - k_{x_p}^2 - k_{y_q}^2} dx' \; dy'$$

$$+ \frac{Z_0}{jk_0}\frac{\partial^2}{\partial x \partial y}\int_{-\frac{b}{2}}^{\frac{b}{2}}\int_{-\frac{d}{2}}^{\frac{d}{2}} J_y(x',y') \sum_{p,q} \frac{e^{-jk_{x_p}(x-x')} \; e^{-jk_{y_q}(y-y')}}{k_0^2 - k_{x_p}^2 - k_{y_q}^2} dx' \; dy' + \frac{J_x(x,y)}{jk_0 Y_0 \left(\varepsilon_r(x,y) - 1\right)}$$

$$= E_x^i(x,y) \quad (3.36a)$$

$$\frac{Z_0}{jk_0}\frac{\partial^2}{\partial x \partial y}\int_{-\frac{b}{2}}^{\frac{b}{2}}\int_{-\frac{d}{2}}^{\frac{d}{2}} J_x(x',y')\sum_{p,q}\frac{e^{-jk_{x_p}(x-x')}\ e^{-jk_{y_q}(y-y')}}{k_0^2-k_{x_p}^2-k_{y_q}^2}dx'\ dy' + \frac{J_y(x,y)}{jk_0Y_0\left(\varepsilon_r(x,y)-1\right)}$$

$$+ jk_0Z_0\left(1+\frac{1}{k_0^2}\frac{\partial^2}{\partial y^2}\right)\int_{-\frac{b}{2}}^{\frac{b}{2}}\int_{-\frac{d}{2}}^{\frac{d}{2}} J_y(x',y')\sum_{p,q}\frac{e^{-jk_{x_p}(x-x')}\ e^{-jk_{y_q}(y-y')}}{k_0^2-k_{x_p}^2-k_{y_q}^2}dx'\ dy'$$

$$= E_y^i(x,y). \quad (3.36b)$$

3.3.2 Method of Moments Formulation

For two-dimensional problems, the choice of discretization can have a significant effect on the reduction of the integral equations into matrix equations. After discretizing the geometry and expanding the unknown equivalent electric current across the dielectric region with a linear combination of subsectional or entire domain basis functions, the equations are tested in order to obtain an adequate number of equations to solve for the unknown coefficients of the basis functions. In order to provide verification of the IE/MoM procedure, computer codes have been written in Fortran to determine the propagating modes of a periodic array of dielectric slabs.

TM$_z$ Case

Piecewise constant expansion / Piecewise constant testing For piecewise constant functions, we discretize the dielectric region into N=N_xN_y subsections of width $\Delta_x = b/N_x$ and $\Delta_y = d/N_y$, respectively, to approximate the original surface and represent J_z by a linear combination of N piecewise constant basis functions $\Pi_n(x,y)$ with unknown current coefficients $\{J_n\}$

$$J_z(x,y) = \sum_{n=1}^{N} J_n\Pi_n(x,y) = \sum_{n=1}^{N} J_n\Pi_n(x)\Pi_n(y) \quad (3.37)$$

where

$$\Pi_n(x) = \begin{cases} 1, & x_n - \frac{\Delta_x}{2} < x < x_n + \frac{\Delta_x}{2}; \\ 0, & \text{otherwise;} \end{cases} \quad (3.38)$$

and

$$\Pi_n(y) = \begin{cases} 1, & y_n - \frac{\Delta_y}{2} < y < y_n + \frac{\Delta_y}{2}; \\ 0, & \text{otherwise;} \end{cases} \quad (3.39)$$

and $x_n = -\frac{b}{2} + \Delta_x(n - \frac{1}{2})$ and $y_n = -\frac{d}{2} + \Delta_y(n - \frac{1}{2})$.

Substituting the currents into (3.31) yields

$$\sum_{n=1}^{N} J_n \left\{ \frac{jk_0 Z_0}{ac} \int\limits_{x_n-\frac{\Delta_x}{2}}^{x_n+\frac{\Delta_x}{2}} \int\limits_{y_n-\frac{\Delta_y}{2}}^{y_n+\frac{\Delta_y}{2}} \sum_{p,q} \frac{e^{-jk_{x_p}(x-x')} e^{-jk_{y_q}(y-y')}}{k_0^2 - k_{x_p}^2 - k_{y_q}^2} \, dy' \, dx' - \frac{\Pi_n(x)\Pi_n(y)}{jk_0 Y_0 \left(\varepsilon_r(x,y) - 1\right)} \right\} = 0. \quad (3.40)$$

Testing (3.40) with piecewise constant functions centered at (x_m, y_m) yields the following equation

$$\sum_{n=1}^{N} J_n \left\{ \frac{jk_0 Z_0}{ac} \int\limits_{x_m-\frac{\Delta_x}{2}}^{x_m+\frac{\Delta_x}{2}} \int\limits_{y_m-\frac{\Delta_y}{2}}^{y_m+\frac{\Delta_y}{2}} \int\limits_{x_n-\frac{\Delta_x}{2}}^{x_n+\frac{\Delta_x}{2}} \int\limits_{y_n-\frac{\Delta_y}{2}}^{y_n+\frac{\Delta_y}{2}} \sum_{p,q} \frac{e^{-jk_{x_p}(x-x')} e^{-jk_{y_q}(y-y')}}{k_0^2 - k_{x_p}^2 - k_{y_q}^2} \, dy' \, dx' \, dy \, dx \right.$$
$$\left. - \int\limits_{x_m-\frac{\Delta_x}{2}}^{x_m+\frac{\Delta_x}{2}} \int\limits_{y_m-\frac{\Delta_y}{2}}^{y_m+\frac{\Delta_y}{2}} \frac{\Pi_n(x)\Pi_n(y)}{jk_0 Y_0 \left(\varepsilon_r(x,y) - 1\right)} \, dx \, dy \right\} = 0, \quad m = 1, 2, \ldots, N. \quad (3.41)$$

By carrying out the integrations in (3.41) and simplifying the resulting expressions, the impedance matrix elements can be determined explicitly and are listed in Appendix C. The resulting matrix equation is written in a form similar to (2.54).

The transforms of the testing and expansion functions, denoted $\tilde{\Pi}_m(k_x)$ and $\tilde{\Pi}_n(k_x)$, are given in (2.56). The transforms of the expansion and testing functions, denoted $\tilde{\Pi}_m(k_y)$ and $\tilde{\Pi}_n(k_y)$, respectively, are

$$\tilde{\Pi}_m(k_y) = \Delta \operatorname{sinc}\left(\frac{k_y \Delta}{2}\right) e^{-jk_y y_m} \quad (3.42)$$

$$\tilde{\Pi}_n(k_y) = \Delta \operatorname{sinc}\left(\frac{k_y \Delta}{2}\right) e^{jk_y y_n}. \quad (3.43)$$

Piecewise linear expansion / Piecewise linear testing For piecewise linear functions, we discretize the dielectric region into $N = N_x N_y$ subsections of width $\Delta_x = b/(N_x - 1)$ and $\Delta_y = d/(N_y - 1)$, respectively, that approximate the original surface and approximate J_z by a linear combination of N piecewise linear basis functions $\Lambda_n(x, y)$ with unknown current coefficients $\{J_n\}$

$$J_z(x,y) = \sum_{n=1}^{N} J_n \Lambda_n(x,y) = \sum_{n=1}^{N} J_n \Lambda_n(x) \Lambda_n(y) \quad (3.44)$$

where

$$\Lambda_n(x) = \begin{cases} 1 - \frac{|x-x_n|}{\Delta_x}, & x_n - \Delta_x < x < x_n + \Delta_x; \\ 0, & \text{otherwise,} \end{cases} \tag{3.45}$$

and

$$\Lambda_n(y) = \begin{cases} 1 - \frac{|y-y_n|}{\Delta_y}, & y_n - \Delta_y < y < y_n + \Delta_y; \\ 0, & \text{otherwise,} \end{cases} \tag{3.46}$$

where $x_n = -\frac{b}{2} + \Delta_x(n-1)$ and $y_n = -\frac{d}{2} + \Delta_y(n-1)$. Substituting (3.44) into (3.31) and testing with piecewise linear basis functions yields

$$\sum_{n=1}^{N} J_n \left\{ \frac{jk_0 Z_0}{ac} \int\limits_{x_n-\Delta_x}^{x_n+\Delta_x} \int\limits_{y_n-\Delta_y}^{y_n+\Delta_y} \Lambda_n(x')\Lambda_n(y') \sum_{p,q} \frac{e^{-jk_{x_p}(x-x')} e^{-jk_{y_q}(y-y')}}{k_0^2 - k_{x_p}^2 - k_{y_q}^2} \, dy' \, dx' \, dy \, dx \right. \\ \left. - \frac{\Lambda_n(x)\Lambda_n(y)}{jk_0 Y_0 \left(\varepsilon_r(x,y) - 1\right)} \right\} = 0. \tag{3.47}$$

The impedance matrix elements shown in Appendix C can be determined evaluating the integrals in (3.47).

The transforms of the testing and expansion functions, denoted $\tilde{\Lambda}_m(k_x)$ and $\tilde{\Lambda}_n(k_x)$ are given in (2.60). The transforms of the testing and expansion functions, denoted $\tilde{\Lambda}_m(k_y)$ and $\tilde{\Lambda}_n(k_y)$ are

$$\tilde{\Lambda}_m(k_y) = \Delta \,\mathrm{sinc}^2 \left(\frac{k_y \Delta}{2} \right) e^{-jk_y y_m}$$
$$\tilde{\Lambda}_n(k_y) = \Delta \,\mathrm{sinc}^2 \left(\frac{k_y \Delta}{2} \right) e^{jk_y y_n}.$$

The transforms of the two "half-basis" functions, denoted $\tilde{\Lambda}_1(k_x)$ and $\tilde{\Lambda}_N(k_x)$, are given in (2.61). The transforms of the two "half-basis" functions, denoted $\tilde{\Lambda}_1(k_y)$ and $\tilde{\Lambda}_N(k_y)$, are

$$\tilde{\Lambda}_1(k_y) = \Delta \frac{e^{jk_y y_1}}{(k_y \Delta)^2} \left(1 + jk_y \Delta - e^{jk_y \Delta} \right)$$
$$\tilde{\Lambda}_N(k_y) = \Delta \frac{e^{jk_y y_N}}{(k_y \Delta)^2} \left(1 - jk_y \Delta - e^{-jk_y \Delta} \right).$$

TE$_z$ Case

Piecewise linear expansion / Piecewise linear testing For piecewise constant functions, we discretize the dielectric region into $N{=}N_x N_y$ subsections of width $\Delta_x = b/(N_y - 1)$

and $\Delta_y = d/(N_y - 1)$, respectively, that approximate the original surface and approximate $\mathbf{J} = \hat{\mathbf{x}}J_x + \hat{\mathbf{y}}J_y$ by a linear combination of N piecewise linear basis functions with unknown current coefficients $\{J_{x_n}, J_{y_n}\}$

$$J_x = \sum_{n=1}^{N} J_{x_n}\Lambda_n(x) \tag{3.48a}$$

$$J_y = \sum_{n=1}^{N} J_{y_n}\Lambda_n(y) \tag{3.48b}$$

with $\Lambda_n(x)$ and $\Lambda_n(y)$ are given in (3.45) and (3.46), respectively. Substituting (3.48) into (3.36) and testing with piecewise linear basis functions produces

$$\begin{aligned}
&\sum_{n=1}^{N} J_{x_n}\Bigg\{ jk_0 Z_0 \left(1 + \frac{1}{k_0^2}\frac{\partial^2}{\partial x^2}\right) \\
&\times \int\limits_{x_n-\Delta_x}^{x_n+\Delta_x}\int\limits_{y_n-\Delta_y}^{y_n+\Delta_y} \Lambda_n(x')\Lambda_n(y') \sum_{p,q} \frac{e^{-jk_{x_p}(x-x')}\ e^{-jk_{y_q}(y-y')}}{k_0^2 - k_{x_p}^2 - k_{y_q}^2} dx'\ dy' + \frac{\Lambda_n(x)\Lambda_n(y)}{jk_0 Y_0\left(\varepsilon_r(x,y) - 1\right)}\Bigg\} \\
&\quad + J_{y_n}\Bigg\{\frac{Z_0}{jk_0}\frac{\partial^2}{\partial x \partial y}\int\limits_{-\frac{b}{2}}^{\frac{b}{2}}\int\limits_{-\frac{d}{2}}^{\frac{d}{2}} \Lambda_n(x')\Lambda_n(y') \sum_{p,q} \frac{e^{-jk_{x_p}(x-x')}\ e^{-jk_{y_q}(y-y')}}{k_0^2 - k_{x_p}^2 - k_{y_q}^2} dx'\ dy'\Bigg\} = E_x^i(x,y)
\end{aligned} \tag{3.49a}$$

$$\begin{aligned}
&\sum_{n=1}^{N} J_{x_n}\Bigg\{\frac{Z_0}{jk_0}\frac{\partial^2}{\partial x \partial y}\int\limits_{x_n-\Delta_x}^{x_n+\Delta_x}\int\limits_{y_n-\Delta_y}^{y_n+\Delta_y} \Lambda_n(x')\Lambda_n(y') \sum_{p,q} \frac{e^{-jk_{x_p}(x-x')}\ e^{-jk_{y_q}(y-y')}}{k_0^2 - k_{x_p}^2 - k_{y_q}^2} dx'\ dy'\Bigg\} \\
&+ J_{y_n}\Bigg\{ jk_0 Z_0 \left(1 + \frac{1}{k_0^2}\frac{\partial^2}{\partial y^2}\right) \int\limits_{x_n-\Delta_x}^{x_n+\Delta_x}\int\limits_{y_n-\Delta_y}^{y_n+\Delta_y} \Lambda_n(x')\Lambda_n(y') \sum_{p,q} \frac{e^{-jk_{x_p}(x-x')}\ e^{-jk_{y_q}(y-y')}}{k_0^2 - k_{x_p}^2 - k_{y_q}^2} dx'\ dy' \\
&\qquad + \frac{\Lambda_n(x)\Lambda_n(y)}{jk_0 Y_0\left(\varepsilon_r(x,y) - 1\right)}\Bigg\} = E_y^i(x,y).
\end{aligned} \tag{3.49b}$$

The impedance matrix elements shown in Appendix C can be obtained by evaluating the coupled integrals in (3.49).

Piecewise constant expansion / Piecewise constant testing For piecewise constant functions, we discretize the dielectric region into $N{=}N_xN_y$ subsections of width $\Delta_x = b/N_x$ and $\Delta_y = d/N_y$, respectively, to approximate the original surface and represent $\mathbf{J} = \hat{\mathbf{x}}J_x + \hat{\mathbf{y}}J_y$ by a linear combination of N piecewise constant basis functions with unknown current coefficients $\{J_{x_n}, J_{y_n}\}$

$$J_z(x,y) = \sum_{n=1}^{N} J_n \Pi_n(x,y) = \sum_{n=1}^{N} J_n \Pi_n(x)\Pi_n(y) \tag{3.50}$$

with $\Pi_n(x)$ and $\Pi_n(y)$ are given in (3.38) and (3.39), respectively. Substituting (3.50) into (3.36) and testing with piecewise linear basis functions produces

$$\begin{aligned}
&\sum_{n=1}^{N} J_{x_n} \left\{ jk_0 Z_0 \left(1 + \frac{1}{k_0^2}\frac{\partial^2}{\partial x^2}\right) \right. \\
&\times \left. \int\limits_{x_n-\Delta_x}^{x_n+\Delta_x} \int\limits_{y_n-\Delta_y}^{y_n+\Delta_y} \Lambda_n(x')\Lambda_n(y') \sum_{p,q} \frac{e^{-jk_{x_p}(x-x')}\, e^{-jk_{y_q}(y-y')}}{k_0^2 - k_{x_p}^2 - k_{y_q}^2} dx'\, dy' + \frac{\Lambda_n(x)\Lambda_n(y)}{jk_0 Y_0\left(\varepsilon_r(x,y)-1\right)} \right\} \\
&+ J_{y_n} \left\{ \frac{Z_0}{jk_0}\frac{\partial^2}{\partial x \partial y} \int\limits_{-\frac{b}{2}}^{\frac{b}{2}} \int\limits_{-\frac{d}{2}}^{\frac{d}{2}} \Lambda_n(x')\Lambda_n(y') \sum_{p,q} \frac{e^{-jk_{x_p}(x-x')}\, e^{-jk_{y_q}(y-y')}}{k_0^2 - k_{x_p}^2 - k_{y_q}^2} dx'\, dy' \right\} = E_x^i(x,y)
\end{aligned} \tag{3.51a}$$

$$\begin{aligned}
&\sum_{n=1}^{N} J_{x_n} \left\{ \frac{Z_0}{jk_0}\frac{\partial^2}{\partial x \partial y} \int\limits_{x_n-\Delta_x}^{x_n+\Delta_x} \int\limits_{y_n-\Delta_y}^{y_n+\Delta_y} \Lambda_n(x')\Lambda_n(y') \sum_{p,q} \frac{e^{-jk_{x_p}(x-x')}\, e^{-jk_{y_q}(y-y')}}{k_0^2 - k_{x_p}^2 - k_{y_q}^2} dx'\, dy' \right\} \\
&+ J_{y_n} \left\{ jk_0 Z_0 \left(1 + \frac{1}{k_0^2}\frac{\partial^2}{\partial y^2}\right) \int\limits_{x_n-\Delta_x}^{x_n+\Delta_x} \int\limits_{y_n-\Delta_y}^{y_n+\Delta_y} \Lambda_n(x')\Lambda_n(y') \sum_{p,q} \frac{e^{-jk_{x_p}(x-x')}\, e^{-jk_{y_q}(y-y')}}{k_0^2 - k_{x_p}^2 - k_{y_q}^2} dx'\, dy' \right. \\
&\qquad \left. + \frac{\Lambda_n(x)\Lambda_n(y)}{jk_0 Y_0\left(\varepsilon_r(x,y)-1\right)} \right\} = E_y^i(x,y).
\end{aligned} \tag{3.51b}$$

The impedance matrix elements shown in Appendix C can be obtained by evaluating the coupled integrals in (3.51).

3.3.3 Matrix Solution

In order to accurately determine the eigenvalues of the impedance matrices given in Appendix C, a sufficient number of Floquet modes N_p in the x direction and N_q in the y direction and subsectional unknowns $N{=}N_xN_y$ must be included. The minimization procedure outlined in Chapter 2 is carried out for two-dimensional periodic media by fixing the frequency of operation and one of the two propagation constants k_{x0} or k_{y0} and allowing the optimization code to vary the other propagation constant until a minimum is found. If more than one minimum (eigenvalue) is found, implying that multiple modes are propagating in the structure, the corresponding eigenvectors are analyzed to determine which eigenvalue corresponds to which propagating mode. A nontrivial solution for the fields requires the matrix determinant to be zero, which results in a characteristic equation. The eigenvalues (propagation constants) $\{k_{x_0}, k_{y_0}\}$ are obtained from the roots of this equation. For a lossless structure, the propagation constant of a guided wave is a real number, however, in the stopbands, the propagation constant is complex-valued.

In order to verify that the solution of the propagation constants computed using the method of moments technique and PWE solution is correct, the band structure of a periodic array of dielectric rods is calculated for a filling fraction b/a=d/c=0.3545 and relative dielectric constant ε_r=8.9. Figure 3.9 shows the calculated band structure for both the TM$_z$ and TE$_z$ cases. The moment method solution includes 225 subsectional bases (N_x=N_y=15) and 961 Floquet modes (N_p=N_q=31). The Fourier series solution uses 121 Floquet modes. It is clear that the solutions obtained by the two methods are again in agreement with each other and are also in agreement with [38, 129].

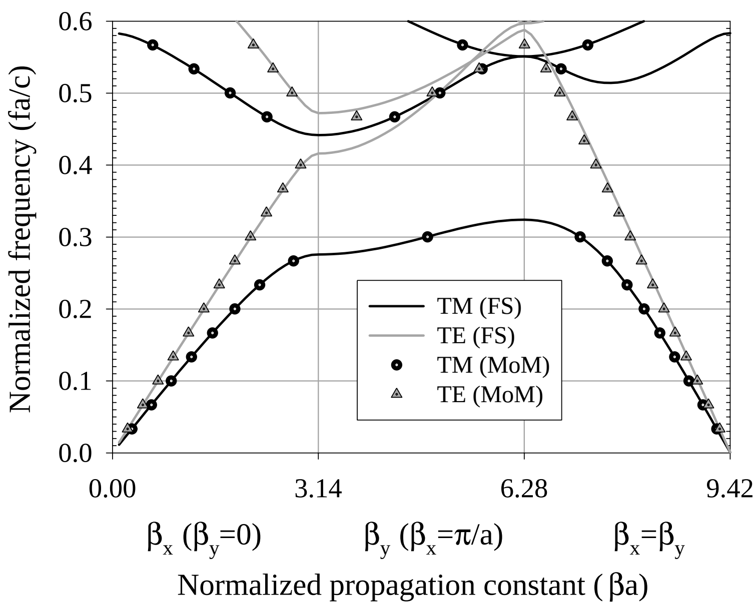

Figure 3.9: Band structure (TM$_z$, TE$_z$) of a periodic lattice of dielectric columns with filling fraction b/a=d/c=0.3545, ε_r=8.9, N_x=N_y=15, and N_p=N_q=31

Similar conclusions for two-dimensional dielectric structures as those expressed for one-dimensional structures can be drawn about the number of unknowns needed to accurately model the dielectric material and the number of requisite Floquet modes to include in the double series to accurately determine the propagation constants. In Tables 2.1 – 2.4 of

Chapter 2, the accuracy of the propagation constant determined for both the TE_x and TM_x cases increases both by increasing the number of Floquet mode contributions and by modeling the equivalent current more carefully by increasing the number of unknowns. A simple pulse basis expansion serves to solve the problem quickly and accurately. This observation holds true as well for two-dimensional dielectric structures. As expected, the accuracy of the propagation constants determined for both the TM_z and TE_z cases increases with increasing Floquet contributions and with increasing subsectional bases. Additionally, the advantage of incorporating higher order basis functions does not significantly increase the accuracy and actually increases the cost and complication of numerical implementation. Tables 2.1 – 2.4 in Chapter 2 clearly show that the accuracy of computing the propagation constant is more sensitive to the number of subsectional bases used in the approximation of the current than the number of Floquet modes used to compute the Floquet series. The computational cost of computing each individual element in the impedance matrix in two dimensions is proportional to N_pN_q. In two dimensions, the total cost of computing the full impedance matrix is proportional to $N_x^2N_y^2N_pN_q$. Thus, incorporating fewer basis functions decreases the cost significantly.

As was mentioned previously in Chapter 2, the restriction that the IE/MoM solution must compute the impedance matrix for each iteration of the optimizer requires significant computational time. Consequently, for the band structure of an infinite lattice of dielectric inserts in a background of differing dielectric constant, the solution obtained using the Fourier series solution is the formulation of choice. The derivation and implementation of the IE/MoM solution developed in Section 3.3 is extended to three-dimensional structures in Chapter 4.

3.4 Effective Medium Theory (EMT)

To simplify the computation of the band structure for two-dimensionally periodic media, *effective medium theory* is applied to reduce the two-dimensional periodic structure to a one-dimensional equivalent structure. This useful technique can be applied when the period of the structure is much smaller than the wavelength. Using EMT, each periodic row of the two-dimensional structure is replaced by a thin homogeneous layer of effective permittivity [50] which is determined solely as a function of the geometrical and electrical parameters of the lattice.

Consider the two-dimensional lattice with dielectric constant ε_2 immersed in a back-

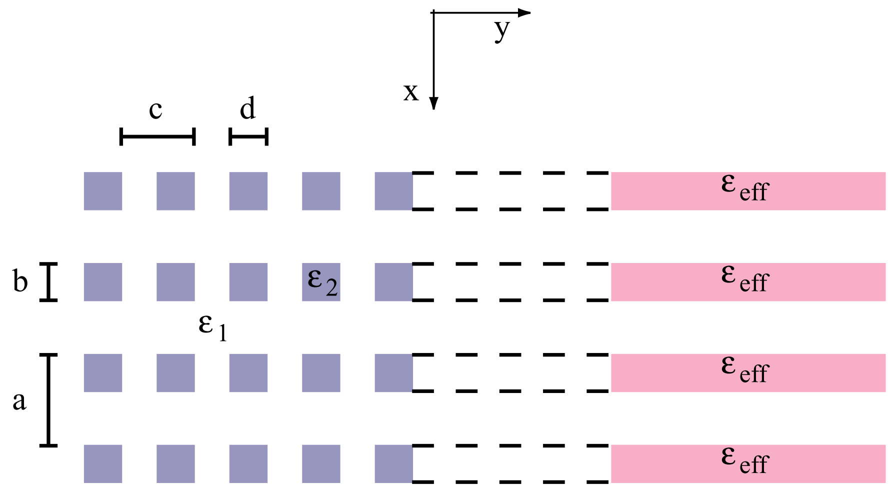

Figure 3.10: Effective medium theory

ground with dielectric constant ε_1 and the equivalent one-dimensional lattice with dielectric constant ε_{eff}, illustrated in cross-section in Figure 3.10. Assume a plane wave is incident along the x direction (Γ–X direction in the BZ). Effective medium theory allows for each row of the square lattice to be replaced by an equivalent layer of permittivity ε_{eff}. For TM$_z$ polarization, where the electric field parallel to z axis, Rytov [82] expands the effective permittivity ε_{eff} in a power series of the period-to-wavelength ratio $\alpha{=}a/\lambda$ and is given by

$$\varepsilon_{\text{eff}} = \varepsilon_0 + \frac{\pi^2}{3}\left[f(1-f)(\varepsilon_2-\varepsilon_1)\right]^2\alpha^2 + \mathcal{O}(\alpha^4) \tag{3.52}$$

where ε_0 is the average relative permittivity $\varepsilon_0 = \varepsilon_2 f - \varepsilon_1(1-f)$, $\alpha = a/\lambda_0$, and f is the filling fraction of the medium defined by the ratio of the width b of the effective homogeneous layer to the lattice constant a. For TE$_z$ polarization, where the electric field parallel to y axis, the effective permittivity is given by

$$\varepsilon_{\text{eff}} = \frac{1}{a_0} + \frac{\pi^2}{3}\left[f(1-f)\frac{(\varepsilon_2-\varepsilon_1)}{\varepsilon_2\varepsilon_1}\right]^2\frac{\varepsilon_0}{a_0^3}\alpha^2 + \mathcal{O}(\alpha^4) \tag{3.53}$$

where a_0 is the arithmetic average of the inverse relative permittivities $a_0 = f/\varepsilon_2 - (1-f)/\varepsilon_1$ and f is defined above.

Two conclusions can be drawn about the results obtained using EMT. First, for large period-to-wavelength ratios, the EMT approximation fails to accurately produce the band structure for either the TM$_z$ or TE$_z$ case. This is expected since the physical boundary conditions that exist in the real structure are not approximated well. Secondly, as the ratio decreases, the validity of the EMT approximation increases. Even for a relatively large period-to-wavelength ratio of 0.5, the results obtained using EMT are surprisingly good.

The band structure of the exact two-dimensional structure determined using the plane wave expansion method and integral equation models outlined in Sections 3.2 and 3.3 and the one-dimensional equivalent structure modeled using EMT is illustrated in Figure 3.11. Thus, the lattice of Figure 3.10 with filling fraction b/a=d/c=0.3545 and dielectric constant ε_r=8.9 is modeled by an array of dielectric slabs with the same filling fraction as the two-dimensional array with effective permittivity ε_{eff}. For the TM$_z$ modes, the EMT results compare favorably to [129] for normalized frequencies $f_0 < 1.0$. The results obtained for the TE$_z$ modes compares less favorably, particularly for higher frequencies.

If the filling fraction b/a=d/c is decreased to 0.2 and if all other geometrical parameters remain the same, the ability of the EMT to effectively model the two-dimensional lattice as an equivalent one-dimensional array can be seen in Figure 3.12 to improve greatly for the TE$_z$ case. Although an improvement over the TM$_z$ case is not seen, the EMT effectively models the first band gap as accurately as might be needed.

3.5 Conclusions

The solution for the propagation of electromagnetic energy through a two-dimensional periodic dielectric structure has been determined using the plane wave expansion method and an integral equation/method of moments solution. The plane wave expansion method solves the two-dimensional (differential) wave equation by expanding the periodic functions in a Fourier series. The integral equation solution is derived and implemented using polarization currents for a two-dimensionally periodic media. For infinite two-dimensional dielectric structures, modeling the dielectric material with increasing number of unknowns increases the accuracy of the solution as does increasing the number of Floquet modes. The disadvantage of the IE/MoM solution is the significant increase in computational time required to compute the eigenvalues (propagation constants) for the two-dimensional structures. The advantage of the IE/MoM solution is its straightforward extension to three-dimensional layered periodic structures with periodic material implants.

An effective medium theory (EMT) approximation for the two-dimensional lattice has been shown to effectively model propagation in specific directions within the lattice structure. The use of EMT to effectively approximate propagation through a periodic structure is significant since, for many of the applications used in microwave devices, the first (and lowest) band structure is the band of interest. The approximation is particularly helpful when one considers the complication of a two-dimensional formulation. Unfortunately, the

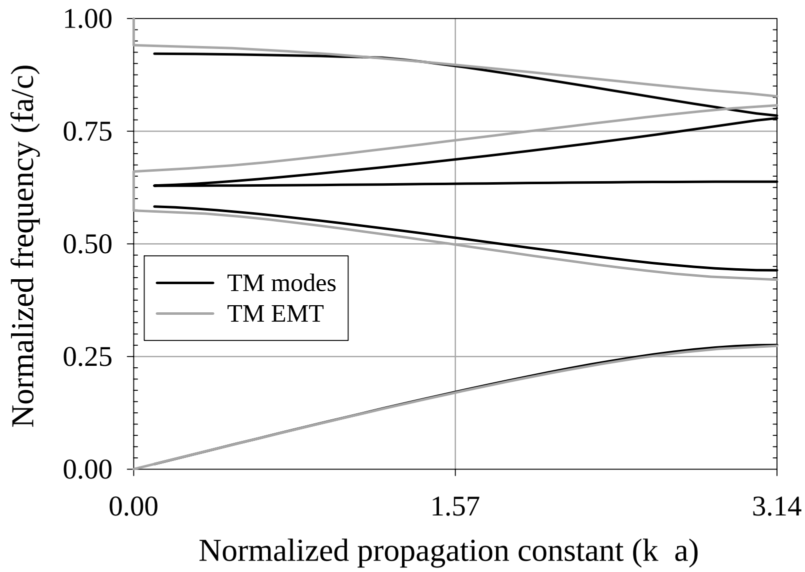

(a)

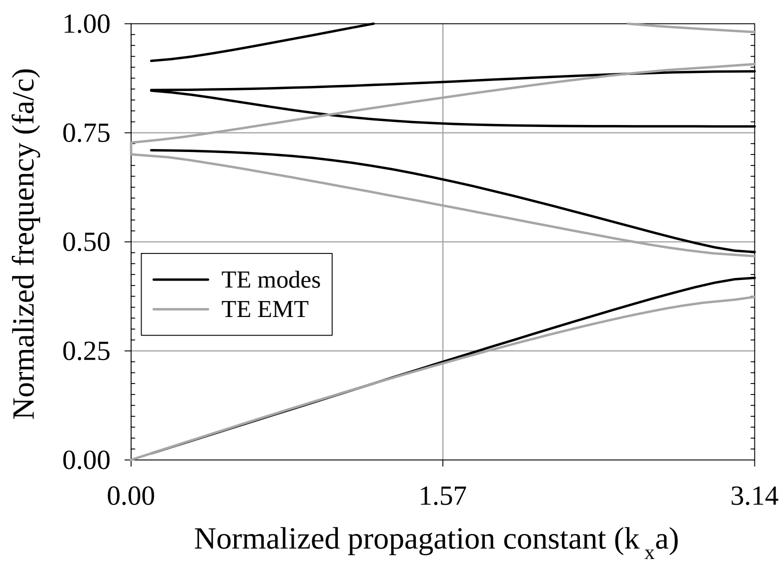

(b)

Figure 3.11: Exact band structure and effective medium theory approximation for periodic lattice of dielectric columns with filling fraction b/a=d/c=0.3545, dielectric constant ε_r=8.9, and period-to-wavelength ratio $\alpha = a/\lambda_0$=0.5 for (a) TM_z case and (b) TE_z case

EMT is restricted to near normal incidence precluding its use for many applications of interest.

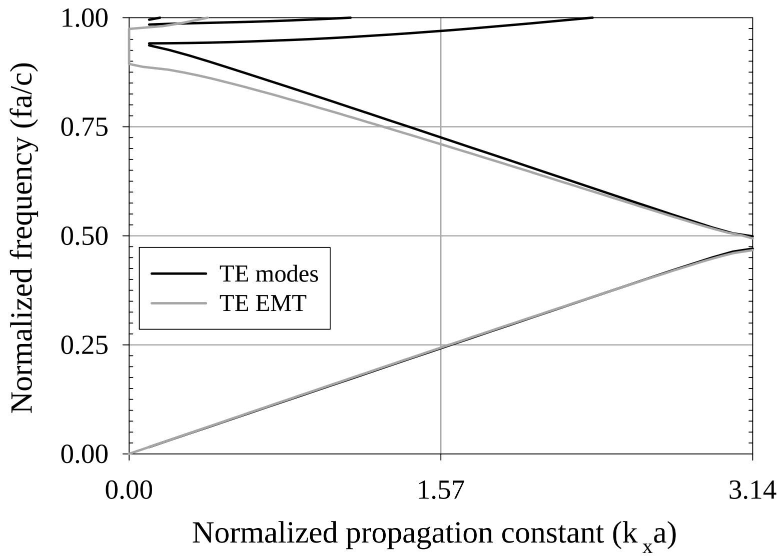

(a)

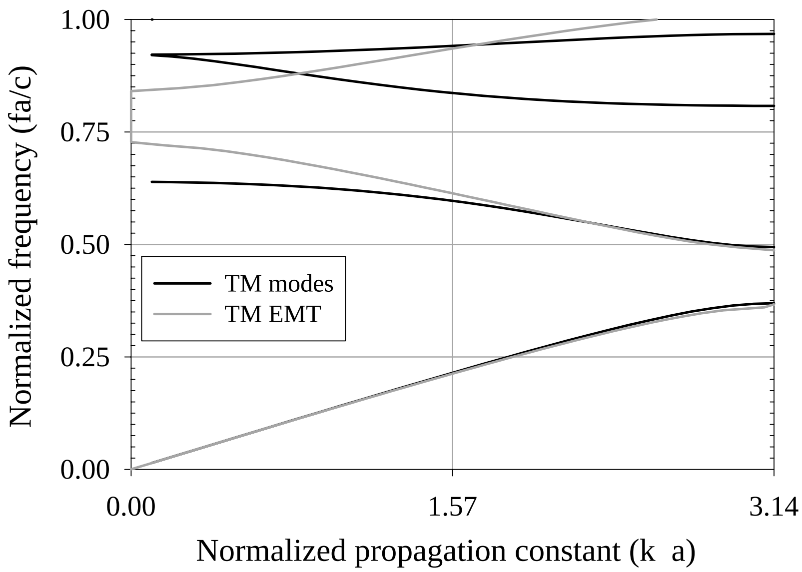

(b)

Figure 3.12: Exact band structure and effective medium theory approximation for periodic lattice of dielectric columns with filling fraction b/a=d/c=0.2, dielectric constant ε_r=8.9, and period-to-wavelength ratio $\alpha = a/\lambda_0$=0.5 for (a) TM_z case and (b) TE_z case

To validate the usefulness and realizability of microwave devices that incorporate substrate materials with periodicities in two directions, the design, fabrication, and implementation of a two-dimensional periodic dielectric structure developed for use in parallel-plate mode reduction in conductor-backed slots is presented extensively in Appendix D. Band structures are designed to produce the requisite substrate properties using the PWE method and IE/MoM solutions developed in this chapter.

CHAPTER 4

Scattering From an Inhomogeneous Doubly Periodic Dielectric Layer Above a Layered Medium

4.1 Introduction

In this chapter, the solution found in [84] for the two-dimensional scattering from an inhomogeneous periodic layer above a half-space layered medium is extended to general three-dimensional scattering from an inhomogeneous doubly periodic layer above a half-space layered medium. The solution of this problem is derived and implemented using a full-wave integral equation/method of moments approach similar to the formulation for the one- and two-dimensional periodic structures of Chapters 2 and 3. In this formulation, coupled integral equations are derived that incorporate both the two-dimensional planar periodic free-space Green's function (PFSGF) and the inclusion of three-dimensional material blocks. Equivalent polarization currents are used to model the material inclusions and the method of moments is used to discretize the geometry and the integral equations. The resulting matrix equation is numerically solved for various quantities of interest. First, the solution of plane wave scattering from an inhomogeneous doubly periodic dielectric layer over a layered medium is derived and implemented in Section 4.2. The reflection coefficient is determined for arbitrary polarization (vertical, horizontal, or a combination thereof) and arbitrary direction of incidence ($\phi_0 \in [0, 2\pi]$, $\theta_0 \in [0, \pi]$) for a number of sample structures and validated with results obtained from canonical problems and results published in the open literature.

Of particular concern in the solution of the periodic structure is the convergence of the resulting Floquet series. Although the contribution of the off-plane periodic elements converges quickly, the convergence of the on-plane periodic elements is notoriously slow. In order to compute the impedance matrix elements in a reasonable amount of time, various series acceleration techniques and transformations have been suggested including the Poisson transformation [70], Kummer's method [51], the Shanks' transform [90], and the Ewald transformation [30]. Summation acceleration techniques convert a slowly converging series to a rapidly converging one by allowing the series to be transformed into a second series that converges to the same limit but does so in a rapid fashion. The aforementioned transforms have all been implemented in conjunction with the slowly-converging PFSGF and each transform has its advantages and disadvantages when applied to the PFSGF in a particular fashion. However, some of the transforms have only been implemented for limited cases of the PFSGF. For the problems of interest in this chapter, a Poisson transformation and a Shanks' transformation are successfully implemented to improve both the speed and the accuracy of the impedance matrix element computations. Additionally, Kummer's method is applied to specific series to compare the convergence rate of these different series acceleration techniques. A complete treatment of these and other series acceleration techniques is found in Section 4.5.

4.2 Formulation of Integral Equations

In this section, volume integral equations (IE) are derived from Maxwell's equations and the boundary conditions that when solved yield equivalent currents from which total scattered fields can be determined. The integral equations are discretized and cast into a matrix equation form through the use of the method of moments (MoM) numerical solution technique. The unknowns are obtained from the solution of the resulting linear system.

4.2.1 Derivation of Electric Field Integral Equation

The derivation of the electric field integral equation outlined in Chapter 2 is repeated below for convenience. The total electric field is viewed as the sum of an incident field $\mathbf{E}^i(\mathbf{r})$ due to radiation from a known source with the scatterer absent and a scattered field $\mathcal{E}[\mathbf{J};\mathbf{r};V]$ which is due to radiation by equivalent volume currents $\mathbf{J}$ which reside in a volume V

$$\mathbf{E}(\mathbf{r}) = \mathcal{E}[\mathbf{J};\mathbf{r};V] + \mathbf{E}^i(\mathbf{r}), \tag{4.1}$$

in which the operator $\mathcal{E}[\mathbf{J};\mathbf{r};V]$ can be expressed in terms of a Hertz potential [108] as

$$\mathcal{E}[\mathbf{J};\mathbf{r};V] = k_0^2\, \mathbf{\Pi}(\mathbf{r}) + \nabla\nabla\cdot\mathbf{\Pi}(\mathbf{r}) \tag{4.2a}$$

where

$$\mathbf{\Pi}(\mathbf{r}) = -\frac{Z_0}{8\pi^2 k_0} \iiint_V \mathbf{J}(\mathbf{r}') \iint_\infty \frac{e^{-jk_z|z-z'|}}{k_z} e^{-jk_y(y-y')} e^{-jk_x(x-x')}\, dk_x\, dk_y\, d\mathbf{r}' \tag{4.2b}$$

with

$$k_z = \begin{cases} \sqrt{k_0^2 - k_x^2 - k_y^2} & k_0^2 > k_x^2 + k_y^2, \\ -j\sqrt{k_x^2 + k_y^2 - k_0^2} & k_0^2 < k_x^2 + k_y^2. \end{cases} \tag{4.2c}$$

and $Z_0 = 1/Y_0$ is the intrinsic impedance of free-space. The electric field must satisfy

$$\mathcal{E}[\mathbf{J}; \mathbf{r}; V] + \mathbf{E}^i(\mathbf{r}) = \mathbf{E}(\mathbf{r}), \quad \mathbf{r} \in V. \tag{4.3}$$

4.2.2 Integral Equations

Plane wave excitation

A representative grounded doubly periodic dielectric layer with period a in the x direction and period c in the y direction is illustrated in Figure 4.1. The perforated dielectric

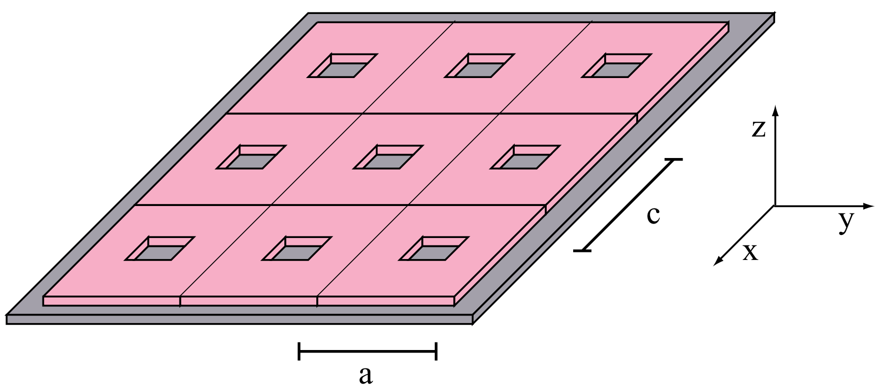

Figure 4.1: Doubly periodic dielectric layer with period a in the x direction and period c in the y direction over a layered medium

layer is excited by an incident time harmonic ($e^{j\omega t}$) plane wave defined by

$$\mathbf{E}^i = \mathbf{P}_i\; e^{-j\mathbf{k}_i\cdot\mathbf{r}} = \left(e_h\hat{\mathbf{h}}_i + e_v\hat{\mathbf{v}}_i\right) e^{-j\mathbf{k}_i\cdot\mathbf{r}} \tag{4.4}$$

where $\mathbf{P}_i = e_h\hat{\mathbf{h}}_i + e_v\hat{\mathbf{v}}_i$ denotes the polarization of the incident wave and $\hat{\mathbf{k}}_i$ is the direction of propagation. The unit vectors $\hat{\mathbf{h}}_i$, $\hat{\mathbf{v}}_i$, and $\hat{\mathbf{k}}_i$ are defined in terms of the spherical angles

(ϕ_0, θ_0) as

$$\hat{\mathbf{k}}_i = \hat{\mathbf{x}} \cos\phi_0 \sin\theta_0 + \hat{\mathbf{y}} \sin\phi_0 \sin\theta_0 - \hat{\mathbf{z}} \cos\theta_0 \tag{4.5a}$$

$$\hat{\mathbf{h}}_i = \frac{\hat{\mathbf{k}}_i \times \hat{\mathbf{z}}}{|\hat{\mathbf{k}}_i \times \hat{\mathbf{z}}|} = \hat{\mathbf{x}} \sin\phi_0 - \hat{\mathbf{y}} \cos\phi_0 \tag{4.5b}$$

$$\hat{\mathbf{v}}_i = \hat{\mathbf{h}}_i \times \hat{\mathbf{k}}_i = \hat{\mathbf{x}} \cos\phi_0 \cos\theta_0 + \hat{\mathbf{y}} \sin\phi_0 \cos\theta_0 + \hat{\mathbf{z}} \sin\theta_0 \tag{4.5c}$$

and are shown in Figure 4.2. The kDB coordinate system [45] consists of the wave vector $\hat{\mathbf{k}}$ and the plane containing the electric and magnetic flux density vectors $\mathbf{D}$ and $\mathbf{B}$. In

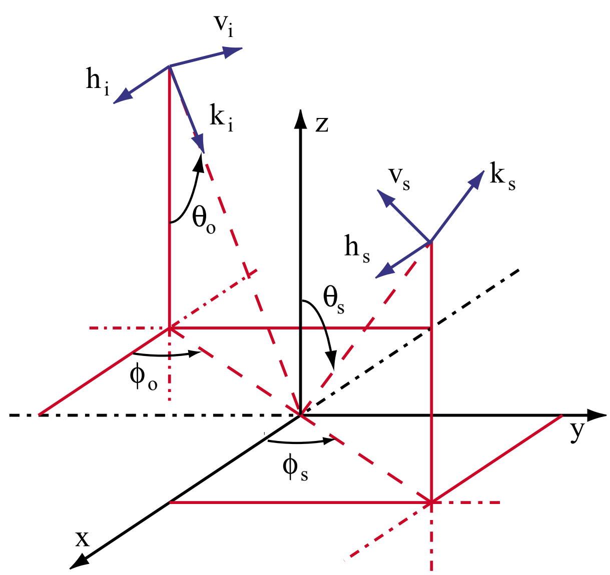

Figure 4.2: Coordinate system (kDB) for incident and scattered field

the absence of the dielectric layer (to be replaced by equivalent polarization currents), the reflected field from a surface can be easily computed as

$$\mathbf{E}^r = \mathbf{P}_r e^{-j\mathbf{k}_s \cdot \mathbf{r}} = \left(R_h e_h \hat{\mathbf{h}}_s + R_v e_v \hat{\mathbf{v}}_s \right) e^{-j\mathbf{k}_s \cdot \mathbf{r}} \tag{4.6}$$

where R_h and R_v are the Fresnel reflection coefficients for horizontal and vertical polarized electric fields, respectively, and $\hat{\mathbf{k}}_s$ is the direction of propagation. The unit vectors $\hat{\mathbf{h}}_s$, $\hat{\mathbf{v}}_s$, and $\hat{\mathbf{k}}_s$ are defined in terms of the spherical angles (ϕ_s, θ_s) as

$$\hat{\mathbf{k}}_s = \hat{\mathbf{x}} \cos\phi_s \sin\theta_s + \hat{\mathbf{y}} \sin\phi_s \sin\theta_s + \hat{\mathbf{z}} \cos\theta_s \tag{4.7a}$$

$$\hat{\mathbf{h}}_s = \frac{\hat{\mathbf{k}}_s \times \hat{\mathbf{z}}}{|\hat{\mathbf{k}}_i \times \hat{\mathbf{z}}|} = \hat{\mathbf{x}} \sin\phi_s - \hat{\mathbf{y}} \cos\phi_s \tag{4.7b}$$

$$\hat{\mathbf{v}}_s = \hat{\mathbf{h}}_s \times \hat{\mathbf{k}}_s = -\hat{\mathbf{x}} \cos\phi_s \cos\theta_s - \hat{\mathbf{y}} \sin\phi_s \cos\theta_s + \hat{\mathbf{z}} \sin\theta_s \tag{4.7c}$$

Note that $\hat{\mathbf{k}}_s = \hat{\mathbf{k}}_i - 2(\hat{\mathbf{z}} \cdot \hat{\mathbf{k}}_i)\hat{\mathbf{z}}$.

The total electric field everywhere is computed as the sum of the incident and reflected electric fields in (4.4) and (4.6) and the scattered field $\mathbf{E}^s(\mathbf{r})$ produced by the equivalent induced electric current. Thus, (4.3) becomes upon substitution

$$\begin{aligned}\frac{\mathbf{J}(\mathbf{r})}{jk_0 Y_0\left(\varepsilon_r(\mathbf{r})-1\right)} &= \mathbf{E}^i(\mathbf{r}) + \mathbf{E}^r(\mathbf{r}) + \mathbf{E}^s(\mathbf{r}) \\ &= \left(e_h \hat{\mathbf{h}}_i + e_v \hat{\mathbf{v}}_i\right) e^{-j\mathbf{k}_i \cdot \mathbf{r}} + \left(R_h e_h \hat{\mathbf{h}}_s + R_v e_v \hat{\mathbf{v}}_s\right) e^{-j\mathbf{k}_s \cdot \mathbf{r}} + \mathbf{E}^s(x,y,z). \quad (4.8)\end{aligned}$$

The three coupled integral equations from (4.8) become

$$\begin{aligned}\frac{J_x(\mathbf{r})}{jk_0 Y_0\left(\varepsilon_r(\mathbf{r})-1\right)} &= \left(e_h \hat{\mathbf{x}} \cdot \hat{\mathbf{h}}_i + e_v \hat{\mathbf{x}} \cdot \hat{\mathbf{v}}_i\right) e^{-j\mathbf{k}_i \cdot \mathbf{r}} + \left(R_h e_h \hat{\mathbf{x}} \cdot \hat{\mathbf{h}}_s + R_v e_v \hat{\mathbf{x}} \cdot \hat{\mathbf{v}}_s\right) e^{-j\mathbf{k}_s \cdot \mathbf{r}} \\ &+ \iiint\limits_{\infty} \left\{ G_{xx}(\mathbf{r};\mathbf{r}')J_x(\mathbf{r}') + G_{xy}(\mathbf{r};\mathbf{r}')J_y(\mathbf{r}') + G_{xz}(\mathbf{r};\mathbf{r}')J_z(\mathbf{r}') \right\} d\mathbf{r}' \quad (4.9)\end{aligned}$$

$$\begin{aligned}\frac{J_y(\mathbf{r})}{jk_0 Y_0\left(\varepsilon_r(\mathbf{r})-1\right)} &= \left(e_h \hat{\mathbf{y}} \cdot \hat{\mathbf{h}}_i + e_v \hat{\mathbf{y}} \cdot \hat{\mathbf{v}}_i\right) e^{-j\mathbf{k}_i \cdot \mathbf{r}} + \left(R_h e_h \hat{\mathbf{y}} \cdot \hat{\mathbf{h}}_s + R_v e_v \hat{\mathbf{y}} \cdot \hat{\mathbf{v}}_s\right) e^{-j\mathbf{k}_s \cdot \mathbf{r}} \\ &+ \iiint\limits_{\infty} \left\{ G_{yx}(\mathbf{r};\mathbf{r}')J_x(\mathbf{r}') + G_{yy}(\mathbf{r};\mathbf{r}')J_y(\mathbf{r}') + G_{yz}(\mathbf{r};\mathbf{r}')J_z(\mathbf{r}') \right\} d\mathbf{r}' \quad (4.10)\end{aligned}$$

$$\begin{aligned}\frac{J_z(\mathbf{r})}{jk_0 Y_0\left(\varepsilon_r(\mathbf{r})-1\right)} &= e_v \hat{\mathbf{z}} \cdot \hat{\mathbf{v}}_i e^{-j\mathbf{k}_i \cdot \mathbf{r}} + R_v e_v \hat{\mathbf{z}} \cdot \hat{\mathbf{v}}_s e^{-j\mathbf{k}_s \cdot \mathbf{r}} \\ &+ \iiint\limits_{\infty} \left\{ G_{zx}(\mathbf{r};\mathbf{r}')J_x(\mathbf{r}') + G_{zy}(\mathbf{r};\mathbf{r}')J_y(\mathbf{r}') + G_{zz}(\mathbf{r};\mathbf{r}')J_z(\mathbf{r}') \right\} d\mathbf{r}' \quad (4.11)\end{aligned}$$

where G_{xx}—G_{zz} are the components of the dyadic free-space Green's function.

Since the dielectric material is periodic in x with period a and prescribed phase shift $k_{x0}a$ and periodic in y with period c and prescribed phase shift $k_{y0}c$, the resulting equivalent currents must satisfy

$$\mathbf{J}(x+pa, y+qc, z) = \mathbf{J}(x,y,z)e^{-jk_{x0}pa}e^{-jk_{y0}qc} \quad (4.12)$$

where

$$\begin{aligned} k_{x0} &= k_0 \cos\phi_0 \sin\theta_0 \\ k_{y0} &= k_0 \sin\phi_0 \sin\theta_0 \end{aligned}$$

and p,q are the Floquet indices in the x- and y-directions, respectively. The x-component of the scattered field integral, I_{xx}, in (4.9) is defined by

$$\begin{aligned} I_{xx} &= \iiint\limits_{\infty} G_{xx}(\mathbf{r};\mathbf{r}')J_x(\mathbf{r}')\ d\mathbf{r}' \\ &= \sum_{p,q} \int\limits_{(p-\frac{1}{2})a}^{(p+\frac{1}{2})a} \int\limits_{(q-\frac{1}{2})c}^{(q+\frac{1}{2})c} \int\limits_{-\infty}^{\infty} G_{xx}(\mathbf{r};\mathbf{r}')J_x(\mathbf{r}')e^{-jk_{x0}pa}e^{-jk_{y0}qc}\ d\mathbf{r}' \\ &= \int\limits_{-\frac{a}{2}}^{\frac{a}{2}} \int\limits_{-\frac{c}{2}}^{\frac{c}{2}} \int\limits_{-\infty}^{\infty} G^p_{xx}(\mathbf{r};\mathbf{r}')J_x(\mathbf{r}')\ d\mathbf{r}' \end{aligned} \tag{4.13}$$

where the periodic free-space Green's function, denoted $G^p(\mathbf{r},\mathbf{r}')$, is defined in terms of the free-space Green's function as

$$G^p(\mathbf{r};\mathbf{r}') = \sum_{p,q} G(x,y,z;x'+pa,y'+qc,z')e^{-jk_{x0}pa}e^{-jk_{y0}qc}. \tag{4.14}$$

The significance of this procedure is that the solution of the periodic structure has now been reduced to solving that of the single unit cell shown in Figure 4.3. Explicitly, $G^p_{xx}(\mathbf{r};\mathbf{r}')$ in

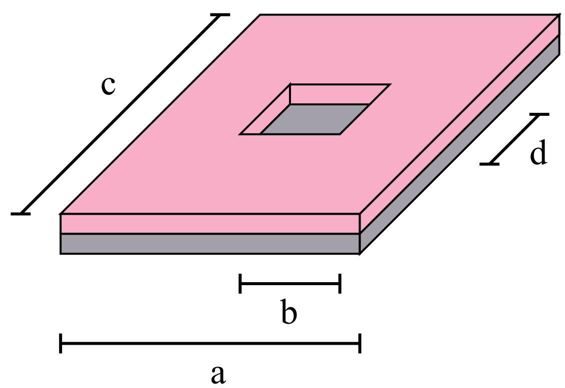

Figure 4.3: Doubly periodic dielectric layered unit cell

(4.13) can be written as

$$\begin{aligned} G^p_{xx}(\mathbf{r};\mathbf{r}') = -\frac{Z_0}{8\pi^2 k_0} \sum_{p,q} \left(k_0^2 + \frac{\partial^2}{\partial x^2}\right) \iint\limits_{\infty} \left[\frac{e^{-jk_z|z-z'|}}{k_z} + R_x \frac{e^{-jk_z(z+z')}}{k_z}\right] \\ \times e^{-jk_y(y-y'-qc)}e^{-jk_x(x-x'-pa)}e^{-jk_{x0}pa}e^{-jk_{y0}qc}\ dk_x\ dk_y, \end{aligned} \tag{4.15}$$

where $R_x = R_h$. If the above is rewritten as

$$G^p_{xx}(\mathbf{r};\mathbf{r}') = -\frac{Z_0}{8\pi^2 k_0}\sum_{p,q}\left(k_0^2 + \frac{\partial^2}{\partial x^2}\right)\iint_{\infty}\left[\frac{e^{-jk_z|z-z'|}}{k_z} + R_x\frac{e^{-jk_z(z+z')}}{k_z}\right]$$
$$\times\, e^{-jk_x(x-x')}e^{-jk_y(y-y')}e^{-j\left(k_{x0}-k_x\right)pa}e^{-j\left(k_{y0}-k_y\right)qc}\; dk_x\; dk_y, \quad (4.16)$$

an important observation can be made which greatly simplifies the formulation. From the theory of Fourier Series we can represent a periodic train of Dirac delta functions by an infinite summation of complex exponentials,

$$\sum_p e^{-j(k_{x0}-k_x)pa} = \frac{2\pi}{a}\sum_p \delta\left[k_x - k_{x0} - \frac{2\pi p}{a}\right] \quad (4.17a)$$

$$\sum_q e^{-j(k_{y0}-k_y)qc} = \frac{2\pi}{c}\sum_q \delta\left[k_y - k_{y0} - \frac{2\pi q}{c}\right]. \quad (4.17b)$$

Substituting the Dirac delta functions representation in (4.17) and carrying out the integrations in (4.16) yields

$$G^p_{xx}(\mathbf{r};\mathbf{r}')$$
$$= -\frac{Z_0}{2k_0 ac}\sum_{p,q}\left(k_0^2 + \frac{\partial^2}{\partial x^2}\right)\left[\frac{e^{-jk_{z_{pq}}|z-z'|}}{k_{z_{pq}}} + R_x\frac{e^{-jk_{z_{pq}}(z+z')}}{k_{z_{pq}}}\right]e^{-jk_{x_p}(x-x')}e^{-jk_{y_q}(y-y')} \quad (4.18a)$$

where

$$k_{x_p} = k_{x0} + \frac{2\pi p}{a} = k_0\cos\phi_0\sin\theta_0 + \frac{2\pi p}{a}$$
$$k_{y_q} = k_{y0} + \frac{2\pi q}{c} = k_0\sin\phi_0\sin\theta_0 + \frac{2\pi q}{c}$$

with

$$k_{z_{pq}} = \begin{cases}\sqrt{k_0^2 - k_{x_p}^2 - k_{y_q}^2}, & k_0^2 > k_{x_p}^2 + k_{y_q}^2,\\ -j\sqrt{k_{x_p}^2 + k_{y_q}^2 - k_0^2}, & k_0^2 < k_{x_p}^2 + k_{y_q}^2.\end{cases}$$

The remaining periodic free-space Green's function components G^p_{xy}–G^p_{zz} are defined by

$$G^p_{xy}(\mathbf{r};\mathbf{r}') = -\frac{Z_0}{2k_0 ac}\sum_{p,q}\frac{\partial^2}{\partial x\partial y}\left[\frac{e^{-jk_{z_{pq}}|z-z'|}}{k_{z_{pq}}} + R_y\frac{e^{-jk_{z_{pq}}(z+z')}}{k_{z_{pq}}}\right]e^{-jk_{x_p}(x-x')}e^{-jk_{y_q}(y-y')} \quad (4.18b)$$

$$G^p_{xz}(\mathbf{r};\mathbf{r}') = -\frac{Z_0}{2k_0 ac}\sum_{p,q}\frac{\partial^2}{\partial x\partial z}\left[\frac{e^{-jk_{z_{pq}}|z-z'|}}{k_{z_{pq}}} + R_z\frac{e^{-jk_{z_{pq}}(z+z')}}{k_{z_{pq}}}\right]e^{-jk_{x_p}(x-x')}e^{-jk_{y_q}(y-y')} \quad (4.18c)$$

$$G_{yx}^{p}(\mathbf{r};\mathbf{r}') = -\frac{Z_0}{2k_0ac}\sum_{p,q}\frac{\partial^2}{\partial y\partial x}\left[\frac{e^{-jk_{z_{pq}}|z-z'|}}{k_{z_{pq}}} + R_x\frac{e^{-jk_{z_{pq}}(z+z')}}{k_{z_{pq}}}\right]e^{-jk_{x_p}(x-x')}e^{-jk_{y_q}(y-y')} \tag{4.18d}$$

$$G_{yy}^{p}(\mathbf{r};\mathbf{r}') = -\frac{Z_0}{2k_0ac}\sum_{p,q}\left(k_0^2+\frac{\partial^2}{\partial y^2}\right)\left[\frac{e^{-jk_{z_{pq}}|z-z'|}}{k_{z_{pq}}} + R_y\frac{e^{-jk_{z_{pq}}(z+z')}}{k_{z_{pq}}}\right]e^{-jk_{x_p}(x-x')}e^{-jk_{y_q}(y-y')} \tag{4.18e}$$

$$G_{yz}^{p}(\mathbf{r};\mathbf{r}') = -\frac{Z_0}{2k_0ac}\sum_{p,q}\frac{\partial^2}{\partial y\partial z}\left[\frac{e^{-jk_{z_{pq}}|z-z'|}}{k_{z_{pq}}} + R_z\frac{e^{-jk_{z_{pq}}(z+z')}}{k_{z_{pq}}}\right]e^{-jk_{x_p}(x-x')}e^{-jk_{y_q}(y-y')} \tag{4.18f}$$

$$G_{zx}^{p}(\mathbf{r};\mathbf{r}') = -\frac{Z_0}{2k_0ac}\sum_{p,q}\frac{\partial^2}{\partial z\partial x}\left[\frac{e^{-jk_{z_{pq}}|z-z'|}}{k_{z_{pq}}} + R_x\frac{e^{-jk_{z_{pq}}(z+z')}}{k_{z_{pq}}}\right]e^{-jk_{x_p}(x-x')}e^{-jk_{y_q}(y-y')} \tag{4.18g}$$

$$G_{zy}^{p}(\mathbf{r};\mathbf{r}') = -\frac{Z_0}{2k_0ac}\sum_{p,q}\frac{\partial^2}{\partial z\partial y}\left[\frac{e^{-jk_{z_{pq}}|z-z'|}}{k_{z_{pq}}} + R_y\frac{e^{-jk_{z_{pq}}(z+z')}}{k_{z_{pq}}}\right]e^{-jk_{x_p}(x-x')}e^{-jk_{y_q}(y-y')} \tag{4.18h}$$

$$G_{zz}^{p}(\mathbf{r};\mathbf{r}') = -\frac{Z_0}{2k_0ac}\sum_{p,q}\left(k_0^2+\frac{\partial^2}{\partial z^2}\right)\left[\frac{e^{-jk_{z_{pq}}|z-z'|}}{k_{z_{pq}}} + R_z\frac{e^{-jk_{z_{pq}}(z+z')}}{k_{z_{pq}}}\right]e^{-jk_{x_p}(x-x')}e^{-jk_{y_q}(y-y')} \tag{4.18i}$$

where $R_y = R_h$ and $R_z = R_v$. If the equivalent currents are assumed to radiate in the presence of a ground plane, the Green's functions listed in (4.18a)–(4.18i) can be easily manipulated to agree with similar expressions in [133] by setting R_h=−1 and R_v=+1.

Reflection from a Dielectric Layer

If the ground plane backing the doubly periodic dielectric layer is replaced by a layered medium, perhaps also grounded, the Fresnel reflection coefficients (R_h and R_v) are no longer simply ±1. The geometry of the layered medium is shown in Figure 4.4 where the

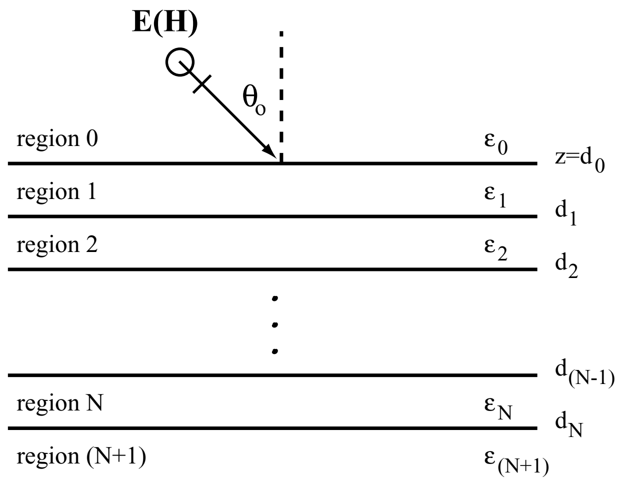

Figure 4.4: Plane wave reflection from layered medium

l^{th} interface is the defined by the plane located at $z{=}d_l$. Region 0 is the region above the layered medium and region $(N+1)$ is the semi-infinite region below the N layers. The solution for the total reflection coefficient of the medium can be obtained by applying the appropriate boundary conditions to the tangential components of the electric and magnetic field at each interface. Consequently, the $(N+1)$ interfaces yield $(2N+2)$ equations to solve for the $(2N+2)$ unknown amplitude coefficients. Explicitly, the $(2N+2)$ unknowns are the two unknowns in each of the N layers (one each for the waves traveling in the $\pm z$ directions), one for the unknown transmission coefficient of the semi-infinite region, and one for the reflection coefficient of interest.

Horizontal polarization Assume the electric field in the l^{th} layer of a medium is polarized in the horizontal direction. From (4.4) and following [84], the electric field in the l^{th} layer is written in the form

$$E_{h_l} = \left[c_l^i e^{jk_{z_l}z} + c_l^r e^{-jk_{z_l}z}\right] e^{-jk_{x_0}x} e^{-jk_{y_0}y} \tag{4.19}$$

where

$$k_{z_l} = k_0\sqrt{\epsilon_l - \sin^2\theta_0} \tag{4.20}$$

and c_l^i and c_l^r are the amplitudes of the $-z$ and $+z$ traveling waves in the l^{th} layer, respectively, and ε_l is the permittivity of the l^{th} layer. The magnetic field in the l^{th} layer can be found by applying (2.1b) to the electric field above. Carrying out the required vector operations, one finds that the tangential components of the vertically polarized magnetic field in the l^{th} layer have the form

$$H_{v_l} = \frac{k_{z_l}}{k_0 Z_0} \left[c_l^i e^{jk_{z_l} z} - c_l^r e^{-jk_{z_l} z} \right] e^{-jk_{x_0} x} e^{-jk_{y_0} y}. \tag{4.21}$$

The following recursive relationship that relates the amplitudes of the l^{th} layer to those of the $(l+1)^{\text{th}}$ layer can be derived by requiring the tangential electric and magnetic field to be continuous across each of the dielectric interfaces

$$\frac{c_l^r}{c_l^i} = \frac{\left(c_{l+1}^r / c_{l+1}^i\right) + \Gamma_l^h e^{-j2k_{z_{(l+1)}} d_l}}{\left(c_{l+1}^r / c_{l+1}^i\right) \Gamma_l^h + e^{-j2k_{z_{(l+1)}} d_l}} e^{-j2k_{z_l} d_l} \tag{4.22}$$

where

$$\Gamma_l^h = \frac{k_{z_l} - k_{z_{(l+1)}}}{k_{z_l} + k_{z_{(l+1)}}}. \tag{4.23}$$

The solution for the total horizontal reflection coefficient R_h is initiated by assuming c_0^i=1 in region 0 and by noting that c_{N+1}^r=0 in the semi-infinite region. Starting from $c_{(N+1)}^r / c_{(N+1)}^i$=0, equations (4.22) and (4.23) are used repeatedly to solve for the amplitudes of the waves in each layer beginning with the interface located at $z = d_N$ and continuing to the interface between the zeroth and first layer. The horizontal reflection coefficient is then determined as R_h=c_0^r / c_0^i.

Vertical polarization If the electric field is vertically polarized, the same recursive relation in (4.22) is found but with Γ_l^h replaced by

$$\Gamma_l^v = \frac{\epsilon_{(l+1)} k_{z_l} - \epsilon_l k_{z_{(l+1)}}}{\epsilon_{(l+1)} k_{z_l} + \epsilon_l k_{z_{(l+1)}}}. \tag{4.24}$$

The solution for the vertical reflection coefficient is found from R_v=c_0^r / c_0^i.

Grounded medium If the N^{th} layer in the medium is grounded, Γ_N^h=-1 and Γ_N^v=$+1$, and the process is executed as before.

4.3 Numerical Implementation

The first step in the method of moments (MoM) numerical method [34] is to discretize the geometry and approximate the unknown electric current in the dielectric region with either subsectional or entire domain basis functions. The equivalent polarization currents are expanded in a linear combination of these basis functions, and the equations are tested in order to obtain an adequate number of equations to solve for the unknown coefficients of the basis functions.

The dielectric region is discretized into $N{=}N_xN_yN_z$ piecewise constant subvolumes of width $\Delta_x = b/N_x$, length $\Delta_y = d/N_y$, and depth $\Delta_z = t/N_z$. The current $\mathbf{J} = \hat{\mathbf{x}}J_x + \hat{\mathbf{y}}J_y + \hat{\mathbf{z}}J_z$ is expanded in a linear combination of N piecewise constant basis functions with unknown current coefficients $\{J_{x_n}, J_{y_n}, J_{z_n}\}$ centered at $x_n = -\frac{b}{2} + \Delta_x(n - \frac{1}{2})$, $y_n = -\frac{d}{2} + \Delta_y(n - \frac{1}{2})$, and $z_n = \Delta_z(n - \frac{1}{2})$

$$J_x = \sum_{n=1}^{N} J_{x_n}\Pi_n(x, y, z) = \sum_{n=1}^{N} J_{x_n}\Pi_n(x)\Pi_n(y)\Pi_n(z) \tag{4.25a}$$

$$J_y = \sum_{n=1}^{N} J_{y_n}\Pi_n(x, y, z) = \sum_{n=1}^{N} J_{y_n}\Pi_n(x)\Pi_n(y)\Pi_n(z) \tag{4.25b}$$

$$J_z = \sum_{n=1}^{N} J_{z_n}\Pi_n(x, y, z) = \sum_{n=1}^{N} J_{z_n}\Pi_n(x)\Pi_n(y)\Pi_n(z) \tag{4.25c}$$

where

$$\Pi_n(x) = \begin{cases} 1, & x_n - \frac{\Delta_x}{2} < x < x_n + \frac{\Delta_x}{2}; \\ 0, & \text{otherwise;} \end{cases} \tag{4.26}$$

and

$$\Pi_n(y) = \begin{cases} 1, & y_n - \frac{\Delta_y}{2} < y < y_n + \frac{\Delta_y}{2}; \\ 0, & \text{otherwise;} \end{cases} \tag{4.27}$$

and

$$\Pi_n(z) = \begin{cases} 1, & z_n - \frac{\Delta_z}{2} < z < z_n + \frac{\Delta_z}{2}; \\ 0, & \text{otherwise.} \end{cases} \tag{4.28}$$

4.3.1 Impedance Matrices

The scattered field is determined by integrating the equivalent currents over the periodic Green's function. By discretizing the resulting coupled equations, they can be cast into the following matrix form

$$\begin{bmatrix} Z_{mn}^{xx} & Z_{mn}^{xy} & Z_{mn}^{xz} \\ Z_{mn}^{yx} & Z_{mn}^{yy} & Z_{mn}^{yz} \\ Z_{mn}^{zx} & Z_{mn}^{zy} & Z_{mn}^{zz} \end{bmatrix} \begin{bmatrix} J_n^x \\ J_n^y \\ J_n^z \end{bmatrix} = \begin{bmatrix} V_m^x \\ V_m^y \\ V_m^z \end{bmatrix}. \tag{4.29}$$

Specifically, for the Z_{xx} submatrix, the current representation is inserted into (4.9) and the integrations are carried out. Testing the resulting equation using point collocation, we obtain for all off-plane, *i.e.* $z_m \neq z_n$, elements

$$
\begin{aligned}
Z_{xx} &= \int_{-\frac{a}{2}}^{\frac{a}{2}} \int_{-\frac{c}{2}}^{\frac{c}{2}} \int_{0}^{t} G^p_{xx}(\mathbf{r};\mathbf{r}')\ J_x(x',y',z')\ dx'\ dy'\ dz' \\
&= -\frac{Z_0}{2k_0 ac} \int_{-\frac{a}{2}}^{\frac{a}{2}} \int_{-\frac{c}{2}}^{\frac{c}{2}} \int_{0}^{t} \sum_{p,q} \left(k_0^2 + \frac{\partial^2}{\partial x^2}\right) \left[\frac{e^{-jk_{z_{pq}}|z-z'|}}{k_{z_{pq}}} + R_x \frac{e^{-jk_{z_{pq}}(z+z')}}{k_{z_{pq}}}\right] \\
&\quad \times e^{-jk_{x_p}(x-x')} e^{-jk_{y_q}(y-y')}\ J_x(x',y',z')\ dx'\ dy'\ dz'
\end{aligned} \tag{4.30}
$$

$$
\begin{aligned}
Z^{xx}_{mn} = -\frac{Z_0 \Delta_x \Delta_y \Delta_z}{2k_0 ac} \sum_{p,q} \left(\frac{k_0^2 - k_{x_p}^2}{k_{z_{pq}}}\right) \left[e^{-jk_{z_{pq}}|z_m - z_n|} + R_x e^{-jk_{z_{pq}}(z_m+z_n)}\right] \\
\times \operatorname{sinc}\left(\frac{k_{x_p}\Delta_x}{2}\right) \operatorname{sinc}\left(\frac{k_{y_q}\Delta_y}{2}\right) \operatorname{sinc}\left(\frac{k_{z_{pq}}\Delta_z}{2}\right) e^{-jk_{x_p}(x_m-x_n)} e^{-jk_{y_q}(y_m-y_n)}
\end{aligned} \tag{4.31}
$$

For $z_m = z_n$, the integration over z must be computed carefully. The resulting on-plane impedance matrix elements for Z_{xx} are

$$
\begin{aligned}
Z^{xx}_{mn} = -\frac{Z_0 \Delta_x \Delta_y \Delta_z}{2k_0 ac} \sum_{p,q} \left(\frac{k_0^2 - k_{x_p}^2}{k_{z_{pq}}}\right) \\
\times \left[\frac{\left(2 - 2e^{-jk_{z_{pq}}\Delta_z/2}\right)}{k_{z_{pq}}\Delta_z} + R_x \operatorname{sinc}\left(\frac{k_{z_{pq}}\Delta_z}{2}\right) e^{-jk_{z_{pq}} 2z_m}\right] \\
\times \operatorname{sinc}\left(\frac{k_{x_p}\Delta_x}{2}\right) \operatorname{sinc}\left(\frac{k_{y_q}\Delta_y}{2}\right) e^{-jk_{x_p}(x_m-x_n)} e^{-jk_{y_q}(y_m-y_n)}.
\end{aligned} \tag{4.32}
$$

The remaining impedance matrix elements Z^{xy}_{mn}–Z^{zz}_{mn} are explicitly below given for on-plane and off-plane elements.

Submatrix Z_{xy}

$$
\begin{aligned}
Z_{xy} &= \int_{-\frac{a}{2}}^{\frac{a}{2}} \int_{-\frac{c}{2}}^{\frac{c}{2}} \int_{0}^{t} G^p_{xy}(\mathbf{r};\mathbf{r}')\ J_x(x',y',z')\ dx'\ dy'\ dz' \\
&= -\frac{Z_0}{2k_0 ac} \int_{-\frac{a}{2}}^{\frac{a}{2}} \int_{-\frac{c}{2}}^{\frac{c}{2}} \int_{0}^{t} \sum_{p,q} \frac{\partial^2}{\partial x \partial y} \left[\frac{e^{-jk_{z_{pq}}|z-z'|}}{k_{z_{pq}}} + R_y \frac{e^{-jk_{z_{pq}}(z+z')}}{k_{z_{pq}}}\right] \\
&\quad \times e^{-jk_{x_p}(x-x')} e^{-jk_{y_q}(y-y')}\ J_x(x',y',z')\ dx'\ dy'\ dz'
\end{aligned} \tag{4.33}
$$

For $z_m \neq z_n$,

$$Z^{xy}_{mn} = \frac{Z_0 \Delta_x \Delta_y \Delta_z}{2k_0 ac} \sum_{p,q} \frac{k_{y_q} k_{x_p}}{k_{z_{pq}}} \left[e^{-jk_{z_{pq}}|z_m - z_n|} + R_y e^{-jk_{z_{pq}}(z_m + z_n)} \right]$$
$$\times \operatorname{sinc}\left(\frac{k_{x_p}\Delta_x}{2}\right) \operatorname{sinc}\left(\frac{k_{y_q}\Delta_y}{2}\right) \operatorname{sinc}\left(\frac{k_{z_{pq}}\Delta_z}{2}\right) e^{-jk_{x_p}(x_m - x_n)} e^{-jk_{y_q}(y_m - y_n)} \quad (4.34)$$

For $z_m = z_n$,

$$Z^{xy}_{mn} = \frac{Z_0 \Delta_x \Delta_y \Delta_z}{2k_0 ac} \sum_{p,q} \frac{k_{y_q} k_{x_p}}{k_{z_{pq}}} \left[\frac{\left(2 - 2e^{-jk_{z_{pq}}\Delta_z/2}\right)}{k_{z_{pq}}\Delta_z} + R_y \operatorname{sinc}\left(\frac{k_{z_{pq}}\Delta_z}{2}\right) e^{-jk_{z_{pq}} 2 z_m} \right]$$
$$\times \operatorname{sinc}\left(\frac{k_{x_p}\Delta_x}{2}\right) \operatorname{sinc}\left(\frac{k_{y_q}\Delta_y}{2}\right) e^{-jk_{x_p}(x_m - x_n)} e^{-jk_{y_q}(y_m - y_n)} \quad (4.35)$$

Submatrix Z_{yx}

$$Z_{yx} = \int_{-\frac{a}{2}}^{\frac{a}{2}} \int_{-\frac{c}{2}}^{\frac{c}{2}} \int_{0}^{t} G^p_{yx}(\mathbf{r};\mathbf{r}')\ J_y(x', y', z')\ dx'\ dy'\ dz'$$
$$= -\frac{Z_0}{2k_0 ac} \int_{-\frac{a}{2}}^{\frac{a}{2}} \int_{-\frac{c}{2}}^{\frac{c}{2}} \int_{0}^{t} \sum_{p,q} \frac{\partial^2}{\partial y \partial x} \left[\frac{e^{-jk_{z_{pq}}|z - z'|}}{k_{z_{pq}}} + R_x \frac{e^{-jk_{z_{pq}}(z + z')}}{k_{z_{pq}}} \right]$$
$$\times e^{-jk_{x_p}(x - x')} e^{-jk_{y_q}(y - y')}\ J_y(x', y', z')\ dx'\ dy'\ dz' \quad (4.36)$$

For $z_m \neq z_n$,

$$Z^{yx}_{mn} = \frac{Z_0 \Delta_x \Delta_y \Delta_z}{2k_0 ac} \sum_{p,q} \frac{k_{y_q} k_{x_p}}{k_{z_{pq}}} \left[e^{-jk_{z_{pq}}|z_m - z_n|} + R_x e^{-jk_{z_{pq}}(z_m + z_n)} \right]$$
$$\times \operatorname{sinc}\left(\frac{k_{x_p}\Delta_x}{2}\right) \operatorname{sinc}\left(\frac{k_{y_q}\Delta_y}{2}\right) \operatorname{sinc}\left(\frac{k_{z_{pq}}\Delta_z}{2}\right) e^{-jk_{x_p}(x_m - x_n)} e^{-jk_{y_q}(y_m - y_n)} \quad (4.37)$$

For $z_m = z_n$,

$$Z^{yx}_{mn} = \frac{Z_0 \Delta_x \Delta_y \Delta_z}{2k_0 ac} \sum_{p,q} \frac{k_{y_q} k_{x_p}}{k_{z_{pq}}} \left[\frac{\left(2 - 2e^{-jk_{z_{pq}}\Delta_z/2}\right)}{k_{z_{pq}}\Delta_z} + R_x \operatorname{sinc}\left(\frac{k_{z_{pq}}\Delta_z}{2}\right) e^{-jk_{z_{pq}} 2 z_m} \right]$$
$$\times \operatorname{sinc}\left(\frac{k_{x_p}\Delta_x}{2}\right) \operatorname{sinc}\left(\frac{k_{y_q}\Delta_y}{2}\right) e^{-jk_{x_p}(x_m - x_n)} e^{-jk_{y_q}(y_m - y_n)} \quad (4.38)$$

Submatrix Z_{yy}

$$
\begin{aligned}
Z_{yy} &= \int_{-\frac{a}{2}}^{\frac{a}{2}} \int_{-\frac{c}{2}}^{\frac{c}{2}} \int_{0}^{t} G_{yy}^{p}(\mathbf{r};\mathbf{r}')\ J_y(x',y',z')\ dx'\ dy'\ dz' \\
&= -\frac{k_0 Z_0}{2ac} \int_{-\frac{a}{2}}^{\frac{a}{2}} \int_{-\frac{c}{2}}^{\frac{c}{2}} \int_{0}^{t} \sum_{p,q} \left(1 + \frac{1}{k_0^2}\frac{\partial^2}{\partial y^2}\right) \left[\frac{e^{-jk_{z_{pq}}|z-z'|}}{k_{z_{pq}}} + R_y \frac{e^{-jk_{z_{pq}}(z+z')}}{k_{z_{pq}}}\right] \\
&\quad \times e^{-jk_{x_p}(x-x')} e^{-jk_{y_q}(y-y')}\ J_y(x',y',z')\ dx'\ dy'\ dz'
\end{aligned} \tag{4.39}
$$

For $z_m \neq z_n$,

$$
\begin{aligned}
Z_{mn}^{yy} = -\frac{Z_0 \Delta_x \Delta_y \Delta_z}{2k_0 ac} \sum_{p,q} \left(\frac{k_0^2 - k_{y_q}^2}{k_{z_{pq}}}\right) \left[e^{-jk_{z_{pq}}|z_m - z_n|} + R_y e^{-jk_{z_{pq}}(z_m+z_n)}\right] \\
\times \operatorname{sinc}\left(\frac{k_{x_p}\Delta_x}{2}\right) \operatorname{sinc}\left(\frac{k_{y_q}\Delta_y}{2}\right) \operatorname{sinc}\left(\frac{k_{z_{pq}}\Delta_z}{2}\right) e^{-jk_{x_p}(x_m-x_n)} e^{-jk_{y_q}(y_m-y_n)}
\end{aligned} \tag{4.40}
$$

For $z_m = z_n$,

$$
\begin{aligned}
Z_{mn}^{yy} = -\frac{Z_0 \Delta_x \Delta_y \Delta_z}{2k_0 ac} \sum_{p,q} \left(\frac{k_0^2 - k_{y_q}^2}{k_{z_{pq}}}\right) \\
\times \left[\frac{\left(2 - 2e^{-jk_{z_{pq}}\Delta_z/2}\right)}{k_{z_{pq}}\Delta_z} + R_y \operatorname{sinc}\left(\frac{k_{z_{pq}}\Delta_z}{2}\right) e^{-jk_{z_{pq}} 2z_m}\right] \\
\times \operatorname{sinc}\left(\frac{k_{x_p}\Delta_x}{2}\right) \operatorname{sinc}\left(\frac{k_{y_q}\Delta_y}{2}\right) e^{-jk_{x_p}(x_m-x_n)} e^{-jk_{y_q}(y_m-y_n)}
\end{aligned} \tag{4.41}
$$

Submatrix Z_{xz}

$$
\begin{aligned}
Z_{xz} &= \int_{-\frac{a}{2}}^{\frac{a}{2}} \int_{-\frac{c}{2}}^{\frac{c}{2}} \int_{0}^{t} G_{xz}^{p}(\mathbf{r};\mathbf{r}')\ J_x(x',y',z')\ dx'\ dy'\ dz' \\
&= -\frac{Z_0}{2k_0 ac} \int_{-\frac{a}{2}}^{\frac{a}{2}} \int_{-\frac{c}{2}}^{\frac{c}{2}} \int_{0}^{t} \sum_{p,q} \frac{\partial^2}{\partial x \partial z} \left[\frac{e^{-jk_{z_{pq}}|z-z'|}}{k_{z_{pq}}} + R_z \frac{e^{-jk_{z_{pq}}(z+z')}}{k_{z_{pq}}}\right] \\
&\quad \times e^{-jk_{x_p}(x-x')} e^{-jk_{y_q}(y-y')}\ J_x(x',y',z')\ dx'\ dy'\ dz'
\end{aligned} \tag{4.42}
$$

For $z_m \neq z_n$,

$$Z_{mn}^{xz} = \frac{Z_0 \Delta_x \Delta_y \Delta_z}{2k_0 ac} \sum_{p,q} k_{x_p} \left[\operatorname{sgn}(z_n - z_m) e^{-jk_{z_{pq}}|z_m - z_n|} + R_z e^{-jk_{z_{pq}}(z_m + z_n)} \right]$$
$$\times \operatorname{sinc}\left(\frac{k_{x_p}\Delta_x}{2}\right) \operatorname{sinc}\left(\frac{k_{y_q}\Delta_y}{2}\right) \operatorname{sinc}\left(\frac{k_{z_{pq}}\Delta_z}{2}\right) e^{-jk_{x_p}(x_m - x_n)} e^{-jk_{y_q}(y_m - y_n)} \tag{4.43}$$

For $z_m = z_n$,

$$Z_{mn}^{xz} = \frac{Z_0 \Delta_x \Delta_y \Delta_z}{2k_0 ac} \sum_{p,q} k_{x_p} \left[R_z \operatorname{sinc}\left(\frac{k_{z_{pq}}\Delta_z}{2}\right) e^{-jk_{z_{pq}} 2 z_m} \right]$$
$$\times \operatorname{sinc}\left(\frac{k_{x_p}\Delta_x}{2}\right) \operatorname{sinc}\left(\frac{k_{y_q}\Delta_y}{2}\right) e^{-jk_{x_p}(x_m - x_n)} e^{-jk_{y_q}(y_m - y_n)} \tag{4.44}$$

Submatrix Z_{zx}

$$Z_{zx} = \int_{-\frac{a}{2}}^{\frac{a}{2}} \int_{-\frac{c}{2}}^{\frac{c}{2}} \int_{0}^{t} G_{zx}^{p}(\mathbf{r};\mathbf{r}')\ J_z(x', y', z')\ dx'\ dy'\ dz'$$
$$= -\frac{Z_0}{2k_0 ac} \int_{-\frac{a}{2}}^{\frac{a}{2}} \int_{-\frac{c}{2}}^{\frac{c}{2}} \int_{0}^{t} \sum_{p,q} \frac{\partial^2}{\partial z \partial x} \left[\frac{e^{-jk_{z_{pq}}|z - z'|}}{k_{z_{pq}}} + R_x \frac{e^{-jk_{z_{pq}}(z + z')}}{k_{z_{pq}}} \right]$$
$$\times e^{-jk_{x_p}(x - x')} e^{-jk_{y_q}(y - y')}\ J_z(x', y', z')\ dx'\ dy'\ dz' \tag{4.45}$$

For $z_m \neq z_n$,

$$Z_{mn}^{zx} = \frac{Z_0 \Delta_x \Delta_y \Delta_z}{2k_0 ac} \sum_{p,q} k_{x_p} \left[\operatorname{sgn}(z_n - z_m) e^{-jk_{z_{pq}}|z_m - z_n|} + R_x e^{-jk_{z_{pq}}(z_m + z_n)} \right]$$
$$\times \operatorname{sinc}\left(\frac{k_{x_p}\Delta_x}{2}\right) \operatorname{sinc}\left(\frac{k_{y_q}\Delta_y}{2}\right) \operatorname{sinc}\left(\frac{k_{z_{pq}}\Delta_z}{2}\right) e^{-jk_{x_p}(x_m - x_n)} e^{-jk_{y_q}(y_m - y_n)} \tag{4.46}$$

For $z_m = z_n$,

$$Z_{mn}^{zx} = \frac{Z_0 \Delta_x \Delta_y \Delta_z}{2k_0 ac} \sum_{p,q} k_{x_p} \left[R_x \operatorname{sinc}\left(\frac{k_{z_{pq}}\Delta_z}{2}\right) e^{-jk_{z_{pq}} 2 z_m} \right]$$
$$\times \operatorname{sinc}\left(\frac{k_{x_p}\Delta_x}{2}\right) \operatorname{sinc}\left(\frac{k_{y_q}\Delta_y}{2}\right) e^{-jk_{x_p}(x_m - x_n)} e^{-jk_{y_q}(y_m - y_n)} \tag{4.47}$$

Submatrix Z_{yz}

$$\begin{aligned}
Z_{yz} &= \int_{-\frac{a}{2}}^{\frac{a}{2}} \int_{-\frac{c}{2}}^{\frac{c}{2}} \int_{0}^{t} G^{p}_{yz}(\mathbf{r};\mathbf{r'})\ J_y(x',y',z')\ dx'\ dy'\ dz' \\
&= -\frac{Z_0}{2k_0ac} \int_{-\frac{a}{2}}^{\frac{a}{2}} \int_{-\frac{c}{2}}^{\frac{c}{2}} \int_{0}^{t} \sum_{p,q} \frac{\partial^2}{\partial y \partial z}\left[\frac{e^{-jk_{z_{pq}}|z-z'|}}{k_{z_{pq}}} + R_z \frac{e^{-jk_{z_{pq}}(z+z')}}{k_{z_{pq}}}\right] \\
&\quad \times e^{-jk_{x_p}(x-x')} e^{-jk_{y_q}(y-y')}\ J_x(x',y',z')\ dx'\ dy'\ dz'
\end{aligned} \tag{4.48}$$

For $z_m \neq z_n$,

$$\begin{aligned}
Z^{yz}_{mn} = \frac{Z_0 \Delta_x \Delta_y \Delta_z}{2k_0ac} \sum_{p,q} k_{y_q} &\left[\text{sgn}\,(z_n - z_m) e^{-jk_{z_{pq}}|z_m - z_n|} + R_z e^{-jk_{z_{pq}}(z_m+z_n)}\right] \\
\times \text{sinc}\left(\frac{k_{x_p}\Delta_x}{2}\right) \text{sinc}\left(\frac{k_{y_q}\Delta_y}{2}\right) &\text{sinc}\left(\frac{k_{z_{pq}}\Delta_z}{2}\right) e^{-jk_{x_p}(x_m-x_n)} e^{-jk_{y_q}(y_m-y_n)}
\end{aligned} \tag{4.49}$$

For $z_m = z_n$,

$$\begin{aligned}
Z^{yz}_{mn} = \frac{Z_0 \Delta_x \Delta_y \Delta_z}{2k_0ac} \sum_{p,q} k_{y_q} &\left[R_z\, \text{sinc}\left(\frac{k_{z_{pq}}\Delta_z}{2}\right) e^{-jk_{z_{pq}} 2z_m}\right] \\
&\times \text{sinc}\left(\frac{k_{x_p}\Delta_x}{2}\right) \text{sinc}\left(\frac{k_{y_q}\Delta_y}{2}\right) e^{-jk_{x_p}(x_m-x_n)} e^{-jk_{y_q}(y_m-y_n)}
\end{aligned} \tag{4.50}$$

Submatrix Z_{zy}

$$\begin{aligned}
Z_{zy} &= \int_{-\frac{a}{2}}^{\frac{a}{2}} \int_{-\frac{c}{2}}^{\frac{c}{2}} \int_{0}^{t} G^{p}_{zy}(\mathbf{r};\mathbf{r'})\ J_z(x',y',z')\ dx'\ dy'\ dz' \\
&= -\frac{Z_0}{2k_0ac} \int_{-\frac{a}{2}}^{\frac{a}{2}} \int_{-\frac{c}{2}}^{\frac{c}{2}} \int_{0}^{t} \sum_{p,q} \frac{\partial^2}{\partial z \partial y}\left[\frac{e^{-jk_{z_{pq}}|z-z'|}}{k_{z_{pq}}} + R_y \frac{e^{-jk_{z_{pq}}(z+z')}}{k_{z_{pq}}}\right] \\
&\quad \times e^{-jk_{x_p}(x-x')} e^{-jk_{y_q}(y-y')}\ J_z(x',y',z')\ dx'\ dy'\ dz'
\end{aligned} \tag{4.51}$$

For $z_m \neq z_n$,

$$\begin{aligned}
Z^{zy}_{mn} = \frac{Z_0 \Delta_x \Delta_y \Delta_z}{2k_0ac} \sum_{p,q} k_{y_q} &\left[\text{sgn}\,(z_n - z_m) e^{-jk_{z_{pq}}|z_m - z_n|} + R_y e^{-jk_{z_{pq}}(z_m+z_n)}\right] \\
\times \text{sinc}\left(\frac{k_{x_p}\Delta_x}{2}\right) \text{sinc}\left(\frac{k_{y_q}\Delta_y}{2}\right) &\text{sinc}\left(\frac{k_{z_{pq}}\Delta_z}{2}\right) e^{-jk_{x_p}(x_m-x_n)} e^{-jk_{y_q}(y_m-y_n)}
\end{aligned} \tag{4.52}$$

For $z_m = z_n$,

$$Z_{mn}^{zy} = \frac{Z_0 \Delta_x \Delta_y \Delta_z}{2k_0 ac} \sum_{p,q} k_{y_q} \left[R_y \operatorname{sinc}\left(\frac{k_{z_{pq}} \Delta_z}{2}\right) e^{-jk_{z_{pq}} 2z_m} \right] \times \operatorname{sinc}\left(\frac{k_{x_p} \Delta_x}{2}\right) \operatorname{sinc}\left(\frac{k_{y_q} \Delta_y}{2}\right) e^{-jk_{x_p}(x_m - x_n)} e^{-jk_{y_q}(y_m - y_n)} \quad (4.53)$$

Submatrix Z_{zz}

$$\begin{aligned} Z_{zz} &= \int_{-\frac{a}{2}}^{\frac{a}{2}} \int_{-\frac{c}{2}}^{\frac{c}{2}} \int_{0}^{t} G_{zz}^{p}(\mathbf{r};\mathbf{r}')\ J_z(x', y', z')\ dx'\ dy'\ dz' \\ &= -\frac{Z_0}{2k_0 ac} \int_{-\frac{a}{2}}^{\frac{a}{2}} \int_{-\frac{c}{2}}^{\frac{c}{2}} \int_{0}^{t} \sum_{p,q} \left(k_0^2 + \frac{\partial^2}{\partial z^2}\right) \left[\frac{e^{-jk_{z_{pq}}|z-z'|}}{k_{z_{pq}}} + R_z \frac{e^{-jk_{z_{pq}}(z+z')}}{k_{z_{pq}}}\right] \\ &\quad \times e^{-jk_{x_p}(x-x')} e^{-jk_{y_q}(y-y')}\ J_z(x', y', z')\ dx'\ dy'\ dz' \end{aligned} \quad (4.54)$$

For $z_m \neq z_n$,

$$Z_{mn}^{zz} = -\frac{Z_0 \Delta_x \Delta_y}{2k_0 ac} \sum_{p,q} \operatorname{sinc}\left(\frac{k_{x_p} \Delta_x}{2}\right) \operatorname{sinc}\left(\frac{k_{y_q} \Delta_y}{2}\right) e^{-jk_{x_p}(x_m - x_n)} e^{-jk_{y_q}(y_m - y_n)}$$
$$\times \left[\int_{z_n - \frac{\Delta_z}{2}}^{z_n + \frac{\Delta_z}{2}} \left(k_0^2 - \frac{\partial^2}{\partial z \partial z'}\right) \frac{e^{-jk_{z_{pq}}|z_m - z'|}}{k_{z_{pq}}}\ dz' + \int_{z_n - \frac{\Delta_z}{2}}^{z_n + \frac{\Delta_z}{2}} \left(k_0^2 + \frac{\partial^2}{\partial z^2}\right) R_z \frac{e^{-jk_{z_{pq}}(z_m + z')}}{k_{z_{pq}}}\ dz' \right] \quad (4.55)$$

Carrying out the integrations in (4.55) leads to the following off-plane elements of the Z_{mn}^{zz} submatrix

$$Z_{mn}^{zz} = -\frac{Z_0 \Delta_x \Delta_y \Delta_z}{2k_0 ac} \sum_{p,q} \left(k_0^2 - k_{z_{pq}}^2\right) \left[\frac{e^{-jk_{z_{pq}}|z_m - z_n|}}{k_{z_{pq}}} + R_z \frac{e^{-jk_{z_{pq}}(z_m + z_n)}}{k_{z_{pq}}}\right] \times \operatorname{sinc}\left(\frac{k_{x_p} \Delta_x}{2}\right) \operatorname{sinc}\left(\frac{k_{y_q} \Delta_y}{2}\right) \operatorname{sinc}\left(\frac{k_{z_{pq}} \Delta_z}{2}\right) e^{-jk_{x_p}(x_m - x_n)} e^{-jk_{y_q}(y_m - y_n)}. \quad (4.56)$$

For $z_m \neq z_n$, particular care must be taken to evaluate (4.54). If in the computation the on-plane matrix elements for the Z_{zz} submatrix the second derivative in (4.54) is not evaluated carefully, erroneous results will be produced [76]. From distribution theory, carrying out the inner derivative of the first integral in (4.55) yields

$$\frac{\partial}{\partial z'} e^{-jk_{z_{pq}}|z-z'|} = jk_{z_{pq}} \operatorname{sgn}(z - z') e^{-jk_{z_{pq}}|z-z'|}. \quad (4.57)$$

where

$$\operatorname{sgn}(z-z') = \begin{cases} +1, & z > z'; \\ -1, & z < z'. \end{cases} \tag{4.58}$$

Applying the outer derivative on the result obtained in (4.57) gives

$$\frac{\partial}{\partial z}\left\{\operatorname{sgn}(z-z')e^{-jk_{z_{pq}}|z-z'|}\right\} = \left[-jk_{z_{pq}} + 2\delta(z-z')\right] e^{-jk_{z_{pq}}|z-z'|}. \tag{4.59}$$

Consequently,

$$\begin{aligned}\frac{\partial^2}{\partial z \partial z'} e^{-jk_{z_{pq}}|z-z'|} &= jk_{z_{pq}}\left[-jk_{z_{pq}} + 2\delta(z-z')\right] e^{-jk_{z_{pq}}|z-z'|} \\ &= \left[k_{z_{pq}}^2 + 2jk_{z_{pq}}\delta(z-z')\right] e^{-jk_{z_{pq}}|z-z'|}. \end{aligned}\tag{4.60}$$

Inserting the above into (4.54) and evaluating the first integral produces

$$\begin{aligned} Z_{mn}^{zz} = &-\frac{Z_0\Delta_x\Delta_y}{2k_0ac}\sum_{p,q}\operatorname{sinc}\left(\frac{k_{x_p}\Delta_x}{2}\right)\operatorname{sinc}\left(\frac{k_{y_q}\Delta_y}{2}\right)e^{-jk_{x_p}(x_m-x_n)}e^{-jk_{y_q}(y_m-y_n)} \\ &\times\left[R_z\left(k_0^2-k_{z_{pq}}^2\right)\frac{e^{-j2k_{z_{pq}}z_m}}{k_{z_{pq}}}\Delta_z\operatorname{sinc}\left(\frac{k_{z_{pq}}\Delta_z}{2}\right) + k_0^2\int_{z_n-\frac{\Delta_z}{2}}^{z_n+\frac{\Delta_z}{2}}\frac{e^{-jk_{z_{pq}}|z-z'|}}{k_{z_{pq}}}\,dz'\right. \\ &\left. - \int_{z_n-\frac{\Delta_z}{2}}^{z_n+\frac{\Delta_z}{2}}\left[k_{z_{pq}}^2 + 2jk_{z_{pq}}\delta(z-z')\right]\frac{e^{-jk_{z_{pq}}|z-z'|}}{k_{z_{pq}}}\,dz'\right]. \end{aligned}\tag{4.61}$$

Rewriting the above as

$$\begin{aligned} Z_{mn}^{zz} = &-\frac{Z_0\Delta_x\Delta_y}{2k_0ac}\sum_{p,q}\operatorname{sinc}\left(\frac{k_{x_p}\Delta_x}{2}\right)\operatorname{sinc}\left(\frac{k_{y_q}\Delta_y}{2}\right)e^{-jk_{x_p}(x_m-x_n)}e^{-jk_{y_q}(y_m-y_n)} \\ &\times\left[R_z\left(k_0^2-k_{z_{pq}}^2\right)\frac{e^{-j2k_{z_{pq}}z_m}}{k_{z_{pq}}}\Delta_z\operatorname{sinc}\left(\frac{k_{z_{pq}}\Delta_z}{2}\right) + \left(k_0^2-k_{z_{pq}}^2\right)\frac{\left(2-2e^{-jk_{z_{pq}}\Delta_z/2}\right)}{k_{z_{pq}}^2}\right. \\ &\left. - \int_{z_n-\frac{\Delta_z}{2}}^{z_n+\frac{\Delta_z}{2}} 2jk_{z_{pq}}\delta(z-z')\frac{e^{-jk_{z_{pq}}|z-z'|}}{k_{z_{pq}}}\,dz'\right] \end{aligned}\tag{4.62}$$

and carrying out the remaining integration yields the on-plane matrix elements for the Z_{zz} submatrix

$$\begin{aligned} Z_{mn}^{zz} = &-\frac{Z_0\Delta_x\Delta_y}{2k_0ac}\sum_{p,q}\operatorname{sinc}\left(\frac{k_{x_p}\Delta_x}{2}\right)\operatorname{sinc}\left(\frac{k_{y_q}\Delta_y}{2}\right)e^{-jk_{x_p}(x_m-x_n)}e^{-jk_{y_q}(y_m-y_n)} \\ &\times\left[R_z\left(k_0^2-k_{z_{pq}}^2\right)\frac{e^{-j2k_{z_{pq}}z_m}}{k_{z_{pq}}}\Delta_z\operatorname{sinc}\left(\frac{k_{z_{pq}}\Delta_z}{2}\right) + \left(k_0^2-k_{z_{pq}}^2\right)\frac{\left(2-2e^{-jk_{z_{pq}}\Delta_z/2}\right)}{k_{z_{pq}}^2} - 2j\right] \end{aligned}\tag{4.63}$$

A similar expression to (4.63) can be found by using dyadic analysis [45] and performing some algebraic manipulation.

4.3.2 Excitation Matrices

The excitation matrix can be found by testing the incidence excitation using point collocation. For plane wave excitation,

$$V_m^x = -\left(e_h\hat{\mathbf{x}}\cdot\hat{\mathbf{h}}_i + e_v\hat{\mathbf{x}}\cdot\hat{\mathbf{v}}_i\right)e^{-j\mathbf{k}_i\cdot\mathbf{r}_m} - \left(R_h e_h\hat{\mathbf{x}}\cdot\hat{\mathbf{h}}_s + R_v e_v\hat{\mathbf{x}}\cdot\hat{\mathbf{v}}_s\right)e^{-j\mathbf{k}_s\cdot\mathbf{r}_m} \tag{4.64a}$$

$$V_m^y = -\left(e_h\hat{\mathbf{y}}\cdot\hat{\mathbf{h}}_i + e_v\hat{\mathbf{y}}\cdot\hat{\mathbf{v}}_i\right)e^{-j\mathbf{k}_i\cdot\mathbf{r}_m} - \left(R_h e_h\hat{\mathbf{y}}\cdot\hat{\mathbf{h}}_s + R_v e_v\hat{\mathbf{y}}\cdot\hat{\mathbf{v}}_s\right)e^{-j\mathbf{k}_s\cdot\mathbf{r}_m} \tag{4.64b}$$

$$V_m^z = -e_v\hat{\mathbf{z}}\cdot\hat{\mathbf{v}}_i e^{-j\mathbf{k}_i\cdot\mathbf{r}_m} - R_v e_v\hat{\mathbf{z}}\cdot\hat{\mathbf{v}}_s e^{-j\mathbf{k}_s\cdot\mathbf{r}_m} \tag{4.64c}$$

4.4 Results

A number of simple checks can be performed that illustrate the validity of the formulation and the correctness of the implementation. A grounded dielectric layer can be modeled using the method of moments solution by setting the filling fractions b/a and d/c to one (1) and setting the horizontal and vertical reflection coefficients for the ground plane to -1 and $+1$, respectively, independent of the incidence angle. The moment method solution for the plane wave scattering from the grounded periodic dielectric structure yields identical results with the analytical solution obtained for the plane wave scattering of a grounded layer. The exact horizontal and vertical reflection coefficients at the surface of the grounded dielectric layer of thickness t and relative permittivity ε_r are

$$R_h = \frac{k_{z_0}\sin k_{z_1}t + jk_{z_1}\cos k_{z_1}t}{k_{z_0}\sin k_{z_1}t - jk_{z_1}\cos k_{z_1}t}\; e^{j2k_{z_0}t} \tag{4.65a}$$

$$R_v = \frac{\varepsilon_r k_{z_0}\cos k_{z_1}t - jk_{z_1}\sin k_{z_1}t}{\varepsilon_r k_{z_0}\cos k_{z_1}t + jk_{z_1}\sin k_{z_1}t}\; e^{j2k_{z_0}t} \tag{4.65b}$$

where $k_{z_0}{=}k_0\cos\theta_0$ and $k_{z_1}{=}k_0\sqrt{\varepsilon_r - \sin^2\theta_0}$. Figure 4.5 shows the calculated phase angle of the reflection coefficient as a function of incidence angle θ_0 using the method of moments solution for 81 subsectional unknowns ($N_x{=}N_y{=}N_z{=}3$ for each of the three polarizations), arbitrary plane of incidence $\phi_0{=}45°$, unit cell size $a{=}0.1\lambda_0$, relative permittivity $\varepsilon_r{=}2.56$, and dielectric thickness $t{=}0.15\lambda_d$ where $\lambda_d{=}\lambda_0/\sqrt{\varepsilon_r}$. The solutions were determined using at most 3721 Floquet modes ($N_p{=}N_q{=}61$). Also included in the figure is the exact analytical solution for the two polarizations. The reflection coefficients are evaluated at a height $z_0{=}20t$ above the ground plane and theoretically should have a magnitude of one (1) for

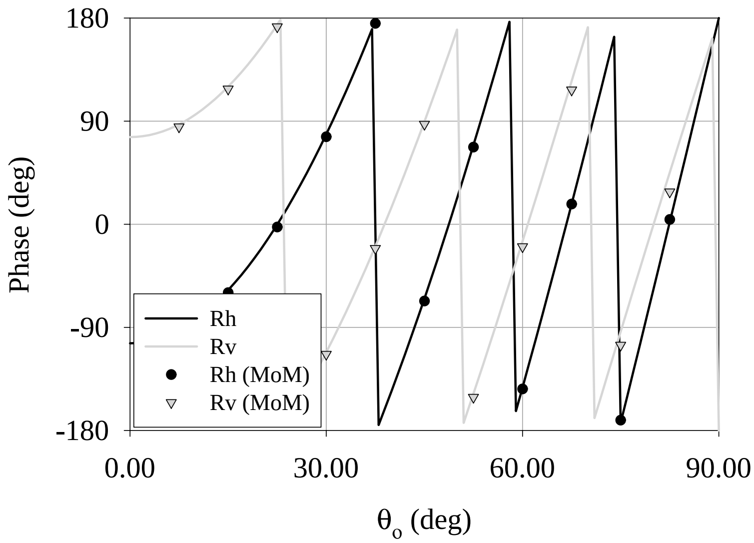

Figure 4.5: Phase angle for R_h and R_v at z_0=20t for a grounded dielectric layer of relative permittivity ε_r=2.56 and dielectric thickness t=0.15λ_d as a function of θ_0 for N_x=N_y=N_z=3, N_p=N_q=61, and a=0.1λ_0

the grounded case. For the data shown in Figure 4.5 where the dielectric is lossless, the magnitudes of R_h and R_v are 1.00±0.08. The accuracy of the phase values obtained for R_v degrades slightly at grazing angles near θ_0=90°. As the angle of incidence increases, the z-variation in the dielectric cannot be modeled accurately using only 3 unknowns. If the z-variation is modeled using five (5) or seven (7) unknowns, the error in the magnitude decreases to less than 2% for all angles of incidence.

Additionally, for the grounded dielectric layer, the value of the reflection coefficients should be independent of both the plane of incidence and the unit cell size. Identical phases for the reflection coefficients are calculated for a number of different values of ϕ_0. However, when the unit cell size is increased, additional unknowns in x- and y-directions must be used to model the material blocks in order to obtain comparable accuracies to cases where the unit cell size is smaller. It is interesting to note that for the grounded dielectric layer, the scattered field produced by the equivalent currents for the two polarizations is exactly 180° out-of-phase. Although the magnitudes and phases of the currents induced by the two polarizations are quite different, the scattered electric field produced by them is shifted in phase by π (R_h=$-R_v$ for the ground plane).

As the filling fraction varies from one (1) to zero (0) and unit cell spacings less than a wavelength, the phase angle of the horizontal and vertical reflection coefficients determined using the method of moments solution should vary between the exact value obtained from a grounded dielectric layer and the exact value obtained from a ground plane alone. This is shown in particular in Table 4.1 for a grounded dielectric layer of relative permittivity ε_r=2.56, dielectric thickness t=0.15λ_d, ϕ_0=45°, θ_0=45°, and a=0.25λ_0 at z_0=20t using 192 subsectional unknowns (N_x=N_y=N_z=4 for each of the three polarizations) and N_p=N_q=61. The exact values for b/a=1 and b/a=0 shown in bold in the table are calculated using the analytical solution of (4.65).

Table 4.1: Phase angle for R_h and R_v at z_0=20t for a grounded dielectric layer of relative permittivity ε_r=2.56 and dielectric thickness t=0.15λ_d as a function of filling fraction b/a for N_x=N_y=N_z=4, N_p=N_q=61, ϕ_0=45°, θ_0=45°, and a=0.25λ_0

b/a	$\angle R_h$	$\angle R_v$
1.00	**-64.99°**	**89.52°**
0.90	-63.42°	95.15°
0.75	-59.90°	103.77°
0.50	-56.56°	115.48°
0.25	-55.01°	123.33°
0.00	**-54.59°**	**125.41°**

The grounded dielectric slab can also be modeled as a grounded layered medium as shown in Figure 4.4. This is accomplished by replacing the homogeneous layer of thickness t and relative dielectric constant ε_r with two layers each of thickness $t/2$. Region 2 is filled with a homogeneous layer of permittivity ε_r, region 1 is replaced with equivalent polarization currents as before, and the ground is located at z=d_2. The significant difference in computation for the layered medium case is the calculation of R_h and R_v. Unlike the previous example, where the dielectric is replaced by equivalent polarization currents and the scattering occurs from the ground plane, the reflection coefficients for equivalent currents radiating over a layered dielectric are, in general, functions of the complex angle, γ_{pq}=arctan$(k_\rho/k_{z_{pq}})$ where k_ρ is the phase constant in the transverse plane equal to $\sqrt{k_{x_p}^2 + k_{y_q}^2}$. Consequently, R_h and R_v must be calculated for every combination of Floquet indices $\{p, q\}$.

The phase angle of the reflection coefficient for the grounded two-layer medium is determined in Figure 4.6 for the same parameters as Figure 4.5. The noticeable increase in the accuracy of the phase obtained in this solution is attributable to the increased accuracy

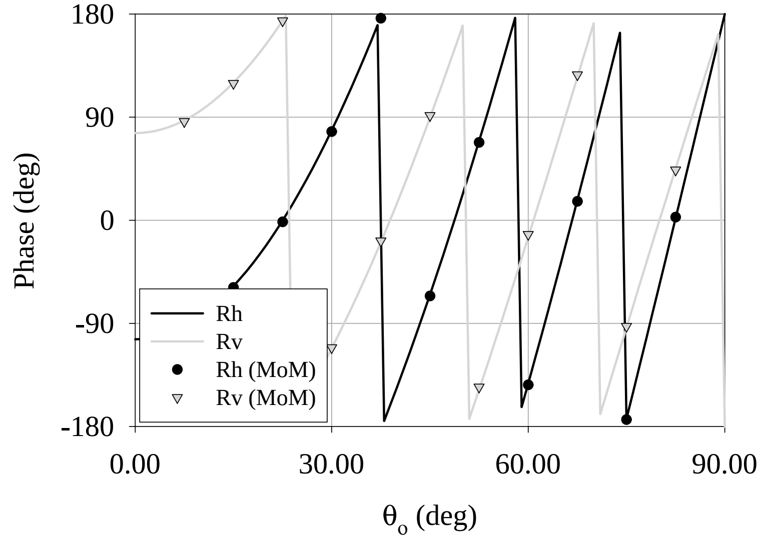

Figure 4.6: Phase angle for R_h and R_v at z_0=20t for a grounded dielectric layer of relative permittivity ε_r=2.56 and dielectric thickness t=0.15λ_d as a function of θ_0 for N_x=N_y=N_z=3, N_p=N_q=61, and a=0.1λ_0 calculated using the multilayered solution

in modeling the dielectric region. The same number of unknowns are used to model the dielectric layer of thickness $t/2$ as were used to model the dielectric layer of thickness t in Figure 4.5. For all angles of incidence, the magnitudes of R_h and R_v are 1.00±0.02. If the polarization currents in the previous example are arbitrarily set to zero ($\mathbf{J}$=$\mathbf{0}$) or if the relative permittivity is allowed to approach one ($\varepsilon_r \rightarrow 1$) and the solution for the total scattered field is recomputed, the reflection coefficients should be equivalent to those of a grounded layer of thickness $t/2$. This is found to be true in particular for θ_0=45° where the phase of R_h and R_v for both the exact and calculated solution are $-55.72°$ and $+110.01°$, respectively.

4.5 Series Acceleration Techniques for the Periodic, Free-Space Green's Function

Unfortunately, the series listed throughout Section 4.3 have serious but well-documented convergence issues when z is very close or equal to z' that must be addressed before an accurate and rapid solution can be found. Summation acceleration techniques convert a slowly converging series to a rapidly converging one by allowing the series to be transformed into a second series that converges to the same limit but does so in a rapid fashion. A number of series acceleration techniques have been applied to the periodic, free-space Green's function (PFSGF) to accelerate the notorious on-plane convergence problem [42]. Some of the more useful ones are listed in the Table 4.2. The transformations listed in the first part of the table are ones implemented in this work; those listed in the second part of the table are ones that are implemented elsewhere. Each acceleration technique has advantages and disadvantages and must be applied carefully to the series of interest in order to obtain the desired results of improved accuracy and increased speed.

Table 4.2: Summary of series transformations

Transformations
Poisson transformation
Shanks' transformation
Wynn's ε-algorithm
Kummer transformation
Ewald transformation
ρ-algorithm
θ-algorithm
Chebyshev-Toeplitz (CT) algorithm
Levin's t-transform

4.5.1 Acceleration Techniques Applied in This Work

Poisson Transformation [70, 51, 99]

The Poisson summation converts a slowly converging series to a rapidly converging one by allowing the series to be summed in the Fourier transform domain. The reciprocal spreading property of the Fourier transform says that narrower support in one domain would necessarily require wider support in the other domain. The transformation can be written as

$$\sum_{n=-\infty}^{\infty} f(t+nT) = \frac{1}{T}\sum_{n=-\infty}^{\infty} e^{-jn\omega_0 t}F(n\omega_0) \quad \omega_0 = \frac{2\pi}{T}. \tag{4.66}$$

The Poisson transformation transforms the PFSGF into its spectral form which makes it amenable for use in spectral domain analysis (SDA) of layered media or periodically loaded dielectrics.

To obtain a summation for a two-dimensional array of point current sources, the Poisson summation formula is first applied to the y coordinate of the three-dimensional Green's function

$$\begin{aligned}\sum_{p,q} f(p,q) &= \sum_{p,q} \left[(x-pa)^2+(y-qc)^2+z^2\right]^{1/2} e^{-jk\left[(x-pa)^2+(y-qc)^2+z^2\right]^{1/2}} \\ &= \sum_{p,q} \frac{1}{2\pi c} K_0 \left(\left[\left(\frac{2\pi q}{c}\right)^2 - k_0^2 \right]^{1/2} \left[(x-pa)^2+z^2\right]^{1/2} \right) e^{-j\frac{2\pi q}{c}y}. \quad (4.67)\end{aligned}$$

An expression equivalent to a two-dimensional Green's function can be recovered by manipulation of the above expression giving

$$\sum_{p,q} f(p,q) = \sum_{p,q} \frac{1}{4cj} H_0^{(2)} \left(\left[k^2 - \left(\frac{2\pi q}{c}\right) \right]^{1/2} \left[(x-pa)^2+z^2\right]^{1/2} \right) e^{-j\frac{2\pi q}{c}y}. \quad (4.68)$$

Applying the Poisson summation formula again, but this time to the x coordinate gives the following Poisson summation formula for the Green's function $f(p,q)$:

$$\sum_{p,q} f(p,q) = \frac{1}{2ac} \sum_{p,q} \frac{e^{-|z|\left[\left(\frac{2\pi p}{a}\right)^2+\left(\frac{2\pi q}{c}\right)^2-k^2\right]^{1/2}}}{\sqrt{\left(\frac{2\pi p}{a}\right)+\left(\frac{2\pi q}{c}\right)-k^2}} e^{-j\frac{2\pi p}{a}x} e^{-j\frac{2\pi q}{c}y}. \quad (4.69)$$

Equation (4.70) becomes upon substitution of a phase shift $\hat{\mathbf{k}} = k_{x_0}\hat{\mathbf{x}} + k_{y_0}\hat{\mathbf{y}}$

$$\sum_{p,q} f(p,q) = \frac{1}{2jac} \sum_{p,q} \frac{e^{-jk_{z_{pq}}|z|}}{\sqrt{k^2-\left(\frac{2\pi p}{a}\right)^2+\left(\frac{2\pi q}{c}\right)^2}} e^{-jk_{x_p}x} e^{-jk_{y_q}y} \quad (4.70)$$

Shanks' Transform [90, 99, 101, 43]

For alternating series, the partial sums of a sequence can be treated as a mathematical transient of the sum S of the series. Assume the n^{th} partial sum is

$$S_n = S + \sum_{k=0}^{n} \alpha_k q_k^n$$

for $|q_k| < 1$. Hence, $S_n \to S$ as $n \to \infty$. The sum S can be found by expressing S_n in terms of S, α, and q for indices $(n-1)$, n, and $(n+1)$,

$$\begin{aligned} S_n &= S + \alpha q^n \\ S_{n-1} &= S + \alpha q^{(n-1)} \\ S_{n+1} &= S + \alpha q^{(n+1)} \end{aligned}$$

and solving for the sum S. The sum is found to be equal to

$$S = \frac{S_{n+1}S_{n-1} - S_n^2}{S_{n+1} + S_{n-1} - 2S_n}. \tag{4.71}$$

Two simple examples will illustrate that the sum S of simple alternating series can be determined without summing an inordinate number of terms.

Example 1. Geometric series The geometric series

$$\sum_{k=0}^{\infty} q^k = 1 + q + q^2 + \cdots \tag{4.72}$$

converges to sum $1/(q-1)$ if $|q| < 1$ and $\alpha_k = 1^k$. Setting $S_0 = 1$, $S_1 = 1 + q$, and $S_2 = 1 + q + q^2$, and solving for S using (4.71) yields

$$\begin{aligned} &= \frac{(1+q+q^2) - (1+q)^2}{1+q+q^2+1-2(1+q)} = \frac{-q}{-q+q^2} \\ &= \frac{1}{q-1}. \end{aligned}$$

Example 2. Alternating geometric series

$$\sum_{k=0}^{\infty} (-1)^k q^k = 1 - q + q^2 - \cdots \tag{4.73}$$

converges to sum $1/(q+1)$ if $|q| < 1$ and $\alpha_k = (-1)^k$. Setting $S_0 = 1$, $S_1 = 1 - q$, and $S_2 = 1 - q + q^2$, and solving for S using (4.71) yields

$$\begin{aligned} S &= \frac{(1-q+q^2) - (1-q)^2}{1-q+q^2+1-2(1-q)} = \frac{q}{q^2+q} \\ &= \frac{1}{q+1}. \end{aligned}$$

Another effective transform for alternating series is the *Shanks' transform*. The algorithm for the Shanks' transform of a sequence of partial sums is

$$S = e_1(S_{n+1}) + \frac{1}{e_1(S_{n+1}) - e_1(S_n)}, \tag{4.74}$$

where

$$e_0(S_n) = S_n, \quad e_1(S_n) = \frac{1}{e_0(S_{n+1}) - e_0(S_n)}.$$

Higher order Shanks transforms can be carried out using Wynn's ε-algorithm [124, 15, 101]:

$$e_{s+1}(S_n) = e_{s-1}(S_{n+1}) + \frac{1}{e_s(S_{n+1}) - e_s(S_n)}, \quad s = 1, 2, \cdots \tag{4.75}$$

where

$$e_0(S_n) = S_n, \quad e_1(S_n) = \frac{1}{e_0(S_{n+1}) - e_0(S_n)}$$

Only the even order terms $e_{2r}(S_n)$ are Shanks' transforms of order r approximating S. The process is applied continually until a desired criterion is reached. For the series used in this work, the following convergence criterion was used. The convergence factor ε_c is defined by

$$\left| \frac{e_k(S_{n-k}) - e_{k-2}(S_{n-k+2})}{e_k(S_{n-k})} \right| \le \varepsilon_c. \tag{4.76}$$

In order to assure that the summation has adequately converged, the algorithm is continued until three successive values of $e_{k+2}(S_{n-k-2})$, $e_{k+4}(S_{n-k-4})$, and $e_{k+6}(S_{n-k-6})$ satisfy (4.76).

Table 4.3: Convergence of higher order Shanks' transforms of Leibnitz series as a function of order and number, π=3.14159265358979 ...

n	$e_0 = S_n$	e_2	e_4	e_6	e_8	e_{10}
0	4.0000000	3.1666667	3.1423423	3.1416149	3.1415933	3.1415926(7)
1	2.6666667	3.1333333	3.1413919	3.1415873	3.1415925	
2	3.4666667	3.1452381	3.1416667	3.1415943	3.1415927	
3	2.8952381	3.1396825	3.1415634	3.1415921		
4	3.3396825	3.1427128	3.1416065	3.1415967		
5	2.9760462	3.1408813	3.1415854			
6	3.2837385	3.1420718	3.1415929			
7	3.0170718	3.1412548				
8	3.2523659	3.1415927				
9	3.0418396					
10	3.2323158					

Example. Leibnitz series

$$\pi = 4 \sum_{n=0}^{\infty} \frac{(-1)^n}{2n+1} = 3.14159265358979\ldots \tag{4.77}$$

Table 4.3 shows the results of applying various order Shanks' transforms to Leibnitz series. One notes that using a fourth-order Shanks' transform is accurate to six significant digits but only requires the computation of 10 terms in the series and 40 floating point operations (FLOPs). A direct summation of the series would require calculating and summing 25×10^6 terms to achieve a similar accuracy of five significant digits.

The Shanks' transform is simple and efficient – the first N terms of the series are the only terms computed. The higher order transforms are applied to the N terms using the simple algorithm listed above. The total number of floating point operations required to compute a (N, k) order Shanks' transform can be calculated to be

$$\begin{aligned} \text{FLOPs} &= \sum_{n=0}^{k}(N-n) = N(k+1) - \sum_{n=1}^{k} n \\ &= \left(N - \frac{k}{2}\right)(k+1). \end{aligned} \tag{4.78}$$

In Table 4.4, the error and relative computation time for various combination order Shanks' transformations on (4.77) are shown. The baseline computation time is determined by

Table 4.4: Error for various (N, k) Shanks' transforms for Leibnitz series

N	k	$e_k(S_N)$	Error	FLOPs
10	0	3.23231580	9.07×10^{-2}	
50	0	3.16119861	1.96×10^{-2}	
100	0	3.15149340	9.90×10^{-3}	
10	2	3.14173610	1.43×10^{-4}	27
10	4	3.14159331	6.58×10^{-7}	40
10	6	3.14159266	5.11×10^{-9}	49
10	8	3.14159265	5.43×10^{-11}	54
50	2	3.14159443	1.78×10^{-6}	147
50	4	3.14159265	5.97×10^{-10}	240
100	2	3.14159443	2.36×10^{-7}	297

assuming that 100 terms of the sum are computed. The relative computational time for the various order transforms are computed by applying the transforms to different numbers of terms in the series. Because the determination of the higher order transforms are computationally inexpensive, it is efficient to set k=N-2. When k=N-2, the error can be minimized without increasing the computational cost significantly. The total number of

FLOPs required for a (N,N-2) order Shanks' transform is

$$\text{FLOPs} = \sum_{n=0}^{N-2}(N-n) = \left(\frac{N}{2}+1\right)(N-1) \simeq \frac{N^2}{2} \tag{4.79}$$

For a double-sided series, the number of FLOPs required is simply twice the number for a single-sided series and can be approximated by N^2. For example, a (10,4) Shanks' transform of (4.77) results in an error of 6.58×10^{-7} and requires 80 FLOPs. However, simply carrying out two more transforms (requiring 28 more FLOPs) yields an error of only 5.43×10^{-11}. Also, note that a (10,8) transform yields a significantly smaller error than a (100,2) transform and does so at a significantly reduced computational cost. For more realistic series where calculating the individual terms is expensive, the determination of the minimum number of terms N and the subsequent order k=N-2 of the transform to accurately compute the sum is imperative.

(30,28) Shanks' transform of inner sum of Z_{mm}^{yy} impedance matrix element

An example of the significant increase in accuracy and decrease in computational cost that implementing a (N,N-2) Shanks' transform produces is easily seen by computing the inner sum for the (m,n) element of the Z^{yy} submatrix in (4.41) and implementing a (30,28) Shanks' transform. In a double summation, such as those found in this work, the Shanks' transform is applied to the sequence of partial sums over the inner indices for a specific outer index. The transform is then applied to the outer sequence. For convenience, the Z^{yy} submatrix is repeated below

$$\begin{aligned} Z_{mn}^{yy} = -\frac{k_0 Z_0 \Delta_x \Delta_y}{2ac} \sum_p \sum_q \left(1-\frac{k_{y_q}^2}{k_0^2}\right) \\ \times \left[\frac{2j - 2je^{-jk_{z_{pq}}\Delta_z/2}}{k_{z_{pq}}^2} + R_y(\gamma_{pq})\Delta_z \operatorname{sinc}\left(\frac{k_{z_{pq}}\Delta_z}{2}\right)\frac{e^{-j2k_{z_{pq}}z_m}}{k_{z_{pq}}}\right] \\ \times \operatorname{sinc}\left(\frac{k_{x_p}\Delta_x}{2}\right)\operatorname{sinc}\left(\frac{k_{y_q}\Delta_y}{2}\right)e^{-jk_{x_p}(x_m-x_n)}e^{-jk_{y_q}(y_m-y_n)} \end{aligned} \tag{4.80}$$

The slowly converging part of the sum in (4.80) is the first expression. Simplifying (4.80) by assuming that $R_y = 0$, $x_m = x_n$, $y_m = y_n$, and $z_m = z_n$ yields an equation whose convergence rate is relatively unchanged by the simplification. The resulting equation is

$$Z_{yy} = -\frac{2k_0 Z_0}{ac}\sum_p \frac{\sin\left(k_{x_p}\Delta_x/2\right)}{k_{x_p}} \sum_q \left(1-\frac{k_{y_q}^2}{k_0^2}\right)\frac{\sin\left(k_{y_q}\Delta_y/2\right)}{k_{y_q}}\left[\frac{2j-2je^{-jk_{z_{pq}}\Delta_z/2}}{k_{z_{pq}}^2}\right]. \tag{4.81}$$

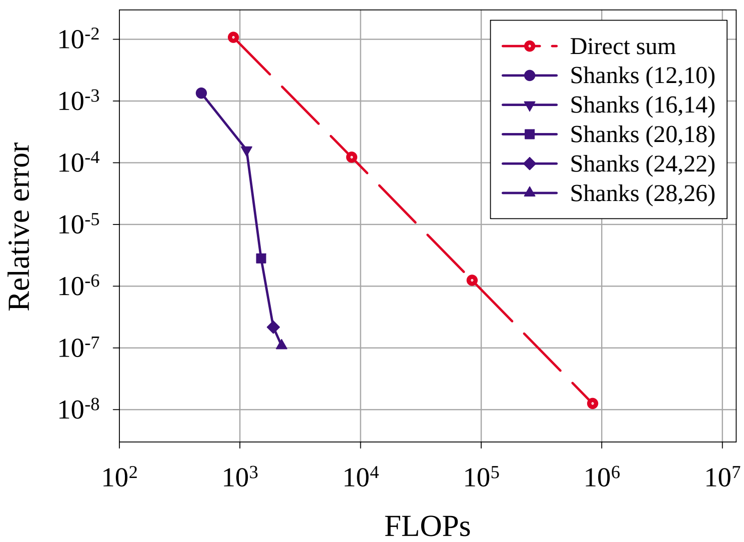

Figure 4.7: Relative error as a function of floating point operations for computing various order Shanks' transforms and the direct sum of the inner sum of (4.80)

The inner sum is evaluated assuming the index of the outer sum $p = 0$. It is clear that implementing a $(N,N\text{-}2)$ Shanks' transform to sum the series minimizes the relative error for a given computational cost. The relative error as a function of computational cost (FLOPs) of implementing various order Shanks' transforms is shown in Figure 4.7. The number of floating point operations for the direct sum of the series is also included for comparison. Notice the dramatic decrease in the relative error of the sum for a given number of FLOPS required to sum the inner sum of (4.80) to a given accuracy by implementing different $(N,N\text{-}2)$ Shanks' transforms. To achieve a relative error of 10^{-4} for the inner sum, only 10^3 FLOPS are required by the Shanks' transform, whereas 10^4 FLOPS are needed by the direct sum. The disparity in computational cost between computing the direct sum and implementing a Shanks' transform is even more significant for a relative error of less than 10^{-6}.

If (4.80) is used without simplification, the series that must be summed is

$$Z_{yy} = -\frac{2k_0 Z_0}{ac} \sum_p \frac{\sin\left(k_{x_p}\Delta_x/2\right)}{k_{x_p}} e^{-jk_{x_p}(x_m - x_n)} \times \sum_q \left(1 - \frac{k_{y_q}^2}{k_0^2}\right) \frac{\sin\left(k_{y_q}\Delta_y/2\right)}{k_{y_q}} e^{-jk_{y_q}(y_m-y_n)} \left[\frac{2j - 2je^{-jk_{z_{pq}}\Delta_z/2}}{k_{z_{pq}}^2}\right] \tag{4.82}$$

However, the same Shanks' transform is used without modification to sum this element. This is significant in light of the fact that all of the sums can be computed using the same general subroutine. This is not true for other summation acceleration techniques.

Kummer's Method [51, 99]

The statement that the rate of convergence of a series is determined by the asymptotic form of the series is the basis for Kummer's method. Suppose a series $f(n)$ has an asymptotic form $f_\infty(n)$. An equivalent expression to $f(n)$ can be found if the asymptotic series is subtracted from and added back to the original series as seen below

$$\sum_{n=-\infty}^{\infty} f(n) = \sum_{n=-\infty}^{\infty} [f(n) - f_\infty(n)] + \sum_{n=-\infty}^{\infty} f_\infty(n). \tag{4.83}$$

Usually, $f_\infty(n)$ is chosen in such a way that the last series has a known closed-form expression. For complicated series, however, obtaining a closed-form expression for the asymptotic series can be a tedious task.

The double summation that is found in this work is written symbolically as

$$S = \sum_{m=0}^{\infty}\sum_{n=0}^{\infty} S_{mn}.$$

The asymptotic series A_{mn} is subtracted from and added to the original series S_{mn}

$$S = \sum_{m=0}^{\infty}\left\{\sum_{n=0}^{\infty}(S_{mn} - A_{mn}) + \sum_{n=0}^{\infty} A_{mn}\right\}.$$

If the asymptotic series A_{mn} has a closed-form solution in terms of the inner index n equal to A_m, then the above equation can be written as

$$S = \sum_{m=0}^{\infty}\left\{\sum_{n=0}^{\infty}(S_{mn} - A_{mn}) + A_m\right\}.$$

The sum $S_{mn} - A_{mn}$ converges much more rapidly than the direct sum of S_{mn}.

Additional series acceleration can be achieved for some series by incorporating a similar technique on the tail contribution of the series. Substituting $Z_{mn} = S_{mn} - A_{mn}$ and writing the series Z_{mn} as the sum of $(N+1)$ terms and the remaining tail contribution yields

$$S = \sum_{m=0}^{\infty}\left\{\sum_{n=0}^{N-1} Z_{mn} + \sum_{n=N}^{\infty} Z_{mn} + A_m\right\}.$$

The asymptotic tail series T_{mn} of the tail contribution is subtracted from and added to the original series Z_{mn} much like before

$$S = \sum_{m=0}^{\infty}\left\{\sum_{n=0}^{N-1} Z_{mn} + \sum_{n=N}^{\infty}(Z_{mn} - T_{mn}) + \sum_{n=N}^{\infty} T_{mn} + A_m\right\}.$$

The tail contribution is now written as $\sum_{n=N}^{\infty} T_{mn} = \sum_{n=0}^{\infty} T_{mn} - \sum_{n=0}^{N-1} T_{mn}$ and the above equation can be written as

$$S = \sum_{m=0}^{\infty} \left\{ \sum_{n=0}^{N-1} Z_{mn} + \sum_{n=N}^{\infty} (Z_{mn} - T_{mn}) + \sum_{n=0}^{\infty} T_{mn} - \sum_{n=0}^{N-1} T_{mn} + A_m \right\}.$$

If T_m is the closed-form solution for the inner sum of T_{mn}, then

$$S = \sum_{m=0}^{\infty} \left\{ \sum_{n=0}^{N-1} Z_{mn} + \sum_{n=N}^{\infty} (Z_{mn} - T_{mn}) + T_m - \sum_{n=0}^{N-1} T_{mn} + A_m \right\}.$$

The sum $Z_{mn} - T_{mn}$ also converges much more rapidly than the direct sum of Z_{mn}.

Kummer's method applied to inner sum of Z_{mm}^{yy}

An example of the usefulness of Kummer's method is seen in computing the same inner sum for the (m, n) element of the Z^{yy} submatrix of (4.41) as was determined using a Shanks' transform. Beginning with (4.80), the inner sum is computed using Kummer's method. Only one expression of the inner series is not exponentially convergent:

$$S'_p = 2j \sum_q \left(1 - \frac{k_{y_q}^2}{k_0^2}\right) \frac{\sin\left(k_{y_q} \Delta_y/2\right)}{k_{y_q} k_{z_{pq}}^2} \tag{4.84}$$

where S'_p is the sum over all q excluding the following $q = 0$ term

$$S_{p0} = \left(1 - \frac{k_{y_0}^2}{k_0^2}\right) \frac{\sin\left(k_{y_0} \Delta_y/2\right)}{k_{y_0}} \left[\frac{2j - 2je^{-jk_{z_{p0}}\Delta_z/2}}{k_{z_{p0}}^2}\right].$$

For large q, the sum in (4.84) can be approximated by

$$\begin{aligned} S'_p &= -\frac{2j}{k_0^2} {\sum_q}' \frac{2\pi q}{c} \frac{1}{k_0^2 - k_{x_p}^2 - \left(\frac{2\pi q}{c}\right)^2} \sin\left(k_{y_q} \Delta_y/2\right) \\ &= \frac{2j}{k_0^2} {\sum_q}' \frac{2\pi q}{c} \left(\frac{c}{2\pi}\right)^2 \frac{1}{q^2 - \left[\left(\frac{ck_0}{2\pi}\right)^2 - \left(\frac{ck_{x_p}}{2\pi}\right)^2\right]} \sin\left(k_{y_q} \Delta_y/2\right) \end{aligned} \tag{4.85}$$

with

$$k_{y_q} \simeq \frac{2\pi q}{c}, \qquad k_{z_{pq}}^2 \simeq k_0^2 - k_{x_p}^2 - \left(\frac{2\pi q}{c}\right)^2.$$

If we represent the denominator as $q^2 - \alpha_p^2$, where $\alpha_p^2 = (ck_0/2\pi)^2 - \left(ck_{x_p}/2\pi\right)^2$, then

$$S'_p = \frac{cj}{\pi k_0^2} {\sum_q}' \frac{q}{q^2 - \alpha_p^2} \sin\left(k_{y_q} \Delta_y/2\right). \tag{4.86}$$

Noting that $k_{y_q} = k_{y_0} + \frac{2\pi q}{c}$ and using a simple trigonometric identity, (4.86) can be written as

$$S_p' = \frac{cj}{\pi k_0^2} \sum_q{}' \frac{q}{q^2 - \alpha_p^2} \Big[\sin(k_{y_0}\Delta_y/2)\cos(q\pi\Delta_y/c) + \cos(k_{y_0}\Delta_y/2)\sin(q\pi\Delta_y/c) \Big]. \quad (4.87)$$

The sums in (4.87) have asymptotic forms that can be evaluated analytically. If we rewrite $\sum_q'$ as $\sum_{q=-\infty}^{-1} + \sum_{q=1}^{\infty}$ and observe that

$$\frac{q}{q^2 - \alpha_p^2}\cos q\zeta = -\frac{q}{q^2 - \alpha_p^2}\cos(-q\zeta)$$
$$\frac{q}{q^2 - \alpha_p^2}\sin q\zeta = \frac{q}{q^2 - \alpha_p^2}\sin(-q\zeta)$$

then (4.87) can be rewritten as

$$S_p' = \frac{2cj}{\pi k_0^2}\cos(k_{y_0}\Delta_y/2)\sum_{q=1}^{\infty}\frac{q}{q^2 - \alpha_p^2}\sin q\zeta \quad (4.89)$$

where $\zeta = \pi\Delta_y/c$. The sum in (4.89) has an exact solution given by

$$\sum_{q=1}^{\infty}\frac{q\sin q\zeta}{q^2 + \alpha_p^2} = \frac{\pi}{2}\frac{\sinh\alpha_p(\pi - \zeta)}{\sinh\alpha_p\pi}, \quad \alpha_p^2 > 0, \quad 0 < \zeta < 2\pi \quad (4.90a)$$
$$\sum_{q=1}^{\infty}\frac{q\sin q\zeta}{q^2 - \alpha_p^2} = \frac{\pi}{2}\frac{\sin\alpha_p(\pi - \zeta)}{\sin\alpha_p\pi}, \quad \alpha_p^2 > 0, \quad 0 < \zeta < 2\pi. \quad (4.90b)$$

The asymptotic value S_p^{∞} of (4.86) is

$$S_p^{\infty} = \frac{cj}{k_0^2}\cos(k_{y_0}\Delta_y/2)\,\frac{\sin\alpha_p(\pi - \zeta)}{\sin\alpha_p\pi}.$$

Since $S_p = S_{p0} + S_p' + S_p^{\infty}$,

$$S_p = \sum_q\left(1 - \frac{k_{y_q}^2}{k_0^2}\right)\frac{\sin\left(k_{y_q}\Delta_y/2\right)}{k_{y_q}}\left[\frac{2j - 2je^{-jk_{z_{pq}}\Delta_z/2}}{k_{z_{pq}}^2}\right] + \frac{cj}{k_0^2}\cos(k_{y_0}\Delta_y/2)\,\frac{\sin\alpha_p(\pi - \zeta)}{\sin\alpha_p\pi}$$
$$- \frac{2cj}{\pi k_0^2}\cos(k_{y_0}\Delta_y/2)\sum_{q=1}^{\infty}\frac{q}{q^2 - \alpha_p^2}\sin q\zeta \quad (4.91)$$

As can be seen in Figure 4.8, this method also significantly reduces the relative error for a given computational cost. Included for reference is the Shanks' transform and direct sum data of Figure 4.7. A similar convergence rate as the Shanks' transform is found using Kummer's method. However, even this simple series requires concentrated analytical effort.

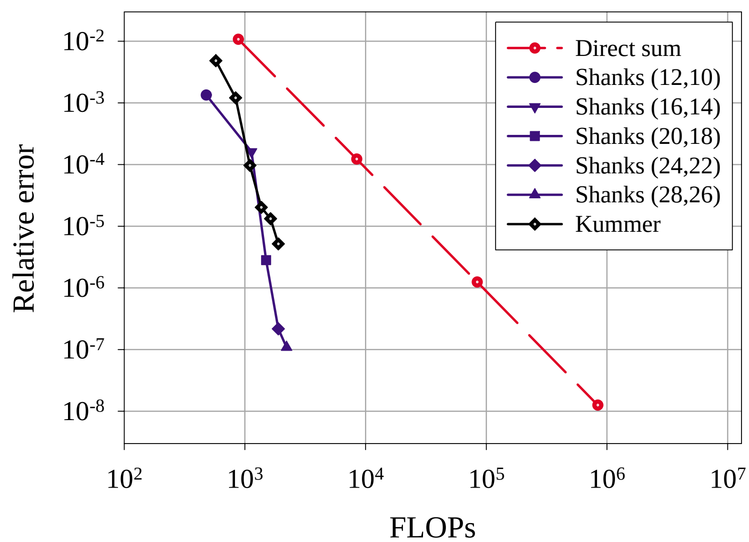

Figure 4.8: Relative error as a function of floating point operations for computing various order Shanks' transforms, Kummer's transforms, and the direct sum of the inner sum of (4.80)

If (4.41) is used without simplification, *i.e.* $R_y \neq 0$, $x_m \neq x_n$, $y_m \neq y_n$, but $z_m = z_n$, the series that must be summed is

$$Z_{yy} = -\frac{2k_0 Z_0}{ac} \sum_p \frac{\sin\left(k_{x_p}\Delta_x/2\right)}{k_{x_p}} e^{-jk_{x_p}(x_m - x_n)} \\ \times \sum_q \left(1 - \frac{k_{y_q}^2}{k_0^2}\right) \frac{\sin\left(k_{y_q}\Delta_y/2\right)}{k_{y_q}} e^{-jk_{y_q}(y_m - y_n)} \left[\frac{2j - 2je^{-jk_{z_{pq}}\Delta_z/2}}{k_{z_{pq}}^2}\right]. \quad (4.92)$$

Implementing the above sum using a Shanks' transform is easily done by applying the general subroutine to the first $(N+1)$ terms of the series. However, a new analytic solution must be determined when implementing Kummer's method. The term of the inner series that is not exponentially convergent is

$$S_p' = \frac{2j}{k_0^2} \sum_q \frac{\left(k_0^2 - k_{y_q}^2\right)}{k_{y_q} k_{z_{pq}}^2} \sin\left(k_{y_q}\Delta_y/2\right) e^{-jk_{y_q}(y_m - y_n)} \quad (4.93)$$

where S_p' is the sum over all q excluding the following $q = 0$ term

$$S_{p0} = \left(1 - \frac{k_{y_0}^2}{k_0^2}\right) \frac{\sin\left(k_{y_0}\Delta_y/2\right)}{k_{y_0}} e^{-jk_{y_0}(y_m - y_n)} \left[\frac{2j - 2je^{-jk_{z_{p0}}\Delta_z/2}}{k_{z_{p0}}^2}\right].$$

For large q, the sum in (4.93) can be approximated by

$$\begin{aligned} S_p' &= -\frac{2j}{k_0^2}\sum_q{}' \frac{2\pi q}{c}\frac{1}{k_0^2 - k_{x_p}^2 - \left(\frac{2\pi q}{c}\right)^2}\sin\left(k_{y_q}\Delta_y/2\right)e^{-jk_{y_q}(y_m-y_n)} \\ &= \frac{2j}{k_0^2}\sum_q{}' \frac{2\pi q}{c}\left(\frac{c}{2\pi}\right)^2\frac{1}{q^2 - \left[\left(\frac{ck_{x_p}}{2\pi}\right)^2 - \left(\frac{ck_0}{2\pi}\right)^2\right]}\sin\left(k_{y_q}\Delta_y/2\right)e^{-jk_{y_q}(y_m-y_n)} \end{aligned} \tag{4.94}$$

with

$$k_{y_q} \simeq \frac{2\pi q}{c}, \qquad k_{z_{pq}}^2 \simeq k_0^2 - k_{x_p}^2 - \left(\frac{2\pi q}{c}\right)^2.$$

If we represent the denominator as $q^2 - \alpha_p^2$, where $\alpha_p^2 = (ck_0/2\pi)^2 - \left(ck_{x_p}/2\pi\right)^2$, then

$$S_p' = \frac{cj}{\pi k_0^2}\sum_q{}' \frac{q}{q^2-\alpha_p^2}\sin\left(k_{y_q}\Delta_y/2\right)e^{-jk_{y_q}(y_m-y_n)} \tag{4.95}$$

Similar to before, (4.95) can be written as

$$\begin{aligned} S_p' =& \frac{cj}{\pi k_0^2}e^{-jk_{y_0}(y_m-y_n)}\sin\left(k_{y_0}\Delta_y/2\right)\sum_q{}' \frac{q}{q^2-\alpha_p^2}\cos\left(q\pi\Delta_y/c\right)e^{-j\frac{2\pi q}{c}(y_m-y_n)} \\ &+ \frac{cj}{\pi k_0^2}e^{-jk_{y_0}(y_m-y_n)}\cos\left(k_{y_0}\Delta_y/2\right)\sum_q{}' \frac{q}{q^2-\alpha_p^2}\sin\left(q\pi\Delta_y/c\right)e^{-j\frac{2\pi q}{c}(y_m-y_n)}. \end{aligned} \tag{4.96}$$

The sums in (4.96) have asymptotic forms that can be evaluated analytically with a little analytical effort. Equation (4.96) can be rewritten as

$$\begin{aligned} S_p' =& \frac{cj}{\pi k_0^2}e^{-jk_{y_0}(y_m-y_n)}\sin\left(k_{y_0}\Delta_y/2\right)\sum_{q=1}^{\infty}\frac{q}{q^2-\alpha_p^2}\left[-j\sin q(\zeta^+) + j\sin q(\zeta^-)\right] \\ &+ \frac{cj}{\pi k_0^2}e^{-jk_{y_0}(y_m-y_n)}\cos\left(k_{y_0}\Delta_y/2\right)\sum_{q=1}^{\infty}\frac{q}{q^2-\alpha_p^2}\left[\sin q(\zeta^+) + \sin q(\zeta^-)\right] \end{aligned} \tag{4.97}$$

where $\zeta^{\pm} = \pi\Delta_y\left[1 \pm 2(m-n)\right]/2$. Using (4.90), the asymptotic value of (4.97) can be written as

$$\begin{aligned} S_p^{\infty} =& \frac{c}{2k_0^2}e^{-jk_{y_0}(y_m-y_n)}\sin\left(k_{y_0}\Delta_y/2\right)\left[\frac{\sin\alpha_p(\pi-\zeta^+)}{\sin\alpha_p\pi} - \frac{\sin\alpha_p(\pi-\zeta^-)}{\sin\alpha_p\pi}\right] \\ &+ \frac{cj}{2k_0^2}e^{-jk_{y_0}(y_m-y_n)}\cos\left(k_{y_0}\Delta_y/2\right)\left[\frac{\sin\alpha_p(\pi-\zeta^+)}{\sin\alpha_p\pi} + \frac{\sin\alpha_p(\pi-\zeta^-)}{\sin\alpha_p\pi}\right]. \end{aligned} \tag{4.98}$$

Again, $S_p = S_{p0} + S_p^{\infty} + S_p'$,

$$\begin{aligned}
S_p = \sum_q \left(1 - \frac{k_{y_q}^2}{k_0^2}\right) \frac{\sin\left(k_{y_q}\Delta_y/2\right)}{k_{y_q}} e^{-jk_{y_q}(y_m-y_n)} \left[\frac{2j - 2je^{-jk_{z_{pq}}\Delta_z/2}}{k_{z_{pq}}^2}\right] \\
- \frac{cj}{\pi k_0^2} e^{-jk_{y_0}(y_m-y_n)} \sin\left(k_{y_0}\Delta_y/2\right) \sum_{q=1}^{\infty} \frac{q}{q^2-\alpha_p^2}\left[-j\sin q(\zeta^+) + j\sin q(\zeta^-)\right] \\
- \frac{cj}{\pi k_0^2} e^{-jk_{y_0}(y_m-y_n)} \cos\left(k_{y_0}\Delta_y/2\right) \sum_{q=1}^{\infty} \frac{q}{q^2-\alpha_p^2}\left[\sin q(\zeta^+) + \sin q(\zeta^-)\right] \\
+ \frac{c}{2k_0^2} e^{-jk_{y_0}(y_m-y_n)} \sin\left(k_{y_0}\Delta_y/2\right) \left[\frac{\sin\alpha_p(\pi-\zeta^+)}{\sin\alpha_p\pi} - \frac{\sin\alpha_p(\pi-\zeta^-)}{\sin\alpha_p\pi}\right] \\
+ \frac{cj}{2k_0^2} e^{-jk_{y_0}(y_m-y_n)} \cos\left(k_{y_0}\Delta_y/2\right) \left[\frac{\sin\alpha_p(\pi-\zeta^+)}{\sin\alpha_p\pi} + \frac{\sin\alpha_p(\pi-\zeta^-)}{\sin\alpha_p\pi}\right]
\end{aligned} \tag{4.99}$$

As can be clearly seen, the analytical effort to determine the asymptotic form of the elements in the impedance matrix is not trivial; the requisite computer coding to implement this solution lends itself to difficult debugging. Additionally, applying Kummer's method to the inner sum does not produce an analytical solution for the outer sum. Thus, one must either compute an addition analytical solution for the outer sum or find another mechanism to compute the sum. In light of the difficulties found in computing realizable double sums, implementing a general Shanks' transform may be more profitable.

Another application of Kummer's method in the acceleration of the PFSGF series is to simply sum the series incorporating a "smoothing" or "acceleration" parameter in the propagation constant. The asymptotic form of the new "modified" Green's function is then subtracted from the original series and the transformed series is added back [40].

4.5.2 Acceleration Techniques Used Elsewhere

Ewald Transformation [30, 39, 65, 27]

The Ewald transformation expresses the periodic free-space Green's function as the sum of two doubly infinite series, namely one series summed in the spectral domain and one series summed in the spatial domain. Similarly to Kummer's method, the Ewald transformation casts the PFSGF into a hybrid form more amenable to acceleration. The Ewald transformation results in series that utilizes the complementary error function yielding two more rapidly converging series.

ρ-algorithm [124, 102]

For monotonic series, the ρ-algorithm is a very rapidly converging series acceleration technique. However, it does not fare as well with alternating series. The simple ρ-algorithm can be computed as follows

$$\rho_k^{(n)} = \rho_{k-2}^{(n+1)} + \frac{k}{\rho_{k-1}^{(n+1)} - \rho_{k-1}^{(n)}}, \quad k = 1, 2, \cdots \tag{4.100}$$

where

$$\rho_{-1}^{(n)} = 0, \quad \rho_0^{(n)} = S_n \tag{4.101}$$

and where k is the order of the algorithm. The even order terms, $\rho_{2k}^{(n)}$, give the estimate of the sum.

θ-algorithm [15, 104]

Another rapidly accelerating series technique for alternating series is the θ-algorithm. The θ-algorithm can be computed as follows

$$\theta_{2k+2}^{(n)} = \theta_{2k}^{(n+1)} + \frac{\left[\theta_{2k}^{(n+2)} - \theta_{2k}^{(n+1)}\right]\left[\theta_{2k+1}^{(n+2)} - \theta_{2k+1}^{(n+1)}\right]}{\left[\theta_{2k+1}^{(n+2)} - 2\theta_{2k+1}^{(n+1)} + \theta_{2k+1}^{(n)}\right]}, \quad k = 0, 1, 2, \cdots \tag{4.102}$$

and the odd order terms by

$$\theta_{2k+1}^{(n)} = \theta_{2k-1}^{(n+1)} + \frac{1}{\left[\theta_{2k}^{(n+1)} - \theta_{2k}^{(n)}\right]}, \quad k = 1, 2, \cdots \tag{4.103}$$

where

$$\theta_{-1}^{(n)} = 0, \quad \theta_0^{(n)} = S_n \tag{4.104}$$

The even order terms, $\theta_{2k+2}^{(n)}$, give the estimate of S. Like the ρ-algorithm, the θ-algorithm is easy to implement.

Chebyshev-Toeplitz algorithm [121, 105]

The Chebyshev-Toeplitz (CT) algorithm can be computed as follows

$$t_{-1}^{(n)} = 0, \quad t_0^{(n)} = S_n, \quad \sigma_0 = 1, \tag{4.105}$$

$$t_1^{(n)} = t_0^{(n)} + 2t_0^{(n+1)}, \quad \sigma_1 = 3, \tag{4.106}$$

$$t_{k+1}^{(n)} = 2t_k^{(n)} + 4t_k^{(n+1)} - t_{k-1}^{(n)}, \quad k = 1, 2, \cdots \tag{4.107}$$

$$\sigma_{k+1} = 6\sigma_k - \sigma_{k-1}, \quad k = 1, 2, \cdots \tag{4.108}$$

$$T_k^{(n)} = \frac{t_k^{(n)}}{\sigma_k}, \quad k = 0, 1, 2, \cdots \tag{4.109}$$

The n^{th} iterate of the CT algorithm is given by $T_k^{(n)}$ which gives as estimate of the sum of the series.

Levin t-transform [54, 106]

The t-transform algorithm can be computed as follows

$$t_k^{(n)} = \frac{\sum_{i=0}^{k} (-1)^i \binom{k}{i} \binom{n+i}{n+k}^{(k-1)} \left(\frac{S_{n+i}}{S_{n+i-1} - S_{n+i}} \right)}{\sum_{i=0}^{k} (-1)^i \binom{k}{i} \binom{n+i}{n+k}^{(k-1)} \left(\frac{1}{S_{n+i-1} - S_{n+i}} \right)}, \quad k = 1, 2, \cdots \tag{4.110}$$

The n^{th} iterate of the Levin t-transform is given by $T_k^{(n)}$ which gives an estimate of sum of the series.

4.6 Conclusions

A full-wave IE/MoM solution that determines the general three-dimensional scattering from an inhomogeneous doubly periodic layer above a half-space medium has been formulated, implemented, and validated. Equivalent volume polarization currents are used to replace the dielectric material and the combination of a Poisson transformation and a Shanks' transformation is used to improve the speed and accuracy of the impedance matrix element computations. The accuracy of the solution is primarily dependent on three factors: (*i.*) representing the dielectric material with an appropriate number of subsectional unknowns, (*ii.*) including enough terms in the resulting Floquet summations, and (*iii.*) the choice of an appropriate series acceleration convergence technique. A general rule-of-thumb in MoM formulations is to use 5–10 subsectional unknowns per half wavelength in the medium. This is the minimum number that should be used when modeling the z variation of the material. Fewer unknowns per wavelength are required to model the transverse variation to obtain a given accuracy because the fields are more smoothly varying in the transverse direction.

The solution procedure is valid for reasonable combinations of unit cell spacing, material shape, dielectric constant, and number of layers. This solution procedure is subsequently used in Chapter 5 to validate the modeling of an equivalent uniaxial layer that replaces the doubly periodic layer for use in rectangular patch antenna applications.

CHAPTER 5

Radiation Properties of a Rectangular Microstrip Patch on a Uniaxial Substrate

5.1 Introduction

Of interest to the applied microwave community is the implementation of a microstrip patch antenna on a doubly periodic dielectric layered medium. Preliminary investigations of simple Hertzian dipoles radiating over this structure have been addressed by Yang [133] using an analytic array scanning technique [67]. However, the solution in [133] is computationally intensive and has not been extended for arbitrary polarization. A simpler (and perhaps more insightful) solution where the doubly periodic dielectric layer is emulated by an equivalent anisotropic (uniaxial) material is developed in the following sections. The uniaxial model for the doubly periodic dielectric layer is validated using plane wave reflection coefficients for a variety of filling fractions, angles, and permittivities. Although the solution of a similar approximation has been developed for two-dimensional scattering from periodicities in one-dimension [85, 87], this is the first known treatment of such a solution for full three-dimensional scattering from dielectric periodicities in two directions.

Traditionally, microstrip patch antennas have been integrated on relatively low permittivity substrates in order to improve antenna performance. Since microstrip patches are effectively a radiating resonator, the large Q produced by confining the stored energy in a thin region under the patch necessarily narrows the bandwidth significantly. Typical bandwidths for traditional patch designs are on the order of 2–4%. New designs for microstrip patch feeds have increased bandwidths but at the cost of increased complexity. Integrating the antenna on higher permittivity substrates is preferred to minimize circuit size and spurious radiation [75, 89] but at the cost of confining the potential radiating energy even more tightly. This trade-off between good antenna performance and good circuit performance is a key design feature found in many microstrip antenna designs. The compromise can be achieved primarily through the proper design of any or all of the three main components in a microstrip structure: radiating element, feed mechanism, and substrate choice. (Extensive bibliographies can be found in [75, 89].) The focus of this chapter is the choice and design of an effective anisotropic substrate for use in microstrip antenna applications. Additionally, the solution for a rectangular patch element radiating over the equivalent uniaxial substrate is carried out accurately and efficiently using Ansoft's High Frequency Structure Simulator that incorporates anisotropic substrates.

In order to reduce the often unwanted formation of surface waves which can lead to pattern degradation and low efficiencies, relatively thin homogeneous substrates (thicknesses less than $0.05\lambda_0$) are used. However, as noted before, this limitation has severe consequences. Although a good deal of attention has focused on integrating microstrip patches on homogeneous substrates, many of the practical substrates in use today such as sapphire, Epsilam-10, and boron nitride, have a significant amount of (uniaxial) anisotropy. The uniaxial materials have two effective homogeneous permittivities: one permittivity aligned parallel to the optical axis of the material and one permittivity aligned perpendicular to the optical axis [47, 85, 87]. Rigorous full-wave solutions, albeit computationally intensive ones, have been developed to characterize the effect of anisotropy on various patch antenna parameters such as resonant length and efficiency [74, 68, 131]. Other investigations [19, 14, 123] have focused on supplementing the conclusions drawn in earlier investigations, namely, that the primary effect of anisotropy on rectangular patch antennas is the change in its resonant length. This is significant because of the narrow bandwidth of the patch itself. The relatively large shift in resonant frequency produced in many of the modern substrates may actually force a rectangular patch designed to operate at a specific frequency to radiate outside of the antenna bandwidth [74]. Additionally, anisotropic effects are found that shape the radiation pattern of the patch and thus in an array configuration, the coupling to other elements.

Because uniaxial substrates are often expensive to manufacture and have limited flexibility for design, uniaxial substrates can be emulated (and easily fabricated) by incorporating periodic inclusions in an otherwise homogeneous substrate. In particular, if the wavelength is sufficiently large compared with the period of the array, the doubly periodic dielectric layer (in the transverse direction) can emulate a uniaxial substrate with an optical axis aligned in a direction normal to the layer [85, 87]. The periodic structure shown in Figure 5.1(a) can be easily constructed using simple milling or etching techniques from simple inexpen-

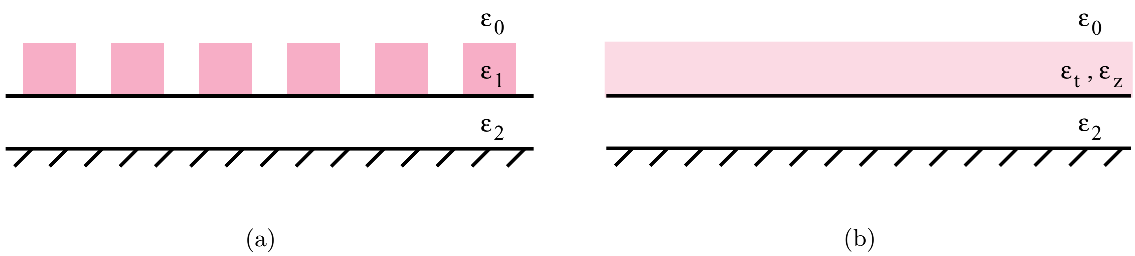

Figure 5.1: (a) Periodic dielectric layer over a layered medium and (b) equivalent uniaxial medium with transverse permittivity ε_t and axial permittivity ε_z over a layered medium

sive, homogeneous substrates. This is significant because some common uniaxial materials such as sapphire that are expensive to grow [6] can be "artificially" replicated easily and inexpensively. Additionally, the artificial nature of the periodic uniaxial substrate permits the creative design of new substrates with the expanded freedom of anisotropic ratio, background permittivity, and/or fabrication technique.

5.2 Equivalent Uniaxial Modeling

The equivalent uniaxial material of Figure 5.1(b) with the optical axis aligned with the z axis has an assumed permittivity tensor of

$$\bar{\bar{\varepsilon}} = \varepsilon_0 \begin{bmatrix} \varepsilon_x & 0 & 0 \\ 0 & \varepsilon_y & 0 \\ 0 & 0 & \varepsilon_z \end{bmatrix} \tag{5.1}$$

where ε_x=ε_y=ε_t is the transverse component and ε_z is the component along the direction of the optical axis.

Two of the well-known dielectric mixing models[1] for two-phase media (*i.e.*, ε is piecewise constant and takes on only two distinct values each) are the Hashin-Shtrikman bounds [35, 47] and the Licktenecker bounds [25]. As with many of the early approximations, these solutions are determined using variational methods, and thus, the solutions take on the form of bounds for the equivalent two-phase materials (permittivities, conductivities, or

[1]These models belong to a more general class of dielectric mixing formulas that include the Maxwell-Garnet mixing formula (accurate for relatively low volume fractions) and the Polder van Santen mixing formula (accurate for relatively low permittivity changes).

permeabilities). For the Hashin-Shtrikman and the Licktenecker models outlined below, both the unit cell and the material inclusions are assumed to have square[2] cross-sections.

5.2.1 Hashin-Shtrikman Model

A good approximation (assuming the inclusions are small with respect to wavelength) for the longitudinal component of the permittivity tensor, ε_z, is simply to take the volumetric averages of the constituent materials and is given by

$$\varepsilon_z = (1 - f^2)\varepsilon_a + f^2\varepsilon_b \tag{5.2}$$

where f is the filling fraction, ε_a is the background permittivity, and ε_b is the permittivity of the material blocks or inclusions. The generalized Hashin-Shtrikman formulas provide upper and lower bounds for the transverse component of the permittivity tensor, ε_t [48, 47]. While no known closed form expression exists for the transverse permittivity, evidence suggests that the lower and upper Hashin-Shtrikman bounds provide good accuracy to approximate the value over a wide range of parameters for many practical substrates. The lower and upper bounds, denoted ε_{HS}^L and ε_{HS}^U, respectively, are defined as

$$\varepsilon_{HS}^L = \varepsilon_a \frac{2\varepsilon_b + f^2\left(\varepsilon_a - \varepsilon_b\right)}{2\varepsilon_a + f^2\left(\varepsilon_b - \varepsilon_a\right)} \tag{5.3a}$$

$$\varepsilon_{HS}^U = \varepsilon_b \frac{\left(\varepsilon_a + \varepsilon_b\right) + f^2\left(\varepsilon_a - \varepsilon_b\right)}{\left(\varepsilon_a + \varepsilon_b\right) + f^2\left(\varepsilon_b - \varepsilon_a\right)}. \tag{5.3b}$$

5.2.2 Licktenecker Model

Another set of bounds that serves to approximate the effective transverse permittivity can be derived using the Licktenecker bounds [25]. The Licktenecker bounds can be written as

$$\int_0^b \frac{dy}{\int_0^a \frac{dx}{\varepsilon(x,y)}} \leq \varepsilon_x \leq \int_0^a \frac{dx}{\int_0^b \frac{dy}{\varepsilon(x,y)}} \tag{5.4a}$$

$$\int_0^a \frac{dx}{\int_0^b \frac{dy}{\varepsilon(x,y)}} \leq \varepsilon_y \leq \int_0^b \frac{dy}{\int_0^a \frac{dx}{\varepsilon(x,y)}}. \tag{5.4b}$$

However, if the inclusion is symmetric about the line $x{=}y$, the bounds take on simpler forms since $\varepsilon_x{=}\varepsilon_y{=}\varepsilon_t$. Carrying out the integrals in (5.4), the lower and upper Licktenecker

[2]Similar results can be derived for circular inclusions in a square unit cell but are not presented. For electrically small cells, the particular geometric shape is insignificant compared to the volumetric averages of the constituent phases.

bounds, denoted ε_L^L and ε_L^U, respectively, are determined to be

$$\varepsilon_L^L = \frac{f\varepsilon_b + (1-f)\varepsilon_a}{f\varepsilon_a + f(1-f)\varepsilon_b + (1-f)^2\varepsilon_a} \tag{5.5a}$$

$$\varepsilon_L^U = \frac{f\varepsilon_b + f(1-f)\varepsilon_a + (1-f)^2\varepsilon_b}{f\varepsilon_a + (1-f)\varepsilon_b} \tag{5.5b}$$

where f is the filling fraction b/a, ε_a is the background permittivity, and ε_b is the permittivity of the material blocks or inclusions. Note that if the phasing of the material is reversed, $1/\varepsilon_L^L = \varepsilon_L^U$.

The effective transverse permittivity of the two-dimensional periodic media determined by the Hashin-Shtrikman and Licktenecker bounds is graphed as a function of filling fraction b/a for $\varepsilon_b = 10\varepsilon_a$ in Figure 5.2. Also included in the figure is the solution obtained from

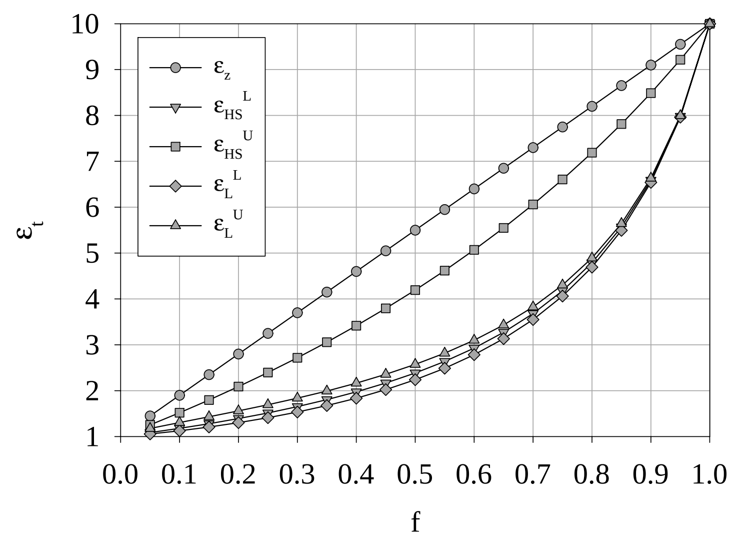

Figure 5.2: Effective transverse permittivity as a function of filling fraction for ε_b=$10\varepsilon_a$

simply weighting the constitutive phases by their respective volume fractions. Note that this is nothing more than the effective permittivity in the axial direction determined from (5.2). Consequently, the assumption that the permittivity of the two dimensional periodic substrate (even for electrically small cells) has an effective homogeneous permittivity leads to erroneous results. Additionally, one observes that the upper Hashin-Shtrikman bound is grossly in error. However, this error has been reported previously in the literature [47]. The other three bounds are reasonably precise and have been reported to have small errors of less than 4%. The solutions obtained for the Licktenecker bounds are precise, and since they are derived using specific information about the geometry of the inclusions, one can conclude these bounds are more accurate. Overall, the precision of the three remaining bounds is found to increase with increasing filling fraction.

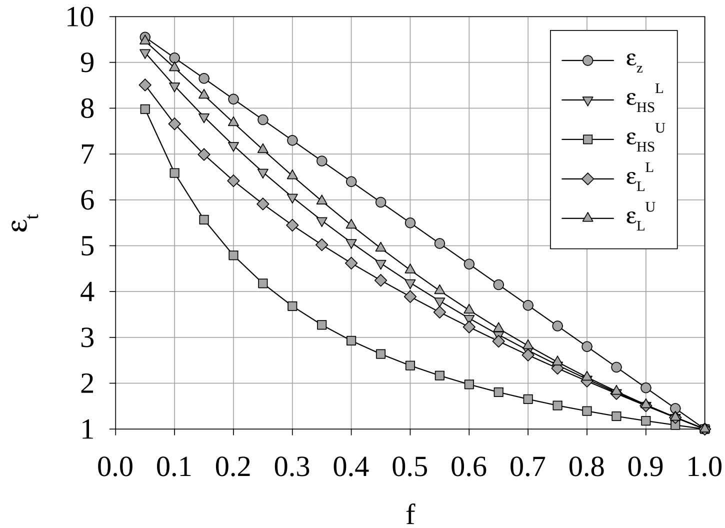

Figure 5.3: Effective transverse permittivity as a function of filling fraction for ε_a=10ε_b

If the phases of the two materials are reversed as shown in Figure 5.3, a noticeable change in precision can be seen. The upper Hashin-Shtrikman bound is again seen to have significant error. The remaining three bounds are reasonably close for large filling fractions, but have some noticeable differences at lower filling fractions. Again, the incorporation of geometrical features necessarily makes the Licktenecker bounds a more accurate solution. Consequently, a good approximation for the effective transverse permittivity can be determined by taking the geometric mean of ε_L^L and ε_L^U

$$\varepsilon_t = \sqrt{\varepsilon_L^L \varepsilon_L^U}. \tag{5.6}$$

Not only are the values obtained using the geometric mean of ε_L^L and ε_L^U remarkably close to the values yielded by the lower Hashin-Shtrikman bound for the phase set in Figure 5.2, but also for the second case shown in Figure 5.3 when the phases are reversed.

An interesting feature of the emulated anisotropic material is the ability to achieve a desired *anisotropic ratio (AR)* by incorporating either a periodic dielectric region in an air background or by including periodic air inclusions in a dielectric background depending on the application and ease of fabrication. The AR is a function of the dielectric contrast between the material blocks or inclusions and the background medium. If the effective transverse permittivity ε_t is greater than the effective axial permittivity ε_z ($\varepsilon_t \geq \varepsilon_z$), the material is said to have *negative* uniaxial anisotropy ($AR > 1$). Conversely, if the effective axial permittivity ε_z is greater than the effective transverse permittivity ε_t ($\varepsilon_t \leq \varepsilon_z$), the material is said to have *positive* uniaxial anisotropy ($AR < 1$). For example, in the microwave region, sapphire (a common substrate material used in microwave integrated circuits) has an AR of 0.81 (ε_t=9.4, ε_z=11.6) [6]. Thus, sapphire has positive uniaxial anisotropy. Boron nitride has an AR of 1.5 (ε_t=5.12, ε_z=3.4) and Epsilam-10 has an AR of 1.26 (ε_t=13.0, ε_z=10.3) [6]. Hence, boron nitride and Epsilam-10 have negative uniaxial anisotropy. Most of the soft composite ceramic-impregnated teflon-type substrates, such as Rogers' RT/Duroid 6000 series, have anisotropic ratios greater than one. The physical significance of the AR will be addressed in the next section.

For the substrates with periodicities in the plane of the substrate, the emulated material is necessarily a positive uniaxial material. Since ε_t and ε_z are known quantities, specifying one of the three unknowns, namely ε_a, ε_b or f, one can solve for the remaining two unknowns of interest from (5.2) and (5.5). For example, sapphire can be emulated by a medium consisting of periodic dielectric rods with a dielectric constant of 12.1 and filling fraction equal to 0.95, or by a medium consisting of periodic air inclusions in a dielectric background with dielectric constant of 16.0 and filling fraction equal to 0.3 as seen in Figure 5.4. The second medium can be viewed more intuitively as doubly periodic set of dielectric veins

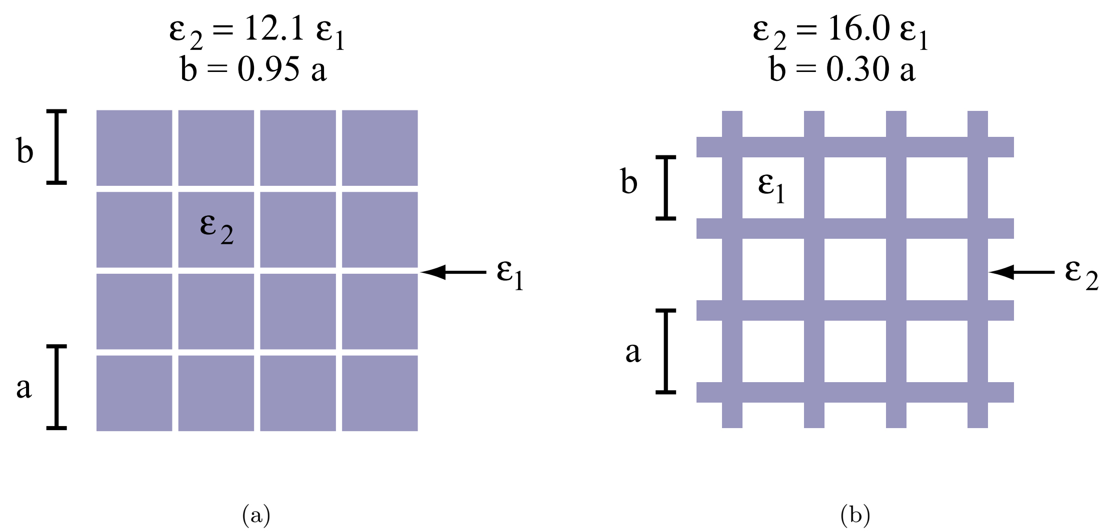

Figure 5.4: Uniaxial nature of sapphire modeled by (a) periodic dielectric rods with ε_2=12.1ε_1 and b/a=0.95 and (b) periodic dielectric veins with ε_2=16.0ε_1 and b/a=0.30

in an air background. This observation is consistent with the two-dimensional periodic structures developed in Chapter 3 and detailed in Section 3.2.2.

As was introduced earlier, the most significant application for the emulated uniaxial materials is the variety of artificial substrate designs available to the RF designer. Naturally occurring uniaxial materials have fixed anisotropic ratios and permittivity tensors and limit important parameter choices. However, depending on the application and the materials available for use, a particular AR can be be emulated. This flexibility allows the RF designer not only the choose of a particular AR, but also the choice of the dielectric constant of the background medium and/or inclusions.

Using the Hashin-Shtrikman or Licktenecker bounds, one can compute the minimum achievable AR of the equivalent positive uniaxial medium by differentiating the ratio $\varepsilon_t/\varepsilon_z$ with respect to the filling fraction f where ε_t is found using (5.3b) or (5.5) and ε_z is found from (5.2). For electrically small cells, the minimum AR that can be achieved for a given dielectric constant ratio, either for $\varepsilon_b/\varepsilon_a > 1$ or $\varepsilon_b/\varepsilon_a < 1$, is shown in Table 5.1. Note

Table 5.1: Minimum achievable anisotropic ratio *(AR)*

$(\varepsilon_b/\varepsilon_a)$	Min AR	ε_t	ε_z	b/a
1.00	1.00	1.00	1.00	1.00
2.32	0.90	1.45	1.61	0.46
4.00	0.74	1.74	2.35	0.45
6.15	0.59	1.94	3.28	0.44
10.20	0.43	2.13	5.00	0.44
$(\varepsilon_a/\varepsilon_b)$	Min AR	ε_t	ε_z	b/a
1.00	1.00	1.00	1.00	1.00
2.32	0.93	1.48	1.58	0.56
4.00	0.85	1.87	2.18	0.61
6.15	0.79	2.23	2.81	0.65
10.20	0.73	2.76	3.78	0.70

that the minimum achievable AR is strongly dependent on the permittivity of the dielectric contrast between the phases. Thus, in order to emulate a given permittivity set (ε_t,ε_z), the ratio of the relative dielectric constant of the two phases must be large enough to both produce the minimum achievable AR listed in Table 5.1 and to also achieve the value of the desired axial component of the permittivity tensor. As will be seen in the next section, the AR is a parameter that has a significant effect on the resonant length of a radiating structure located on or near such a material.

In order to verify that using the previous models are valid approximations for the uniaxial layer, the reflection coefficient for the equivalent uniaxial medium is compared to the IE/MoM numerical solution of the reflection coefficient obtained from the doubly periodic grounded dielectric layer modeled using polarization currents. Thus, the exact horizontal and vertical reflection coefficients at the surface of the grounded uniaxial dielectric layer of thickness t with dielectric permittivity tensor given in (5.1) must be found.

5.3 Plane Wave Reflection Coefficients for a Grounded Uniaxial Layer

Assuming the equivalent uniaxial layer has the permittivity tensor $\bar{\bar{\varepsilon}}$ given in (5.1) and and starting from Maxwell's equations for a uniaxial medium

$$\nabla \times \mathbf{E} = -j\omega\mu\mathbf{H} \tag{5.7}$$

$$\nabla \times \mathbf{H} = j\omega\bar{\bar{\varepsilon}} \cdot \mathbf{E}, \tag{5.8}$$

one can solve for the wave equations that must be satisfied in the medium. Following [74] the wave equation for the z-component of the electric field can be determined to be

$$\frac{\partial^2}{\partial x^2}E_z + \frac{\partial^2}{\partial y^2}E_z + \frac{\varepsilon_z}{\varepsilon_t}\frac{\partial^2}{\partial z^2}E_z + \varepsilon_z k_0^2 E_z = 0 \tag{5.9}$$

where $k_0 {=} \omega\sqrt{\mu_0\varepsilon_0} {=} 2\pi/\lambda_0$. The wave equation for the z-component of the magnetic field can also be determined and is found to be

$$\frac{\partial^2}{\partial x^2}H_z + \frac{\partial^2}{\partial y^2}H_z + \frac{\partial^2}{\partial z^2}H_z + \varepsilon_t k_0^2 E_z = 0. \tag{5.10}$$

The dispersion relations for (5.9) and (5.10) can be found by assuming waves of the form $e^{\pm jk_x x}e^{\pm jk_y y}e^{\pm jk_z z}$. Thus, for TE$_z$ (transverse electric to z) or *horizontal* polarized waves,

$$k_z^2 = \varepsilon_t k_0^2 - \beta^2 = k_a^2 \tag{5.11}$$

where $\beta^2 = k_x^2 + k_y^2$ and k_a is the z-component of the propagation vector. For TM$_z$ (transverse magnetic to z) or *vertical* polarized waves,

$$k_z^2 = \varepsilon_t k_0^2 - \frac{\varepsilon_t}{\varepsilon_z}\beta^2 = k_b^2 \tag{5.12}$$

where k_b is the z-component of the propagation vector. Note that the uniaxial material produces two different propagation vectors in the medium for the two polarizations.

We now define the Fourier transform pair

$$E(x,y,z) = \iint\limits_{\infty} \tilde{E}(k_x,k_y,z) e^{jk_z z} e^{jk_y y} \; dk_x \; dk_y \tag{5.13a}$$

$$\tilde{E}(k_x,k_y,z) = \frac{1}{4\pi^2} \iint\limits_{\infty} E(x,y,z) e^{-jk_z z} e^{-jk_y y} \; dx \; dy. \tag{5.13b}$$

In the transform domain, the transverse fields can be written in terms of $\tilde{E}_z$ and $\tilde{H}_z$ as

$$\left(\varepsilon_t k_0^2 + \frac{\partial^2}{\partial z^2}\right) \tilde{E}_x = jk_x \frac{\partial}{\partial z} \tilde{E}_z + \omega\mu_0 k_y \tilde{H}_z \tag{5.14a}$$

$$\left(\varepsilon_t k_0^2 + \frac{\partial^2}{\partial z^2}\right) \tilde{E}_y = jk_y \frac{\partial}{\partial z} \tilde{E}_z - \omega\mu_0 k_x \tilde{H}_z \tag{5.14b}$$

$$\left(\varepsilon_t k_0^2 + \frac{\partial^2}{\partial z^2}\right) \tilde{H}_x = jk_x \frac{\partial}{\partial z} \tilde{H}_z - \omega\varepsilon_0 \varepsilon_t k_y \tilde{E}_z \tag{5.14c}$$

$$\left(\varepsilon_t k_0^2 + \frac{\partial^2}{\partial z^2}\right) \tilde{H}_y = jk_y \frac{\partial}{\partial z} \tilde{H}_z + \omega\varepsilon_0 \varepsilon_t k_x \tilde{E}_z \tag{5.14d}$$

where $\frac{\partial^2}{\partial z^2} = -k_z^2$ and k_z is either k_a for TE_z or k_b for TM_z waves. Using the dispersion relations in (5.11) and (5.12), the above equations can be simplified to

$$\tilde{E}_x = \frac{jk_x \varepsilon_z}{\varepsilon_t \beta^2} \frac{\partial}{\partial z} \tilde{E}_z + \frac{\omega\mu_0 k_y}{\beta^2} \tilde{H}_z \tag{5.15a}$$

$$\tilde{E}_y = \frac{jk_y \varepsilon_z}{\varepsilon_t \beta^2} \frac{\partial}{\partial z} \tilde{E}_z - \frac{\omega\mu_0 k_x}{\beta^2} \tilde{H}_z \tag{5.15b}$$

$$\tilde{H}_x = \frac{jk_x}{\beta^2} \frac{\partial}{\partial z} \tilde{H}_z - \frac{\omega\varepsilon_0 \varepsilon_z k_y}{\beta^2} \tilde{E}_z \tag{5.15c}$$

$$\tilde{H}_y = \frac{jk_y}{\beta^2} \frac{\partial}{\partial z} \tilde{H}_z + \frac{\omega\varepsilon_0 \varepsilon_z k_x}{\beta^2} \tilde{E}_z. \tag{5.15d}$$

Extending [74], if we assume solutions for $\tilde{E}_z$ and $\tilde{H}_z$ in region 1 have the form

$$\tilde{E}_z = e^{jk_{z_0} z} + Ae^{-jk_{z_0} z} \tag{5.16a}$$

$$\tilde{H}_z = e^{jk_{z_0} z} + Be^{-jk_{z_0} z} \tag{5.16b}$$

and in region 2 have the form

$$\tilde{E}_z = C\cos k_b z + D\sin k_b z \tag{5.17a}$$

$$\tilde{H}_z = E\sin k_a z + F\cos k_a z, \tag{5.17b}$$

and apply the appropriate boundary conditions, the solution for the reflection coefficients for horizontal (A) and vertical (B) polarized electric fields can be determined. The exact horizontal and vertical reflection coefficients at the surface of the grounded uniaxial dielectric layer of thickness t with dielectric permittivity tensor given in (5.1) are

$$R_h = A = \frac{k_{z_0}\sin k_a t + jk_a \cos k_a t}{k_{z_0}\sin k_a t - jk_a \cos k_a t}\; e^{j2k_{z_0}t} \tag{5.18a}$$

$$R_v = B = \frac{\varepsilon_t k_{z_0}\cos k_b t - jk_b \sin k_b t}{\varepsilon_t k_{z_0}\cos k_b t + jk_b \sin k_b t}\; e^{j2k_{z_0}t} \tag{5.18b}$$

where $k_{z_0}=k_0\cos\theta_0$, $k_a=k_0\sqrt{\varepsilon_t-\sin^2\theta_0}$, and $k_b=k_0\sqrt{\varepsilon_t-\varepsilon_t/\varepsilon_z\sin^2\theta_0}$. The explicit expressions for the reflection coefficients in (4.65) and (5.18) have not been found in the literature.

A simple check of (5.2), (5.3), and (5.5) reveals that when the filling fraction approaches zero (0), the permittivities ε_t and ε_z approach the permittivity of a homogeneous background, ε_a. When the filling fraction approaches one (1), the permittivities ε_t and ε_z approach the permittivity of the materials blocks or inclusions, ε_b. Consequently, the solutions for the horizontal and vertical reflection coefficients in (5.18) reduce to the exact horizontal and vertical reflection coefficients at the surface of the grounded dielectric layer of thickness t and relative permittivity ε_r found in (4.65a) and (4.65b).

As the filling fraction varies from one (1) to zero (0) for electrically small cells, the phase angle of the horizontal and vertical reflection coefficients determined using the method of moments solution should vary between the exact value obtained from a grounded dielectric layer and the exact value obtained from a ground plane alone. The phase angles of the horizontal and vertical reflection coefficients for grounded substrates having filling fractions between these bounds are calculated in columns two through five of Table 5.2 using the IE/MoM solution employing polarization currents. The values listed in columns two and three are calculated using 192 unknown subsectional bases (N_x=N_y=N_z=4 for each of the three polarizations) and in columns four and five using 288 unknown subsectional bases (N_x=N_y=4 and N_z=6 for each polarization). As was mentioned at the end of Chapter 4, fewer unknowns per wavelength are required to model the transverse variation to obtain a given accuracy because the fields are more smoothly varying in the transverse direction. The phase angles for the equivalent grounded uniaxial medium are calculated using the analytical solutions in (5.18) and are listed in columns six and seven. The longitudinal and transverse components of the permittivity tensor calculated from (5.2) and (5.6) are listed in columns eight and nine of Table 5.2. Both solutions are obtained for a grounded dielectric layer of relative permittivity ε_r=2.56 with thickness t=0.15λ_d, incident angles ϕ_0=45° and θ_0=45°, and unit cell size of a=0.25λ_0 at z_0=20t. Again, the solutions were

Table 5.2: Phase angle for R_h and R_v at z_0=20t for a grounded dielectric layer of relative permittivity ε_r=2.56 and dielectric thickness t=0.15λ_d as a function of filling fraction b/a for 192 unknowns and 288 unknowns for N_p=N_q=61, ϕ_0=45°, θ_0=45°, and a=0.25λ_0

	IE/MoM (N_x=N_y=N_z=4)		IE/MoM (N_x=N_y=4, N_z=6)		Uniaxial			
b/a	$\angle R_h$	$\angle R_v$	$\angle R_h$	$\angle R_v$	$\angle R_h$	$\angle R_v$	ε_z	ε_t
1.00	-67.00°	87.30°	-66.20°	88.67°	**-64.99°**	**89.52°**	2.56	2.56
0.90	-63.42°	95.15°	-62.87°	95.20°	**-61.43°**	**95.25°**	2.26	2.10
0.75	-59.90°	103.77°	-59.60°	103.30°	**-58.40°**	**102.05°**	1.88	1.65
0.50	-56.56°	115.48°	-56.48°	114.79°	**-55.95°**	**112.16°**	1.39	1.25
0.25	-55.01°	123.33°	-55.00°	123.83°	**-54.90°**	**121.27°**	1.10	1.06
0.00	-54.59°	125.41°	-54.59°	125.41°	**-54.59°**	**125.41°**	1.00	1.00

determined using at most 3721 Floquet modes (N_p=N_q=61). However, the error criterion given in (4.76) of $\varepsilon_c < 0.001$ was often satisfied by far fewer Floquet contributions. For the data shown in Tables 5.2–5.4, the magnitudes of R_h and R_v are close to the expected value of 1. Although the IE/MoM solution procedure is valid for any number of subsectional bases, the effort to evaluate the impedance matrix elements for unit cell spacings larger than a=0.25λ_0 can become so large as to be computationally difficult. Fortunately, the accuracy of the emulated uniaxial model increases with decreasing unit cell size (electrically small unit cells). The accuracy of the magnitude and phase of the horizontal and vertical reflection coefficients determined from the IE/MoM solutions suggests the model for the equivalent uniaxial medium is valid.

In Table 5.3, the computation of the horizontal and vertical reflection coefficients is carried out for the same parameter set as in the previous table but for an asymmetric incident angle (ϕ_0=60° and θ_0=30°) and is seen to again compare favorably with the solution obtained for the uniaxial model.

In Table 5.4, the computation of the horizontal and vertical reflection coefficients is carried out for the same parameters as Table 5.2 but for a dielectric constant of ε_r=6.15 and is seen to again compare favorably with the solution obtained for the uniaxial model. However, the solution obtained using only 192 unknowns (N_x=N_y=N_z=4 for each of the three polarizations) is less accurate than the case tabulated in Table 5.2. This is to be expected

Table 5.3: Phase angle for R_h and R_v at z_0=20t for a grounded dielectric layer of relative permittivity ε_r=2.56 and dielectric thickness t=0.15λ_d as a function of filling fraction b/a for 188 unknowns, N_p=N_q=61, ϕ_0=60°, θ_0=30°, and a=0.25λ_0

	IE/MoM		Uniaxial			
b/a	$\angle R_h$	$\angle R_v$	$\angle R_h$	$\angle R_v$	ε_z	ε_t
1.00	76.75°	-113.02°	**78.49°**	**-111.78°**	2.56	2.56
0.90	80.58°	-107.70°	**82.70°**	**-106.71°**	2.26	2.10
0.75	84.62°	-101.67°	**86.30°**	**-101.56°**	1.88	1.65
0.50	88.52°	-94.52°	**89.24°**	**-95.48°**	1.39	1.25
0.25	90.36°	-90.32°	**90.50°**	**-91.00°**	1.10	1.06
0.00	90.87°	-89.13°	**90.87°**	**-89.13°**	1.00	1.00

since the electrical length in the dielectric material increases with increasing permittivity. The solution obtained using 288 unknowns (N_x=N_y=4 and N_z=6 for each polarization) is more accurate and suggests the model for the equivalent uniaxial medium is valid.

Table 5.4: Phase angle for R_h and R_v at z_0=20t for a grounded dielectric layer of relative permittivity ε_r=6.15 and dielectric thickness t=0.15λ_d as a function of filling fraction b/a for 192 unknowns and 288 unknowns for N_p=N_q=61, ϕ_0=45°, θ_0=45°, and a=0.25λ_0

	IE/MoM (N_x=N_y=N_z=4)		IE/MoM (N_x=N_y=4, N_z=6)		Uniaxial			
b/a	$\angle R_h$	$\angle R_v$	$\angle R_h$	$\angle R_v$	$\angle R_h$	$\angle R_v$	ε_z	ε_t
1.00	-86.95°	63.27°	-88.05°	64.12°	**-86.45°**	**65.42°**	6.15	6.15
0.90	-85.45°	71.96°	-84.17°	72.52°	**-80.74°**	**74.19°**	5.17	3.80
0.75	-81.19°	81.21°	-80.50°	80.84°	**-78.05°**	**79.83°**	3.90	2.37
0.50	-77.51°	93.40°	-77.42°	92.43°	**-76.57°**	**86.96°**	2.29	1.46
0.25	-76.15°	101.71°	-76.15°	101.27°	**-76.05°**	**96.76°**	1.32	1.11
0.00	-75.91°	104.09°	-75.91°	1104.09°	**-75.91°**	**104.09°**	1.00	1.00

5.4 Rectangular Patch Antenna on a Positive Uniaxial Substrate

Some general observations concerning patch antenna performance are in order before the effect of anisotropy is addressed. The bandwidth and efficiency of a patch are increased by increasing the thickness of the substrate or decreasing the relative dielectric constant. This statement is physically reconciled by viewing the patch antenna as a resonant cavity with two radiating slots at the end of the patch. As the radiating cavity is more loosely bound either by increasing the substrate thickness or by decreasing the permittivity, the Q of the resonator lessens; thus, the bandwidth widens. However, as was mentioned in the introduction, integrating antenna structures on high permittivity substrates is advantageous for circuit integration and for minimizing circuit/antenna size. The resulting consequence of using the higher permittivity substrates is that the potential radiating energy is confined even more tightly, narrowing the bandwidth. Higher permittivity substrates also necessitates additionally thinning the substrate to reduce the formation of unwanted surface waves, further reducing the bandwidth and efficiency.

Additionally, many of the practical substrates in use today have some amount of (uniaxial) anisotropy. Anisotropy occurs naturally in some materials, whereas in others, it is artificially produced in the manufacturing process. The characterization of the effect of anisotropy on resonant length (frequency), bandwidth, and other design parameters is of importance to the microwave community. The primary effect of uniaxial anisotropy on patch antennas is the change in resonant length (frequency). This is significant because of the narrow bandwidth of the patch itself. The relatively large shift in resonant frequency produced in many of the modern substrates may actually force a rectangular patch designed to operate at a specific frequency to radiate outside of the antenna bandwidth [74].

In Figure 5.5 is depicted an example design where the patch length L is 2.29 cm, the patch width W is 1.9 cm, and the substrate thickness d is 0.159 cm. A coaxial probe is used to feed the patch. It is necessary to match the probe impedance to the input impedance of the patch. The input impedance Z_A at the edge of a radiating patch is approximated [110] as

$$Z_A = 90\frac{\varepsilon_r^2}{\varepsilon_r - 1}\left(\frac{L}{W}\right)^2 (\Omega) \tag{5.19}$$

where ε_r is the permittivity of the homogeneous substrate. For the example patch of Figure 5.5, Z_A=163 Ω. In order to properly match the coax probe to the patch, the probe

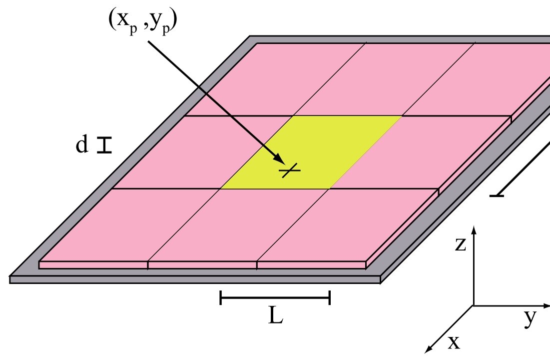

Figure 5.5: Geometry for a rectangular patch on a grounded dielectric substrate

is inset a distance Δx_p from the patch edge. The input resistance of (5.19) is reduced by the factor $\cos^2(\pi \Delta x_p/L)$ as the distance Δx_p from the edge is increased [37]. To correctly match a 50 Ω coaxial probe to the example patch, the inset distance should be 0.40 cm from the radiating edge.

For a rectangular patch on a homogeneous substrate with relative dielectric constant ε_r, the lowest resonant frequency can be accurately predicted from [7] as

$$f_r = \frac{c}{2\left(L + 2\Delta L\right)\sqrt{\varepsilon_{\text{eff}}}} \tag{5.20a}$$

where

$$\Delta L = 0.412d \frac{(\varepsilon_{\text{eff}} + 0.3)}{(\varepsilon_{\text{eff}} - 0.256)} \frac{(W/d + 0.264)}{(W/d + 0.8)} \tag{5.20b}$$

and

$$\varepsilon_{\text{eff}} = \frac{\varepsilon_r + 1}{2} + \frac{\varepsilon_r - 1}{2} \frac{1}{\sqrt{1 + 12d/W}}, \quad \text{for } W/h >> 1. \tag{5.20c}$$

Thus, for the patch design of Figure 5.5, the effective dielectric constant is ε_{eff}=2.13 and the resonant frequency f_r is predicted to be 4.194 GHz. A simulation of the patch using Ansoft HFSS finds the lowest resonant frequency to be 4.125 GHz. This is close to the value of 4.123 GHz calculated in [14] using a spectral domain MoM approach and also to the measured value of 4.014 GHz given in [7]. The bandwidth BW of the resonant patch can be approximated from [110] as

$$BW = 3.77 \frac{\varepsilon_r - 1}{\varepsilon_r^2} \frac{W}{L} \frac{d}{\lambda}. \tag{5.21}$$

For the example design shown in Figure 5.5, the bandwidth is 1.85%.

When the anisotropic ratio is decreased to 0.5 (ε_t=2.32, ε_z=4.64), the resonant frequency found from the finite element simulation shifts to the lower frequency of 3.015 GHz. This value is consistent with the value of 3.032 GHz given in [14] for the same AR shift. However, for the same AR=0.5 but ε_z=2.32, the resonant frequency shifts to 4.200 GHz and the fractional change is on the order of the bandwidth of the antenna (Δ_f/f_r=1.82). This value is also consistent with with the value of 4.175 GHz given in [14] for the same configuration. However, if the AR remains fixed and ε_z is increased to 4.64, the fractional change in resonant frequency is *significantly* larger than the bandwidth. The dependence of the resonant frequency f_r and bandwidth Δ_f/f_r on the anisotropy for the rectangular patch design is presented in Table 5.5.

Table 5.5: Dependence of resonant frequency on substrate permittivity

ε_t	ε_z	AR	f_r (GHz)	$\Delta f/f_r$
2.32	2.32	1	4.125	0
1.16	2.32	0.5	4.200	1.82
2.32	4.64	0.5	3.015	26.9

Unlike (5.20), no general expression has been found to predict patch behavior on a uniaxial substrate. However, it is well-known that the effect of anisotropy increases with substrate thickness. While a significant amount of energy is coupled into the z-component of the electric field of the TM modes for electrically small substrates, very little energy is directed into the TE modes. However, as the substrate thickness increases, more energy is coupled into the transverse component of the electric field that comprise the TE modes. Consequently, the dependence on the transverse permittivity is increased and the effect of the anisotropy more pronounced [74, 123]. Hence, for electrically thin substrates, the dependence of design parameters such as resonant length and bandwidth should be strongly dependent only on ε_z.

If, for the previous example where the anisotropic ratio has been decreased to 0.5 and ε_z=4.64, the relative dielectric constant in (5.20) is replaced with the corresponding ε_z, the predicted resonant frequency of the patch is 3.042 GHz. This is reasonably close to the value determined from the simulation and to the value of 3.032 GHz given in [14]. This observation is also consistent with results presented in [14] that the fractional change in the resonant frequency is strongly dependent on ε_z. By modeling the uniaxial material as a doubly periodic dielectric layer, the understanding of this dependence can be shown even more clearly.

Consider a rectangular patch integrated on a uniaxial substrate. The uniaxial substrate can be modelled as a homogeneous dielectric layer with periodic inclusions in two directions. Because the axial and transverse components of the permittivity tensor of the uniaxial substrate are known, the homogeneous permittivity and filling fraction of the doubly periodic substrate can be found through (5.5) and (5.2). For an electrically thin substrate, the effect of removing material from underneath the patch is a volumetric "averaging" of the dielectric constant. This assumption is intuitively appealing and is probably valid for thin substrates, but may not hold as the thickness of the substrate increases (and consequently the dependence on the transverse permittivity).

As was pointed out earlier, the equivalent axial component of the permittivity tensor of the emulated periodic substrate is effectively the volumetric average of the two phases. For example, sapphire which has an AR of 0.81 (ε_t=9.4, ε_z=11.6) is modelled in the HFSS material library as a homogeneous substrate with relative dielectric constant ε_r=10. However, sapphire can be modeled by a medium consisting of periodic air inclusions in a dielectric background with dielectric constant of 16.0 and filling fraction equal to 0.3 as seen in Figure 5.4(b). If one simply takes the volume averages of the two phases as the effective permittivity ε_{eff} of the equivalent substrate, one finds that ε_{eff}=11.6 *which is very close the value of the axial component of the permittivity tensor*. This effective permittivity is not to be confused with the equivalent homogeneous permittivity that can be determined from (5.20). Clearly, modeling a sapphire substrate as a homogeneous substrate with an "effective" permittivity would yield a very different resonant frequency than if the uniaxial nature of the material is taken into account. In fact, the lowest resonant frequency of the patch shown in Figure 5.5 when integrated on a substrate of permittivity ε_r=10 yields a predicted resonant frequency from (5.20) of 2.173 GHz. However, if the true uniaxial nature is taken into account, the resonant frequency should be 2.022 GHz. Since the resonant frequency and electrical length of the patch are directly related, one can interpret the effect of the increased axial component as an effective lengthening of the patch. This interpretation is confirmed when one views the patterns produced by the patch antenna.

Anisotropic effects shape the radiation pattern of the patch and thus in an array configuration, the coupling to other elements. For the example depicted in Figure 5.5, the E- and H-plane patterns are determined for both homogeneous (ε_t=2.32, ε_z=2.32) and anisotropic (ε_t=2.32, ε_z=4.64) substrates. The H-plane patterns shown in Figure 5.6(b) are relatively independent of the AR and ε_z. However, the E-plane patterns shown in Figure 5.6(a)

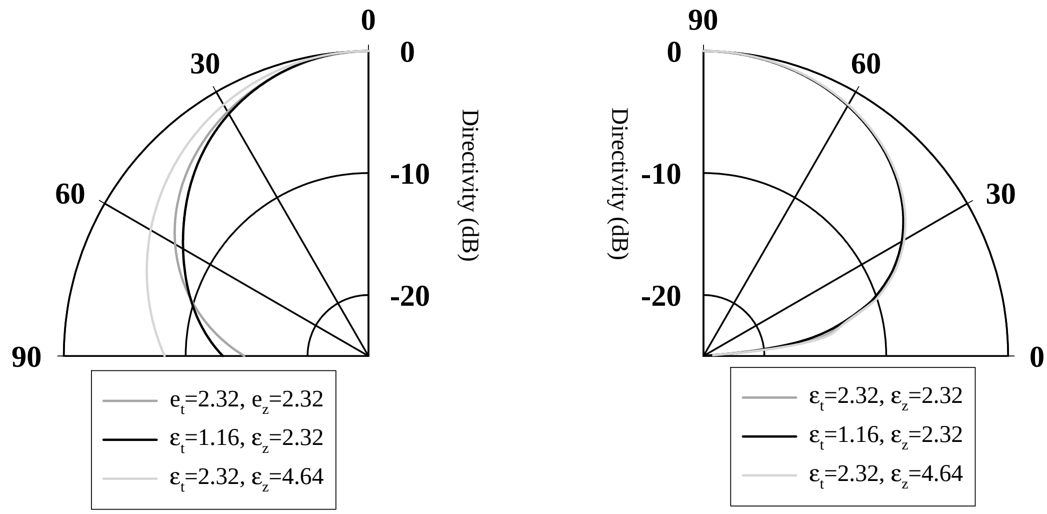

(a) E-plane

(b) H-plane

Figure 5.6: Directivity patterns for reference patch with AR=1 and AR=0.5

show a strong dependence on ε_z. This is intuitively correct if one assumes that for thin substrates, the dependence is on ε_z alone. Thus, if the true axial component is ignored for substrates with positive anisotropic ratios, the beamwidth will be wider than designed and consequently the mutual coupling in an array environment may affect the performance of such an antenna. The observation that the E-plane beamwidth is affected by the anisotropy while the H-plane beamwidth is not affected by it is consistent with approximations for the beamwidths given in [11]. The E-plane and H-plane beamwidths can be approximated by [11]

$$\Theta_E \simeq 2\cos^{-1}\sqrt{\frac{7.03\lambda_0^2}{4(3L_e^2 + d^2)\pi^2}} \tag{5.22a}$$

$$\Theta_H \simeq 2\cos^{-1}\sqrt{\frac{1}{2 + k_0 W}} \tag{5.22b}$$

where L_e is the effective length of the patch. As the effective length of the patch is increased, the E-plane beamwidth decreases. The H-plane beamwidth is independent of L_e.

5.5 Conclusions

Because uniaxial substrates are often expensive to manufacture and have limited flexibility for design, uniaxial substrates can be emulated (and easily fabricated) by incorporating periodic inclusions in an otherwise homogeneous substrate. The doubly periodic structure can be easily constructed using simple milling or etching techniques from simple inexpensive, homogeneous substrates. This is significant because some common uniaxial materials such as sapphire that are expensive to grow can be "artificially" replicated easily and inexpensively. Additionally, the artificial nature of the periodic uniaxial substrate permits the creative design of new substrates with the expanded freedom of anisotropic ratio, background permittivity, and/or fabrication technique. The primary effect of anisotropy on rectangular patch antennas is the change in its resonant length (frequency). This is significant because of the narrow bandwidth of the patch. The relatively large shift in resonant frequency produced in many of the modern substrates may actually force a rectangular patch designed to operate at a specific frequency to radiate outside of the antenna bandwidth. In addition to providing freedom of design, modeling uniaxial materials using the doubly periodic model provides an insightful understanding of the dependence of the performance of the substrate on its uniaxial nature.

CHAPTER 6

Recommendations For Future Work

One of the more interesting physical features that can be altered in the solution of the one- and two-dimensional periodic media is the specification of an arbitrarily shaped dielectric. Both the IE/MoM solution and plane wave expansion method can be adapted to provide for optimized dielectric functions. Two potential applications for effective medium theory that promise to be of value are the extension of EMT to off-axis propagation in two-dimensional lattices and to out-of-plane propagation in two-dimensional lattices. A number of new applications can be developed using the solution technique implemented in Chapter 4 and 5 including new frequency selective volumes, incorporating noncommensurate periodicities for each layer, incorporating material implants within each layer of differing relative permittivity (dielectric and/or metallic loading), and the extension of the solution to large planar antenna elements. The formulation also has the flexibility of providing that each layer have different element shape and/or permittivity.

6.1 Arbitrarily Shaped Dielectric Function

By optimizing the dielectric function, improvements in design and performance can be achieved for applications at both optical and microwave frequencies. The optimization is accomplished through the use of genetic algorithms, neural networks, and other "smart" algorithms. The design of a unique dielectric function is achieved by allowing the optimizing algorithm or morphing program to vary the different parameters, such as unit cell size, filling fraction, element shape, and/or relative permittivity, until a desired response is obtained. Using the IE/MoM solution, unique configurations can be formed by selectively removing individual polarization currents from the solution, commonly referred to in antenna engineering as *thinning*. This is accomplished in a similar fashion to thinning the number of elements in a phased array antenna. For the plane wave expansion method, the optimization is accomplished by computing the fast Fourier transform (FFT) of the discretized dielectric function. Each time the dielectric function is changed, a new FFT is performed to determine the new Fourier coefficients.

Figure 6.1: Optimized frequency selective layer (volume)

New materials with unique spectral characteristics are constantly being developed and can be incorporated into existing designs that in turn can be optimized for performance. An example of a structure that might be produced by an optimizing algorithm is seen in Figure 6.1, where specific individual blocks of material have been removed from a large unit cell. The optimized structure might have application as a frequency selective layer (volume) for use in radome applications. Additionally, lattices of dielectric elements with differing dielectric constants can be included to provide additional freedom in the design. In the IE/MoM solution, the polarization currents incorporate the permittivity change. In the plane wave expansion method, a new dielectric function must be developed. As illustrated in Figure 6.2, electrical loading of the layer is realized by incorporating two

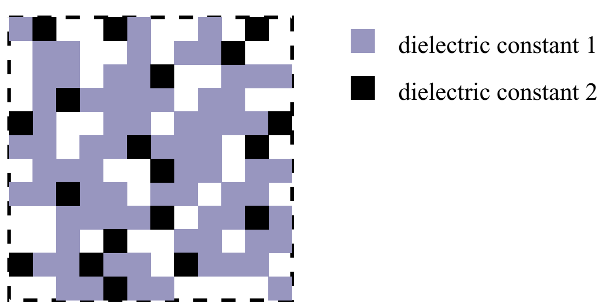

Figure 6.2: Dielectric and/or metallic loading

different dielectrics or perhaps including metallic regions in the design. Currently, an entire class of PBG materials, metallic photonic band-gap (MPBG) materials composed of metallic lattice elements, are being investigated [62].

Another application where optimizing the dielectric function might be useful is supercell theory. A supercell is a unique geometrical configuration comprised of two or more unit cells, each with same structure. An example of a supercell can be seen in Figure 6.3 where the individual unit cell of Figure 6.1 has been periodically repeated. In order that the spectral response of the supercell layer be distinct from the response of a uniform layer of effective permittivity, the spacing between the individual elements must be on the order of a quarter of a wavelength. Consequently, applications that use the supercell design have the disadvantage of being electrically and, depending on the frequency, physically large. Although the response of the supercell might be excellent, the electrical and physical size of the resulting structure might by impractical.

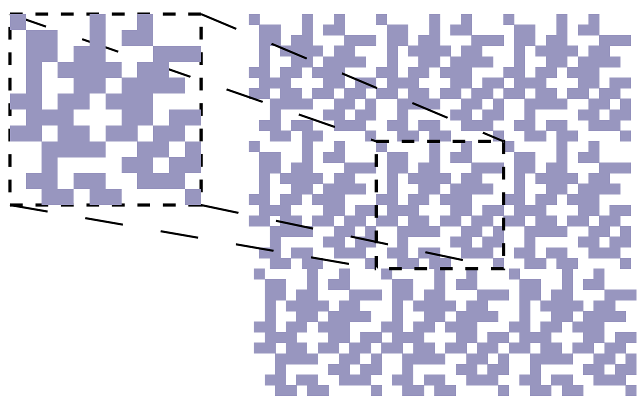

Figure 6.3: Frequency selective supercell

6.2 Extensions of Effective Medium Theory

To simplify the computation of the band structure for two-dimensionally periodic media, *effective medium theory* was applied in Chapter 3 to reduce the two-dimensional periodic structure to a one-dimensional equivalent structure. Using EMT, each periodic row is replaced by a thin homogeneous layer of effective permittivity [50] which is determined solely as a function of the geometrical and electrical parameters of the lattice. Unfortunately, traditional EMT is restricted to near normal incidence precluding its use for many applications of interest. Consider the two-dimensional lattice with dielectric constant ε_2 immersed in a background with dielectric constant ε_1 illustrated in cross-section in Figure 6.4. Assume a plane wave is incident in a direction along a ray direction defined by an angle ϕ with respect

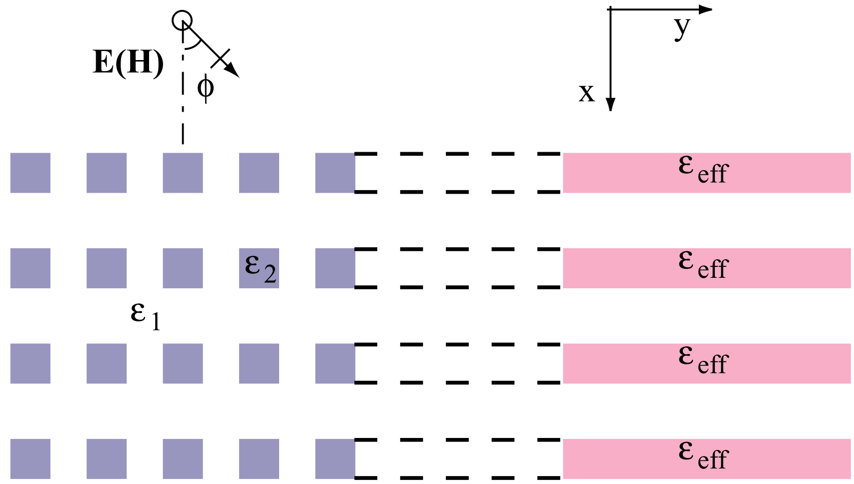

Figure 6.4: Higher-order effective medium theory

to the x axis ($\phi = 0°$). An extension of EMT to off-axis propagation would allow EMT to be useful in some planar antenna applications. Another effective EMT extension would be to model the hybrid modes that are formed for off-plane propagation in two-dimensional lattices.

6.3 Noncommensurate Periodicities

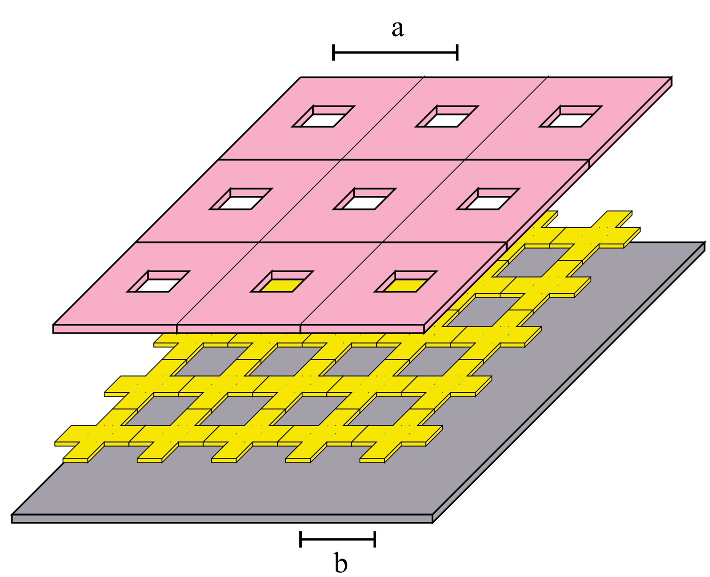

Figure 6.5: Noncommensurate periodicities

The solution of scattering from a multilayered medium is often accomplished using a generalized scattering matrix (GSM) technique [136] which relates the modes that propagate in one layer to the corresponding modes in adjacent layers. The solution of scattering from a multilayered medium where each layer has a unique period has only recently be solved and then only for commensurate periodicities [12]. An example of a multilayered medium where each layer has a unique period is illustrated in Figure 6.5. The solution found in [12] relates the local Floquet modes within each layer to the global Floquet modes in the structure. The solution is straightforward but relies on a tremendous amount of bookkeepping. A new solution to this problem would be of tremendous value.

6.4 Extensive Parametric Study of Antenna Performance Near a Periodic Structure

An extensive parametric study of the factors that impact the performance of an antenna integrated on a periodic surface would be valuable to the microwave community. The salient properties of the antenna, such as its input impedance, bandwidth, beamwidth, directivity, gain, efficiency, polarization, and mutual coupling in an array environment, are all determined by the antenna's electrical size, physical configuration, and the environment in which it is located. For planar resonant patches alone, the designer has a multiplicity of factors that must be considered. These include, but are not limited to, the material properties of the substrate such as dielectric constant, loss tangent, anisotropy, and the ease of fabrication; the physical considerations of patch shape, patch size, and system integration; and for realizable antennas, the practical considerations of feed location, feeding technique, and design cost.

Although some attention has been directed at patch antenna performance on uniaxial substrates, it has been limited to idealized cases and simple observations. The need exists for a complete treatment of antennas located near periodic surfaces and structures. This can only be accomplished if extensive parametric studies are performed to determine the resulting effects. For example, planar antennas mounted on substrates of significant thickness (often used to increase bandwidth) radiate most of their energy into the substrate creating surface waves that propagate in specific directions. The reduction or elimination of these surface waves in planar antenna application has been the Holy Grail of microwave antenna engineers for many years. If an appropriate design for a periodic substrate that supports the planar antenna can be found that reduces or eliminates the formation of these waves, significant improvements in performance will be achieved.

As the need for very wideband, omni-directional antennas for use in mobile communication networks grows at an increasing rate, so does the need to develop new fabrication technologies, advanced materials engineering, and novel antenna architectures to meet the challenge. Tomorrow's RF engineer has the task of developing new and useful ideas in addition to developing previously found materials and concepts to their fullest potential.

APPENDICES

APPENDIX A

Transmission Line Formulation for the One-Dimensional Periodic Array of Dielectric Slabs

Transmission line theory allows one to formulate a simple solution for the propagation of transverse electromagnetic waves (TEM) through periodic dielectric slabs. The dielectric slabs and free-space regions are modeled by short sections of transmission line as seen in Figure A.1(a) where b is the length of the shorter section BB' with characteristic impedance Z_d and propagation constant $\gamma_d = j\beta_d$, a is the length of the entire transmission line section AA', Z_0 is the characteristic impedance of the free-space transmission line sections, $j\beta_0$ is the propagation constant of the free-space sections, and $d = (b-a)/2$. Due to the periodic nature of the structure, the propagation constant through the structure can be determined by analyzing one unit cell. For waves propagating through the structure, the voltage $\mathbf{V}_{A'}$ and current $\mathbf{I}_{A'}$ at the A' plane is required to be the same, except for a propagation factor, as the value of $\mathbf{V}_A$ and $\mathbf{I}_A$ at the A plane, or

$$\mathbf{V}_{A'} = \mathbf{V}_A e^{-\gamma a} \quad \text{and} \quad \mathbf{I}_{A'} = \mathbf{I}_A^{-\gamma a} \tag{A.1}$$

where $\gamma = \alpha + j\beta$ is the propagation constant of the line and a is the length of the line. The input impedance at the A and A' planes is defined as

$$Z_p = \frac{\mathbf{V}_A}{\mathbf{I}_A} = \frac{\mathbf{V}_{A'}}{\mathbf{I}_{A'}}. \tag{A.2}$$

The equivalent transmission line model is shown in Figure A.1(b).

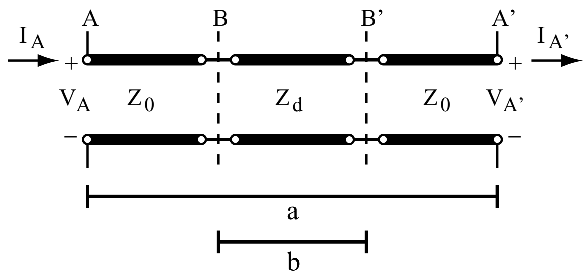

(a) Loaded transmission line circuit

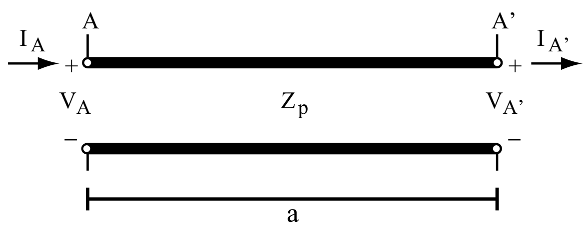

(b) Equivalent transmission line circuit

Figure A.1: Loaded and equivalent transmission line circuits

The ABCD matrix for the transmission line in Figure A.1(a) is

$$A = \cosh \gamma_d b \;\; \cos 2\beta_0 d + j\left(\frac{Z_d^2 + Z_0^2}{2Z_d Z_0}\right) \sinh \gamma_d b \;\; \sin 2\beta_0 d \tag{A.3}$$

$$B = jZ_0 \cosh \gamma_d b \;\; \sin 2\beta_0 d + \sinh \gamma_d \left(\frac{Z_d^2}{Z_0} \cos^2 \beta_0 d - \frac{Z_0^2}{Z_d} \sin^2 \beta_0 d\right) \tag{A.4}$$

$$C = \frac{j}{Z_0} \cosh \gamma_d b \;\; \sin 2\beta_0 d + \sinh \gamma_d \left(\frac{Z_0^2}{Z_d} \cos^2 \beta_0 d - \frac{Z_d}{Z_0^2} \sin^2 \beta_0 d\right) \tag{A.5}$$

$$D = \cosh \gamma_d b \;\; \cos 2\beta_0 d + j\left(\frac{Z_d^2 + Z_0^2}{2Z_d Z_0}\right) \sinh \gamma_d b \;\; \sin 2\beta_0 d. \tag{A.6}$$

The ABCD matrix for the equivalent transmission line in Figure A.1(b) is

$$A = \cosh \gamma a \tag{A.7}$$

$$B = Z_p \sinh \gamma a \tag{A.8}$$

$$C = \frac{1}{Z_p} \sinh \gamma a \tag{A.9}$$

$$D = \cosh \gamma a \tag{A.10}$$

where Z_p is the effective input impedance of the equivalent section and γ is the propagation constant of the line.

The propagation constant γ of the equivalent circuit, and thus, for the periodic structure, is obtained easily from the two ABCD matrices to be the solution of the following transcendental equation

$$\cosh\gamma a = \cosh\gamma_d b\ \cos 2\beta_0 d + j\left(\frac{Z_d^2 + Z_0^2}{2Z_d Z_0}\right)\sinh\gamma_d b\ \sin 2\beta_0 d \tag{A.11}$$

which can be solved using a numerical solver such as MATLAB. The input impedance of the line can be found by equating the ratio of (A.4) and (A.5) and the ratio of (A.8) and (A.9)

$$Z_p = Z_0\left[\frac{jZ_0\cosh\gamma_d b\ \sin 2\beta_0 d + \sinh\gamma_d b\left(\frac{Z_d^2}{Z_0}\cos^2\beta_0 d - \frac{Z_0^2}{Z_d}\sin^2\beta_0 d\right)}{\frac{j}{Z_0}\cosh\gamma_d b\ \sin 2\beta_0 d + \sinh\gamma_d b\left(\frac{Z_0^2}{Z_d}\cos^2\beta_0 d - \frac{Z_d^2}{Z_0}\sin^2\beta_0 d\right)}\right]^{1/2}. \tag{A.12}$$

The frequencies where the right hand side of (A.11) returns a value greater than unity and γ is purely real ($\gamma = \alpha$) define the stopband of the structure. At frequencies where $\cosh\gamma a < 1$, the propagation constant is purely imaginary ($\gamma = j\beta$). These frequencies define the passband of the structure. The results obtained from these equations yield solutions that agree with the results obtained using the method moments solution and the solution of the exact eigenvalue equation. Additionally, the solutions obtained in (A.11) and (A.12) are identical to (9-153) and (9-154) in [78] with the exception that the solutions contained herein are more general, being derived for a short section of reactively loaded line of length b, as opposed to an inductively loaded case as in [78].

Other useful forms, analogies, and derivations of the exact dispersion relation for one-dimensionally periodic dielectric slabs can be found in [16, 55, 107, 26].

APPENDIX B

Bravais Lattices and the Brillouin Zone

An important concept in propagation through two- and three-dimensional periodic media are direct and reciprocal lattices. For two-dimensional periodic structures, the direct lattice must belong to one of the five two-dimensional Bravais (or space) lattices illustrated in Figure B.3 on page 143. Three-dimensional lattices (crystals) have 32 unique space lattices (with three dimensions of freedom) that can be formed. A discussion of three-dimensional crystalline structures is beyond the scope of this work and the reader is referred to an introductory text on solid state physics such as Kittel [44].

Direct lattice

The direct lattice in Figure B.1(a) is defined by the length of the two primitive lattice vectors $\mathbf{a}$ and $\mathbf{b}$ and the angle γ between the vectors in the plane perpendicular to $\mathbf{a} \times \mathbf{b}$. The unit cell of Figure B.1 is completed by the dashed lines, has an area of $|\mathbf{a}||\mathbf{b}| \sin \gamma$, and

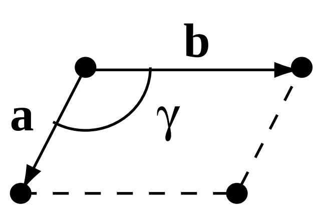

(a) Direct lattice

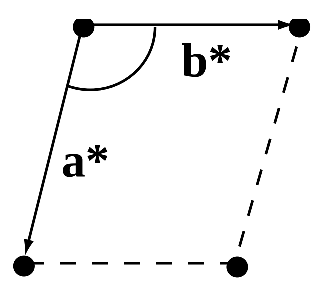

(b) Reciprocal lattice

Figure B.1: Direct lattice defined using the primitive lattice vectors $\mathbf{a}$ and $\mathbf{b}$ and the reciprocal lattice defined using the primitive reciprocal lattice vectors $\mathbf{a}^*$ and $\mathbf{b}^*$

is invariant under the translation $m\mathbf{a}+n\mathbf{b}$ for any integers $\{m, n\}$. For the two-dimensional structures implemented in this work, the primitive lattice vectors represent the physical distance between the periodic elements (dielectric rods or air columns).

Reciprocal lattice

In many instances the solution of a problem defined on a periodic lattice is more convenient to implement in Fourier space. Thus, it is convenient to define a reciprocal lattice space. The reciprocal lattice in Figure B.1(b) is defined by two primitive reciprocal lattice vectors $\mathbf{a}^*$ and $\mathbf{b}^*$. The construction of $\mathbf{a}^*$ and $\mathbf{b}^*$ is simple — the only requirement being that $\mathbf{a}\cdot\mathbf{a}^*=\mathbf{b}\cdot\mathbf{b}^*=2\pi$ and $\mathbf{a}\cdot\mathbf{b}^*=\mathbf{a}^*\cdot\mathbf{b}=0$. As a consequence of using plane waves to expand the periodic function, the normalization is set equal to 2π.

Example 1. Square lattice of Figure B.3(b) with spacing *d*

$$\begin{aligned} \mathbf{a} &= -d\,\hat{\mathbf{y}} & \qquad \mathbf{b} &= d\,\hat{\mathbf{x}} \\ \mathbf{a}^* &= -\frac{2\pi}{d}\,\hat{\mathbf{y}} & \qquad \mathbf{b}^* &= \frac{2\pi}{d}\,\hat{\mathbf{x}} \end{aligned}$$

Example 2. Hexagonal lattice of Figure B.3(c) with spacing *d*

$$\begin{aligned} \mathbf{a} &= -\frac{d}{2}\,\hat{\mathbf{x}} - \frac{d\sqrt{3}}{2}\,\hat{\mathbf{y}} & \qquad \mathbf{b} &= d\,\hat{\mathbf{x}} \\ \mathbf{a}^* &= -\frac{4\pi}{d\sqrt{3}}\,\hat{\mathbf{y}} & \qquad \mathbf{b}^* &= \frac{2\pi}{d}\,\hat{\mathbf{x}} - \frac{2\pi}{d\sqrt{3}}\,\hat{\mathbf{y}} \end{aligned}$$

Clearly, for both examples, $\mathbf{a}\cdot\mathbf{a}^*=\mathbf{b}\cdot\mathbf{b}^*=2\pi$ and $\mathbf{a}\cdot\mathbf{b}^*=\mathbf{a}^*\cdot\mathbf{b}=0$.

Brillouin Zone

Periodic structures, particularly those with two- and three-dimensional periodicity, are by definition highly symmetric. Consequently, propagation through such media necessarily contains many redundant propagation vectors. The unique vectors can be found and categorized systematically using the concept of the *Brillouin zone* (BZ) [44] shown for a square regular lattice in Figure B.2. For the square lattice, all of the possible directions of propagation are grouped into eight regions with specific symmetry.[2] However, symmetry considerations reduce the number of unique regions of propagation to one. The colored region in the figure is called the *irreducible Brillouin zone* and represents the smallest region where propagation within the lattice is unique. This region is further defined by symmetric

[2] For the hexagonal lattice of Example 2, the Brillouin zone contains six groupings.

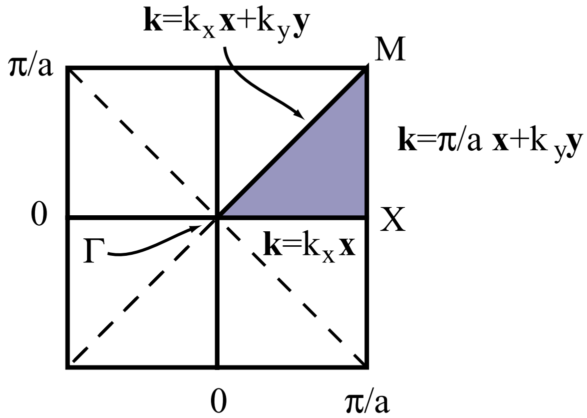

Figure B.2: Irreducible Brillouin Zone (BZ)

points within the lattice denoted Γ, M, and X. The Γ coordinate is defined by (k_x, k_y)=$(0, 0)$, the M coordinate by (k_x, k_y)=$(2\pi/a, 0)$, and the X coordinate by (k_x, k_y)=$(2\pi/a, 2\pi/a)$. In order to determine whether a mode is allowed to propagate, every possible vector that is located within the irreducible Brillouin zone must be checked. Fortunately, the band structure can be determined approximately by sampling the edges of the zone along the Γ–M line for modes of the form $\mathbf{k} = k_x\hat{\mathbf{x}} + 0\ \hat{\mathbf{y}}$, the M–X line for modes of the form $\mathbf{k} = 2\pi/a\ \hat{\mathbf{x}} + k_y\hat{\mathbf{y}}$ and the Γ–X line for modes of the form $\mathbf{k} = k_x\hat{\mathbf{x}} + k_y\hat{\mathbf{y}}$.

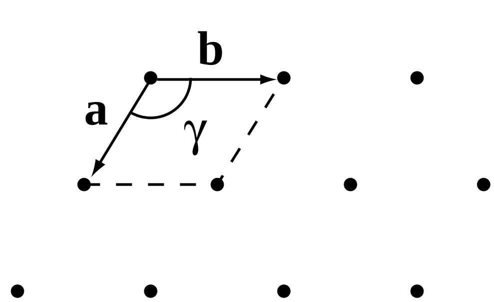

(a) Oblique lattice: $|\mathbf{a}| \neq |\mathbf{b}|; \gamma \neq 90^\circ$

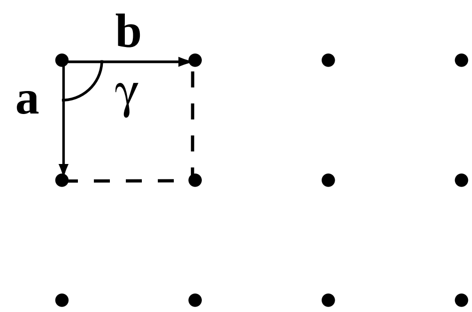

(b) Square lattice: $|\mathbf{a}| = |\mathbf{b}|; \gamma = 90^\circ$

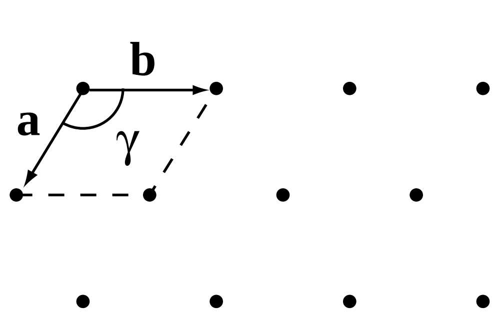

(c) Hexagonal lattice: $|\mathbf{a}| = |\mathbf{b}|; \gamma = 120^\circ$

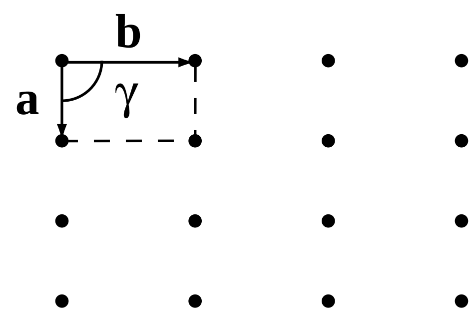

(d) Rectangular lattice: $|\mathbf{a}| \neq |\mathbf{b}|;\gamma = 90^\circ$

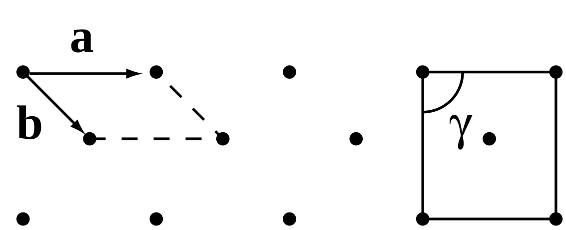

(e) Centered rectangular lattice: $|\mathbf{a}| \neq |\mathbf{b}|; \gamma = 90^\circ$

Figure B.3: Two-dimensional Bravais (or space) lattices

APPENDIX C

Impedance Matrix Elements for Two-Dimensional Periodic Structures

TM$_z$ Case

Piecewise constant expansion / Piecewise constant testing

$$Z_{mn} = \frac{jk_0 Z_0 \Delta_x^2 \Delta_y^2}{ac} \sum_{p,q} \operatorname{sinc}^2\left(\frac{k_{x_p}\Delta_x}{2}\right) \operatorname{sinc}^2\left(\frac{k_{y_q}\Delta_y}{2}\right) \frac{e^{-jk_{x_p}(x_m - x_n)} e^{-jk_{y_q}(y_m - y_n)}}{k_0^2 - k_{x_p}^2 - k_{y_q}^2} \quad \text{(C.1)}$$

$$\delta Z = -\frac{\delta_{mn}\Delta_x \Delta_y}{jk_0 Y_0 (\varepsilon_r - 1)}. \quad \text{(C.2)}$$

Piecewise linear expansion / Piecewise linear testing

$$Z_{11} = \frac{jk_0 Z_0 \Delta_x^2 \Delta_y^2}{ac} \sum_{p,q} \operatorname{sinc}^2\left(\frac{k_{x_p}\Delta_x}{2}\right) \operatorname{sinc}^2\left(\frac{k_{y_q}\Delta_y}{2}\right) \times \frac{\left(1 + jk_{x_p}\Delta_x - e^{jk_{x_p}\Delta_x}\right)}{\left(k_{x_p}\Delta_x\right)^2} \frac{\left(1 + jk_{y_q}\Delta_y - e^{jk_{y_q}\Delta_y}\right)}{\left(k_{y_q}\Delta_y\right)^2} \frac{1}{k_0^2 - k_{x_p}^2 - k_{y_q}^2} \quad \text{(C.3)}$$

$$Z_{1n} = \frac{jk_0 Z_0 \Delta_x^2 \Delta_y^2}{ac} \sum_{p,q} \operatorname{sinc}^4\left(\frac{k_{x_p}\Delta_x}{2}\right) \operatorname{sinc}^4\left(\frac{k_{y_q}\Delta_y}{2}\right) \frac{e^{-jk_{x_p}(x_1 - x_n)} e^{-jk_{y_q}(y_1 - y_n)}}{k_0^2 - k_{x_p}^2 - k_{y_q}^2} \quad \text{(C.4)}$$

$$Z_{1N} = \frac{jk_0 Z_0 \Delta_x^2 \Delta_y^2}{ac} \sum_{p,q} \operatorname{sinc}^2\left(\frac{k_{x_p}\Delta_x}{2}\right) \operatorname{sinc}^2\left(\frac{k_{y_q}\Delta_y}{2}\right) \frac{e^{-jk_{x_p}(x_1 - x_N)} e^{-jk_{y_q}(y_1 - y_N)}}{k_0^2 - k_{x_p}^2 - k_{y_q}^2} \times \frac{\left(1 - jk_{x_p}\Delta_x - e^{-jk_{x_p}\Delta_x}\right)}{\left(k_{x_p}\Delta_x\right)^2} \frac{\left(1 - jk_{y_q}\Delta_y - e^{-jk_{y_q}\Delta_y}\right)}{\left(k_{y_q}\Delta_y\right)^2} \quad \text{(C.5)}$$

$$Z_{m1} = \frac{jk_0 Z_0 \Delta_x^2 \Delta_y^2}{ac} \sum_{p,q} \mathrm{sinc}^2\left(\frac{k_{x_p}\Delta_x}{2}\right) \mathrm{sinc}^2\left(\frac{k_{y_q}\Delta_y}{2}\right) \frac{e^{-jk_{x_p}(x_m - x_1)} e^{-jk_{y_q}(y_m - y_1)}}{k_0^2 - k_{x_p}^2 - k_{y_q}^2} \times \frac{\left(1 + jk_{x_p}\Delta_x - e^{jk_{x_p}\Delta_x}\right)}{\left(k_{x_p}\Delta_x\right)^2} \frac{\left(1 + jk_{y_q}\Delta_y - e^{jk_{y_q}\Delta_y}\right)}{\left(k_{y_q}\Delta_y\right)^2} \tag{C.6}$$

$$Z_{mn} = \frac{jk_0 Z_0 \Delta_x^2 \Delta_y^2}{ac} \sum_{p,q} \mathrm{sinc}^4\left(\frac{k_{x_p}\Delta_x}{2}\right) \mathrm{sinc}^4\left(\frac{k_{y_q}\Delta_y}{2}\right) \frac{e^{-jk_{x_p}(x_m - x_n)} e^{-jk_{y_q}(y_m - y_n)}}{k_0^2 - k_{x_p}^2 - k_{y_q}^2} \tag{C.7}$$

$$Z_{mN} = \frac{jk_0 Z_0 \Delta_x^2 \Delta_y^2}{ac} \sum_{p,q} \mathrm{sinc}^2\left(\frac{k_{x_p}\Delta_x}{2}\right) \mathrm{sinc}^2\left(\frac{k_{y_q}\Delta_y}{2}\right) \frac{e^{-jk_{x_p}(x_m - x_N)} e^{-jk_{y_q}(y_m - y_N)}}{k_0^2 - k_{x_p}^2 - k_{y_q}^2} \times \frac{\left(1 - jk_{x_p}\Delta_x - e^{-jk_{x_p}\Delta_x}\right)}{\left(k_{x_p}\Delta_x\right)^2} \frac{\left(1 - jk_{y_q}\Delta_y - e^{-jk_{y_q}\Delta_y}\right)}{\left(k_{y_q}\Delta_y\right)^2} \tag{C.8}$$

$$Z_{N1} = \frac{jk_0 Z_0 \Delta_x^2 \Delta_y^2}{ac} \sum_{p,q} \mathrm{sinc}^2\left(\frac{k_{x_p}\Delta_x}{2}\right) \mathrm{sinc}^2\left(\frac{k_{y_q}\Delta_y}{2}\right) \frac{e^{-jk_{x_p}(x_N - x_1)} e^{-jk_{y_q}(y_N - y_1)}}{k_0^2 - k_{x_p}^2 - k_{y_q}^2} \times \frac{\left(1 + jk_{x_p}\Delta_x - e^{jk_{x_p}\Delta_x}\right)}{\left(k_{x_p}\Delta_x\right)^2} \frac{\left(1 + jk_{y_q}\Delta_y - e^{jk_{y_q}\Delta_y}\right)}{\left(k_{y_q}\Delta_y\right)^2} \tag{C.9}$$

$$Z_{Nn} = \frac{jk_0 Z_0 \Delta_x^2 \Delta_y^2}{ac} \sum_{p,q} \mathrm{sinc}^4\left(\frac{k_{x_p}\Delta_x}{2}\right) \mathrm{sinc}^4\left(\frac{k_{y_q}\Delta_y}{2}\right) \frac{e^{-jk_{x_p}(x_N - x_n)} e^{-jk_{y_q}(y_N - y_n)}}{k_0^2 - k_{x_p}^2 - k_{y_q}^2} \tag{C.10}$$

$$Z_{NN} = \frac{jk_0 Z_0 \Delta_x^2 \Delta_y^2}{ac} \sum_{p,q} \mathrm{sinc}^2\left(\frac{k_{x_p}\Delta_x}{2}\right) \mathrm{sinc}^2\left(\frac{k_{y_q}\Delta_y}{2}\right) \frac{1}{k_0^2 - k_{x_p}^2 - k_{y_q}^2} \times \frac{\left(1 - jk_{x_p}\Delta_x - e^{-jk_{x_p}\Delta_x}\right)}{\left(k_{x_p}\Delta_x\right)^2} \frac{\left(1 - jk_{y_q}\Delta_y - e^{-jk_{y_q}\Delta_y}\right)}{\left(k_{y_q}\Delta_y\right)^2} \tag{C.11}$$

$$\delta Z = -\frac{\delta_{mn}\Delta_x\Delta_y}{jk_0 Y_0 \left(\varepsilon_r - 1\right)}. \tag{C.12}$$

$\mathbf{TE}_z$ Case

Piecewise linear expansion / Piecewise linear testing

$$Z_{11}^{xx} = \frac{jk_0 Z_0 \Delta_x^2 \Delta_y^2}{ac} \sum_{p,q} \left(1 - \frac{k_{x_p}^2}{k_0^2}\right) \mathrm{sinc}^2\left(\frac{k_{x_p}\Delta_x}{2}\right) \mathrm{sinc}^2\left(\frac{k_{y_q}\Delta_y}{2}\right) \frac{1}{k_0^2 - k_{x_p}^2 - k_{y_q}^2} \times \frac{\left(1 + jk_{x_p}\Delta_x - e^{jk_{x_p}\Delta_x}\right)}{\left(k_{x_p}\Delta_x\right)^2} \frac{\left(1 + jk_{y_q}\Delta_y - e^{jk_{y_q}\Delta_y}\right)}{\left(k_{y_q}\Delta_y\right)^2} \tag{C.13}$$

$$Z_{1n}^{xx} = \frac{jk_0 Z_0 \Delta_x^2 \Delta_y^2}{ac} \sum_{p,q} \left(1 - \frac{k_{x_p}^2}{k_0^2}\right) \mathrm{sinc}^4\left(\frac{k_{x_p}\Delta_x}{2}\right) \mathrm{sinc}^4\left(\frac{k_{y_q}\Delta_y}{2}\right) \times \frac{e^{-jk_{x_p}(x_1-x_n)} e^{-jk_{y_q}(y_1-y_n)}}{k_0^2 - k_{x_p}^2 - k_{y_q}^2} \quad \text{(C.14)}$$

$$Z_{1N}^{xx} = \frac{jk_0 Z_0 \Delta_x^2 \Delta_y^2}{ac} \sum_{p,q} \left(1 - \frac{k_{x_p}^2}{k_0^2}\right) \mathrm{sinc}^2\left(\frac{k_{x_p}\Delta_x}{2}\right) \mathrm{sinc}^2\left(\frac{k_{y_q}\Delta_y}{2}\right) \times \frac{\left(1 - jk_{x_p}\Delta_x - e^{-jk_{x_p}\Delta_x}\right)}{\left(k_{x_p}\Delta_x\right)^2} \frac{\left(1 - jk_{y_q}\Delta_y - e^{-jk_{y_q}\Delta_y}\right)}{\left(k_{y_q}\Delta_y\right)^2} \frac{e^{-jk_{x_p}(x_1-x_N)} e^{-jk_{y_q}(y_1-y_N)}}{k_0^2 - k_{x_p}^2 - k_{y_q}^2} \quad \text{(C.15)}$$

$$Z_{m1}^{xx} = \frac{jk_0 Z_0 \Delta_x^2 \Delta_y^2}{ac} \sum_{p,q} \left(1 - \frac{k_{x_p}^2}{k_0^2}\right) \mathrm{sinc}^2\left(\frac{k_{x_p}\Delta_x}{2}\right) \mathrm{sinc}^2\left(\frac{k_{y_q}\Delta_y}{2}\right) \times \frac{\left(1 + jk_{x_p}\Delta_x - e^{jk_{x_p}\Delta_x}\right)}{\left(k_{x_p}\Delta_x\right)^2} \frac{\left(1 + jk_{y_q}\Delta_y - e^{jk_{y_q}\Delta_y}\right)}{\left(k_{y_q}\Delta_y\right)^2} \frac{e^{-jk_{x_p}(x_m-x_1)} e^{-jk_{y_q}(y_m-y_1)}}{k_0^2 - k_{x_p}^2 - k_{y_q}^2} \quad \text{(C.16)}$$

$$Z_{mn}^{xx} = \frac{jk_0 Z_0 \Delta_x^2 \Delta_y^2}{ac} \sum_{p,q} \left(1 - \frac{k_{x_p}^2}{k_0^2}\right) \mathrm{sinc}^4\left(\frac{k_{x_p}\Delta_x}{2}\right) \mathrm{sinc}^4\left(\frac{k_{y_q}\Delta_y}{2}\right) times \frac{e^{-jk_{x_p}(x_m-x_n)} e^{-jk_{y_q}(y_m-y_n)}}{k_0^2 - k_{x_p}^2 - k_{y_q}^2} \quad \text{(C.17)}$$

$$Z_{mN}^{xx} = \frac{jk_0 Z_0 \Delta_x^2 \Delta_y^2}{ac} \sum_{p,q} \left(1 - \frac{k_{x_p}^2}{k_0^2}\right) \mathrm{sinc}^2\left(\frac{k_{x_p}\Delta_x}{2}\right) \mathrm{sinc}^2\left(\frac{k_{y_q}\Delta_y}{2}\right) \times \frac{\left(1 - jk_{x_p}\Delta_x - e^{-jk_{x_p}\Delta_x}\right)}{\left(k_{x_p}\Delta_x\right)^2} \frac{\left(1 - jk_{y_q}\Delta_y - e^{-jk_{y_q}\Delta_y}\right)}{\left(k_{y_q}\Delta_y\right)^2} \frac{e^{-jk_{x_p}(x_m-x_N)} e^{-jk_{y_q}(y_m-y_N)}}{k_0^2 - k_{x_p}^2 - k_{y_q}^2} \quad \text{(C.18)}$$

$$Z_{N1}^{xx} = \frac{jk_0 Z_0 \Delta_x^2 \Delta_y^2}{ac} \sum_{p,q} \left(1 - \frac{k_{x_p}^2}{k_0^2}\right) \mathrm{sinc}^2\left(\frac{k_{x_p}\Delta_x}{2}\right) \mathrm{sinc}^2\left(\frac{k_{y_q}\Delta_y}{2}\right) \times \frac{\left(1 + jk_{x_p}\Delta_x - e^{jk_{x_p}\Delta_x}\right)}{\left(k_{x_p}\Delta_x\right)^2} \frac{\left(1 + jk_{y_q}\Delta_y - e^{jk_{y_q}\Delta_y}\right)}{\left(k_{y_q}\Delta_y\right)^2} \frac{e^{-jk_{x_p}(x_N-x_1)} e^{-jk_{y_q}(y_N-y_1)}}{k_0^2 - k_{x_p}^2 - k_{y_q}^2} \quad \text{(C.19)}$$

$$Z_{Nn}^{xx} = \frac{jk_0 Z_0 \Delta_x^2 \Delta_y^2}{ac} \sum_{p,q} \left(1 - \frac{k_{x_p}^2}{k_0^2}\right) \mathrm{sinc}^4\left(\frac{k_{x_p}\Delta_x}{2}\right) \mathrm{sinc}^4\left(\frac{k_{y_q}\Delta_y}{2}\right) \times \frac{e^{-jk_{x_p}(x_N-x_n)} e^{-jk_{y_q}(y_N-y_n)}}{k_0^2 - k_{x_p}^2 - k_{y_q}^2} \quad \text{(C.20)}$$

$$Z_{NN}^{xx} = \frac{jk_0 Z_0 \Delta_x^2 \Delta_y^2}{ac} \sum_{p,q} \left(1 - \frac{k_{x_p}^2}{k_0^2}\right) \operatorname{sinc}^2\left(\frac{k_{x_p}\Delta_x}{2}\right) \operatorname{sinc}^2\left(\frac{k_{y_q}\Delta_y}{2}\right)$$
$$\times \frac{\left(1 - jk_{x_p}\Delta_x - e^{-jk_{x_p}\Delta_x}\right)}{\left(k_{x_p}\Delta_x\right)^2} \frac{\left(1 - jk_{y_q}\Delta_y - e^{-jk_{y_q}\Delta_y}\right)}{\left(k_{y_q}\Delta_y\right)^2} \frac{1}{k_0^2 - k_{x_p}^2 - k_{y_q}^2} \quad \text{(C.21)}$$

$$Z_{11}^{xy} = \frac{jk_0 Z_0 \Delta_x^2 \Delta_y^2}{ac} \sum_{p,q} \left(-k_{x_p} k_{y_q}\right) \operatorname{sinc}^2\left(\frac{k_{x_p}\Delta_x}{2}\right) \operatorname{sinc}^2\left(\frac{k_{y_q}\Delta_y}{2}\right)$$
$$\times \frac{\left(1 + jk_{x_p}\Delta_x - e^{jk_{x_p}\Delta_x}\right)}{\left(k_{x_p}\Delta_x\right)^2} \frac{\left(1 + jk_{y_q}\Delta_y - e^{jk_{y_q}\Delta_y}\right)}{\left(k_{y_q}\Delta_y\right)^2} \frac{1}{k_0^2 - k_{x_p}^2 - k_{y_q}^2} \quad \text{(C.22)}$$

$$Z_{1n}^{xy} = \frac{jk_0 Z_0 \Delta_x^2 \Delta_y^2}{ac} \sum_{p,q} \left(-k_{x_p} k_{y_q}\right) \operatorname{sinc}^4\left(\frac{k_{x_p}\Delta_x}{2}\right) \operatorname{sinc}^4\left(\frac{k_{y_q}\Delta_y}{2}\right)$$
$$\times \frac{e^{-jk_{x_p}(x_1 - x_n)} e^{-jk_{y_q}(y_1 - y_n)}}{k_0^2 - k_{x_p}^2 - k_{y_q}^2} \quad \text{(C.23)}$$

$$Z_{1N}^{xy} = \frac{jk_0 Z_0 \Delta_x^2 \Delta_y^2}{ac} \sum_{p,q} \left(-k_{x_p} k_{y_q}\right) \operatorname{sinc}^2\left(\frac{k_{x_p}\Delta_x}{2}\right) \operatorname{sinc}^2\left(\frac{k_{y_q}\Delta_y}{2}\right)$$
$$\times \frac{\left(1 - jk_{x_p}\Delta_x - e^{-jk_{x_p}\Delta_x}\right)}{\left(k_{x_p}\Delta_x\right)^2} \frac{\left(1 - jk_{y_q}\Delta_y - e^{-jk_{y_q}\Delta_y}\right)}{\left(k_{y_q}\Delta_y\right)^2} \frac{e^{-jk_{x_p}(x_1 - x_N)} e^{-jk_{y_q}(y_1 - y_N)}}{k_0^2 - k_{x_p}^2 - k_{y_q}^2} \quad \text{(C.24)}$$

$$Z_{m1}^{xy} = \frac{jk_0 Z_0 \Delta_x^2 \Delta_y^2}{ac} \sum_{p,q} \left(-k_{x_p} k_{y_q}\right) \operatorname{sinc}^2\left(\frac{k_{x_p}\Delta_x}{2}\right) \operatorname{sinc}^2\left(\frac{k_{y_q}\Delta_y}{2}\right)$$
$$\times \frac{\left(1 + jk_{x_p}\Delta_x - e^{jk_{x_p}\Delta_x}\right)}{\left(k_{x_p}\Delta_x\right)^2} \frac{\left(1 + jk_{y_q}\Delta_y - e^{jk_{y_q}\Delta_y}\right)}{\left(k_{y_q}\Delta_y\right)^2} \frac{e^{-jk_{x_p}(x_m - x_1)} e^{-jk_{y_q}(y_m - y_1)}}{k_0^2 - k_{x_p}^2 - k_{y_q}^2} \quad \text{(C.25)}$$

$$Z_{mn}^{xy} = \frac{jk_0 Z_0 \Delta_x^2 \Delta_y^2}{ac} \sum_{p,q} \left(-k_{x_p} k_{y_q}\right) \operatorname{sinc}^4\left(\frac{k_{x_p}\Delta_x}{2}\right) \operatorname{sinc}^4\left(\frac{k_{y_q}\Delta_y}{2}\right)$$
$$\times \frac{e^{-jk_{x_p}(x_m - x_n)} e^{-jk_{y_q}(y_m - y_n)}}{k_0^2 - k_{x_p}^2 - k_{y_q}^2} \quad \text{(C.26)}$$

$$Z_{mN}^{xy} = \frac{jk_0 Z_0 \Delta_x^2 \Delta_y^2}{ac} \sum_{p,q} \left(-k_{x_p} k_{y_q}\right) \operatorname{sinc}^2\left(\frac{k_{x_p}\Delta_x}{2}\right) \operatorname{sinc}^2\left(\frac{k_{y_q}\Delta_y}{2}\right)$$
$$\times \frac{\left(1 - jk_{x_p}\Delta_x - e^{-jk_{x_p}\Delta_x}\right)}{\left(k_{x_p}\Delta_x\right)^2} \frac{\left(1 - jk_{y_q}\Delta_y - e^{-jk_{y_q}\Delta_y}\right)}{\left(k_{y_q}\Delta_y\right)^2} \frac{e^{-jk_{x_p}(x_m - x_N)} e^{-jk_{y_q}(y_m - y_N)}}{k_0^2 - k_{x_p}^2 - k_{y_q}^2} \quad \text{(C.27)}$$

$$Z_{N1}^{xy} = \frac{jk_0 Z_0 \Delta_x^2 \Delta_y^2}{ac} \sum_{p,q} \left(-k_{x_p} k_{y_q}\right) \operatorname{sinc}^2\left(\frac{k_{x_p}\Delta_x}{2}\right) \operatorname{sinc}^2\left(\frac{k_{y_q}\Delta_y}{2}\right)$$
$$\times \frac{\left(1 + jk_{x_p}\Delta_x - e^{jk_{x_p}\Delta_x}\right)}{\left(k_{x_p}\Delta_x\right)^2} \frac{\left(1 + jk_{y_q}\Delta_y - e^{jk_{y_q}\Delta_y}\right)}{\left(k_{y_q}\Delta_y\right)^2} \frac{e^{-jk_{x_p}(x_N - x_1)} e^{-jk_{y_q}(y_N - y_1)}}{k_0^2 - k_{x_p}^2 - k_{y_q}^2} \quad \text{(C.28)}$$

$$Z_{Nn}^{xy} = \frac{jk_0 Z_0 \Delta_x^2 \Delta_y^2}{ac} \sum_{p,q} \left(-k_{x_p} k_{y_q}\right) \operatorname{sinc}^4\left(\frac{k_{x_p}\Delta_x}{2}\right) \operatorname{sinc}^4\left(\frac{k_{y_q}\Delta_y}{2}\right)$$
$$\times \frac{e^{-jk_{x_p}(x_N - x_n)} e^{-jk_{y_q}(y_N - y_n)}}{k_0^2 - k_{x_p}^2 - k_{y_q}^2} \quad \text{(C.29)}$$

$$Z_{NN}^{xy} = \frac{jk_0 Z_0 \Delta_x^2 \Delta_y^2}{ac} \sum_{p,q} \left(-k_{x_p} k_{y_q}\right) \operatorname{sinc}^2\left(\frac{k_{x_p}\Delta_x}{2}\right) \operatorname{sinc}^2\left(\frac{k_{y_q}\Delta_y}{2}\right)$$
$$\times \frac{\left(1 - jk_{x_p}\Delta_x - e^{-jk_{x_p}\Delta_x}\right)}{\left(k_{x_p}\Delta_x\right)^2} \frac{\left(1 - jk_{y_q}\Delta_y - e^{-jk_{y_q}\Delta_y}\right)}{\left(k_{y_q}\Delta_y\right)^2} \frac{1}{k_0^2 - k_{x_p}^2 - k_{y_q}^2} \quad \text{(C.30)}$$

$$Z_{11}^{yx} = \frac{jk_0 Z_0 \Delta_x^2 \Delta_y^2}{ac} \sum_{p,q} \left(-k_{x_p} k_{y_q}\right) \operatorname{sinc}^2\left(\frac{k_{x_p}\Delta_x}{2}\right) \operatorname{sinc}^2\left(\frac{k_{y_q}\Delta_y}{2}\right)$$
$$\times \frac{\left(1 + jk_{x_p}\Delta_x - e^{jk_{x_p}\Delta_x}\right)}{\left(k_{x_p}\Delta_x\right)^2} \frac{\left(1 + jk_{y_q}\Delta_y - e^{jk_{y_q}\Delta_y}\right)}{\left(k_{y_q}\Delta_y\right)^2} \frac{1}{k_0^2 - k_{x_p}^2 - k_{y_q}^2} \quad \text{(C.31)}$$

$$Z_{1n}^{yx} = \frac{jk_0 Z_0 \Delta_x^2 \Delta_y^2}{ac} \sum_{p,q} \left(-k_{x_p} k_{y_q}\right) \operatorname{sinc}^4\left(\frac{k_{x_p}\Delta_x}{2}\right) \operatorname{sinc}^4\left(\frac{k_{y_q}\Delta_y}{2}\right)$$
$$\times \frac{e^{-jk_{x_p}(x_1 - x_n)} e^{-jk_{y_q}(y_1 - y_n)}}{k_0^2 - k_{x_p}^2 - k_{y_q}^2} \quad \text{(C.32)}$$

$$Z_{1N}^{yx} = \frac{jk_0 Z_0 \Delta_x^2 \Delta_y^2}{ac} \sum_{p,q} \left(-k_{x_p} k_{y_q}\right) \operatorname{sinc}^2\left(\frac{k_{x_p}\Delta_x}{2}\right) \operatorname{sinc}^2\left(\frac{k_{y_q}\Delta_y}{2}\right)$$
$$\times \frac{\left(1 - jk_{x_p}\Delta_x - e^{-jk_{x_p}\Delta_x}\right)}{\left(k_{x_p}\Delta_x\right)^2} \frac{\left(1 - jk_{y_q}\Delta_y - e^{-jk_{y_q}\Delta_y}\right)}{\left(k_{y_q}\Delta_y\right)^2} \frac{e^{-jk_{x_p}(x_1 - x_N)} e^{-jk_{y_q}(y_1 - y_N)}}{k_0^2 - k_{x_p}^2 - k_{y_q}^2} \quad \text{(C.33)}$$

$$Z_{m1}^{yx} = \frac{jk_0 Z_0 \Delta_x^2 \Delta_y^2}{ac} \sum_{p,q} \left(-k_{x_p} k_{y_q}\right) \operatorname{sinc}^2\left(\frac{k_{x_p}\Delta_x}{2}\right) \operatorname{sinc}^2\left(\frac{k_{y_q}\Delta_y}{2}\right)$$
$$\times \frac{\left(1 + jk_{x_p}\Delta_x - e^{jk_{x_p}\Delta_x}\right)}{\left(k_{x_p}\Delta_x\right)^2} \frac{\left(1 + jk_{y_q}\Delta_y - e^{jk_{y_q}\Delta_y}\right)}{\left(k_{y_q}\Delta_y\right)^2} \frac{e^{-jk_{x_p}(x_m - x_1)} e^{-jk_{y_q}(y_m - y_1)}}{k_0^2 - k_{x_p}^2 - k_{y_q}^2} \quad \text{(C.34)}$$

$$Z_{mn}^{yx} = \frac{jk_0 Z_0 \Delta_x^2 \Delta_y^2}{ac} \sum_{p,q} \left(-k_{x_p} k_{y_q}\right) \operatorname{sinc}^4\left(\frac{k_{x_p}\Delta_x}{2}\right) \operatorname{sinc}^4\left(\frac{k_{y_q}\Delta_y}{2}\right) \times \frac{e^{-jk_{x_p}(x_m - x_n)} e^{-jk_{y_q}(y_m - y_n)}}{k_0^2 - k_{x_p}^2 - k_{y_q}^2} \tag{C.35}$$

$$Z_{mN}^{yx} = \frac{jk_0 Z_0 \Delta_x^2 \Delta_y^2}{ac} \sum_{p,q} \left(-k_{x_p} k_{y_q}\right) \operatorname{sinc}^2\left(\frac{k_{x_p}\Delta_x}{2}\right) \operatorname{sinc}^2\left(\frac{k_{y_q}\Delta_y}{2}\right) \times \frac{\left(1 - jk_{x_p}\Delta_x - e^{-jk_{x_p}\Delta_x}\right)}{\left(k_{x_p}\Delta_x\right)^2} \frac{\left(1 - jk_{y_q}\Delta_y - e^{-jk_{y_q}\Delta_y}\right)}{\left(k_{y_q}\Delta_y\right)^2} \frac{e^{-jk_{x_p}(x_m - x_N)} e^{-jk_{y_q}(y_m - y_N)}}{k_0^2 - k_{x_p}^2 - k_{y_q}^2} \tag{C.36}$$

$$Z_{N1}^{yx} = \frac{jk_0 Z_0 \Delta_x^2 \Delta_y^2}{ac} \sum_{p,q} \left(-k_{x_p} k_{y_q}\right) \operatorname{sinc}^2\left(\frac{k_{x_p}\Delta_x}{2}\right) \operatorname{sinc}^2\left(\frac{k_{y_q}\Delta_y}{2}\right) \times \frac{\left(1 + jk_{x_p}\Delta_x - e^{jk_{x_p}\Delta_x}\right)}{\left(k_{x_p}\Delta_x\right)^2} \frac{\left(1 + jk_{y_q}\Delta_y - e^{jk_{y_q}\Delta_y}\right)}{\left(k_{y_q}\Delta_y\right)^2} \frac{e^{-jk_{x_p}(x_N - x_1)} e^{-jk_{y_q}(y_N - y_1)}}{k_0^2 - k_{x_p}^2 - k_{y_q}^2} \tag{C.37}$$

$$Z_{Nn}^{yx} = \frac{jk_0 Z_0 \Delta_x^2 \Delta_y^2}{ac} \sum_{p,q} \left(-k_{x_p} k_{y_q}\right) \operatorname{sinc}^4\left(\frac{k_{x_p}\Delta_x}{2}\right) \operatorname{sinc}^4\left(\frac{k_{y_q}\Delta_y}{2}\right) \times \frac{e^{-jk_{x_p}(x_N - x_n)} e^{-jk_{y_q}(y_N - y_n)}}{k_0^2 - k_{x_p}^2 - k_{y_q}^2} \tag{C.38}$$

$$Z_{NN}^{yx} = \frac{jk_0 Z_0 \Delta_x^2 \Delta_y^2}{ac} \sum_{p,q} \left(-k_{x_p} k_{y_q}\right) \operatorname{sinc}^2\left(\frac{k_{x_p}\Delta_x}{2}\right) \operatorname{sinc}^2\left(\frac{k_{y_q}\Delta_y}{2}\right) \times \frac{\left(1 - jk_{x_p}\Delta_x - e^{-jk_{x_p}\Delta_x}\right)}{\left(k_{x_p}\Delta_x\right)^2} \frac{\left(1 - jk_{y_q}\Delta_y - e^{-jk_{y_q}\Delta_y}\right)}{\left(k_{y_q}\Delta_y\right)^2} \frac{1}{k_0^2 - k_{x_p}^2 - k_{y_q}^2} \tag{C.39}$$

$$Z_{11}^{yy} = \frac{jk_0 Z_0 \Delta_x^2 \Delta_y^2}{ac} \sum_{p,q} \left(1 - \frac{k_{y_q}^2}{k_0^2}\right) \operatorname{sinc}^2\left(\frac{k_{x_p}\Delta_x}{2}\right) \operatorname{sinc}^2\left(\frac{k_{y_q}\Delta_y}{2}\right) \times \frac{\left(1 + jk_{x_p}\Delta_x - e^{jk_{x_p}\Delta_x}\right)}{\left(k_{x_p}\Delta_x\right)^2} \frac{\left(1 + jk_{y_q}\Delta_y - e^{jk_{y_q}\Delta_y}\right)}{\left(k_{y_q}\Delta_y\right)^2} \frac{1}{k_0^2 - k_{x_p}^2 - k_{y_q}^2} \tag{C.40}$$

$$Z_{1n}^{yy} = \frac{jk_0 Z_0 \Delta_x^2 \Delta_y^2}{ac} \sum_{p,q} \left(1 - \frac{k_{y_q}^2}{k_0^2}\right) \operatorname{sinc}^4\left(\frac{k_{x_p}\Delta_x}{2}\right) \operatorname{sinc}^4\left(\frac{k_{y_q}\Delta_y}{2}\right) \times \frac{e^{-jk_{x_p}(x_1 - x_n)} e^{-jk_{y_q}(y_1 - y_n)}}{k_0^2 - k_{x_p}^2 - k_{y_q}^2} \tag{C.41}$$

$$Z_{1N}^{yy} = \frac{jk_0 Z_0 \Delta_x^2 \Delta_y^2}{ac} \sum_{p,q} \left(1 - \frac{k_{y_q}^2}{k_0^2}\right) \operatorname{sinc}^2\left(\frac{k_{x_p}\Delta_x}{2}\right) \operatorname{sinc}^2\left(\frac{k_{y_q}\Delta_y}{2}\right)$$
$$\times \frac{\left(1 - jk_{x_p}\Delta_x - e^{-jk_{x_p}\Delta_x}\right)}{\left(k_{x_p}\Delta_x\right)^2} \frac{\left(1 - jk_{y_q}\Delta_y - e^{-jk_{y_q}\Delta_y}\right)}{\left(k_{y_q}\Delta_y\right)^2} \frac{e^{-jk_{x_p}(x_1 - x_N)} e^{-jk_{y_q}(y_1 - y_N)}}{k_0^2 - k_{x_p}^2 - k_{y_q}^2} \quad \text{(C.42)}$$

$$Z_{m1}^{yy} = \frac{jk_0 Z_0 \Delta_x^2 \Delta_y^2}{ac} \sum_{p,q} \left(1 - \frac{k_{y_q}^2}{k_0^2}\right) \operatorname{sinc}^2\left(\frac{k_{x_p}\Delta_x}{2}\right) \operatorname{sinc}^2\left(\frac{k_{y_q}\Delta_y}{2}\right)$$
$$\times \frac{\left(1 + jk_{x_p}\Delta_x - e^{jk_{x_p}\Delta_x}\right)}{\left(k_{x_p}\Delta_x\right)^2} \frac{\left(1 + jk_{y_q}\Delta_y - e^{jk_{y_q}\Delta_y}\right)}{\left(k_{y_q}\Delta_y\right)^2} \frac{e^{-jk_{x_p}(x_m - x_1)} e^{-jk_{y_q}(y_m - y_1)}}{k_0^2 - k_{x_p}^2 - k_{y_q}^2} \quad \text{(C.43)}$$

$$Z_{mn}^{yy} = \frac{jk_0 Z_0 \Delta_x^2 \Delta_y^2}{ac} \sum_{p,q} \left(1 - \frac{k_{y_q}^2}{k_0^2}\right) \operatorname{sinc}^4\left(\frac{k_{x_p}\Delta_x}{2}\right) \operatorname{sinc}^4\left(\frac{k_{y_q}\Delta_y}{2}\right)$$
$$\times \frac{e^{-jk_{x_p}(x_m - x_n)} e^{-jk_{y_q}(y_m - y_n)}}{k_0^2 - k_{x_p}^2 - k_{y_q}^2} \quad \text{(C.44)}$$

$$Z_{mN}^{yy} = \frac{jk_0 Z_0 \Delta_x^2 \Delta_y^2}{ac} \sum_{p,q} \left(1 - \frac{k_{y_q}^2}{k_0^2}\right) \operatorname{sinc}^2\left(\frac{k_{x_p}\Delta_x}{2}\right) \operatorname{sinc}^2\left(\frac{k_{y_q}\Delta_y}{2}\right)$$
$$\times \frac{\left(1 - jk_{x_p}\Delta_x - e^{-jk_{x_p}\Delta_x}\right)}{\left(k_{x_p}\Delta_x\right)^2} \frac{\left(1 - jk_{y_q}\Delta_y - e^{-jk_{y_q}\Delta_y}\right)}{\left(k_{y_q}\Delta_y\right)^2} \frac{e^{-jk_{x_p}(x_m - x_N)} e^{-jk_{y_q}(y_m - y_N)}}{k_0^2 - k_{x_p}^2 - k_{y_q}^2} \quad \text{(C.45)}$$

$$Z_{N1}^{yy} = \frac{jk_0 Z_0 \Delta_x^2 \Delta_y^2}{ac} \sum_{p,q} \left(1 - \frac{k_{y_q}^2}{k_0^2}\right) \operatorname{sinc}^2\left(\frac{k_{x_p}\Delta_x}{2}\right) \operatorname{sinc}^2\left(\frac{k_{y_q}\Delta_y}{2}\right)$$
$$\times \frac{\left(1 + jk_{x_p}\Delta_x - e^{jk_{x_p}\Delta_x}\right)}{\left(k_{x_p}\Delta_x\right)^2} \frac{\left(1 + jk_{y_q}\Delta_y - e^{jk_{y_q}\Delta_y}\right)}{\left(k_{y_q}\Delta_y\right)^2} \frac{e^{-jk_{x_p}(x_N - x_1)} e^{-jk_{y_q}(y_N - y_1)}}{k_0^2 - k_{x_p}^2 - k_{y_q}^2} \quad \text{(C.46)}$$

$$Z_{Nn}^{yy} = \frac{jk_0 Z_0 \Delta_x^2 \Delta_y^2}{ac} \sum_{p,q} \left(1 - \frac{k_{y_q}^2}{k_0^2}\right) \operatorname{sinc}^4\left(\frac{k_{x_p}\Delta_x}{2}\right) \operatorname{sinc}^4\left(\frac{k_{y_q}\Delta_y}{2}\right)$$
$$\times \frac{e^{-jk_{x_p}(x_N - x_n)} e^{-jk_{y_q}(y_N - y_n)}}{k_0^2 - k_{x_p}^2 - k_{y_q}^2} \quad \text{(C.47)}$$

$$Z_{NN}^{yy} = \frac{jk_0 Z_0 \Delta_x^2 \Delta_y^2}{ac} \sum_{p,q} \left(1 - \frac{k_{y_q}^2}{k_0^2}\right) \operatorname{sinc}^2\left(\frac{k_{x_p}\Delta_x}{2}\right) \operatorname{sinc}^2\left(\frac{k_{y_q}\Delta_y}{2}\right)$$
$$\times \frac{\left(1 - jk_{x_p}\Delta_x - e^{-jk_{x_p}\Delta_x}\right)}{\left(k_{x_p}\Delta_x\right)^2} \frac{\left(1 - jk_{y_q}\Delta_y - e^{-jk_{y_q}\Delta_y}\right)}{\left(k_{y_q}\Delta_y\right)^2} \frac{1}{k_0^2 - k_{x_p}^2 - k_{y_q}^2} \quad \text{(C.48)}$$

$$\delta Z^{xx} = -\frac{\delta_{mn}\Delta_x\Delta_y}{jk_0 Y_0 \left(\varepsilon_r - 1\right)}. \quad \text{(C.49)}$$

$$\delta Z^{yy} = -\frac{\delta_{mn}\Delta_x\Delta_y}{jk_0 Y_0 \left(\varepsilon_r - 1\right)}. \quad \text{(C.50)}$$

Piecewise constant expansion / Piecewise constant testing

$$Z_{mn}^{xx} = \frac{jk_0 Z_0 \Delta_x^2 \Delta_y^2}{ac} \sum_{p,q} \left(1 - \frac{k_{x_p}^2}{k_0^2}\right) \operatorname{sinc}^2\left(\frac{k_{x_p}\Delta_x}{2}\right) \operatorname{sinc}^2\left(\frac{k_{y_q}\Delta_y}{2}\right) \times \frac{e^{-jk_{x_p}(x_m - x_n)} e^{-jk_{y_q}(y_m - y_n)}}{k_0^2 - k_{x_p}^2 - k_{y_q}^2} \tag{C.51}$$

$$Z_{mn}^{xy} = \frac{jk_0 Z_0 \Delta_x^2 \Delta_y^2}{ac} \sum_{p,q} \left(-k_{x_p} k_{y_q}\right) \operatorname{sinc}^2\left(\frac{k_{x_p}\Delta_x}{2}\right) \operatorname{sinc}^2\left(\frac{k_{y_q}\Delta_y}{2}\right) \times \frac{e^{-jk_{x_p}(x_m - x_n)} e^{-jk_{y_q}(y_m - y_n)}}{k_0^2 - k_{x_p}^2 - k_{y_q}^2} \tag{C.52}$$

$$Z_{mn}^{yx} = Z_{mn}^{xy} \tag{C.53}$$

$$Z_{mn}^{yy} = \frac{jk_0 Z_0 \Delta_x^2 \Delta_y^2}{ac} \sum_{p,q} \left(1 - \frac{k_{y_q}^2}{k_0^2}\right) \operatorname{sinc}^2\left(\frac{k_{x_p}\Delta_x}{2}\right) \operatorname{sinc}^2\left(\frac{k_{y_q}\Delta_y}{2}\right) \times \frac{e^{-jk_{x_p}(x_m - x_n)} e^{-jk_{y_q}(y_m - y_n)}}{k_0^2 - k_{x_p}^2 - k_{y_q}^2} \tag{C.54}$$

$$\delta Z^{xx} = -\frac{\delta_{mn} \Delta_x \Delta_y}{jk_0 Y_0 \left(\varepsilon_r - 1\right)}. \tag{C.55}$$

$$\delta Z^{yy} = -\frac{\delta_{mn} \Delta_x \Delta_y}{jk_0 Y_0 \left(\varepsilon_r - 1\right)}. \tag{C.56}$$

APPENDIX D

Parallel-Plate Mode Reduction In Conductor-Backed Slots Using Periodic Dielectric Substrates

Periodic dielectric substrates offer the possibility of changing the propagation characteristics of planar circuits and antennas. A number of applications for such materials can be imagined and have been implemented including various slow-wave structures, dielectric mirrors, resonant cavities, and frequency selective surfaces (FSS). A number of researchers have recently begun to design electromagnetic crystal structures for use in planar antenna applications, particularly for use as reflectors in planar dipole antenna structures. One of the early demonstrations of the potential for these materials in the microwave and millimeter-wave band was shown by Brown *et al.* in [18, 17] while investigating the radiation properties of a planar dipole on a photonic crystal substrate. Cheng *et al.* [21] followed by optimizing planar dipole antennas by using PBG crystals as a perfectly reflecting planar substrate. Kesler *et al.* [41] designed finite thickness slabs of two-dimensional PBG materials for use as an effective reflection plane for planar dipole antennas. The reflection and transmission properties of two- and three-dimensional PBG materials were studied by Sigalas *et al.* [95, 97] for calculating the radiation properties of planar dipole antennas. Leung *et al.* [53] measured the radiation patterns of a slot antenna placed on a layer-by-layer photonic band gap crystal. For a slot operating at a frequency in the band-gap of the three-dimensional PBG crystal, energy which would have been radiated into the substrate is reflected. However, at the interface between the PBG and the air, the periodicity of the PBG is broken and a parasitic mode (surface state) can exist. These surface states decrease the efficiency by stripping power away from the radiating element.

By fabricating a resonant slot over a reflecting back plate and filling the resulting parallel-plate with an appropriately designed periodic dielectric substrate, noticeable enhancements in both radiation pattern and bandwidth are achieved using a significantly lower profile than traditional designs. Measured and simulated data for conductor-backed slots with homogeneous substrates and with periodic dielectric substrates are compared.

In order to reduce backside radiation and increase the gain of planar slot antennas, traditional designs typically place some type of reflecting surface or cavity behind the slot. Unfortunately, increasing the profile of the slot negates one advantage of the planar radiating element. In addition, placing reflecting surfaces behind the slot reduces the efficiency by creating parasitic modes and using a cavity-backed design often necessitates narrowing the bandwidth. If the slot antenna is backed by a metal plate to increase the front-to-back ratio, parallel-plate waveguide (PPW) modes will be excited, both decreasing the efficiency and distorting the pattern. To completely block radiation from the backside of the slot from propagating to the finite edges of the resulting parallel-plate cavity, the cavity can be filled with a two-dimensional periodic dielectric substrate.

The theory and design of the periodic dielectric structure placed behind the conductor-backed slot is developed in Section D.1. In Chapter 3, the theory of electromagnetic plane wave propagation through simple two-dimensional periodic dielectric structures is developed both analytically (Fourier series solution) and numerically (IE/MoM solution). The plane wave expansion solution expands the propagating electric field as a periodic function with a prescribed phase shift and expands the periodic dielectric rods as another periodic function with no phase shift. Consequently, the electric field and dielectric rods are expanded in Fourier series and inserted into the wave equation. The resulting band structures can easily be determined by solving the the resulting matrix equation for the eigenvalues of the system. In the MoM model, the dielectric rods are replaced by equivalent (polarization) volume currents. The total field is determined as the sum of a known incident TEM wave propagating in a direction transverse to the cylinder axis with its electric field parallel to the cylinder axis and a scattered field which is due to radiation by the equivalent currents induced in the dielectric by the incident field. A nontrivial solution for the field requires the determinant of the impedance matrix to be zero, which results in a characteristic equation. The eigenvalues (propagation constants) are obtained from the roots of this equation. The folded slot antenna design and fabrication are outlined in Section D.2. Observations concerning the performance of the periodic dielectric structure and its use for backing slot antennas is detailed in Section D.3. General observations about the usefulness and possible applications for these special materials are found in the conclusions.

D.1 Electromagnetic Band-Gap Theory and Design

If the reflecting plate shown in Figure D.1 is located near enough to the slot such that the

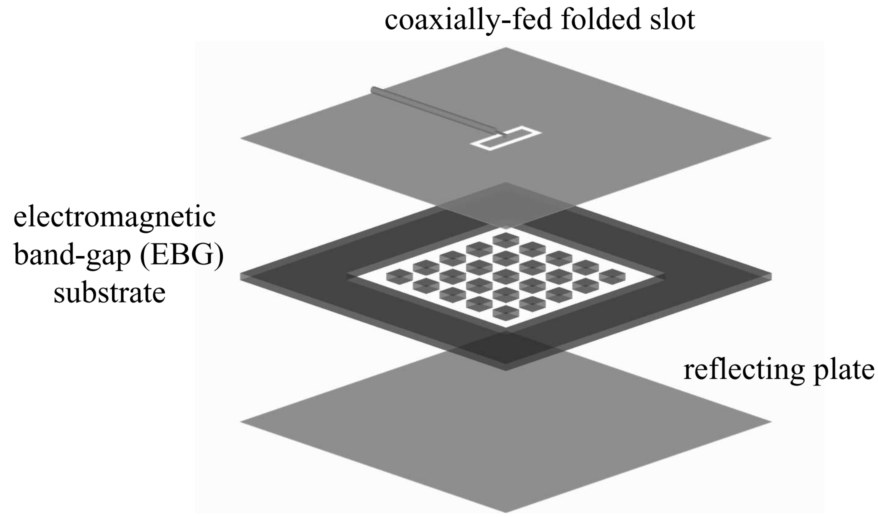

Figure D.1: Conductor-backed folded slot with periodic dielectric substrate

operating frequency is below the cutoff of the first TE/TM mode, only the dominant TEM mode (TM_0) with zero cutoff frequency will propagate. A single TEM mode is produced by keeping the separation distance between the plates less than half the guide wavelength. Because the propagation characteristics of the TEM mode of the resulting waveguide are very similar to the propagation characteristics of a uniform plane wave propagating normal to the axis of a infinite height dielectric structure, the substrate can be modeled as a doubly-periodic array of infinite dielectric rods in free space. The rods are imaged infinitely in height by using a PEC (perfect electric conductor) boundary and infinitely in width by using an PMC (perfect magnetic conductor) boundary located one-half unit cell away from the center of the rods (Figure D.2).

D.1.1 Substrate Design

For a simple two-dimensional periodic array of dielectric cylinders, the parameter combinations of unit cell size, element size, element shape (square/circle), lattice class (square, triangular, hexagonal), and dielectric contrast between the insert and the background material are the significant contributors to the resulting band structure.

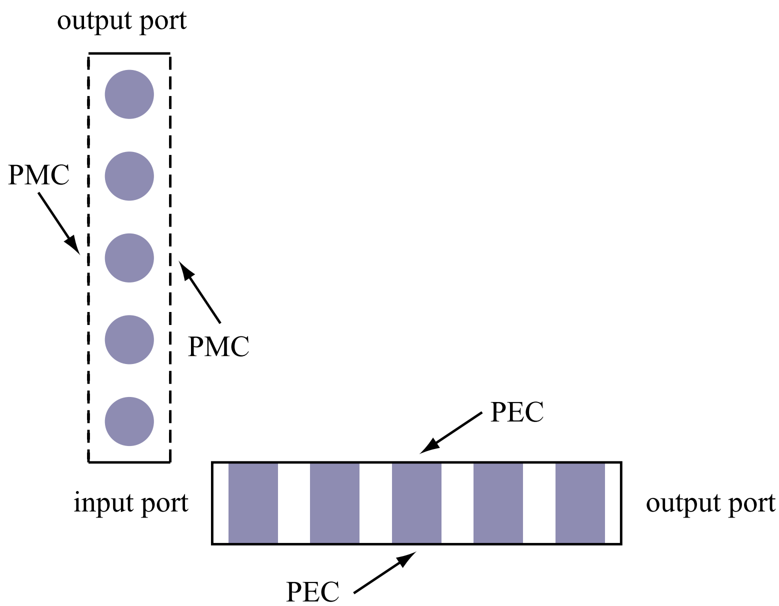

Figure D.2: Simulation unit cell

Lattice shape

A square lattice of dielectric columns is chosen to both simplify the fabrication and because it produces a larger gap for relatively lower frequencies (for parallel (TM) polarization) than do traditional hexagonal or honeycomb lattices [116, 63]. A brief discussion of other two-dimensional lattice structures can be found in Appendix B. For dielectric rod spacings of fractions of a wavelength, the primary TM band-gap of interest is the lowest band. The lower the lowest frequency band, the more applicable the periodic dielectric structure is for compact circuit applications.

Element shape

Although early two-dimensional research focused on using circular rods, square rods of commensurate size are chosen to simplify the formulation and fabrication. Band structures calculated in Chapter 3 justify replacing the traditional circular rods by square rods in this application. The geometries of the circular and square dielectric elements are shown in Figure D.3. Using circular rods of diameter b=4.8 mm and square rods of edge length b=4.8 mm produces a similar band structure (first gap) for the combination of unit cell size a=1.2 cm and relative dielectric constant $\varepsilon_r = 10.2$. In Figure D.4, one can clearly see that both the circular and square rods have relative large first gap-to-midgap ratios of 0.176 and 0.167, respectively. Consequently, small errors in the fabrication of the substrate can be

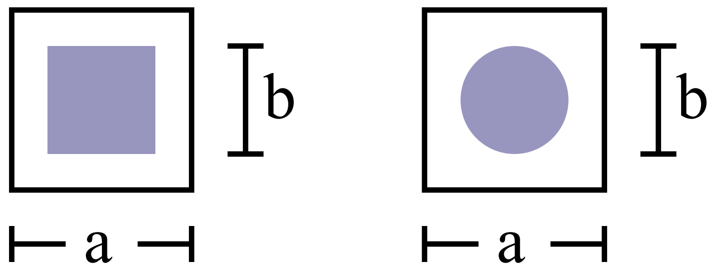

(a) (b)

Figure D.3: Unit cell dimensions for (a) square dielectric rods and (b) circular dielectric rods where for the square rod, a is the unit cell size, b is the element edge length, and for the circular rod, a is the unit cell size and b is the diameter

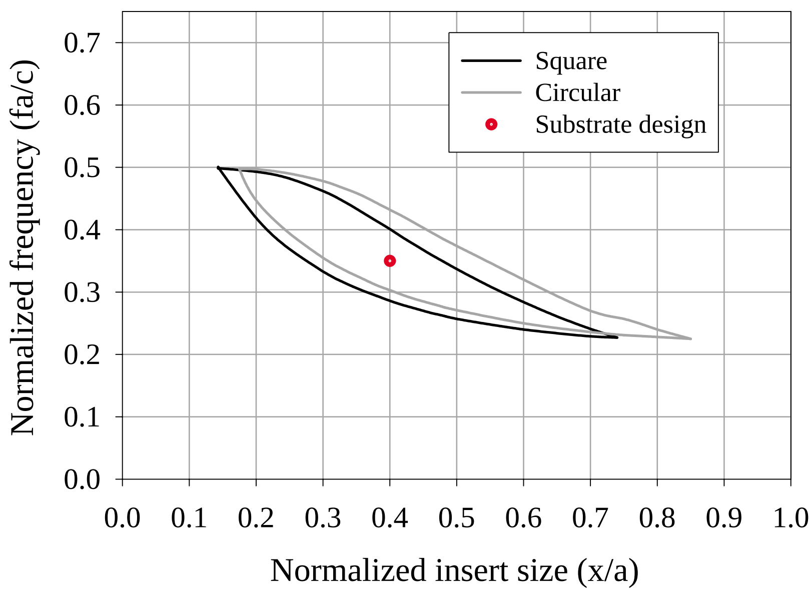

Figure D.4: Band-gap plot as a function normalized insert size b/a

absorbed with little or no consequence. The final design of the periodic structure is shown as a circle in the center of the gaps and produces an omni-directional stopband between 7.5 and 10 GHz. The full band structure of a square lattice of dielectric columns as a function of b/a is seen in Figure D.5 for circular or square rods.

Design validation for finite lattice

In parallel to the the method of moments solution and plane wave (Fourier series – eigenvalue) expansion solution, finite element simulations have been implemented to cor-

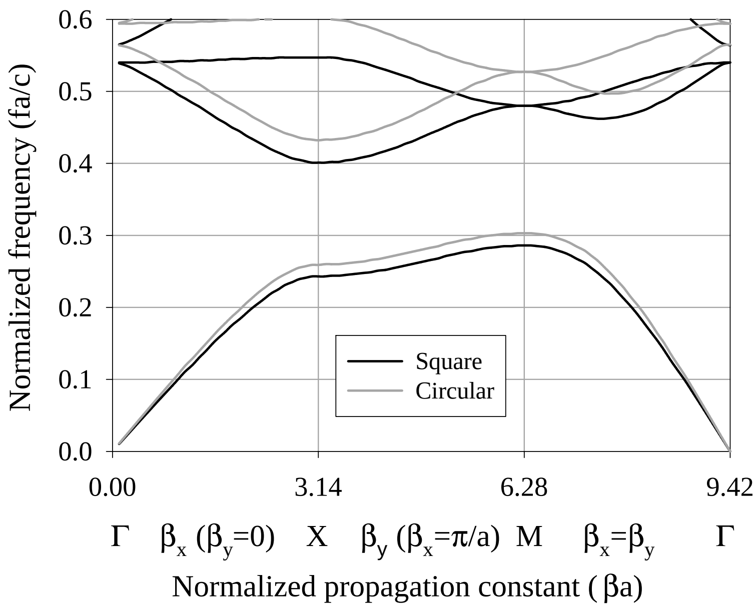

Figure D.5: Full band structure of a square lattice of dielectric columns as a function of normalized insert size b/a

roborate the band structure of a realizable (finite) structure. In order to achieve a useful stopband, a large (ideally, infinite) number of periods are required. However, significant attenuations can still be achieved using only a small number of periods by designing an appropriate periodic structure. The periodically dielectric-loaded parallel-plate is simulated using the Agilent EEsof EDA High-Frequency Structure Simulator (HFSS). For a square lattice of five periods, the simulations take between four seconds for the Γ–X direction of the irreducible Brillouin zone[1] (Figure D.6) and eight seconds for the Γ–M direction per frequency point on a 400 MHz Pentium II PC. Because the speed of the simulation is so

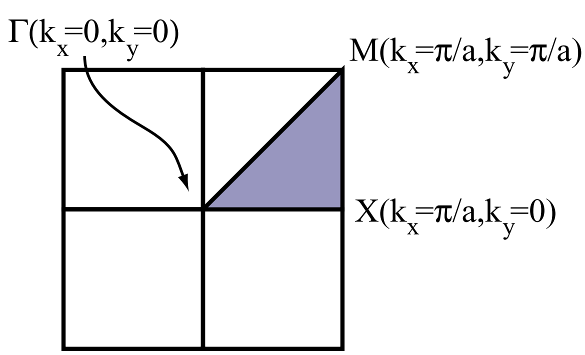

Figure D.6: Irreducible Brillouin Zone (BZ)

[1]The concept of the irreducible Brillouin zone for two-dimensional periodic structures is developed further in Appendix B.

rapid, these structures can be repetitively designed and validated quickly.

In the finite structure, the center frequency of the first stopband for the square rods is 8.5 GHz (Γ–X direction, b/a=0.4, ε_r=10.2). As expected, the center frequency of the first stopband for the circular rods is 9.0 GHz (Γ–X direction, b/a=0.4, ε_r=10.2), about 5% higher than the case using square elements. However, the 10 dB bandwidth of the stopband is 4.0 GHz for square dielectric elements and 4.7 GHz for circular dielectric elements. The significant increase in the gap-to-midgap ratio (bandwidth) for the finite structure can be attributed to the certain widening of the stopband – a necessary consequence of using a finite number of elements – and to the requirement of a finite attenuation inside the stopband. At the center frequency of the band-gap, omni-directional attenuations of at least 20 dB and upwards of 45 dB attenuation in specific directions can be obtained using only 3–4 periods (Figure D.7). This is compared to the ideally infinite attenuations within the stopband of an unrealizable infinite structure.

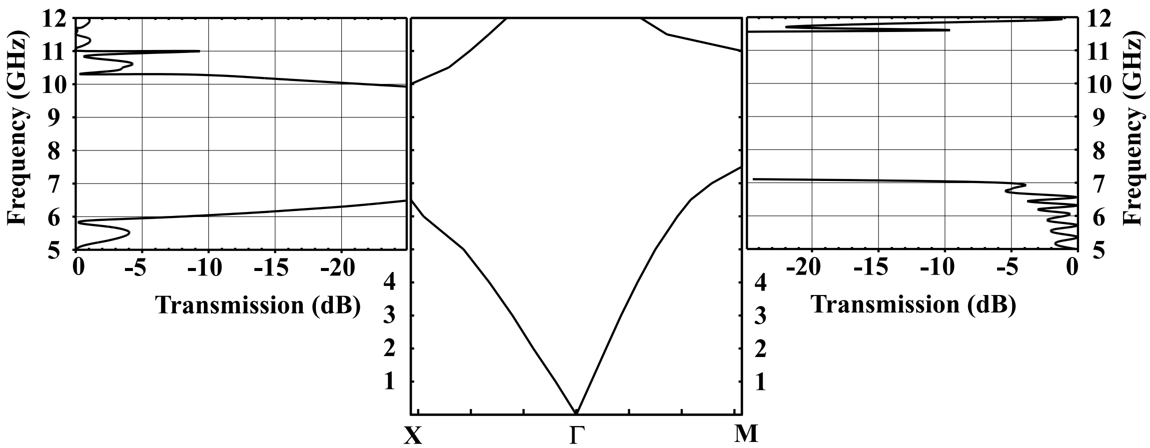

Figure D.7: Simulated (HFSS) transmission spectra for Γ–X (left) and Γ–M (right) directions and calculated (MoM) band diagram (center) of a two-dimensional EBG with a=1.2 cm, b=4.8 mm, and ε_r=10.2 for TM polarization.

D.2 Slot Antenna Design and Fabrication

A conductor-backed folded slot with a homogeneous substrate was designed initially to provide an acceptable match when center-fed. Preliminary work using this $\lambda_g/2$ reference slot revealed the difficulty in matching the high input impedance of the slot to the coaxial feed. Consequently, the single $\lambda_g/2$ slot was replaced with a folded λ_g slot. Not only is the folded λ_g slot easier to match to the input impedance of the coaxial feed than the $\lambda_g/2$ slot but it also has increased bandwidth.

D.2.1 Reference Slot

A half-wave reference folded slot of length 14.3 mm and width of 2.0 mm shown in Figure D.8, where slot dimensions in parentheses refer particularly to the reference slot

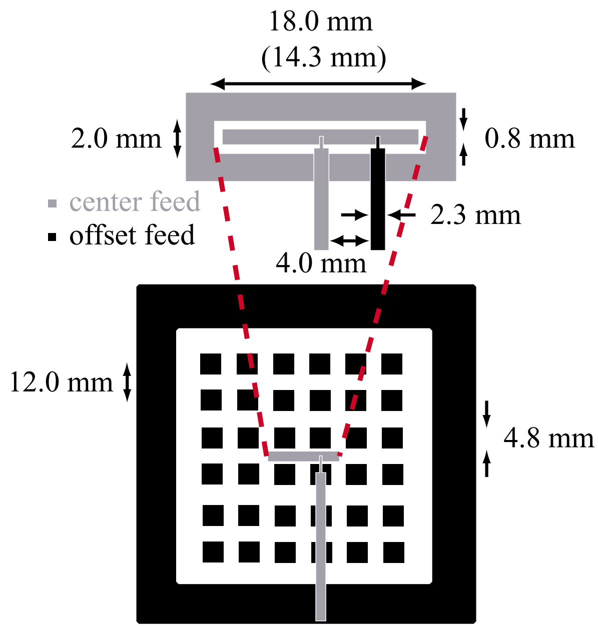

Figure D.8: Top view of conductor-backed folded slot design with periodic dielectric substrate (a=1.2 cm, b=4.8 mm, and ε_r=10.2) where slot dimension in parentheses refers only to the reference slot design on an homogeneous substrate

design, was fabricated using wet etching on a square copper clad RT/duroid homogeneous substrate with dielectric constant of 2.2, a 127 mm (5 in) edge length, and a thickness of 1.65 mm (65 mil). The reference slot was then center-fed using a simple coaxial line [46]. Note that the reference slot is simply a truncated conductor-backed slot with a homogeneous dielectric substrate. The periodically-machined dielectric shown in the figure corresponds to the following folded slot design.

D.2.2 Folded Slot

Similarly to the reference slot, a folded slot of length 18.0 mm and width of 2.0 mm was fabricated using wet etching on a square copper clad RT/duroid substrate with dielectric constant of 2.2, a 127 mm (5 in) edge length, but a thickness of only 127 μm (5 mil). A top view of the conductor-backed folded slot design integrated with periodic dielectric substrate

(a=1.2 cm, b=4.8 mm, and ε_r=10.2) is shown in Figure D.8. The difference in size of the two slots allows for resonances at equivalent frequencies. In order to design the slot antenna for optimal performance, the slot is designed to resonate near the center frequency of the designed substrate band-gap. When the folded slot design is integrated with the substrate, as shown in Figure D.8, the energy from the slot is coupled into the parallel-plate mode which is then stored in the dielectric lattice, loading the slot inductively. Consequently, an off-center feed is used to provide a better impedance match.

The thin substrate was then bonded to a square copper clad RT/duroid substrate with dielectric constant of 10.2, a 127 mm (5 in) edge length, and a thickness of 2.54 mm (100 mil) milled as shown in Figure D.8. A small amount of dielectric ($\approx$ 10 mil) was left on the lower plate in order to provide some stability for mounting the slot plate. Simulations have shown that the remaining small amounts of dielectric ($\approx$ 10% of the total substrate height) on the back plate change the center frequency and attenuation per period of the band-gap slightly ($\approx$ 5%). This observation is similar to the small change in the propagation constant of a partially-loaded parallel-plate waveguide. For instance, the low frequency approximation for the propagation constant β in an partially-loaded parallel plate waveguide is [24]

$$\beta = \sqrt{\frac{\varepsilon_r b}{a + \varepsilon_r (b - a)}} k_0 = \sqrt{\varepsilon_e} k_0 \tag{D.1}$$

where a is the dielectric sheet thickness, b is the plate separation, and ε_e is the effective dielectric constant. For a frequency of 10 GHz, plate separation of 2.54 mm, dielectric sheet thickness of 0.254 mm, and dielectric constant 10.2, the effective dielectric constant ε_e is estimated to be 1.1, corresponding to less than a 5% change the propagation constant.

To provide additional support to mount the slot plate, material at the outer edge of the substrate was not milled as can also be seen in Figure D.8. HFSS simulations have shown that this supporting material does not significantly affect the performance of the slot (see Section D.3). The frequency response of the fabricated folded slot design, with noticeable resonances at 9.4 GHz and 9.6 GHz, is displayed in Figure D.9. The slots were designed to radiate at 9.2 GHz. Unfortunately, difficulty in bonding the slot plate to the perforated substrate may have introduced additional unwanted modes and/or a shifting of the slot resonance. In the same figure, the finite-element simulation (HFSS) of the folded slot design finds a resonance slightly below 9.0 GHz. The difference between the simulations and the experiment is due to the simplifications introduced in the structure analyzed by HFSS to reduce computer memory and simulation time and the fabrication errors mentioned previously.

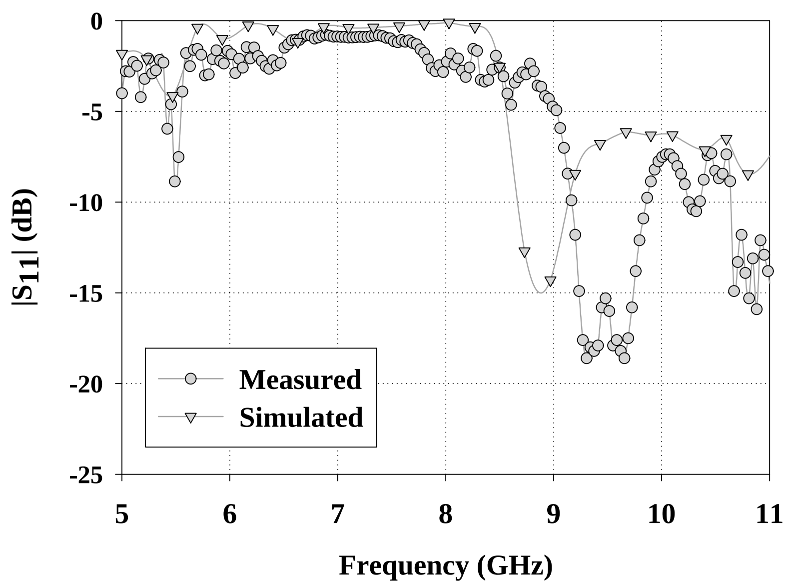

Figure D.9: Measured and simulated frequency response of conductor-backed slot with periodic dielectric substrate

D.3 Results and Discussion

Simulations of coaxially-fed slots in a metal plate in free space have relatively large 10 dB bandwidths on the order of 10–15%. However, since the slot radiates equally into each half-space, the front-to-back ratio is 0 dB. If a metal sheet is used as a reflector, the front-to-back ratio is increased, but unwanted energy is trapped in parallel-plate modes and radiates away from the slot. Simulations of a finite-sized reflector-backed slot with an absorbing boundary condition at the edges of the resulting cavity, effectively modeling an infinite parallel-plate, yield a 10 dB bandwidth of 30%. The large bandwidth is the result of the slot radiating most of its power into the infinite waveguide. If, however, the infinite sheet is replaced by a finite one, an undulating field pattern will be seen. This is particularly true for ground planes that are larger than one-half wavelength [46]. Consequently, the 127 mm edge length of the sheet in this design, corresponding to about 4 free space wavelengths, yields significant pattern degradation. Notice the classic interference pattern (7–8 dB "dips" in the pattern) reported earlier [13, 79] to be caused by the radiation from the edges of the finite ground can be clearly seen in the pattern for the reference in Figure D.10. Some suppression technique must be implemented to eliminate this parasitic radiation.

In order to reduce the effects of the finite ground, a number of suppression techniques are known, including integrating the antenna on a substrate lens [31]. Although useful for

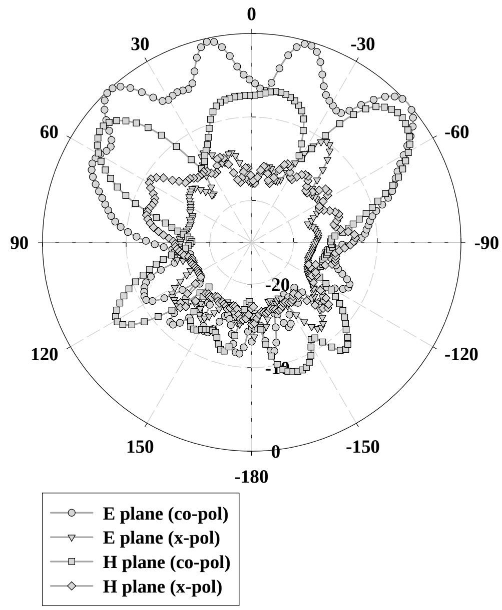

Figure D.10: Measured normalized E- and H-plane antenna patterns (co- and x-pol) of reference slot at 9.7 GHz

providing unidirectional radiation patterns by suppressing substrate surface wave formation, lenses are not necessarily low-profile. Cavity-backed slots are another effective method of increasing the front-to-back ratio. A simulation of a $\lambda/4$ cavity-backed slot [46] yielded a 10 dB bandwidth of 7.5%. Careful design can minimize the necessarily narrower bandwidth of cavity-backed slots. If vertical integration space is a premium, cavity-backed designs much like a lens may not be appropriate. Recently, a slot on a synthesized three-dimensional metallic photonic band-gap crystal was fabricated by composing alternating layers of thin metallic rods [53]. Unfortunately the response of the slot is very sensitive to the placement of the slot over the rods. Gains of 2–3 dB were reported with low cross-polarization levels for specific slot locations and for narrow frequency bands. The bandwidth and frequency response of the antenna was not reported. Although the three-dimensional electromagnetic crystal acts as a good reflector, it does not enhance the transmission signal as much as was expected. As was mentioned earlier, parasitic surface states, which reduce the radiated power, can exist when the periodicity of the three-dimensional structure is broken.

The field distribution inside a slot-fed finite parallel-plate is similar to that of a slot-fed metallic cavity with PMC edge boundaries. Reflections from the edges of the parallel-plate waveguide effectively create an over-moded cavity. This parasitic radiation from the edges is dependent on the mode that is formed in the cavity. Energy leakage from the substrate through the edges of the cavity manifests itself in unwanted effects such as reduced front-to-back ratio, reduced efficiency, increased cross-polarization level, and pattern distortion as shown in the reference antenna pattern of Figure D.10. This effect is significantly reduced when the specially designed periodic dielectric substrate is implemented. If the slot is designed to radiate at a frequency inside the band-gap, the parallel-plate TEM mode will be trapped in the dielectric lattice. Consequently, very little power is lost to substrate modes. An effective cavity is formed, since the energy in the parallel-plate mode is reflected back to the radiating slot (Figure D.11). The field structure inside the parallel plate waveguide shown in Figure D.11 was determined from a HFSS simulation implemented by Chappell [91]. The darker regions in the figure are areas of higher field intensity; the lighter regions are areas of lower field intensity. As mentioned previously, the supporting material remaining at the edge of the substrate does not affect the performance of the slot. The removed material was replaced with a metallic boundary condition and the simulations were repeated. No significant change in field strength or field structure was observed. The periodic dielectric substrate has two benefits over traditional metallic cavities. Namely, the reflection from the cavity boundaries can be controlled – adding more layers of periodic material around the slot will increase the reflectivity of the boundaries – and the boundary conditions of the resulting effective cavity are frequency dependent.

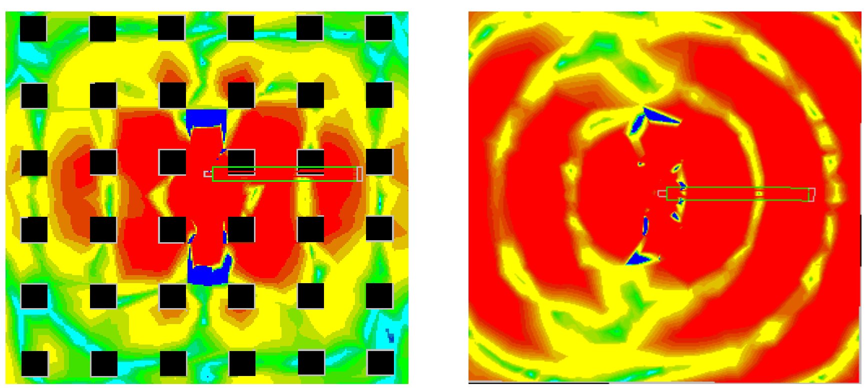

Figure D.11: Evanescent field structure inside EBG-backed substrate (left) and propagating mode in homogeneously-filled parallel-plate (right)

As can be clearly seen in Figure D.12, the slot has a front-to-back ratio of more than 15 dB. Low cross-polarization levels were measured in both the E and H planes. The 10 dB bandwidth is measured to be 7.5%, lower than that of the single planar slot and similar to the bandwidth of traditional cavity-backed designs as expected. It is observed that the antenna patterns are similar to that of a slot in an infinite ground plane; the significant

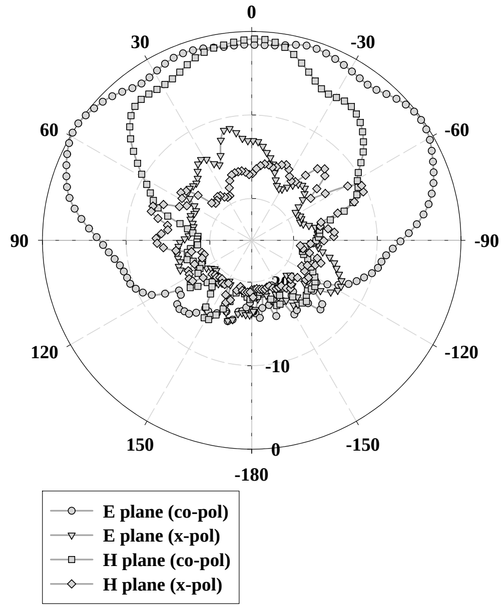

Figure D.12: Measured normalized E- and H-plane antenna patterns (co- and x-pol) of conductor-backed slot with EBG substrate at 9.7 GHz

7–8 dB "dips" in the reference slot pattern are reduced to 1–2 dB in the pattern of the slot backed by the periodic dielectric (Figure D.13).

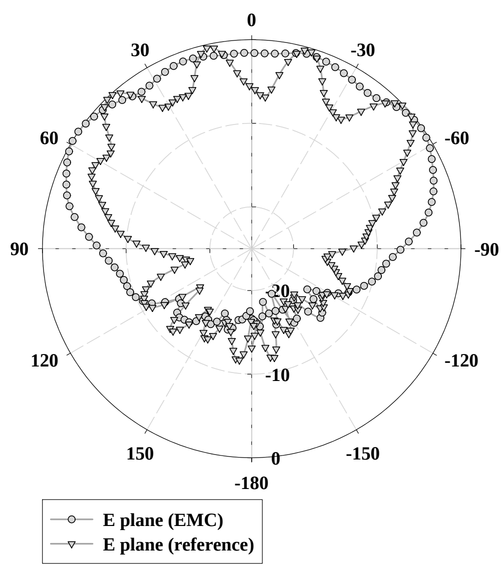

Figure D.13: Measured normalized E-plane antenna patterns (co-pol) of the reference slot and the slot backed with the periodic dielectric at 9.7 GHz

D.3.1 Gain Measurement

A common method for gain measurement is the relative gain measurement technique or *gain-transfer (gain-comparison)* method [8]. This approach is based on the substitution of a test antenna (unknown gain) with an antenna with a known gain (standard gain) and comparing the corresponding received power levels. Since all of the parameters are fixed except for the gain of the receiver antenna, it can be easily shown that the Friis Transmission equation reduces to

$$G_u = \frac{P_r^u}{P_r^s} G_s \tag{D.2}$$

where G_u and G_s are the gains of the unknown and standard antennas, respectively, and P_u^r and P_s^r are the received powers for the antenna under test and the standard gain antenna, respectively. The maximum received powers (E-plane) for the slotted antenna and for a Narda standard gain horn antenna were measured and the gain of the conductor-backed antenna mounted over the artificial dielectric substrate antenna was found to be approximately 3.1±0.2 dB.

The field patterns of the slot antenna mounted on the EBG-backed substrate shown in the preceding figures are similar to those obtained for an ideal slot. For an ideal, perfectly matched, one-half wavelength slot mounted in an perfectly conducting infinite plate, the variation of E_θ as a function of θ can be approximated by

$$E_\theta = \frac{\cos\left[(\pi/2)\cos\theta\right]}{\sin\theta} \tag{D.3}$$

and the variation of E_θ as a function of ϕ is constant.

D.3.2 Directivity Measurement

Directivity is a indication of the directional properties of an antenna. The directivity can be found by finding the maximum increase in power density in a given direction from a fixed transmitting antenna, relative to the power density with the same transmit power distributed equally in all directions [109]. Accurate determinations of the directivity require that the full three-dimensional antenna pattern be known or measured. Because a full (θ, ϕ) pattern cannot be obtained easily for all antennas, a number of different methods have been proposed to approximate the directivity. The predicted directivity (gain) for an ideal slot in infinite ground is 1.6 (2.2 dB) [46]. For the ideal slot radiating only into the upper hemisphere, the directivity (gain) is doubled to approximately 3.2 (5.2 dB) [13].

Principal-plane or half-power beamwidth approximation

An approximate value for the directivity D of antenna can be found by dividing the directivity-beamwidth product DB by the principal-plane beamwidths, HP_{E° and HP_{H°,

$$D = \frac{DB}{HP_{E^\circ} HP_{H^\circ}}. \tag{D.4}$$

Appropriate values for DB range from $4\pi(180/\pi)^2 = 41\ 253\,\text{deg}^2$ for a rectangular beam with no-sidelobe pattern to more realistic values of 30 000 [8] and 26 000 [110, 109] for practical antenna measurements. Using the latter value of 26 000 as a worst-case scenario for the directivity-beamwidth product and determining the principal-plane beamwidths of the folded slot to be 160° and 60°, a coarse estimate for the directivity is 2.7 (4.3 dB) yielding an efficiency of about 80%.

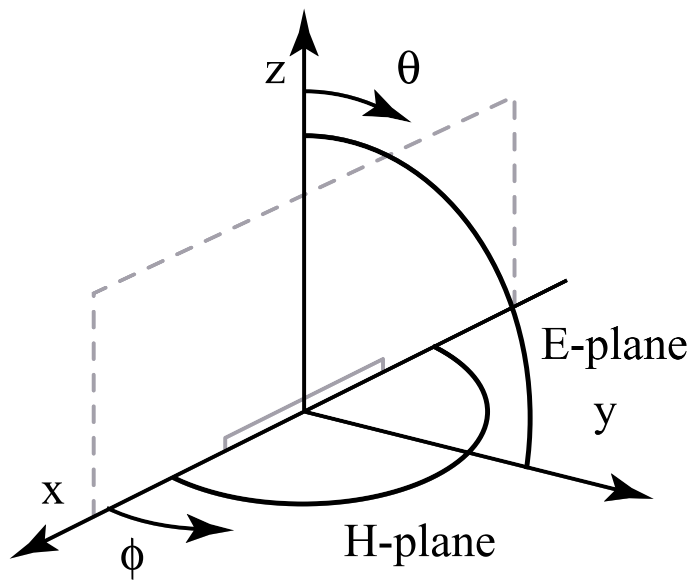

Figure D.14: Axis and pattern cut definitions of the measurement systems

Pattern integration

Although half-power beamwidth measurements are simple antenna measurements that provide a coarse estimate for the directivity, more accurate calculations can be performed by integrating known θ and ϕ cuts. Assuming the radiation intensity of a given antenna is separable in θ and ϕ, an estimate for the total radiated power can be determined by integrating E_θ and E_ϕ over the E-plane (θ) shown in Figure D.14 while assuming the ϕ-variation is constant. By integrating the pattern over θ and multiplying the result by 2π, an estimate for the directivity is 2.76 (4.4 dB) yielding an efficiency of around 80%, similar to the efficiency obtained previously. More accurate values of the radiated power density, and consequently efficiency, can be obtained by introducing additional θ and ϕ cuts.

In order to verify that the estimated efficiencies calculated for the antenna are reasonable, HFSS simulations of the finite-size, conductor-backed folded-slot antenna mounted over the designed artificial dielectric were conducted by Chappell [91] that yield an efficiency of over 90%, which is significantly higher than the estimates determined from the measurements. However, it should be noted that the simulation assumed no conductor loss which is one of the dominant loss mechanisms in the system.

D.4 Conclusions

Although relatively thick substrates were used in this chapter to demonstrate the usefulness of the conductor-backed folded slot with periodic dielectric substrates, similar results can be obtained using significantly thinner substrates. This is very desirable for applications involving packaging, such as layered circuits or vertical integration of components, particularly where ground plane proximity is a concern. In addition, the effective cavity resulting from the lattice is frequency dependent and tunable. Above and below the band-gap, the periodic structure allows energy to propagate through virtually unimpeded. In the center of the gap, the structure is virtually impassible to electromagnetic propagation. Near the band edges, proper design could further increase the bandwidth of this antenna by decreasing the attenuation per period or by allowing specific modes to propagate unattenuated.

APPENDIX E

Review Of The Method Of Moments

The use of the methods of moments [34] to numerically solve various electromagnetic problems has been used effectively since the mid-1960's. It has since become one of the standard techniques used by computational electromagnetic (CEM) theorists because of its accuracy and ease of implementation.

Consider the following nonhomogeneous equation

$$L\mathbf{u} = \mathbf{f} \tag{E.1}$$

where L is a linear operator, $\mathbf{f}$ is known vector quantity , and $\mathbf{u}$ is unknown vector quantity to be determined. In electromagnetics, L is often a linear intergro-differential operator, $\mathbf{f}$ is the known excitation, and $\mathbf{u}$ is the unknown field or current. We begin by expanding $\mathbf{u}$ in a linear combination of basis (or expansion) functions

$$\mathbf{u} = \sum_n a_n \mathbf{u}_n \tag{E.2}$$

where a_n are the coefficients of the basis $\mathbf{u}_n$. Finite computational resources require the sum in (E.2) to be finite. Thus, the method of moments, although exact in theory, is an approximate technique in practice. Substituting (E.2) into (E.1) one obtains

$$\sum_n a_n L\mathbf{u}_n = \mathbf{f}. \tag{E.3}$$

To determine the coefficients of the unknown basis, (E.3) is tested by performing an inner product of the linear combination of basis functions with N weighting (or testing) functions

$$\sum_n a_n \langle \mathbf{w}_m, L\mathbf{u}_n \rangle = \langle \mathbf{w}_m, \mathbf{f} \rangle \quad m = 1, 2, \ldots, N \tag{E.4}$$

where the inner product $\langle \mathbf{a}, \mathbf{b} \rangle$ can be defined as

$$\langle \mathbf{a}, \mathbf{b} \rangle = \int \mathbf{a} \cdot \mathbf{b}^* \, d\,\mathbf{x} \tag{E.5}$$

where $\mathbf{x}$ is a multidimensional variable and * denotes the complex conjugate. (E.4) can be written in matrix form as

$$\left[L_{mn}\right]\left[a_n\right] = \left[f_m\right], \tag{E.6}$$

where

$$\left[L_{mn}\right] = \begin{bmatrix} \langle \mathbf{w}_1, L\mathbf{u}_1 \rangle & \langle \mathbf{w}_1, L\mathbf{u}_2 \rangle & \cdots & \langle \mathbf{w}_1, L\mathbf{u}_N \rangle \\ \langle \mathbf{w}_2, L\mathbf{u}_1 \rangle & \langle \mathbf{w}_2, L\mathbf{u}_2 \rangle & \cdots & \langle \mathbf{w}_2, L\mathbf{u}_N \rangle \\ \vdots & \vdots & \ddots & \vdots \\ \langle \mathbf{w}_N, L\mathbf{u}_1 \rangle & \langle \mathbf{w}_N, L\mathbf{u}_2 \rangle & \cdots & \langle \mathbf{w}_N, L\mathbf{u}_N \rangle \end{bmatrix}, \tag{E.7a}$$

$$\left[a_n\right] = \begin{bmatrix} a_1 \\ a_2 \\ \vdots \\ a_N \end{bmatrix}, \tag{E.7b}$$

and

$$\left[f_m\right] = \begin{bmatrix} \langle \mathbf{w}_1, f \rangle \\ \langle \mathbf{w}_2, f \rangle \\ \vdots \\ \langle \mathbf{w}_N, f \rangle \end{bmatrix}. \tag{E.7c}$$

In electromagnetics, $[L_{mn}]$ is often represented as an impedance matrix $[Z_{mn}]$ relating the excitation to the unknown.

If $[L_{mn}]^{-1}$ exists, the solution for the coefficients a_n can be found from

$$\left[a_n\right] = \left[L_{mn}\right]^{-1}\left[f_m\right], \tag{E.8}$$

using a number of well-known linear solution techniques.

BIBLIOGRAPHY

BIBLIOGRAPHY

[1] *Journal of the Optical Society of America B*, vol. 10, Feb 1993. Special issue on photonic band-gap structures.

[2] *Journal of Modern Optics*, vol. 41, Feb 1994. Special issue on photonic band-gap structures.

[3] *IEEE Transactions on Microwave Theory and Techniques*, vol. 47, Nov 1999. Mini-special issue on electromagnetic crystal structures, design, synthesis, and applications.

[4] *Journal of Lightwave Technology*, vol. 17, Nov 1999. Special section on electromagnetic crystal structures, design, synthesis, and applications.

[5] *Electromagnetics*, vol. 41, Feb 1999. Special issue on theory and applications of photonic band-gap structures.

[6] N. G. Alexopoulos, "Integrated-circuit structures on anisotropic substrates," *IEEE Transactions on Microwave Theory and Techniques*, vol. MTT-33, no. 10, pp. 847–881, Oct 1985.

[7] I. J. Bahl, P. Bhartia, and S. S. Stuchly, "Design of microstrip antennas covered with a dielectric layer," *IEEE Transactions on Antennas and Propagation*, vol. AP-30, no. 2, pp. 314–317, Mar 1982.

[8] C. A. Balanis, *Antenna Theory: Analysis and Design*, Harper & Row Publishers, New York, NY, 1982.

[9] C. A. Balanis, *Advanced Engineering Electromagnetics*, John Wiley & Sonce, Inc., New York, NY, 1989.

[10] H. Bertoni, L.-H. Cheo, and T. Tamir, "Frequency-selective reflection and transmission by a periodic dielectric layer," *IEEE Transactions on Antennas and Propagation*, vol. AP-37, no. 1, pp. 78–83, Jan 1989.

[11] P. Bhartia, K. V. S. Rao, and R. S. Tomar, *Millimeter-wave Microstrip and Printed Circuit Antennas*, Artech House, Boston, MA, 1991.

[12] A. K. Bhattacharyya, "Analysis of multilayer infinite periodic array structures with different periodicities and axes orientation," *IEEE Transactions on Antennas and Propagation*, vol. AP-48, no. 3, pp. 357–369, Mar 2000.

[13] H. G. Booker, "Slot aerials and their relation to complementary wire aerials," *Journal of the Institution of Electrical Engineers*, vol. 93, no. 4, , 1946. IIIA.

[14] F. Bouttout, F. Benabdelaziz, A. Benghalia, D. Khedrouche, and T. Fortaki, "Uniaxially anisotropic substrate effects on resonance of rectangular microstrip patch antenna," *Electronics Letters*, vol. 35, no. 4, pp. 255–256, Feb 1999.

[15] C. Brezinski, "Some new convergence acceleration methods," *Mathematics of Computing*, vol. 39, pp. 133–145, 1982.

[16] L. Brillouin, *Wave Propagation in Periodic Structures*, McGraw–Hill, New York, NY, 1946.

[17] E. R. Brown and O. B. McMahon, "High zenithal directivity from a dipole antenna on a photonic crystal," *Applied Physics Letters*, vol. 68, no. 9, pp. 1300–1302, Feb 1996.

[18] E. R. Brown, C. D. Parker, and E. Yablonovitch, "Radiation properties of a planar antenna on a photonic-crystal substrate," *Journal of the Optical Society of America B*, vol. 10, no. 2, pp. 404–407, Feb 1993.

[19] Z. Cai and J. Bornemann, "Rigorous analysis of radiation properties of lossy patch resonantors on complex anisotropic media and lossy ground metallization," *IEEE Transactions on Antennas and Propagation*, vol. AP-42, no. 10, pp. 1443–1446, Oct 1994.

[20] C. H. Chan, "Analysis of frequency selective surfaces," in *Frequency Selective Surface and Grid Array*, T. K. Wu, editor, chapter 2, pp. 27–85, John Wiley & Sons, Inc., New York, NY, 1985.

[21] S. D. Cheng, R. Biswas, E. Ozbay, S. McCalmont, G. Tuttle, and K.-M. Ho, "Optimized dipole antennas on photonic band gap crystals," *Applied Physics Letters*, vol. 67, no. 23, pp. 3399–3401, Dec 1995.

[22] D. N. Chigrin, A. V. Lavrinenko, D. A. Yarotsky, and S. V. Gaponenko, "Observation of total omnidirectional reflection from a one-dimensional dielectric lattice," *Applied Physics A*, vol. 68, pp. 25—28, 1999.

[23] R. E. Collin, "A simple artificial anisotropic dielectric medium," *IRE Transactions on Microwave Theory and Techniques*, pp. 206–209, 1958.

[24] R. E. Collin, *Foundations for Microwave Engineering*, McGraw–Hill, Inc., New York, NY, 1992.

[25] S. R. Coriell and J. L. Jackson, "Bounds on transport coefficients of two-phase materials," *Journal of Applied Physics*, vol. 39, no. 10, pp. 4733–4736, September 1968.

[26] J. P. Dowling and C. M. Bowden, "Anomalous index of refraction in photonic bandgap materials," *Journal of Modern Optics*, vol. 41, no. 2, pp. 345–351, 1994.

[27] T. F. Eibert, J. L. Volakis, D. R. Wilton, and D. R. Jackson, "Hybrid FE/BI modeling of 3-D doubly periodic structures utilizing triangular prsimatic elements and an MPIE formulation accelerated by the Ewald transformation," *IEEE Transactions on Antennas and Propagation*, vol. AP-47, no. 5, pp. 843—850, May 1999.

[28] R. S. Elliott, *Antenna Theory and Design*, Prentice–Hall, Inc., Englewood Cliffs, NJ, 1981.

[29] T. Ellis, J. D. Shumpert, L. P. B. Katehi, and G. M. Rebeiz, "Do two dimensional periodic structures exhibit photonic bandgap properties?," in *1998 URSI North American Radio Science Meeting Digest*, p. 120, Jun 1998.

[30] P. P. Ewald, "Die Berechnung optisher und elektrostatischer Gitterpotentiale," *Annalen der Physik*, vol. 64, no. 3, pp. 253–286, 1921.

[31] D. F. Filipovic, S. S. Gearhart, and G. M. Rebeiz, "Double-slot antennas on extended hemi-spherical and elliptical silicon dielectric lenses," *IEEE Transactions on Microwave Theory and Techniques*, vol. MTT-41, no. 10, pp. 1738–1749, Oct 1993.

[32] S. D. Gedney, J. F. Lee, and R. Mittra, "A combined FEM/MoM approach to analyze the plane wave diffraction by arbitrary gratings," *IEEE Transactions on Microwave Theory and Techniques*, vol. MTT-40, no. 2, pp. 363–370, Feb 1992.

[33] R. F. Harrington, *Time-Harmonic Electromagnetic Fields*, McGraw–Hill, New York, NY, 1961.

[34] R. F. Harrington, *Field Computation by Moment Methods*, Kreiger Publishing Company, Malabar, FL, 1993.

[35] Z. Hashin and S. Shtrikman, "A variational approach to the theory of effective magnetic permeability of multiphase materials," *Journal of Applied Physics*, vol. 33, pp. 3125–3131, 1962.

[36] K. M. Ho, C. T. Chan, and C. M. Soukoulis, "Existence of a photonic gap in periodic dielectric structures," *Physical Review Letters*, vol. 65, no. 25, pp. 3152–3155, Dec 1990.

[37] D. R. Jackson and N. G. Alexopoulos, "Simple approximate formulas for input resistance, bandwidth, and efficiency of a resonant rectangular patch," *IEEE Transactions on Antennas and Propagation*, vol. AP-39, no. 3, pp. 407–410, Mar 1991.

[38] J. D. Joannopoulos, R. D. Meade, and J. N. Winn, *Photonic Crystals: Molding the Flow of Light*, Princeton University Press, Princeton, NJ, 1995.

[39] K. E. Jordan, G. R. Richter, and P. Sheng, "An efficient numerical evaluation of the Green's function for the Helmholtz operator on periodic structures," *Journal of Computational Physics*, vol. 63, pp. 222–235, 1986.

[40] R. E. Jorgenson and R. Mittra, "Efficient calculation of the free-space Green's function," *IEEE Transactions on Antennas and Propagation*, vol. AP-38, no. 5, pp. 633–642, May 1990.

[41] M. P. Kesler, J. G. Maloney, B. L. Shirley, and G. S. Smith, "Antenna design with the use of photonic band-gap materials as all-dielectric planar reflectors," *Microwave and Optical Technology Letters*, vol. 11, no. 4, pp. 169–174, Mar 1996.

[42] N. Kinayman and M. I. Aksum, "Comparative study of acceleration techniques for integrals and series in electromagnetic problems," *Radio Science*, vol. 30, no. 6, pp. 1713–1722, Nov–Dec 1995.

[43] R. L. Kipp and C. H. Chan, "A numerically efficient technique for the method of moments solution for planar periodic structures in layered media," *IEEE Transactions on Microwave Theory and Techniques*, vol. MTT-42, no. 4, pp. 635–643, Apr 1994.

[44] C. Kittel, *Introduction to Solid State Physics*, John Wiley & Sons, Inc., New York, NY, seventh edition, 1996.

[45] J. A. Kong, *Electromagnetic Wave Theory*, John Wiley & Sons, Inc., New York, NY, 1990.

[46] J. D. Kraus, *Antennas*, McGraw–Hill Publishing, New York, NY, 1950.

[47] E. F. Kuester and C. L. Holloway, "Comparison of approximations for effective parameters of artificial dielectrics," *IEEE Transactions on Microwave Theory and Techniques*, vol. MTT-38, no. 11, pp. 1752–1755, Nov 1990.

[48] E. F. Kuester and C. L. Holloway, "A low-frequency model for wedge or pyramid absorber arrays — I: theory," *IEEE Transactions on Electromagnetic Compatability*, vol. EMC-36, no. 4, pp. 300–306, Nov 1994.

[49] C. A. Kyriazidou, H. F. Contopanagos, W. M. Merrill, and N. G. Alexopoulos, "Artificial versus natural crystals: effective wave impedance of printed photonic bandgap materials," *IEEE Transactions on Antennas and Propagation*, vol. AP-48, no. 1, pp. 95–104, Jan 2000.

[50] P. Lalanne, "Effective medium theory applied to photonic crystals composed of cubic or square cylinders," *Applied Optics*, vol. 35, no. 27, pp. 5369–5380, Sep 1996.

[51] R. Lampe, P. Klock, and P. Mayes, "Integral transforms useful for the accelerated summation of periodic, free-space Green's functions," *IEEE Transactions on Microwave Theory and Techniques*, vol. MTT-33, no. 8, pp. 734–736, Aug 1985.

[52] K. M. Leung and Y. F. Liu, "Full vector calculation of photonic band structures in face-centered-cubic dielectric media," *Physical Review Letters*, vol. 65, no. 21, pp. 2646–2649, Nov 1990.

[53] W. Y. Leung, R. Biswas, S.-D. Cheng, M. M. Sigalas, J. S. McCalmont, G. Tuttle, and K.-M. Ho, "Slot antennas on photonic band gap crystals," *IEEE Transactions on Antennas and Propagation*, vol. AP-45, no. 10, pp. 1569–1570, Oct 1997.

[54] D. Levin, "Development of nonlinear transformations for improving convergence of sequences," *International Journal of Computational Mathematics*, vol. 3, no. B, pp. 371–388, 1973.

[55] L. R. Lewis and A. Hessel, "Propagation constants of periodic arrays of dielectric slabs," *IEEE Transactions on Microwave Theory and Techniques*, vol. MTT-19, pp. 276–286, Mar 1971.

[56] D. E. Livesay and K.-M. Chen, "Electromagnetic field induced inside arbitrary shaped biological bodies," *IEEE Transactions on Microwave Theory and Techniques*, vol. MTT-22, no. 12, pp. 1273–1280, Dec 1974.

[57] J. Maddox, "Do photonic band-gaps really exist?," *Nature*, vol. 348, pp. 481, 1990.

[58] A. A. Maradudin and A. R. McGurn, "Photonic band structure of a truncated, two-dimensional, periodic dielectric medium," *Journal of the Optical Society of America B*, vol. 10, no. 2, pp. 307–313, Feb 1993.

[59] A. A. Maradudin and A. R. McGurn, "Out-of-plane propagation of electromagnetic waves in a two-dimensional periodic dielectric medium," *Journal of Modern Optics*, vol. 41, no. 2, pp. 275–284, 1994.

[60] S. L. McCall, P. M. Platzman, R. Dalichaouch, D. Smith, and S. Schultz, "Microwave propagation in two-dimensional dielectric lattice," *Physical Review Letters*, vol. 67, no. 17, pp. 2017–2020, Oct 1991.

[61] D. T. McGrath and V. P. Pyati, "Periodic structure analysis using a hybrid finite element method," *Radio Science*, vol. 31, no. 5, pp. 1173–1179, Sep-Oct 1996.

[62] A. R. McGurn and A. A. Maradudin, "Photonic band structures of two- and three-dimensional periodic metal or semiconductor arrays," *Physics Review B*, vol. 48, no. 23, pp. 17576–17579, Dec 1993.

[63] R. D. Meade, O. Alerhand, and J. D. Joannopoulos, *Handbook of Photonic Band-Gap Materials*, JAMTex, Belmont, MA, 1993.

[64] R. D. Meade, K. D. Brommer, A. M. Rappe, and J. D. Joannopoulos, "Existence of a photonic band gap in two dimensions," *Applied Physics Letters*, vol. 61, no. 27, pp. 495–497, Jul 1992.

[65] E. Michielssen, *Electromagnetic Plane Wave Scattering from Periodically Loaded Cylinders and Doubly Periodic Slabs*, PhD dissertation, University of Illinois, Urbana-Champaign, 1992.

[66] R. Mittra, C. H. Chan, and T. Cwik, "Techniques for analyzing frequency selective surfaces – a review," *Proceedings of the IEEE*, vol. 76, no. 12, pp. 1593–1614, Dec 1988.

[67] B. A. Munk and G. A. Burrell, "Plane wave expansion for arrays of arbitrarily oriented piecewise linear elements and its application in determining the impedance of a single linear antenna in a lossy half-space," *IEEE Transactions on Antennas and Propagation*, vol. AP-27, no. 3, pp. 331–343, May 1979.

[68] R. M. Nelson, D. A. Rogers, and A. G. D'Assunção, "Resonant frequency of a rectangular microstrip patch on several uniaxial substrates," *IEEE Transactions on Antennas and Propagation*, vol. 38, no. 7, pp. 973–981, Jul 1990.

[69] A. A. Oliner, "Periodic structures and photonic band-gap terminology: historical perspectives," in *29th European Microwave Conference*, Oct 1999.

[70] A. Papoulis, *The Fourier Integral and Its Applications*, McGraw–Hill, New York, NY, 1962.

[71] M.-J. Park, J. Park, and S. Nam, "Efficient calculation of the Green's function for the rectangular cavity," *IEEE Microwave and Guided Wave Letters*, vol. 8, no. 3, pp. 1958–1962, Mar 1998.

[72] S. T. Peng, T. Tamir, and H. L. Bertoni, "Theory of periodic dielectric waveguides," *IEEE Transactions on Microwave Theory and Techniques*, vol. MTT-23, no. 1, pp. 123–133, Jan 1975.

[73] M. Plihal, A. Shambrook, A. A. Maradadin, and P. Sheng, "Two-dimensional photonic band structures," *Optics Communications*, vol. 80, no. 3/4, pp. 199–204, Jan 1991.

[74] D. M. Pozar, "Radiation and scattering from a microstrip patch antenna on a uniaxial substrate," *IEEE Transactions on Antennas and Propagation*, vol. AP-35, no. 6, pp. 613–621, Jun 1987.

[75] D. M. Pozar, "Microstrip antennas," *Proceedings of the IEEE*, vol. 80, no. 1, pp. 79–91, Jan 1992.

[76] Y. Rahmat-Samii, "On the question of computation of the dyadic Green's function at the source region in waveguide cavities," *IEEE Transactions on Microwave Theory and Techniques*, vol. MTT-23, no. 9, pp. 762–765, Sept 1975.

[77] R. Remski, "Modeling and optimizing photonic bandgap (PBG) structures," in *Ansoft "No Boundaries" Workshop*, Baltimore, MD, October 2000.

[78] P. A. Rizzi, *Microwave Engineering*, Prentice Hall, Englewood Cliffs, NJ, 1988.

[79] S. V. Robertson, L. P. B. Katehi, and G. M. Rebeiz, "A planar quasi-optical mixer using a folded-slot antenna," *IEEE Transactions on Microwave Theory and Techniques*, vol. MTT-43, no. 4, pp. 896–898, Apr 1995.

[80] P. Russell, "Photonic band-gaps," *Physics World*, vol. 5, no. 8, pp. 37–42, 1 Aug 1992.

[81] D. B. Rutledge, D. P. Neikirk, and D. P. Kasilingham, "Integrated-circuit antennas," in *Millimeter Components and Techniques, Part II*, K. J. Button, editor, vol. 10 of *Infrared and Millimeter Waves*, chapter 1, pp. 1–90, Academic Press, Orlando, FL, 1983.

[82] S. M. Rytov, "Electromagnetic properties of a finely stratified medium," *Soviet Physics Journal of Experimental and Theoretical Physics of the Academy of Science of the USSR*, vol. 2, pp. 466–475, 1956.

[83] M. N. O. Sadiku, *Numerical Techniques in Electromagnetics*, CRC Press, Boca Raton, FL, 1992.

[84] K. Sarabandi, *Electromagnetic Scattering from Vegetation Canopies*, PhD dissertation, University of Michigan, 1989.

[85] K. Sarabandi, "Simulation of a periodic dielectric corrugation with an equivalent anisotropic layer," *International Journal of Infrared and Millimeter Waves*, vol. 11, no. 11, pp. 1303–1321, Nov 1990.

[86] K. Sarabandi and P. F. Polatin, "Electromagnetic scattering from two adjacent objects," *IEEE Transactions on Antennas and Propagation*, vol. AP-42, no. 4, pp. 510–517, Apr 1994.

[87] K. Sarabandi and F. T. Ulaby, "High frequency scattering from corrugated stratified cylinders," *IEEE Transactions on Antennas and Propagation*, vol. AP-39, no. 4, pp. 512–520, Apr 1991.

[88] M. Scalora, M. J. Bloemer, J. P. Dowling, C. M. Bowden, and A. S. Manka, "Transparent, metallo-dielectric, one-dimensional, photonic band-gap structures," *Journal of Applied Physics*, vol. 83, no. 5, pp. 2377–2383, Mar 1998.

[89] D. H. Schaubert, "Microstrip antennas," *Electromagnetics*, vol. 12, pp. 381–401, 1992.

[90] D. Shanks, "Non-linear transformations of divergent and slowly convergent sequences," *Journal of Mathematical Physics*, vol. 34, pp. 1–42, 1955.

[91] J. D. Shumpert, W. J. Chappell, and L. P. B. Katehi, "Parallel-plate mode reduction in conductor-backed slots using electromagnetic band-gap substrates," *IEEE Transactions on Microwave Theory and Techniques*, vol. MTT-47, no. 11, pp. 2099–2105, Nov 1999.

[92] J. D. Shumpert, T. Ellis, G. M. Rebeiz, and L. P. B. Katehi, "Microwave and millimeter-wave propagation through photonic band-gap structures," in *1997 URSI North American Radio Sciece Meeting Digest*, p. 678, Jul 1997.

[93] J. D. Shumpert, T. Ellis, G. M. Rebeiz, and L. P. B. Katehi, "Microwave and millimeter-wave propagation in photonic band-gap structures," Radiation Lab Report RL-953, The University of Michigan, Oct 1997.

[94] J. D. Shumpert, T. Ellis, G. M. Rebeiz, and L. P. B. Katehi, "Two-dimensional band-gap formation in finite substrates," in *1998 URSI North American Radio Science Meeting Digest*, p. 123, Jun 1998.

[95] M. M. Sigalas, R. Biswas, and K.-M. Ho, "Theoretical study of dipole antennas on photonic band-gap materials," *Microwave and Optical Technology Letters*, vol. 13, no. 4, pp. 205–209, Nov 1996.

[96] M. M. Sigalas, R. Biswas, K. M. Ho, and C. M. Soukoulis, "Theoretical investigation of off-plane propagation of electromagnetic waves in two-dimensional photonic crystals," *Physical Review B*, vol. 58, no. 11, pp. 6791–6794, Sept 1998.

[97] M. M. Sigalas, R. Biswas, Q. Li, D. Crouch, W. Leung, R. Jacobs-Woodbury, B. Laogh, S. Nielsen, S. McCalmont, G. Tuttle, and K.-M. Ho, "Dipole antennas on photonic band-gap crystals: experiment and simulation," *Microwave and Optical Technology Letters*, vol. 15, no. 3, pp. 153–158, Jun 1997.

[98] J. Singh, *Quantum Mechanics: Fundamentals and Applications to Technology*, John Wiley & Sons, Inc., New York, NY, 1997.

[99] S. Singh, W. F. Richards, J. R. Zinecker, and D. R. Wilton, "Accelerating the convergence of series representing the free space periodic Green's function," *IEEE Transactions on Antennas and Propagation*, vol. AP-38, no. 12, pp. 1958–1962, Dec 1990.

[100] S. Singh and R. Singh, "Application of transforms to accelerate the summation of periodic free-space Green's functions," *IEEE Transactions on Microwave Theory and Techniques*, vol. MTT-38, no. 11, pp. 1746–1748, Nov 1990.

[101] S. Singh and R. Singh, "Efficient computation of the free-space periodic Green's function," *IEEE Transactions on Microwave Theory and Techniques*, vol. MTT-39, no. 7, pp. 1226–1229, Jul 1991.

[102] S. Singh and R. Singh, "On the use of ρ algorithm in series acceleration," *IEEE Transactions on Antennas and Propagation*, vol. AP-39, no. 10, pp. 1514–1517, Oct 1991.

[103] S. Singh and R. Singh, "On the use of Shanks' transform to accelerate the summation of slowly converging series," *IEEE Transactions on Microwave Theory and Techniques*, vol. MTT-39, no. 3, pp. 608–610, Mar 1991.

[104] S. Singh and R. Singh, "A convergence acceleration procedure for computing slowly converging series," *IEEE Transactions on Microwave Theory and Techniques*, vol. MTT-40, no. 1, pp. 168–171, Jan 1992.

[105] S. Singh and R. Singh, "On the use of Chebyshev-Toeplitz algorithm in accelerating the numerical convergence of infinite series," *IEEE Transactions on Microwave Theory and Techniques*, vol. MTT-40, no. 1, pp. 171–173, Jan 1992.

[106] S. Singh and R. Singh, "On the use of Levin's t-transform in accelerating the summation of series representing the free-space Green's functions," *IEEE Transactions on Microwave Theory and Techniques*, vol. MTT-41, no. 5, pp. 884–886, May 1993.

[107] D. R. Smith, R. Dalichaouch, N. Kroll, S. Schultz, S. L. McCall, and P. M. Platzman, "Photonic band structure and defects in one and two dimensions," *Journal of the Optical Society of America B*, vol. 10, no. 2, pp. 314–321, Feb 1993.

[108] J. A. Stratton, *Electromagnetic Theory*, McGraw–Hill, New York, NY, 1941.

[109] W. L. Stutzman, "Estimating directivity and gain of antennas," *IEEE Antennas and Propagation Magazine*, vol. 40, no. 4, pp. 7–10, Aug 1998.

[110] W. L. Stutzman and G. A. Thiele, *Antenna Theory and Design*, John Wiley & Sons, Inc., New York, NY, second edition, 1998.

[111] C.-T. Tai, *Dyadic Green Functions in Electromagnetic Theory*, IEEE Press, New York, NY, second edition, 1994.

[112] A. Tavakoli, K. Sarabandi, and F. T. Ulaby, "Horizontal propagation through periodic vegetation canopies," *IEEE Transactions on Antennas and Propagation*, vol. AP-39, no. 7, pp. 1014–1023, Jul 1991.

[113] W.-J. Tsay, *Radiation and Scattering from Periodic Geometries in Inhomogeneous Media*, PhD dissertation, University of Massachusetts Amherst, 1995.

[114] W.-J. Tsay and D. M. Pozar, "Radiation and scattering from infinite periodic printed antennas with inhomogeneous media," *IEEE Transactions on Antennas and Propagation*, vol. AP-46, no. 11, pp. 1641–1650, Nov 1998.

[115] B. Veidt, "Selecting 3-D electromagnetic software," *Microwave Journal*, vol. 41, no. 9, pp. 126–137, Sept 1998.

[116] P. R. Villeneuve and M. Piché, "Photonic band gaps in two-dimensional square and hexagonal lattices," *Physical Review B*, vol. 46, no. 8, pp. 4969–4972, Aug 1992.

[117] P. R. Villeneuve and M. Piché, "Photonic band gaps in two-dimensional square lattices: square and circular rods," *Physical Review B*, vol. 46, no. 8, pp. 4973–4975, Aug 1992.

[118] J. J. H. Wang, "Analysis of a three-dimensional arbitrary shaped dielectric or biological body inside a rectangular waveguide," *IEEE Transactions on Microwave Theory and Techniques*, vol. MTT-26, no. 7, pp. 457–462, Aug 1978.

[119] J. J. H. Wang, *Generalized Moment Methods in Electromagnetics: Formulation and Computer Solution of Integral Equations*, John Wiley & Sons, Inc., New York, NY, 1991.

[120] E. T. Whittaker and G. N. Watson, *A Course of Modern Analysis*, Cambridge University Press, Cambridge, MA, fourth edition, 1927.

[121] J. Wimp, "Toeplitz arrays, linear sequence transformations, and orthogonal polynomials," *Numerical Mathematics*, vol. 23, pp. 1–17, 1974.

[122] J. N. Winn, R. D. Meade, and J. D. Joannolpoulos, "Two-dimensional photonic bandgap materials," *Journal of Modern Optics*, vol. 41, no. 2, pp. 257–273, 1994.

[123] K.-L. Wong, J.-S. Row, C.-W. Kuo, and K.-C. Huang, "Resonance of a rectangular microstrip patch on a uniaxial substrate," *IEEE Transactions on Microwave Theory and Techniques*, vol. MTT-41, no. 4, pp. 698–701, Apr 1993.

[124] P. Wynn, "On a device for computing the $e_m(s_n)$ transformation," *Mathematical Tables and Other Aids for Computation*, vol. 10, pp. 91–96, 1956.

[125] E. Yablonovitch, "Inhibited spontaneous emission in solid-state physics and electronics," *Physical Review Letters*, vol. 58, no. 2, pp. 2059–2062, 1987.

[126] E. Yablonovitch and T. J. Gmitter, "Photonic band structure: the face-centered-cubic case," *Physical Review Letters*, vol. 63, no. 18, pp. 1950–1953, 1989.

[127] E. Yablonovitch, T. J. Gmitter, and K. M. Leung, "Photonic band structure: the face-centered-cubic case employing non-spherical atoms," *Physical Review Letters*, vol. 67, no. 17, pp. 2295–2298, Oct 1991.

[128] C.-F. Yang, W. D. Burnside, and R. C. Rudduck, "A doubly periodic moment method solution for the analysis and design of an absorber covered wall," *IEEE Transactions on Antennas and Propagation*, vol. AP-41, no. 5, pp. 600–609, May 1993.

[129] H.-Y. Yang, "Finite difference analysis of 2-D photonic crystals," *IEEE Transactions on Microwave Theory and Techniques*, vol. MTT-44, no. 12, pp. 2688–2695, Dec 1996.

[130] H.-Y. Yang, "Characteristics of guided and leaky waves on multilayer thin-film structures with planar material gratings," *IEEE Transactions on Microwave Theory and Techniques*, vol. MTT-45, no. 3, pp. 428–435, Mar 1997.

[131] H.-Y. Yang and J. A. Castaneda, "Infinite phased arrays of microstrip antennas on generalized anisotropic substrates," *Electromagnetics*, vol. 11, pp. 107–124, 1991.

[132] H.-Y. Yang, J. A. Casteneda, and N. G. Alexopolous, "An integral equation analysis of an infinite array of rectangular dielectric waveguides," *IEEE Transactions on Microwave Theory and Techniques*, vol. MTT-38, no. 7, pp. 873–879, Jul 1990.

[133] H.-Y. D. Yang, "Theory of antenna radiation from photonic band-gap materials," *Electromagnetics*, vol. 19, no. 3, pp. 255–276, May-June 1999.

[134] H.-Y. D. Yang, "Theory of microstrip lines on artificial periodic substrates," *IEEE Transactions on Microwave Theory and Techniques*, vol. MTT-47, no. 5, pp. 629–635, May 1999.

[135] H.-Y. D. Yang, N. G. Alexopolous, and E. Yablonovitch, "Photonic band-gap materials for high-gain printed circuit antennas," *IEEE Transactions on Antennas and Propagation*, vol. AP-45, no. 1, pp. 185–187, Jan 1997.

[136] H.-Y. D. Yang, R. Diaz, and N. G. Alexopolous, "Reflection and transmission of waves from multilayer structures with planar-implanted periodic material blocks," *Journal of the Optical Society of America B*, vol. 14, no. 10, pp. 2513–2521, Oct 1997.

[137] A. Yariv and P. Yeh, *Optical Waves in Crystals*, John Wiley & Sons, Inc., New York, NY, 1984.

[138] Z. Zhang and S. Satpathy, "Electromagnetic wave propagation in periodic structures: bloch wave solution of Maxwell's equations," *Physical Review Letters*, vol. 65, no. 21, pp. 2650–2653, Nov 1990.

[139] *IMSL Fortran 90 MP Numerical Libraries Version 3.0.*